分 类 号: O572　　**单位代码**: 10422
密　　级: **公开**　　**学　　号**: 201812156

博士学位论文

Dissertation for Doctoral Degree

论文题目： RHIC-STAR **实验上极化质子-质子对撞中纵向双自旋不对称和自旋转移的测量**

Measurements of Longitudinal Double Spin Asymmetry and Spin Transfer in Polarized Proton-Proton Collisions at RHIC-STAR

作 者 姓 名 于毅

培 养 单 位 前沿交叉科学青岛研究院

专 业 名 称 粒子物理与原子核物理

指 导 教 师 徐庆华教授

合 作 导 师

2024 年 5 月 30 日

原 创 性 声 明

本人郑重声明：所呈交的学位论文，是本人在导师指导下，独立进行研究所取得的成果。除文中已经注明引用的内容外，本论文不包含任何其他个人或集体已经发表或撰写过的科研成果。对本论文的研究作出重要贡献的个人和集体，均已在文中以明确方式标明。本声明的法律责任由本人承担。

论文作者签名：_____ 日 期：_____

关于学位论文使用授权的声明

本人完全了解山东大学有关保留、使用学位论文的规定，同意学校保留或向国家有关部门或机构送交论文的复印件和电子版，允许论文被查阅和借阅；本人授权山东大学可以将本学位论文全部或部分内容编入有关数据库进行检索，可以采用影印、缩印或其他复制手段保存论文和汇编本学位论文。

（保密的论文在解密后应遵守此规定）

论文作者签名：_____ 导师签名：_____ 日 期：_____

分 类 号: O572　　单位代码: 10422
密　　级: 公开　　学　　号: 201812156

山东大学
SHANDONG UNIVERSITY

博士学位论文

Dissertation for Doctoral Degree

论文题目: RHIC-STAR实验上极化质子-质子对撞中纵向双自旋不对称和自旋转移的测量
Measurements of Longitudinal Double Spin Asymmetry and Spin Transfer in Polarized Proton-Proton Collisions at RHIC-STAR

作者姓名 于毅
培养单位 前沿交叉科学青岛研究院
专业名称 粒子物理与原子核物理
指导教师 徐庆华教授
合作导师

2024年5月30日

原 创 性 声 明

本人郑重声明：所呈交的学位论文，是本人在导师指导下，独立进行研究所取得的成果。除文中已经注明引用的内容外，本论文不包含任何其他个人或集体已经发表或撰写过的科研成果。对本论文的研究作出重要贡献的个人和集体，均已在文中以明确方式标明。本声明的法律责任由本人承担。

论文作者签名：于毅 日 期：2024年5月30日

关于学位论文使用授权的声明

本人完全了解山东大学有关保留、使用学位论文的规定，同意学校保留或向国家有关部门或机构送交论文的复印件和电子版，允许论文被查阅和借阅；本人授权山东大学可以将本学位论文全部或部分内容编入有关数据库进行检索，可以采用影印、缩印或其他复制手段保存论文和汇编本学位论文。

（保密的论文在解密后应遵守此规定）

论文作者签名：于毅 导师签名：徐玲华 日 期：2024年5月30日

摘　要

对于如何理解质子的自旋结构一直是量子色动力学（QCD）领域中一个具有挑战性的问题。1988 年 EMC 合作组发表了关于质子的自旋依赖的结构函数 g_1 的测量结果，这一令人吃惊的结果显示出夸克和反夸克的自旋对质子自旋的贡献很小。这一结果与夸克模型的预测大相径庭，由此引发了对质子自旋结构的深入研究。目前，通过单举的极化轻子-强子深度非弹性散射（DIS）实验和半单举 DIS（SIDIS）实验的测量得知，夸克和反夸克的自旋对质子自旋的贡献大约仅占 30%，其余贡献来自胶子的自旋以及夸克和胶子的轨道角动量。在 QCD 部分子模型中，在纵向极化的质子中，部分子（夸克和胶子）的自旋分布由纵向极化的部分子分布函数，又称螺旋度分布函数，描述。目前，价夸克（u 夸克和 d 夸克）的螺旋度分布函数已经通过 DIS 实验和 SIDIS 实验得到了很好的限制。然而，由于轻子不参与强相互作用，DIS 实验和 SIDIS 实验无法直接探测胶子的螺旋度分布。因此，在这类实验中对其的限制也相对较差。此外，由于 SIDIS 实验中所引入的碎裂函数目前仍有相对较大的误差，所以海夸克的螺旋度分布也没有得到很好的限制。

美国布鲁克海文国家实验室的相对论重离子对撞机（RHIC）是世界上第一台也是目前唯一一台可以运行高能极化质子-质子对撞的对撞机。它能够在对撞质心能量 200 GeV 和 510 GeV 下进行纵向极化和横向极化的质子-质子对撞。纵向极化的质子-质子对撞为研究质子内部胶子和海夸克的螺旋度分布提供了独特的机会。2005 年以来，RHIC 上开展了一系列单举的喷注和双喷注的纵向双自旋不对称 A_{LL} 的测量。测量结果发现在部分子所占质子动量分数 $0.05 < x < 0.2$ 内胶子具有相当大的正向极化。然而，杰斐逊实验室角动量（JAM）合作组最近提出，RHIC 上对于单举的喷注的 A_{LL} 的测量并不能排除胶子具有负的极化的可能。在 RHIC 能区，夸克-胶子的散射是其中一个主导的 QCD 部分子散射过程。因为 u 夸克和 d 夸克的螺旋度分布函数的符号是相反的，所以它们跟胶子的散射对于胶子的螺旋度分布函数的符号是敏感的。同时，由于在碎裂过程中 u 夸克和 d 夸克分别倾向于产生领头的 π^+ 介子和 π^- 介子，因此通过测量 $\pi^\pm$ 介子标记的喷注的纵向双自旋不对称 A_{LL} 可以对胶子螺旋度分布函数的符号提供限制。

另一方面，目前奇异夸克和反奇异夸克的螺旋度分布在实验上仍然没有很好的限制。由于 Λ、$\overline{\Lambda}$ 和 K^0_S 中包含奇异夸克或反奇异夸克，因此测量这些粒子的纵向双自旋不对称 A_{LL} 可以对奇异夸克和反奇异夸克的螺旋度分布提供限制。此外，理论研究表明，在极化的质子-质子对撞中，Λ 和 $\overline{\Lambda}$ 超子的纵向自旋转移 D_{LL} 不仅对奇异夸克和反奇异夸克的螺旋度分布敏感，还可以探测相对应的极化的碎裂函数。值

得一提的是，最近的理论计算表明，测量 D_{LL} 随着 Λ 超子所携带喷注的动量分数 z 的变化可以直接对极化的碎裂函数提供约束。

2015 年，RHIC 运行了最后一次纵向极化的质子-质子对撞，对撞的质心能量是 200 GeV。STAR 实验采集了积分亮度大约为 52pb^{-1} 的对撞数据，这是在该能量下 RHIC 上所采集的最大的数据样本。利用这个数据样本，我们首次测量了 $\pi^{\pm}$ 标记的喷注、Λ 超子和 K^0_S 的纵向双自旋不对称 A_{LL}。对 Λ 超子纵向自旋转移 D_{LL} 随着超子横动量 p_T 的变化进行了更加精确的测量。同时，首次测量了 D_{LL} 随着超子所携带的喷注的动量分数 z 的变化。

对于 $\pi^{\pm}$ 标记的喷注的 A_{LL} 的测量，结果显示 $A^{\pi^+}_{LL}$ 大于 $A^{\pi^-}_{LL}$。基于 PYTHIA 模拟的样本，我们分别利用 NNPDF 合作组和 JAM 合作组给出的螺旋度分布对 A_{LL} 进行了计算。NNPDF 合作组给出的胶子的螺旋度分布函数的符号是正的，而 JAM 合作组给出的胶子的螺旋度分布函数的符号是负的。测量的结果符合基于 NNPDF 合作组的螺旋度分布函数的计算，明显不符合基于 JAM 合作组的螺旋度分布函数的计算。因此，实验测量结果不支持胶子螺旋度分布函数为负的假设。对于 Λ 超子和 K^0_S 的 A_{LL} 的首次测量，在误差范围内与零一致，表明奇异夸克和反奇异夸克的螺旋度分布较小。对于 D_{LL} 随着超子 p_T 的测量结果，分析中使用的数据大约比 STAR 2009 年所采集的数据大了 2 到 3 倍，并且新的测量将超子的 p_T 扩展到 8 GeV/c。我们将新的测量结果与之前使用 STAR 2009 年采集的数据的测量结果进行了合并，并且跟基于不同极化的碎裂函数的假设的理论预言进行了比较。我们的测量结果排除了其中一个假设。首次对 D_{LL} 随着 z 的变化的测量也与理论预测进行了比较。测得的 D_{LL} 结果相对较小。这一结果表明奇异夸克和反奇异夸克的螺旋度分布较小或者极化碎裂函数较小。这些测量为研究胶子极化、奇异夸克螺旋度分布和极化碎裂函数提供了重要的实验输入。

关键词: 质子自旋结构; 螺旋度分布函数; 纵向双自旋不对称; 纵向自旋转移; RHIC-STAR

ABSTRACT

Understanding the spin structure of the proton has been a challenging question in the Quantum Chromodynamics (QCD). The first surprising result on the measurement of the proton spin-dependent g_1 structure function from the EMC Collaboration indicates that quark and anti-quark spin contribute little to the proton spin. This result is in great contradiction with the prediction from naive quark model and inspired tremendous studies in the understanding of the spin decomposition of the proton. Precision measurements from the inclusive polarized lepton-nucleon deep inelastic scattering (DIS) experiments and semi-inclusive DIS (SIDIS) experiments have confirmed that the contribution of quark and anti-quark spin to the proton spin only counts for about 30% with the remaining contribution from the spin of the gluons and orbital angular momentum of quarks and gluons. In the QCD parton model, the parton (quarks and gluons) spin in a longitudinally polarized proton is described by the longitudinally polarized parton distribution function, namely the helicity distribution. Helicity distributions for the valence quarks, u quark and d quark, have been well constrained by the DIS and the SIDIS experiments. However, as the lepton does not participate in the strong interaction, the helicity distribution of the gluon cannot be directly probed, and was poorly constrained in such experiments. In addition, due to the relatively large uncertainties of the fragmentation functions involved in the SIDIS experiments, helicity distributions of sea quarks were not well constrained either.

The Relativistic Heavy Ion Collider (RHIC), located at the Brookhaven National Laboratory in the US, is the first and only high energy polarized proton-proton collider around the world. It is capable to collide both longitudinally and transversely polarized proton-proton beams at $\sqrt{s}$ = 200 GeV and $\sqrt{s}$ = 510 GeV. The longitudinally polarized proton-proton collisions provide unique opportunities to study the helicity distributions of the gluons and sea quarks. Series measurements of the longitudinal double spin asymmetry, A_{LL}, for inclusive jets and di-jets since 2005 have confirmed a sizeable positive gluon polarization in the x range $0.05 < x < 0.2$. However, the Jefferson Lab Angular Momentum (JAM) Collaboration recently proposed that the A_{LL} measurements for inclusive jets do not exclude negative solution of the gluon polarization. At RHIC energy, the quark-gluon scattering is one of the dominant QCD subprocesses. In addition, the helicity distributions of the u quark and d quark are in

opposite sign. The A_{LL} of the $\pi^{\pm}$-tagged jets is thus expected to be sensitive to the sign of the gluon helicity distribution as the u quark and d quark favor π^{+} and π^{-} in the fragmentation processes, respectively.

On the other hand, the helicity distributions of the strange quark and anti-quark are still poorly constrained by the experimental data. The A_{LL} of the Λ, $\overline{\Lambda}$ and K^{0}_{S} is expected to be sensitive to the helicity distributions of the strange quark and anti-quark as they all contain a valence (anti-)strange quark. In addition, theoretical studies have shown that the longitudinal spin transfer D_{LL} of the Λ and $\overline{\Lambda}$ in the polarized proton-proton collisions can not only shed light on the helicity distributions of the strange quark and anti-quark but also can probe the polarized fragmentation functions. It is worth mentioning that recent theoretical calculations suggest that measurements of D_{LL} as a function of jet momentum fraction z carried by the Λ hyperons can provide direct constraints on the polarization fragmentation function.

In 2015, RHIC concluded its longitudinally polarized proton-proton collisions with the largest $\sqrt{s} = 200$ GeV data set taken at STAR, which corresponds to an integrated luminosity of about 52 pb^{-1}. With this data set, we performed the first measurements of the A_{LL} of the $\pi^{\pm}$-tagged jets, Λ hyperons and K^{0}_{S}, and the improved measurements of D_{LL} as a function of the hyperon p_T and the first measurements of the D_{LL} as a function of momentum fraction z in a jet.

For the $\pi^{\pm}$-tagged jets A_{LL} measurements, we found that the $A^{\pi^{+}}_{LL}$ is larger than $A^{\pi^{-}}_{LL}$. Predictions based on PYTHIA simulation using the helicity distributions from the NNPDF Collaboration and the JAM Collaboration are compared with the measurements. The gluon helicity distribution from the NNPDF Collaboration is positive while the gluon helicity distribution from the JAM Collaboration can be chosen to be negative. The predictions based on the helicity distributions from NNPDF Collaboration can describe the measurements. However, the measurements strongly disfavor the predictions based on the negative solution of gluon helicity distributions from the JAM Collaboration. Thus, the measurements disfavor the negative gluon helicity distribution. The first measurements of the A_{LL} for Λ hyperons and K^{0}_{S} are consistent with zero within uncertainties indicating small helicity distributions of the strange quark and anti-quark. For the D_{LL} vs p_T measurements, the statistics used in the analysis are about 2-3 times larger than the D_{LL} measurements using the STAR 2009 data. This analysis extends the hyperon p_T up to 8 GeV/c. We combined the new measurements

with previously published results using STAR 2009 data, and theoretical calculations based on three scenarios of the polarized fragmentation functions are compared with measurements. Our measurements strongly disfavor one extreme scenario. The first measurements of the D_{LL} vs z are also compared with the theoretical predictions. The measured D_{LL} results are small and consistent with zero, which indicate small helicity distributions of the strange quark and anti-quark and/or small polarized fragmentation functions. These measurements provide important experimental inputs in the study of gluon polarization, strange quark helicity distribution and polarized fragmentation functions.

Key words: proton spin structure; helicity distribution; longitudinal double spin asymmetry; longitudinal spin transfer; RHIC-STAR

目 录

Contents

List of Figures

List of Tables

Chapter 1 Introduction

In 1917, the proton was discovered by Ernest Rutherford [1], which at that time was thought to be a fundamental particle. About 10 years later, the spin-$\frac{1}{2}$ nature of the proton was revealed [2]. Subsequently, the measurement of its magnetic moment [3-4] shown a notable deviation from the expected value of a point-like particle [5]. The surprising anomalous magnetic moment of the proton since then challenged our understanding of the proton structure indicating firstly the composite nature of the proton. In 1964, the quark model has been proposed independently by Murray Gell-Mann and George Zweig [6-8] and achieved great success in the classification of the discovered hadrons. In the quark model, the proton is composed of three spin-$\frac{1}{2}$ quarks, namely two u quarks and one d quark. The deep inelastic scattering experiments conducted in last 1960's refreshed the understanding of the internal structure of the proton. In particular, for the spin structure of the proton, the surprising EMC results [9-10] in the late 1980's since then triggered tremendous efforts on the understanding of the proton spin structure. In this chapter, I will present an brief overview about journey in understanding the proton spin structure starting from the deep inelastic scattering experiments. I will then focus on the experiments conducted at the Relativistic Heavy Ion Collider, which are relevant to the work presented in this thesis. A brief guide about the structure of the thesis will be presented at the end of this chapter.

1.1 The Lepton-Nucleon Deep Inelastic Scattering

1.1.1 Unpolarized Lepton-Nucleon Deep Inelastic Scattering and Parton Distribution Functions

Historically, our knowledge about the internal structure of the proton was firstly obtained via the lepton-nucleon deep inelastic scattering (DIS) experiments. In DIS, a high-energy lepton (such as an electron or a muon) is scattered off a target nucleon (proton or neutron). The interaction between the lepton and the nucleon is mainly mediated via a virtual photon transferring large momentum q between the lepton and the nucleon. The virtual photon interacts with the internal objects of the nucleon and breaks the nucleon up, which is schematically shown in Fig. 1.1. Detailed introduction

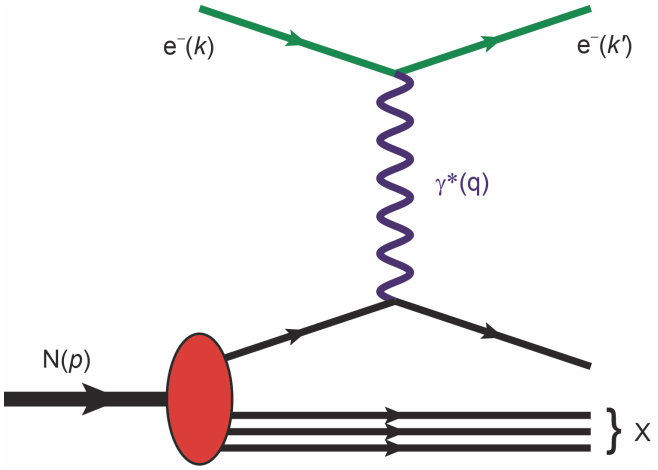

Figure 1.1: Schematic diagram of the deep inelastic scattering mediated by a virtual photon. The diagram is taken from Ref. [15]

about DIS process can be found in Refs. [11-14].

One of the key observables in DIS is the inclusive cross section of the scattered lepton, which can be expressed as the following:

$$\frac{\mathrm{d}^2\sigma}{\mathrm{d}x\mathrm{d}Q^2} = \frac{4\pi\alpha^2}{Q^4}\left[\left(1-y-\frac{M^2y^2}{Q^2}\right)\frac{F_2\left(x,Q^2\right)}{x}+y^2F_1\left(x,Q^2\right)\right], \tag{1.1}$$

where $Q^2 \equiv -q^2$ is the momentum transfer squared and q is the momentum of the mediated virtual photon. $x \equiv Q^2/2Mq$ is the so-called Bjorken x. $F_1(x,Q^2)$ and $F_2(x,Q^2)$ are the structure functions describing the internal structure of the scattered nucleon. A set of DIS experiments have been firstly conducted at the Spectrometer Facility of the Stanford Linear Accelerator (SLAC) in the late 1967 with electron beams scattering off a liquid hydrogen. Two striking features of the structure functions have been revealed in the experiments:

- **Bjorken Scaling**: $F_1(x,Q^2)$ and $F_2(x,Q^2)$ are almost independent with the Q^2, namely $F_1(x,Q^2) \to F_1(x)$ and $F_2(x,Q^2) \to F_2(x)$.
- **Callan-Gross Relation**: $2xF_1(x) = F_2(x)$

The Q^2 reflects the spatial resolution of the virtual photon. Constant structure functions indicate that the virtual photon interact with some point-like particles inside the nucleon and the Callan-Gross relation reflects their spin-$\frac{1}{2}$ nature of such particles. Figure 1.2 illustrates two features of the structure functions discovered at SLAC. Sub-

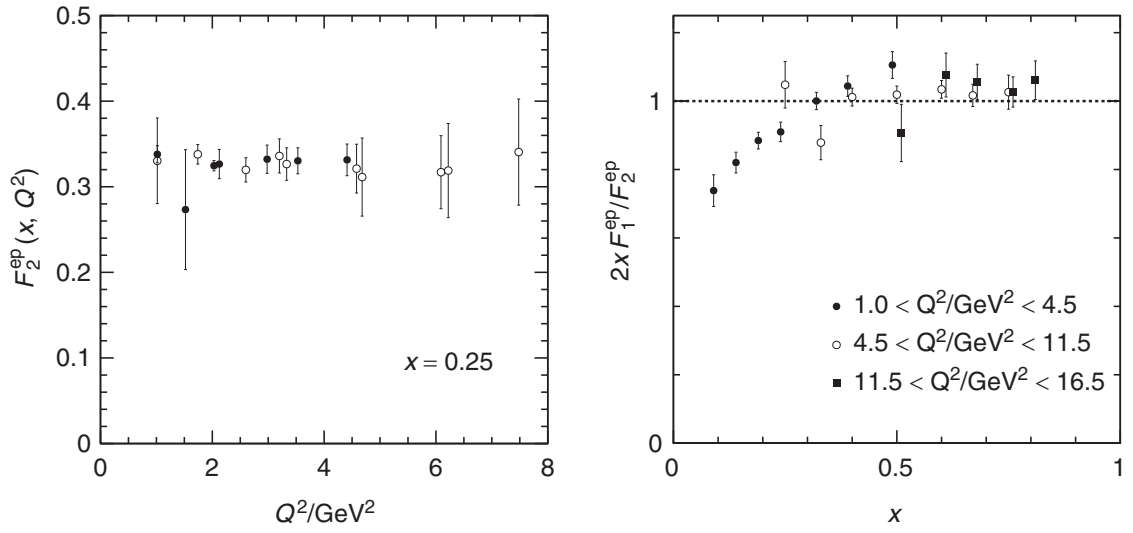

Figure 1.2: Measured structure functions at SLAC. Left: the structure function F_2 as a function of Q^2 showing Bjorken scaling. Right: the measured $2xF_1/F_2$ showing Callan-Gross relation. Plots are taken from Ref. [14].

sequent experiments extended the coverage of x and Q^2. Figure 1.3 shows the world data of the measured F_2 as a function of Q^2. The groundbreaking discoveries at SLAC inspired Richard Feynman and others to formulate and develop the parton model [16-17]. In the model, a nucleon is composited of free, point-like particles called 'parton' and the basic process in DIS is the elastic scattering between the virtual photon and the parton described with the parton distribution function (PDF) formulated in the so-called 'infinite momentum frame'. The structure functions $F_1(x)$ and $F_2(x)$ are defined in terms of PDFs as following:

$$F_2(x) = 2xF_1(x) = x\sum_i e_q^2 q(x), \tag{1.2}$$

where e_q is the electric charge of a parton, which has been confirmed to be fractional charge and has been linked to quark postulated in the quark model [6-8]. x is the momentum fraction of the nucleon carried by a parton. DIS experiments and the parton model plays an important role in the establishment of the Quantum Chromodynamics (QCD), a fundamental quantum field theory about strong interaction. In QCD, interactions between quarks inside a proton are mediated by gluons and gluons can split into quark-antiquark pairs. Therefore, within a proton, there are not only three valence quarks postulated in the quark model but also sea quarks (quark-antiquark pairs) and gluons. The parton distribution functions of quarks and gluons can be extracted from

the experiments via global QCD analysis. There are many groups working on the PDF extraction, such as HERAPDF, CTEQ, MSTH, and NNPDF etc. Figure 1.4, as an example, presents the extracted PDFs of proton from MSTH [18].

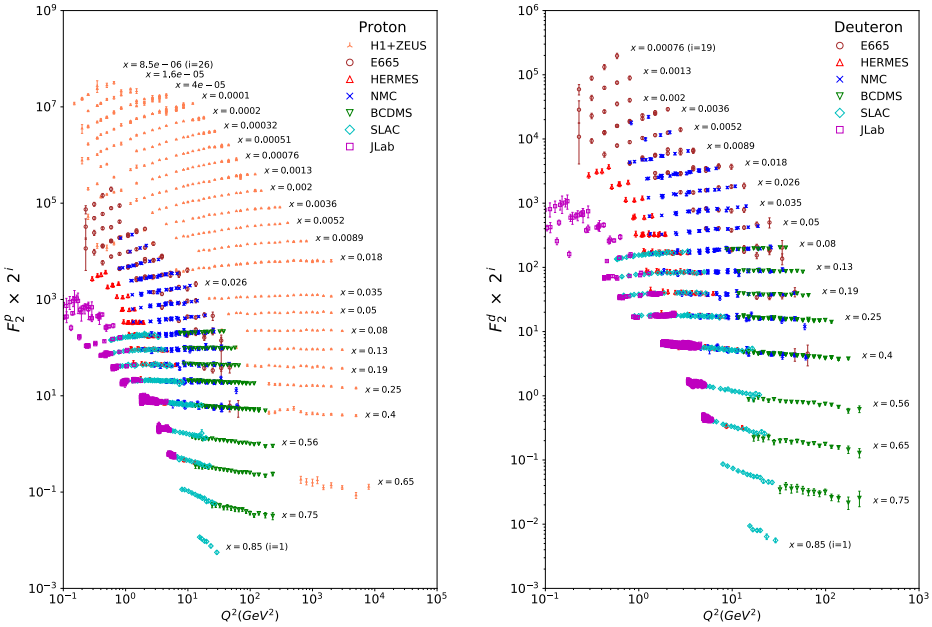

Figure 1.3: The world data of the structure function F_2 as a function of Q^2. Left plot: the F_2 of the proton. Right plot: the F_2 of the neutron. Plots are taken from Ref. [19]

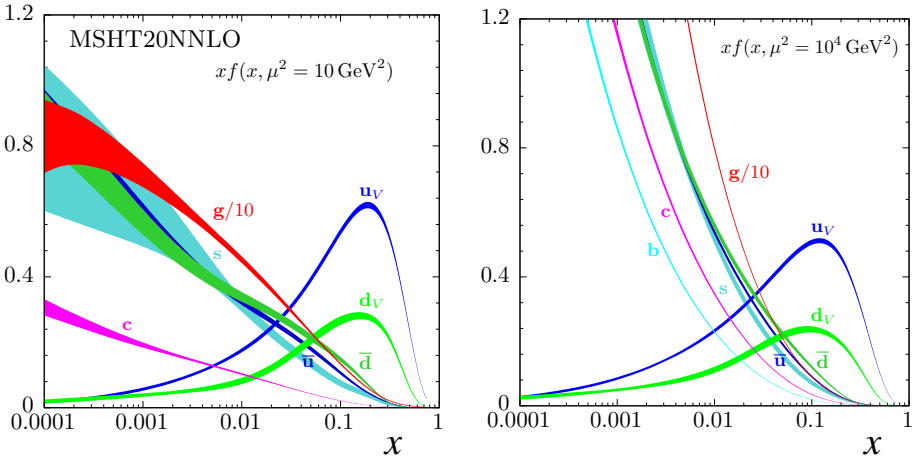

Figure 1.4: The parton distribution functions of proton from MSTH20 NNLO [18]. Plots are taken from Ref. [19]

1.1.2 Polarized DIS Experiments

DIS experiments as introduced above have revealed and confirmed that proton is composed of not only valence quarks but also sea quarks and gluons. Experimental studies on how is the spin of a proton composed of its constituent quarks and gluons were firstly carried out via the polarized lepton-nucleon deep inelastic scattering (pDIS), where both leptons and nucleons are polarized. For longitudinally polarized lepton and nucleon, the difference of the inclusive cross section for the scattered lepton with its polarization direction parallel ($\uparrow\Uparrow$) and anti-parallel ($\uparrow\Downarrow$) to the nucleon polarization can be expressed with the following formula [20]:

$$\left(\frac{d^2\sigma^{\uparrow\Uparrow}}{d\Omega dE'} - \frac{d^2\sigma^{\uparrow\Downarrow}}{d\Omega dE'}\right) = \frac{4\alpha^2}{M\nu}\frac{E'}{Q^2E}\left[(E + E'\cos\theta)\, g_1\left(x, Q^2\right) - 2xMg_2\left(x, Q^2\right)\right], \quad (1.3)$$

where $g_1(x, Q^2)$ and $g_2(x, Q^2)$ are the spin-dependent structure functions. In the parton model, $g_1(x, Q^2)$ can be written as the linear combination of the longitudinally polarized parton distribution functions $\Delta q(x, Q^2)$, also called helicity distribution:

$$g_1(x, Q^2) = \frac{1}{2}\sum_q e_q^2 \Delta q(x, Q^2), \quad (1.4)$$

$$\Delta q(x, Q^2) = q^+(x, Q^2) - q^-(x, Q^2), \quad (1.5)$$

where $q^+(x, Q^2)$ and $q^-(x, Q^2)$ are the parton distribution functions with parton spin parallel and anti-parallel to the nucleon spin, respectively.

Following the pioneering pDIS experiments at SLAC [21-24], the European Muon Collaboration (EMC) published the surprising results on the proton g_1 structure function and the flavor-singlet axial-charge g_A^0 [9-10] in the late 1980's. The results suggested that the quarks' spin contribute little to the proton spin showing great contradiction to the prediction from relativistic quark model, in which 60% of the proton spin is carried by quarks spin. This striking result has led to the so-called 'spin crisis' in history and triggered tremendous experimental and theoretical studies on the nucleon spin structure. Subsequent measurements conducted at CERN, DESY and JLab extended the kinematic coverage and improve the precision of g_1 structure function. Figure 1.5 summarizes the world data of the measured proton g_1 structure function as a function of Q^2 [10, 25-31]. The measured g_1 structure function together with assump-

tions of SU(6) symmetry and data from β decay of neutron and hyperon [32] allow one to extract proton spin contributions from u, d and s quarks, separately, which are [33]:

- $\Delta u = 0.84 \pm 0.01(\text{stat.}) \pm 0.02(\text{syst.})$
- $\Delta d = -0.43 \pm 0.01(\text{stat.}) \pm 0.02(\text{syst.})$
- $\Delta s = -0.08 \pm 0.01(\text{stat.}) \pm 0.02(\text{syst.})$

According to Eq. (1.4), the g_1 structure function is the linear combination of helicity distributions weighted with the electrical charge squared. Therefore, the flavor-separated helicity distributions can not be directly probed in the inclusive DIS experiments. In order to separately measure the helicity distributions of different flavors, the semi-inclusive DIS (SIDIS) experiments [10] have been performed. In addition to the scattered lepton, a final state hadron (like $\pi^{\pm}$ or $K^{\pm}$) is also measured in these experiments. The g_1 structure function in SIDIS process can be written as [34]:

$$g_1^h\left(x, Q^2, z\right) = \frac{1}{2}\sum_q e_q^2\left[\Delta q(x) D_q^h\left(z, Q^2\right) + \Delta\bar{q}(x) D_{\bar{q}}^h\left(z, Q^2\right)\right], \tag{1.6}$$

where $D_q^h\left(z, Q^2\right)$ is the fragmentation function of parton q to hadron h, which varies with parton flavors. However, the flavor-separated helicity distributions for sea quarks have not been constrained well due to the relative large uncertainties of fragmentation functions [33]. Detailed information about polarized deep inelastic scattering can be found in these review articles [35-36, 33, 37, 15, 38]. Similar to the extraction of unpolarized parton distribution functions, the helicity distributions are also obtained via global QCD analysis from different groups, like DSSV, NNPDF and JAM. Figure 1.6 shows the extracted helicity distributions from NNPDF Collaboration [39]. The helicity distributions of u quark and d quark have been constrained reasonably well. However, helicity distribution of sea quarks and gluons still remain relatively large uncertainties.

1.2 Proton Spin Structure Study at RHIC

The Relativistic Heavy Ion Collider (RHIC), located at the Brookhaven National Laboratory in the US, is the first and only high energy polarized proton-proton collider around the world. It is capable to collide both longitudinally and transversely polarized proton-proton beams at $\sqrt{s} = 200$ GeV and $\sqrt{s} = 510$ GeV [41]. The detailed overview

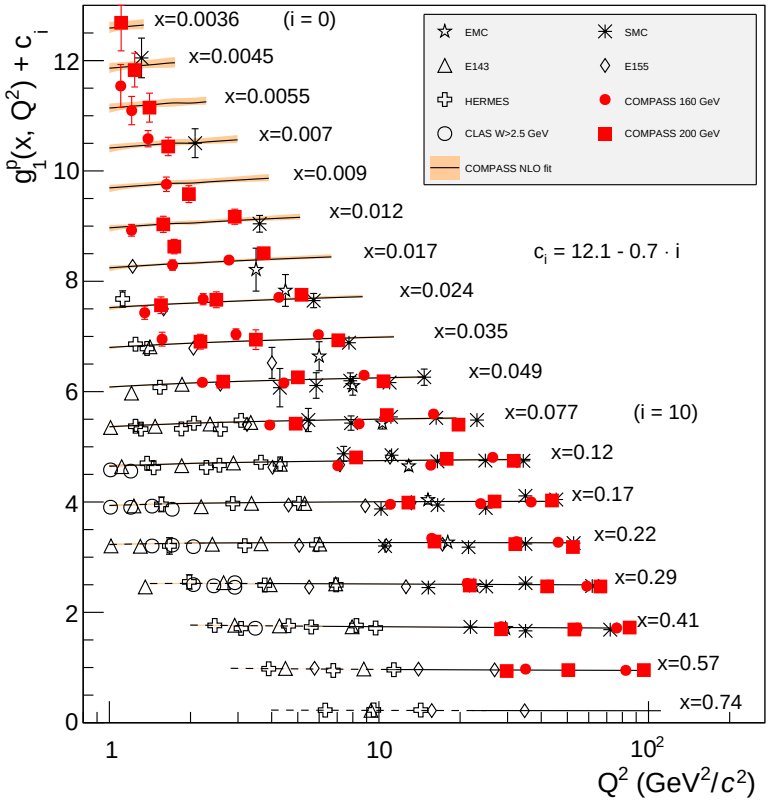

Figure 1.5: The world data of measured proton g_1 structure function as a function of Q^2 [19].

about RHIC will be presented in Chapter 2. The gluon helicity distribution, Δg, is mainly constrained via the longitudinal double spin asymmetry, A_{LL}, for inclusive jets, di-jets etc. The flavor-separated constraints on the helicity distributions of $\bar{u}$ and $\bar{d}$ are realized via the single spin asymmetry, A_L, of the $W^{\pm}$ bosons. For the helicity distribution of strange quark and anti-quark (Δs and $\Delta\bar{s}$), theoretical studies have suggested that the longitudinal spin transfer, D_{LL}, for Λ and $\overline{\Lambda}$ can provide sensitivity. In this section, I will briefly review the key measurements performed at RHIC and mainly focus on the A_{LL} measurements of jets and D_{LL} of Λ and $\overline{\Lambda}$, which are relative to the works presented in this thesis.

1.2.1 Constraining Helicity Distribution of Gluon

Jet and hadron production in proton-proton collisions at RHIC provides direct access to the gluon helicity at leading order. At RHIC energy, the dominated gluon-related QCD subprocesses are quark-gluon scattering ($gq \to gq$) and gluon-gluon scattering ($gg \to gg$) [42-43]. Figure 1.7 illustrates the relative fraction of different QCD sub-processes for inclusive jets production at RHIC energy.

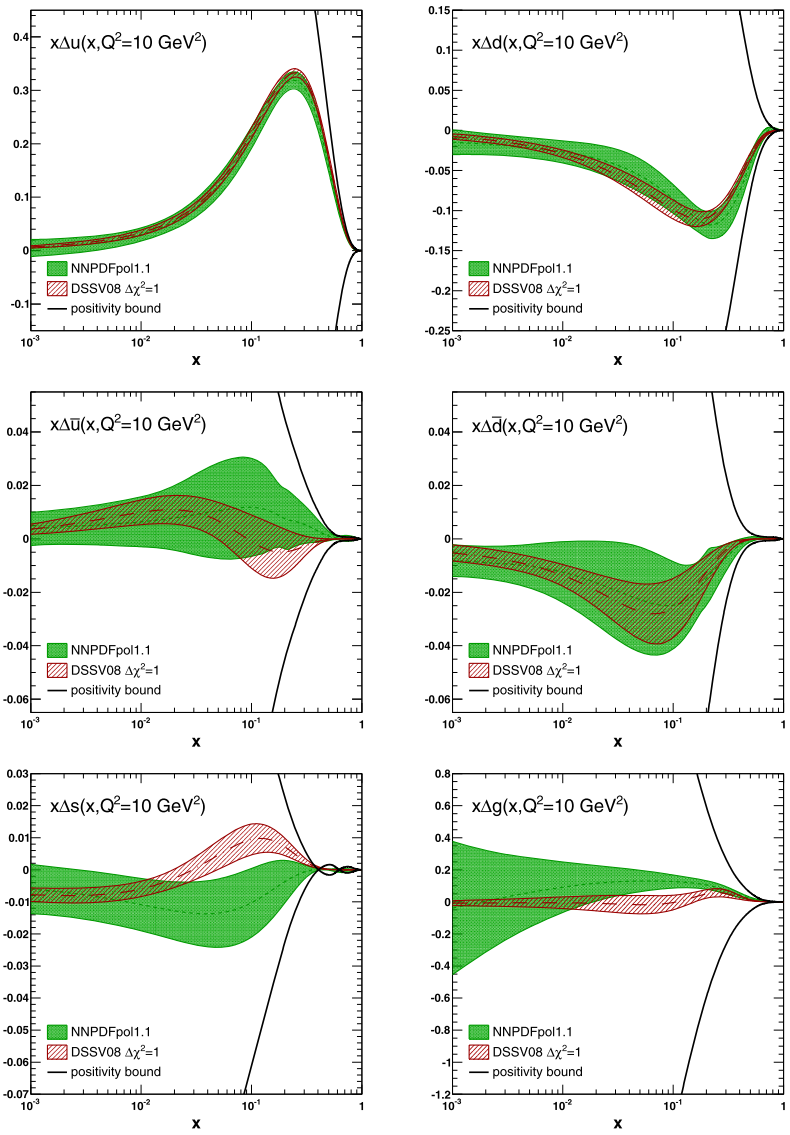

Figure 1.6: The helicity distributions of quarks and gluons extracted from NNPDF Collaboration [39]. Results from DSSV2008 [40] are compared.

• Longitudinal Double Spin Asymmetry of Inclusive Jets

The longitudinal double spin asymmetry, A_{LL}, of inclusive jets is defined as the cross section asymmetry as following:

$$A_{LL} \equiv \frac{\sigma_{++} - \sigma_{+-}}{\sigma_{++} + \sigma_{+-}} = \frac{\Delta\sigma}{\sigma}, \tag{1.7}$$

where σ_{++} and σ_{+-} represent the cross section of jets from equal and opposite helicity states of proton beams. The A_{LL} can be factorized in the following way at the leading

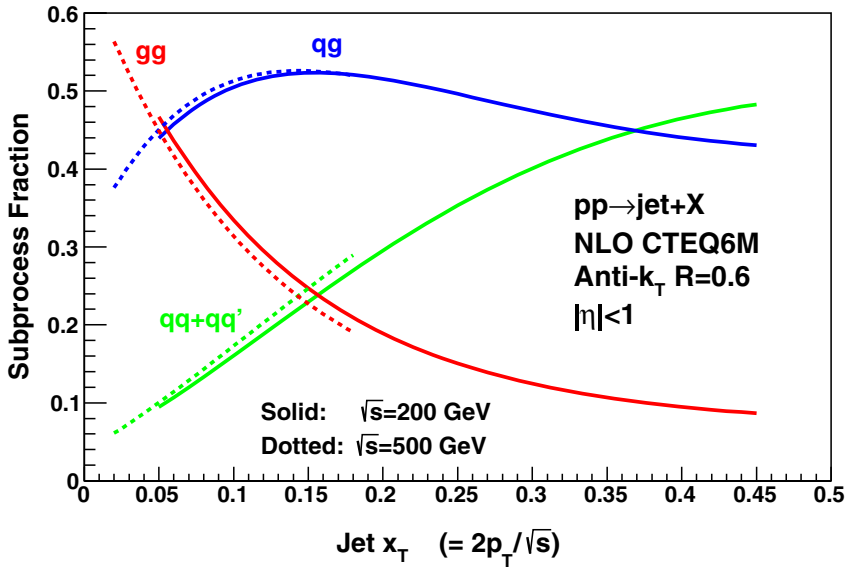

Figure 1.7: Next-to-leading-order sub-processes fraction as a function of $x_T = 2p_T/\sqrt{s}$ for inclusive jets production [42-43]. Plot is taken from Ref. [44].

order:

$$A_{LL} = \frac{\sum_{ab} \Delta f_a \bigotimes \Delta f_b \bigotimes \mathrm{d}\hat{\sigma}^{f_a f_b \to jet+X} \hat{a}_{LL}^{f_a f_b \to jet+X}}{\sum_{ab} f_a \bigotimes f_b \bigotimes \mathrm{d}\hat{\sigma}^{f_a f_b \to jet+X}}, \tag{1.8}$$

where Δf and f correspond to helicity distribution and unpolarized parton distribution function. The partonic cross section $\mathrm{d}\hat{\sigma}$ and partonic spin asymmetry $\hat{a}_{LL}$ can be calculated by the perturbative QCD [45]. As g-q scattering and g-g scattering are dominant QCD hard scatterings in the jet production and the $\hat{a}_{LL}$ is relative large [45], the A_{LL} of inclusive jets provide unique probe to the gluon helicity distribution without involving fragmentation processes.

Limited by statistics, early STAR published A_{LL} measurements [46-48] did not provide significant impact on gluon helicity distribution. The first influential A_{LL} result of inclusive jets [49] using the STAR data taken in 2009 was published in 2015. The results have been included into global QCD analysis [39, 50] and have significantly impacted on gluon helicity distribution. The left panel of Fig. 1.8 presents the gluon helicity distribution from the DSSV2014 [50]. This new gluon helicity distribution implied a positive gluon polarization inside the proton at Bjorken-x range $0.05 < x < 1$ as shown in the right panel of Fig. 1.8. The subsequent measurements of the A_{LL} for inclusive jets and di-jets [44, 51-55] extended kinematic coverage and improved the measurement precision, providing more precise constraints on the gluon helicity dis-

tribution of the proton. The left panel of Fig. 1.9 summarizes the recent STAR A_{LL} measurements of inclusive jets [44, 49, 53-54] as a function of $x_T = 2p_T/\sqrt{s}$. The new DSSV2014 + RHIC$_{\leq 2022}$ preliminary result [56] of gluon helicity distribution after including all the RHIC measurements up to 2022 is presented in the right panel of Fig. 1.9. The truncated integration of Δg over $x > 0.05$ suggests that gluon contributes to about 40% of proton spin.

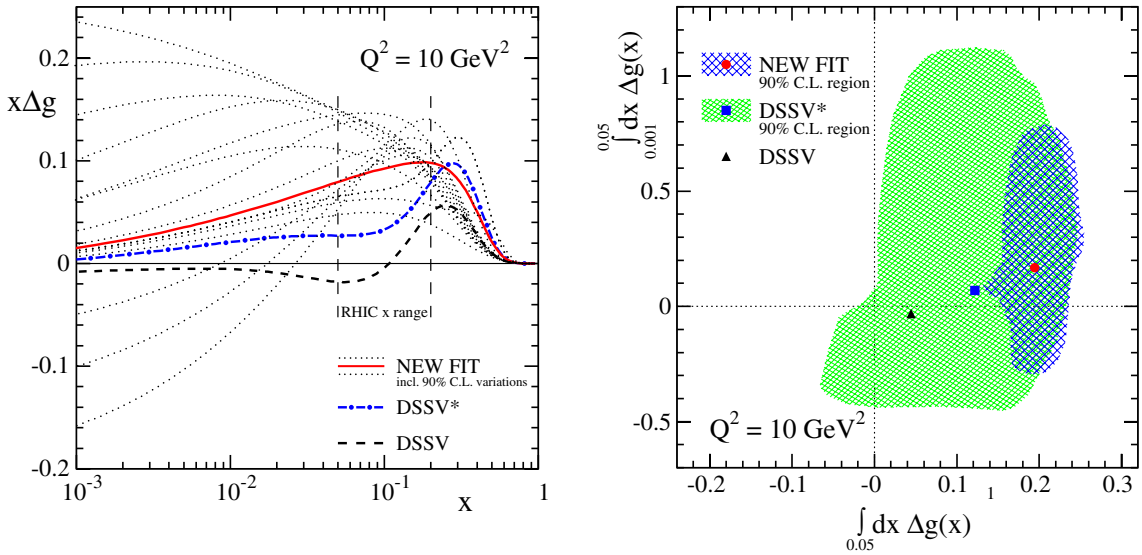

Figure 1.8: Left: the red curve (NEW FIT) presents the gluon helicity distribution from DSSV2014 [50] after including the measured A_{LL} results [49] using STAR 2009 data. Right: truncated moment of gluon helicity distribution. The green and blue areas present the 90% C.L. region from DSSV2008 [40] and DSSV2014 [50], respectively.

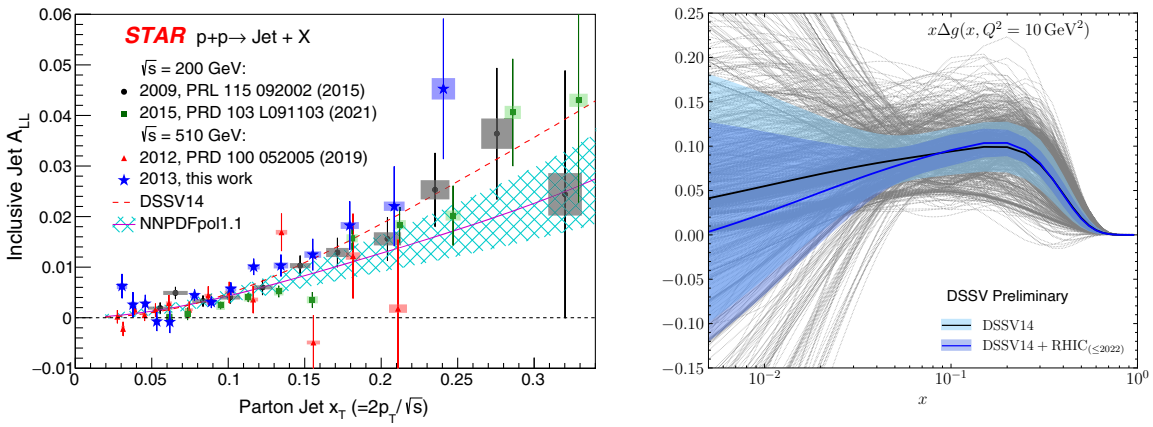

Figure 1.9: Left: some STAR A_{LL} measurements of inclusive jets [49, 44, 53-54] as a function of $x_T = 2p_T/\sqrt{s}$ at $\sqrt{s} = 200$ and 500 GeV. Right: new DSSV2014 + RHIC$_{\leq 2022}$ preliminary result [56] of gluon helicity distribution after including all the RHIC measurements up to 2022.

• Is Negative Gluon Polarization Possible?

As mentioned above, measurements conducted at RHIC have confirmed sizable positive gluon polarization inside the proton [50, 56]. However, the Jefferson Lab Angular Momentum (JAM) Collaboration [57] recently proposed that the gluon helicity distribution Δg is strongly dependent on the theoretical assumptions applied, namely the positivity constrain on the helicity distribution [50], SU(2) isospin symmetry and the SU(3) flavor symmetry. The left panel of Fig. 1.10 shows the Δg from the JAM Collaboration [57] with/without applying these constraints while the right panel of Fig. 1.10 presents the prediction of A_{LL} for inclusive jets for both positive and negative solutions of gluon helicity distributions, which shows that both predictions can describe the STAR measurements. Why does A_{LL} of inclusive jets allow a negative gluon Δg? One of the reason is that A_{LL} is proportional to the Δg^2 in the dominant g-g scattering channel, which is not sensitive to the sign of Δg. Some measurements conducted at RHIC, for example, the A_{LL} measurement of direct photons [58], which are mainly produced via the quark-gluon scattering at RHIC energy making A_{LL} a linear dependence on Δg, and the di-jets A_{LL} measurements [51-52, 44, 53-55] reducing parton scattering kinematics have shown their ability to distinguish between two scenarios of Δg. Figure 1.11 shows the measured A_{LL} of direct photons at PHENIX and A_{LL} of di-jets at STAR. In Fig. 1.11, measured A_{LL} results disfavor the predictions from JAM negative Δg.

In addition to these two measurements, the A_{LL} of jets tagged with charged pions carrying large momentum fraction of jets can shed light on the sign of the Δg. The A_{LL} of $\pi^{\pm}$-tagged jets can be factorized as following:

$$A_{LL} = \frac{\sum_{ab} \Delta f_a \bigotimes \Delta f_b \bigotimes \mathrm{d}\hat{\sigma}^{f_a f_b \to f_c + X} \hat{a}_{LL}^{f_a f_b \to f_c + X} \bigotimes D_{f_c}^{\pi^{\pm}}}{\sum_{abc} f_a \bigotimes f_b \bigotimes \mathrm{d}\hat{\sigma}^{f_a f_b \to f_c + X} \bigotimes D_{f_c}^{\pi^{\pm}}}, \tag{1.9}$$

where $D_{f_c}^{\pi^{\pm}}$ is the jet fragmentation function from parton f_c to $\pi^{\pm}$. In the fragmentation processes, the u quark and d quark preferentially fragment into π^+ and π^-. As quark-gluon scattering is one of dominant subprocesses at RHIC energy, the $\pi^{\pm}$ tagging not only enhances the u-g and d-g scattering but also suppresses the g-g scattering, which is blind in discrimination on the sign of Δg. As we can see from the Fig. 1.6, helicity distributions of u quark and d quark have been well constrained and they are in opposite sign. Therefore, one would expect $A_{LL}^{\pi^+} > 0$ and $A_{LL}^{\pi^+} > A_{LL}^{\pi^-}$ for positive

Δg and the opposite case for negative Δg. Figure 1.12 shows the A_{LL} measurements of inclusive $\pi^{\pm}$ conducted at PHENIX Collaboration [59-60], and predictions with JAM positive and negative gluon Δg [57, 61] are compared. Though, the measurements are not precise to distinguish two Δg scenarios, the predictions clearly show that the $\pi^{\pm}$ A_{LL} is sensitive to the sign of Δg. In this thesis, more precise A_{LL} measurements of the $\pi^{\pm}$-tagged jets have been performed, and details about the measurements will be discussed in Chapter 3.

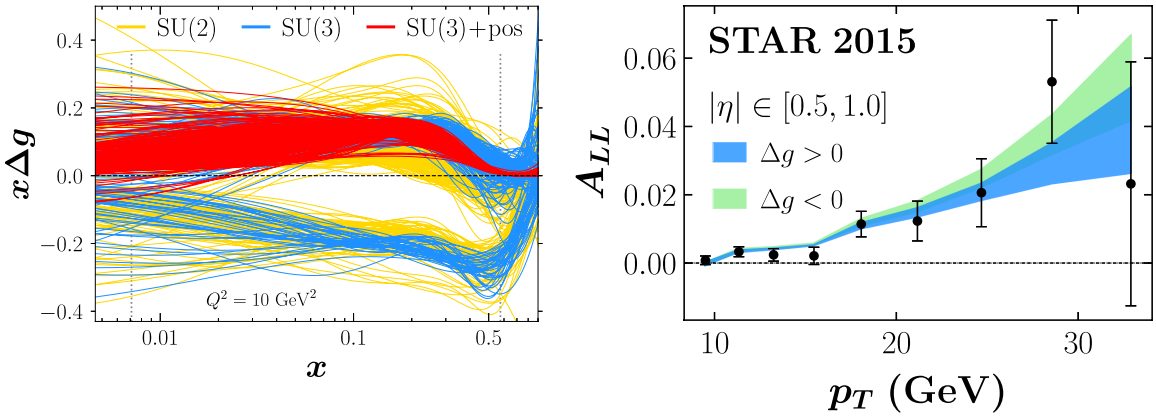

Figure 1.10: Left: gluon helicity distribution Δg from JAM Collaboration [57]. Right: longitudinal double spin asymmetry of inclusive jets with STAR 2015 data [53] together with the predictions with JAM positive and negative Δg.

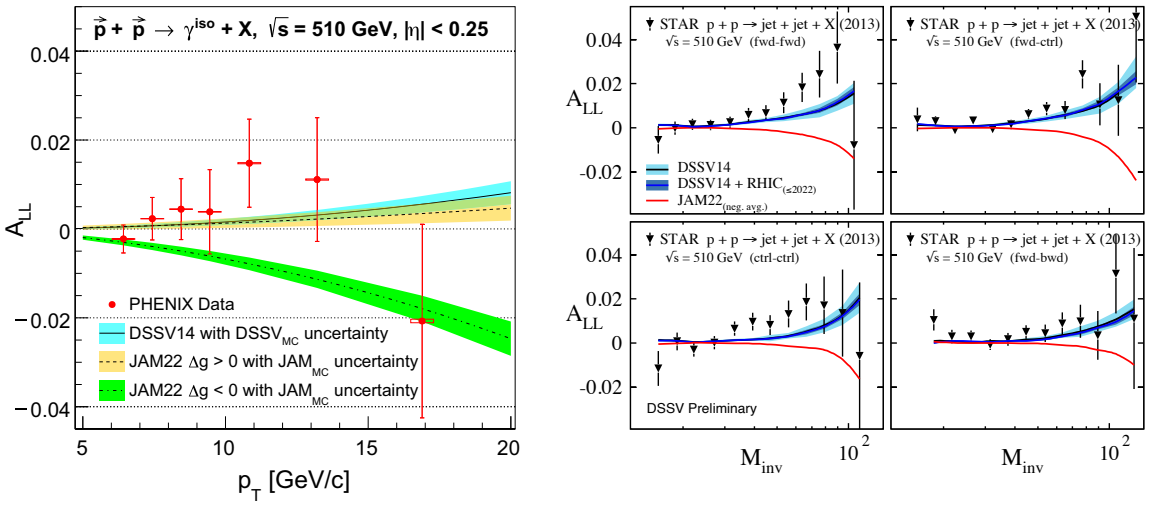

Figure 1.11: Left: longitudinal double spin asymmetry of direct photon as a function of p_T in proton-proton collision at $\sqrt{s} = 510$ GeV. Right: the longitudinal double spin asymmetry of di-jets as a function of di-jet invariant mass in proton-proton collision at $\sqrt{s} = 510$ GeV.

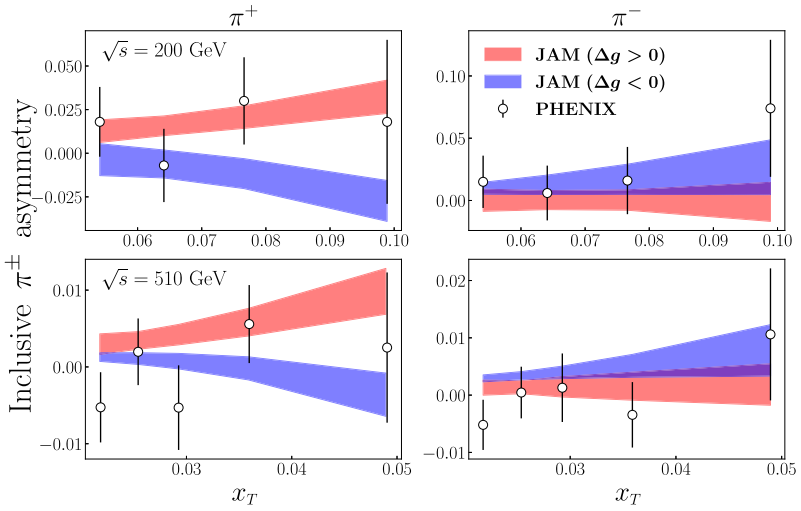

Figure 1.12: Longitudinal double spin asymmetry of inclusive charge pions as a function of x_T in proton-proton collisions at $\sqrt{s} = 200$ GeV (first row) and $\sqrt{s} = 510$ GeV (second row) together with predictions from JAM [57].

1.2.2 Constraining Helicity Distributions of $\bar{u}$ and $\bar{d}$ Quarks

At RHIC, constraints on the flavor-separated helicity distributions of $\bar{u}$ and $\bar{d}$ come from the measurements of the single spin asymmetry A_L of the $W^{\pm}$ bosons, which are mainly produced via $u + \bar{d} \to W^+$ and $\bar{u} + d \to W^-$ at RHIC energy. Due to the $V - A$ nature of the weak interaction, W^+ (W^-) can only be produced with positive-helicity $\bar{d}$ ($\bar{u}$) quark and negative-helicity u (d) quark, as illustrated in Fig. 1.13.

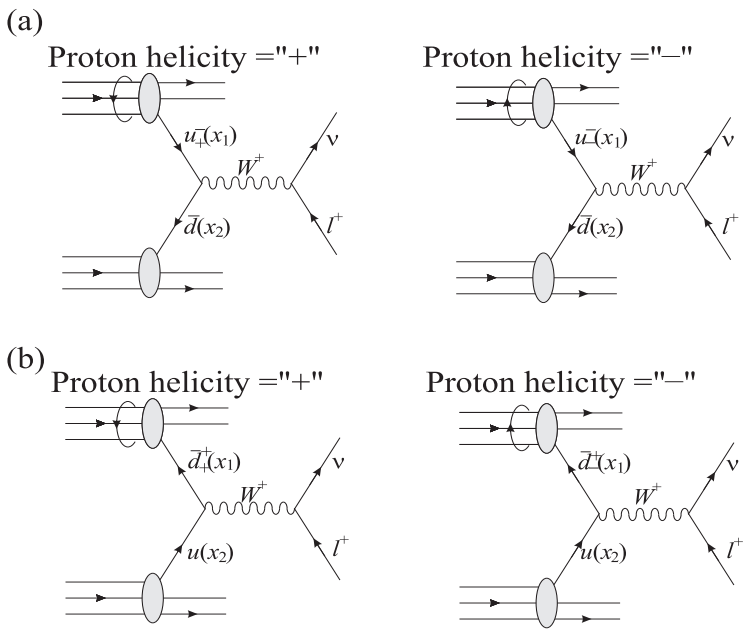

Figure 1.13: The lowest order Feynman diagrams of the W^+ production [41].

The single spin asymmetry A_L is defined as following:

$$A_L = \frac{\sigma^+ - \sigma^-}{\sigma^+ + \sigma^-}, \tag{1.10}$$

where σ^+ and σ^- are the cross section from positive and negative proton beam helicity. This formula, at the leading order, can be written in terms of parton distribution functions as following:

$$A_L^{W^+}(y_w) = \frac{-\Delta u(x_1)\,\bar{d}(x_2) + \Delta\bar{d}(x_1)\,u(x_2)}{u(x_1)\,\bar{d}(x_2) + \bar{d}(x_1)\,u(x_2)}, \tag{1.11}$$

$$A_L^{W^-}(y_w) = \frac{-\Delta d(x_1)\,\bar{u}(x_2) + \Delta\bar{u}(x_1)\,d(x_2)}{d(x_1)\,\bar{u}(x_2) + \bar{u}(x_1)\,d(x_2)}, \tag{1.12}$$

where y_w is the rapidity of $W^\pm$ bosons. x_1 and x_2 are proton momentum fraction carried by scattering partons from two proton beams, respectively. In general, the momentum fraction x carried by valence quarks is much larger than that carried by sea quarks. Therefore, for $y_W \gg 0$ ($y_W \ll 0$) with respect to the polarized beam, $A_L^{W^+}$ will be reduced to $A_L^{W^+} = -\Delta u/u$ ($A_L^{W^+} = -\Delta\bar{d}/\bar{d}$) and $A_L^{W^-}$ will be reduced to $A_L^{W^-} = -\Delta d/d$ ($A_L^{W^-} = -\Delta\bar{u}/\bar{u}$) [41, 62-63]. Series measurements performed at RHIC [64-69] (see Fig. 1.14) have confirmed that the $\Delta\bar{u}$ is positive and the $\Delta\bar{d}$ is negative and have found the violation of the isospin symmetry between $\bar{u}$ and $\bar{d}$ in polarized proton. Figure 1.15 (left) shows the $\Delta\bar{u}$ and $\Delta\bar{d}$ from DSSV2014 [50] and DSSV2014 + RHIC$_{\leq 2022}$ [56]. The NNPDFpol1.1rw in Fig. 1.15 (right) represents the $\Delta\bar{u} - \Delta\bar{d}$ results after including the measured $A_L^{W^\pm}$ [69] with STAR 2013 data.

1.2.3 Constraining Helicity Distributions of Strange Quarks

• Longitudinal Spin Transfer D_{LL} of Λ and $\overline{\Lambda}$

The self-analyzing weak decay of Λ and $\overline{\Lambda}$ [70-72] guarantees that its polarization can be measured experimentally. As a large fraction of Λ's spin is carried by its valence strange quark, extensive studies on Λ polarization have been carried out in both lepton-nucleon DIS and proton-proton collisions providing insights of the spin content of strange quark in the proton and the spin effects in the hadronization processes [73-74]. Theoretical studies on the longitudinal spin transfer D_{LL} of Λ hyperons in DIS processes [75-80] and proton-proton collisions [81-86] have shown that measuring of D_{LL} can not only shed light on the helicity distribution of strange quark and anti-quark but

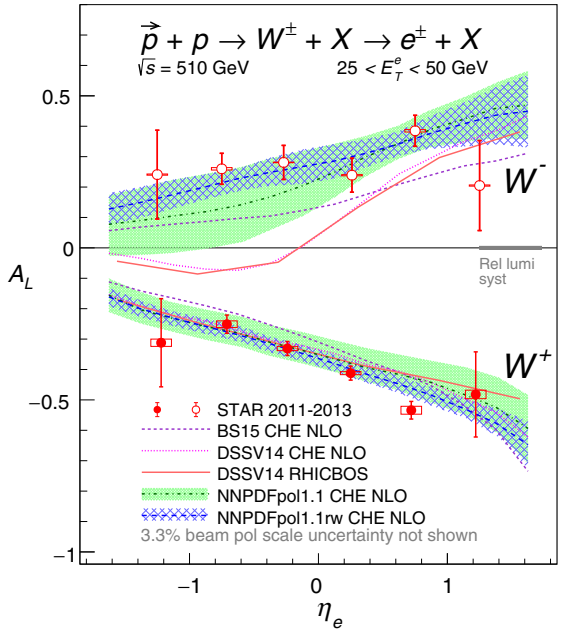

Figure 1.14: The longitudinal single spin asymmetry of $W^{\pm}$ bosons with STAR data taken from 2011-2013 [69].

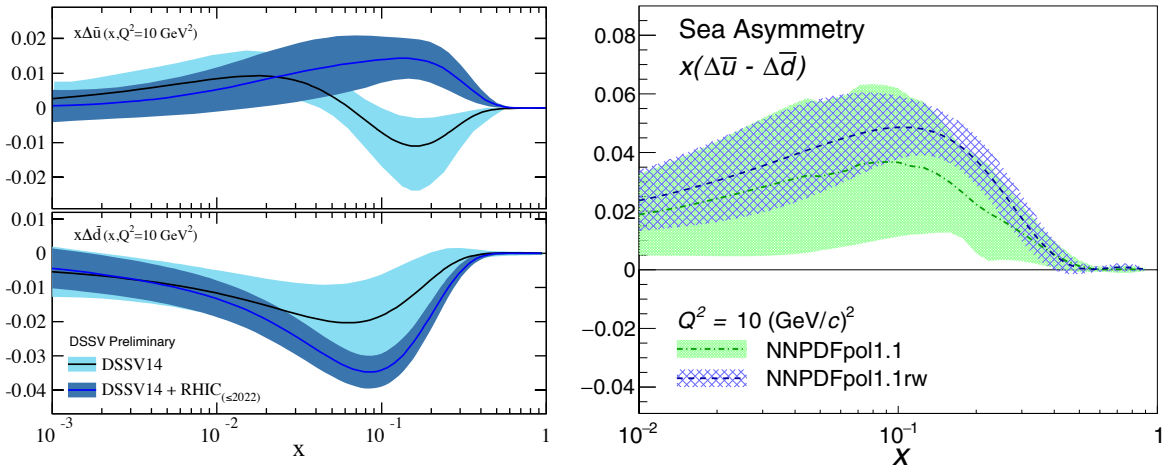

Figure 1.15: Left: the helicity distributions of $\bar{u}$ quark and $\bar{d}$ quark from DSSV2014 [50] and DSSV2014 + RHIC$_{\leq 2022}$ [56] including all the measured results at RHIC before 2022. Right: the asymmetry between $\Delta\bar{u}$ and $\Delta\bar{d}$ from [39].

also provide sensitivity to the polarized fragmentation functions. In polarized proton-proton collisions, longitudinal spin transfer D_{LL} of Λ hyperons is defined as:

$$D_{LL} \equiv \frac{\mathrm{d}\sigma_{p^+p\to\Lambda^+X} - \mathrm{d}\sigma_{p^+p\to\Lambda^-X}}{\mathrm{d}\sigma_{p^+p\to\Lambda^+X} + \mathrm{d}\sigma_{p^+p\to\Lambda^-X}} = \frac{\mathrm{d}\Delta\sigma}{\mathrm{d}\sigma}, \tag{1.13}$$

where '+' and '−' denote the helicity of proton or Λ hyperon. The spin-dependent differential cross section $\mathrm{d}\Delta\sigma$, for example, can be factorized into the convolution

of parton distribution functions, partonic scattering cross section and fragmentation functions:

$$\mathrm{d}\Delta\sigma \propto \int \mathrm{d}x_a\ \mathrm{d}x_b \sum_{abcd} \Delta f_a\left(x_a\right) f_b\left(x_b\right) \Delta D_c^{\Lambda}\ \mathrm{d}\Delta\hat{\sigma}^{ab\to cd}, \tag{1.14}$$

where Δf is the helicity distribution of a parton and ΔD_c^{Λ} is the polarized fragmentation function. The spin-dependent partonic scattering cross section $\mathrm{d}\Delta\hat{\sigma}^{ab\to cd}$ can be calculated via the perturbative QCD. Figure 1.16 (left) shows the theoretical calculations of the D_{LL} from Ref. [84] with three scenarios of polarized fragmentation functions [87] considered. The right panel of Fig. 1.16 presents the D_{LL} prediction of $\overline{\Lambda}$ from Ref. [83], which is sensitive to the helicity distribution of the anti-strange quark.

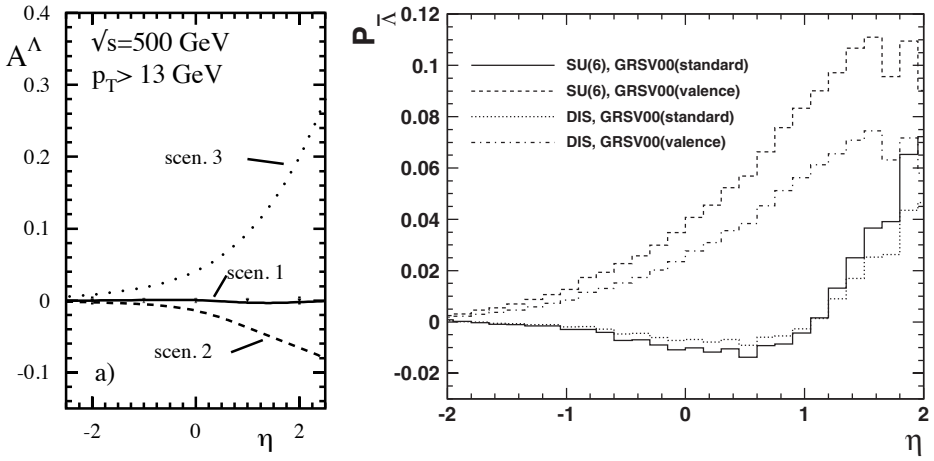

Figure 1.16: Left: prediction of D_{LL} of Λ [84] as a function of rapidity of Λ in proton-proton collision at $\sqrt{s} = 500$ GeV. Three scenarios of polarized fragmentation functions from Ref. [87] are considered. Right: theoretical calculation of D_{LL} of $\overline{\Lambda}$ as a function of pseudo-rapidity with hyperon $p_T > 8$ GeV in proton-proton collisions at $\sqrt{s} = 200$ GeV with different parameterizations of anti-strange quark helicity distribution from GRSV [88].

Measurements on the D_{LL} have been conducted at STAR [89-90] using the data taken in 2009, as illustrated in Fig. 1.17 (left), which have been fed into a model [91] showing that the measurements can provide constraints on the strange quark and anti-quark helicity distributions shown in Fig. 1.17 (right). It is worth to mention that recent theoretical study [92], as illustrated in Fig. 1.18, has demonstrated that measuring D_{LL} as a function of jet momentum fraction carried by Λ hyperons can directly probe the polarized fragmentation functions. In this thesis, we have performed improved measurements on the D_{LL} of Λ and $\overline{\Lambda}$ as a function of p_T using $\sqrt{s} = 200$

GeV proton-proton collisions data taken at STAR in 2015. We also conducted the first measurements of D_{LL} as a function of jet momentum fraction carried by the Λ hyperons as suggested in Ref. [92]. Details about the measurements will be discussed in Chapter 5.

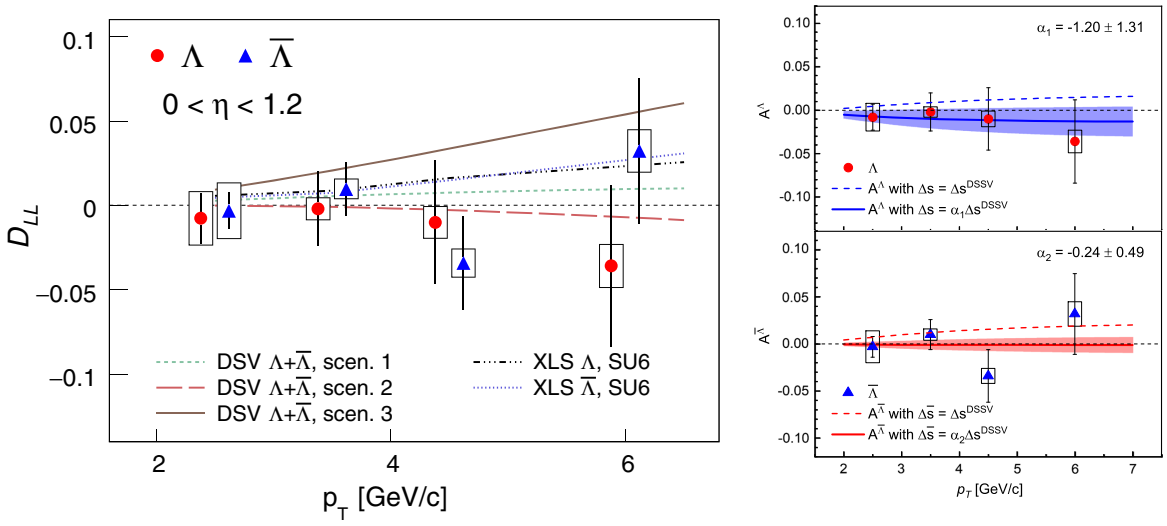

Figure 1.17: Left: longitudinal spin transfer D_{LL} of Λ and $\overline{\Lambda}$ as a function of p_T in proton-proton collisions at $\sqrt{s} = 200$ GeV with STAR data taken at 2009 [90]. Theoretical predictions from [84, 93, 83] are compared with the measurements. Right: a model from Ref. [91] fitting the measured D_{LL} [90] provides constraints on the strange quark and anti-quark helicity distributions.

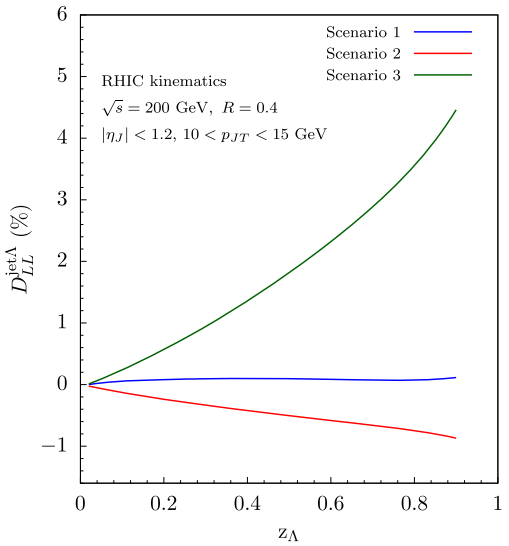

Figure 1.18: Theoretical predictions of longitudinal spin transfer D_{LL} of Λ and $\overline{\Lambda}$ at RHIC energy [92]. Three scenarios of polarized fragmentation from Ref. [87] are considered.

1.3 Thesis Structure

This chapter presented an brief overview on the DIS and polarized DIS experiments and several measurements conducted at RHIC regarding on the helicity distributions for gluon and sea quarks and outlined two works of this thesis: (1) longitudinal double spin asymmetry A_{LL} of $\pi^{\pm}$-tagged jets, which can shed light on the sign of gluon helicity distribution; (2) longitudinal spin transfer D_{LL}, which can not only provide constraints on the helicity distribution of strange quark and anti-quark but also can probe the polarized fragmentation functions. Chapter 2 briefly introduces the Relativistic Heavy Ion Collider, the relevant STAR detectors and the dataset used in this thesis. Three measurements performed are discussed in the following three chapters. Chapter 3 focuses on the details of A_{LL} measurements of $\pi^{\pm}$-tagged jets. In Chapter 4, details about the A_{LL} measurements of Λ, $\overline{\Lambda}$ and K^0_S will be discussed, which aim to shed light on the helicity distributions of strange quark and anti-quark. The details about the measurements of longitudinal spin transfer D_{LL} of Λ and $\overline{\Lambda}$ are presented in Chapter 5, followed by a brief summary and outlook presented in the Chapter 6.

Chapter 2 Experimental Setup

This chapter will briefly introduce the Relativistic Heavy Ion Collider, the STAR detectors relevant to the analyses presented in this thesis and the data set used in the analyses.

2.1 RHIC: A Polarized Proton-Proton Collider

The Relativistic Heavy Ion Collider (RHIC), located at Brookhaven National Laboratory, New York, US, is also the first and only high energy polarized proton-proton collider in the world. RHIC consists of two approximately circular accelerators/storage rings with a circumference of 3.8 km each. The two rings are situated in the same horizontal plane, with one ring (blue) having a clockwise beam, and the other (yellow) having a counterclockwise beam. Each ring contains 120 bunches of proton beams, which are filled separately. It takes about 10 minutes to fill all bunches into both rings. The duration between the initial bunch injection and the moment when the beam is intentionally dumped is called a 'fill'. Taking into account the decay of the beam polarization and luminosity, a 'fill' typically lasts approximately 3-8 hours for different beam energy. The orientation of the polarization direction for each bunch can be independently chosen. The RHIC is capable of colliding both longitudinally and transversely polarized proton beams at the center-of-mass energy up to $\sqrt{s} = 510$ GeV and heavy ion beams at the center-of-mass energy per nucleon up to $\sqrt{s_{NN}} = 200$ GeV. Figure 2.1 shows the layout of the RHIC facility.

2.1.1 Acceleration of Polarized Proton Beams

At RHIC, an optically pumped polarized ion source (OPPIS) [95] are used to produce polarized proton beams. The OPPIS produces polarized beam of H^- at rates of up to 10^{12} particles per 300 μs, achieving a high polarization level ranging from 82% to 84%. Subsequently, the generated H^- beams undergo injection into the 200 MeV Linac and are further accelerated to 1.1 GeV. Following this, the beams are directed to the Booster synchrotron, where charge-exchange injection with a carbon foil strips the electrons from the H^- beams. The resulting proton beams then experience three successive synchrotron accelerations. Initially, the proton beams are accelerated in

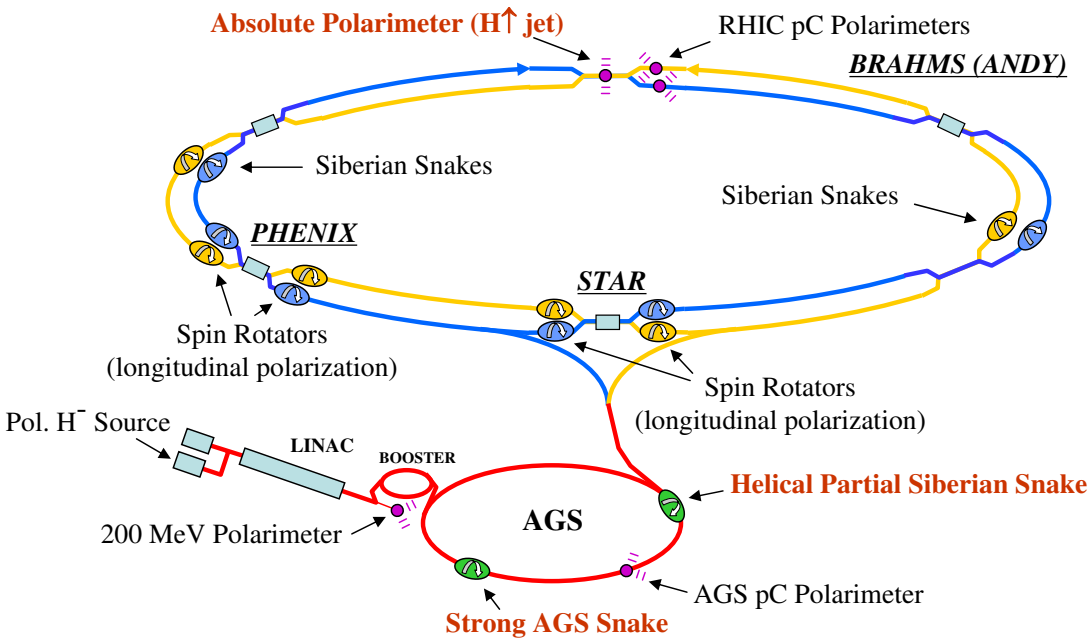

Figure 2.1: The layout of the RHIC facility [94].

the Booster to reach 2.3 GeV, followed by an increase to 23 GeV in the Alternating Gradient Synchrotron (AGS). Finally, the proton beams are injected into the RHIC rings and accelerated to full energy up to 255 GeV.

2.1.2 The Spin Dynamics of the Polarized Beams

The orbital motion of the proton beam in an external magnetic field **B** is governed by the Lorentz force by the following formula,

$$\frac{d\boldsymbol{\beta}}{dt} = \frac{q}{\gamma mc}\boldsymbol{\beta} \times \mathbf{B}, \tag{2.1}$$

where $\boldsymbol{\beta}$ is the velocity of the proton and q is the proton electric charge. γ is the Lorentz factor and the m is the mass of proton at rest. Similar to the orbital motion equation, the evolution of the spin vector for the polarized proton in an external magnetic field is given by the Thomas-BMT equation [45, 96-97],

$$\frac{d\mathbf{s}}{dt} = \frac{q}{\gamma mc}\mathbf{s} \times \left[(\gamma G + 1)\,\mathbf{B} - \frac{\gamma^2 G}{\gamma + 1}(\boldsymbol{\beta} \cdot \mathbf{B})\boldsymbol{\beta}\right], \tag{2.2}$$

where **s** is the spin vector of proton in the frame that moves with the proton, $G = 1.7928$ is the anomalous magnetic moment of the proton. Ideally, the external magnetic field

B is perfectly transverse. The spin vector **s** will precess around the axis of the external magnetic field **B**. By solving the Eq. (2.1) and (2.2), we can get the angular frequencies for both orbital motion Ω_c and the precession of the spin vector Ω_s as followings:

- For orbital motion: $\Omega_c = \frac{q}{\gamma mc}\mathrm{B}$
- For spin precession: $\Omega_s = (\gamma G + 1)\frac{q}{\gamma mc}\mathrm{B} = (\gamma G + 1)\Omega_c$

This means the precession of the spin vector is γG (called spin tune) times faster than the orbital motion. However, in the reality, there are several effects that lead to disturbation of the ideally transverse magnetic field, such as:

(i) non-zero longitudinal component and variant transverse component in the radial direction of the quadrupole magnetic field using to focus proton beam

(ii) imperfections of the magnetic field due to the errors of the field and the misalignment of the magnets

Therefore, the accelerating proton beam will undergo various depolarizing resonances, i.e., the intrinsic resonance caused by effect (i) and the imperfection resonances due to effect (ii). It is crucially important to maintain the beam polarization during the acceleration. This is achieved by the so called 'Siberian Snakes' [98], which are arrays of constant field helical dipole magnets and are installed diametrically opposed on each RHIC ring. The 'Siberian Snakes' can apply a full spin-flip of the proton beams in a single passage, which results in a complete cancellation of depolarization at the first order [99]. The proton beams are transversely polarized during the acceleration, which is the stable orientation as this orientation is approximately parallel to the external magnetic field. To achieve longitudinal collisions, two spin rotators are installed on each side of the interaction points, like STAR or sPHENIX. They can switch the beam polarization direction from transverse direction to longitudinal direction before the collision and switch it back after the collision.

2.1.3 Measurement of the Beam Polarization

In addition to the maintenance of the beam polarization, it is crucially important to measure the beam polarization precisely, which is an indispensable input for the Spin Physics Program carried out at RHIC. Two types of polarimeter, as shown in Fig. 2.1,

are employed: (1) proton-Carbon (p-C) polarimetry [100], which is installed on each RHIC rings at 12 o'clock and (2) hydrogen gas jet (H-jet) polarimeter [101] installed at the collision point at 12 o'clock of the RHIC ring. The beam polarization is measured based on measuring the left-right spin asymmetry in the Coulomb-Nuclear Interference (CNI) region with the following formula:

$$\varepsilon_N = PA_N = \frac{N_L - N_R}{N_L + N_R}, \tag{2.3}$$

where ε_N is the measured asymmetry, and P is the polarization of the beam or target A_N is the analyzing power.

The pC polarimetry consists of a thin carbon ribbon target and six silicon strip detectors in a vacuum chamber shown in Fig. 2.2. The beam polarization is measured based on the left-right spin asymmetry of the p-C elastic scattering at the CNI region. However, as the analyzing power of the p-C elastic scattering, A_N^{pC}, is not known at RHIC energy, the absolute beam polarization cannot be measured by the p-C polarimetry. Due to the relative large p-C elastic scattering cross section, the measurement can be performed quickly. Therefore, the p-C polarimetry is used to measure the relative beam polarization and the depolarization rate of the beams.

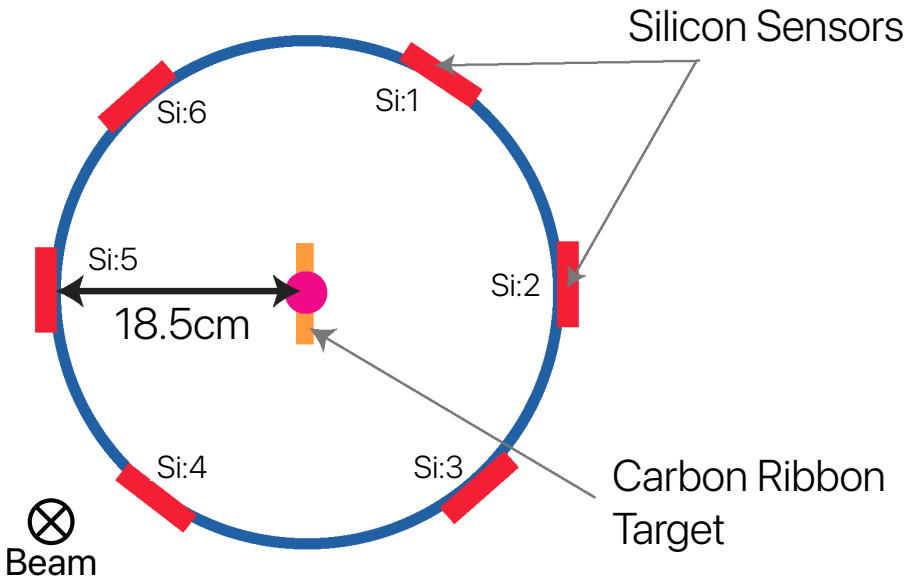

Figure 2.2: Cross section of the p-C polarimetry at RHIC [100].

The absolute beam polarization is measured with the H-jet polarimeter shown in Fig. 2.3. The measurement is based on the p-p elastic scattering between the polarized

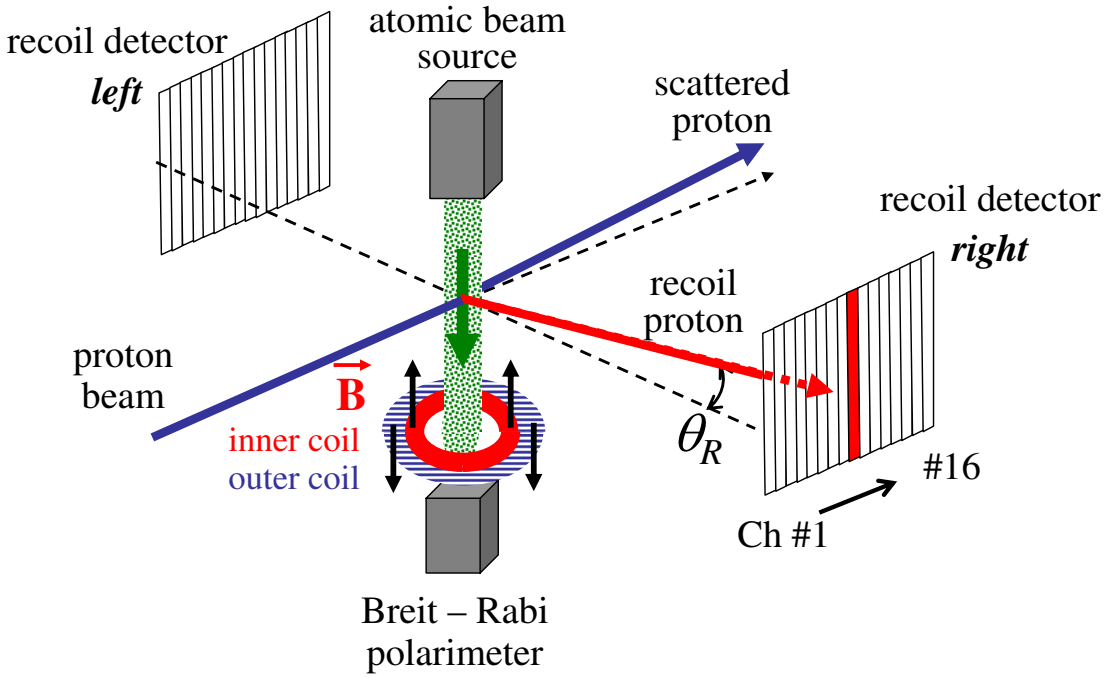

Figure 2.3: Schematic layout of the hydrogen gas jet polarimeter at RHIC [101].

hydrogen gas target and the polarized proton beams at CNI region. As the both beam and target are the proton, the analyzing power, A_N for beam and target are the same. Therefore, based on Eq. (2.3), the beam polarization P_{beam} can be calculated as:

$$P_{\text{beam}} = \frac{\varepsilon_N^{\text{beam}}}{\varepsilon_N^{\text{target}}} P_{\text{target}}, \tag{2.4}$$

where the $\varepsilon_N^{\text{beam}}$ and $\varepsilon_N^{\text{targer}}$ are the measured left-right asymmetry for proton beam and hydrogen gas target, respectively. P_{target} is the polarization of the hydrogen gas jet target, which is measured with a Breit-Rabi polarimeter with the relative precision of about 2% [101].

2.2 The STAR Detectors

The Solenoidal Track at RHIC (STAR) is one of two large detector systems at RHIC located at the 6 o'clock of the RHIC ring as shown in Fig. 2.1. It is designed to measure both hadronic and electromagnetic particles generated in heavy ion and proton-proton collisions. As illustrated in Fig. 2.4, STAR comprises multiple specialized detector subsystems serving various purposes. The key sub-detectors related to the analyses in this thesis are listed in below:

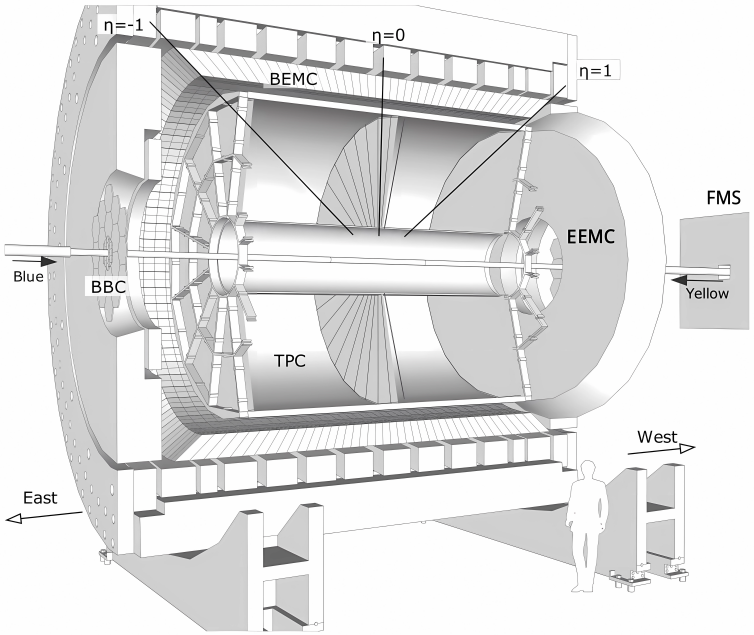

Figure 2.4: The perspective view of the STAR detector.

- Time Projection Chamber, covering pseudo-rapidity $|\eta| < 1.5$ and 2π in azimuth
- Barrel Electromagnetic Calorimeter, covering $|\eta| < 1.0$ and 2π in azimuth
- End-cap Electromagnetic Calorimeter, covering $1.086 < \eta < 2.0$ and 2π in azimuth
- Time of Flight Detector, covering $|\eta| < 0.9$ and 2π in azimuth
- Vertex Position Detector, covering $4.24 < |\eta| < 5.1$, and 2π in azimuth. It is used to measure the relative luminosity of proton beams.
- Zero Degree Calorimeter, 18 meters away from the center of the Time Projection Chamber. It is also used to measure the relative luminosity of proton beams.

2.2.1 The Time Projection Chamber

The Time Projection Chamber (TPC) [102] is a crucial component within the STAR detector system. As shown schematically in Fig. 2.5, the TPC is 4.2 meters long and 4 meters in diameter, which is surrounded by a large solenoidal magnet operating at the 0.5 T magnetic field [103]. The acceptance of the TPC covers the pseudo-rapidity $|\eta| < 1.3$, which has been extended to $|\eta| < 1.5$ after the iTPC upgrade [104-105], and 2π in the azimuthal direction. It records the charged particles produced in a

collision and is capable of measuring their momenta over a range of 100 MeV/c to 30 GeV/c. Filled with P10 gas (90% argon + 10% methane) [106], the TPC allows charged particles to ionize the gas as they traverse its volume. Subsequently, electrons liberated by the gas atoms will drift towards the readout end caps at the ends of the chamber under an uniform electric field of approximately 135 V/cm. This electric field is generated by a thin conductive Central Membrane at the center of the TPC as shown in Fig. 2.5. The P10 gas is regulated at 2 mbar above the atmospheric pressure [102] making the drift velocity of the electrons stable and insensitive to the fluctuation of the temperature and the gas pressure.

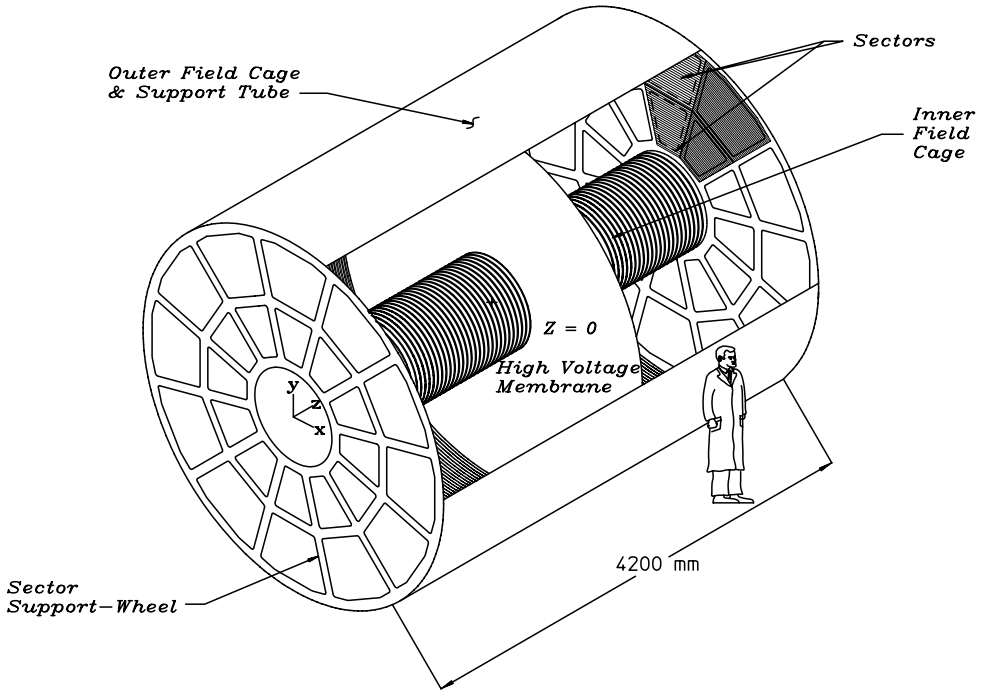

Figure 2.5: The layout of the STAR Time Projection Chamber [102].

The drifted electrons are collected by the end-cap readout system, which is based on Multi-Wire Proportional Chambers (MWPC). The readout sectors are arranged as on a clock with 12 sectors around the circle. Figure 2.6 shows one sector of the readout planes. The inner sectors are instrumented with 13 pad-row readouts and had been upgraded to 40 pad-row readouts in the iTPC upgrade project [104-105]. The avalanche of the drifted electrons at the anode wires provide an amplification of about 1000-3000. Positive ions generated in such process induce image charges on several adjacent pads. Therefore, the x-y position of the drifted electrons can be determined and their arrival

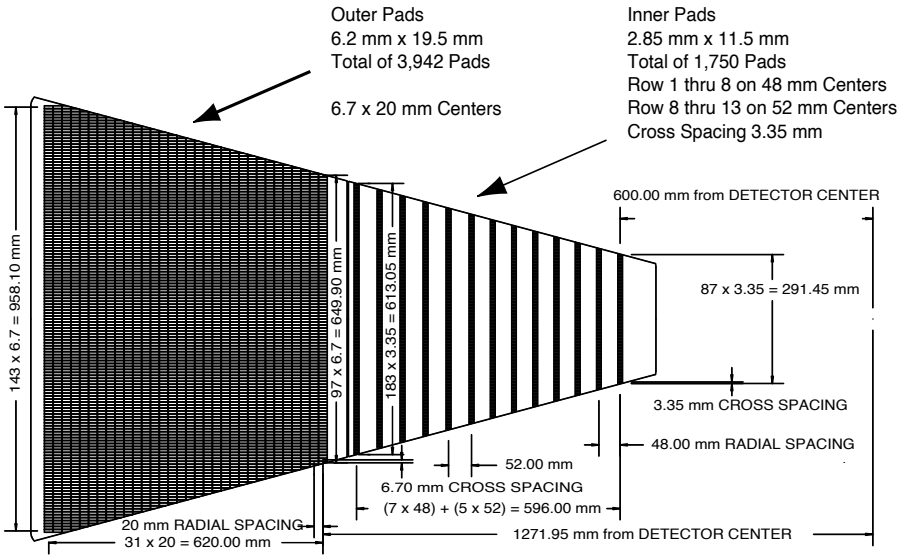

Figure 2.6: The layout of one sector of the anode pad plane [102].

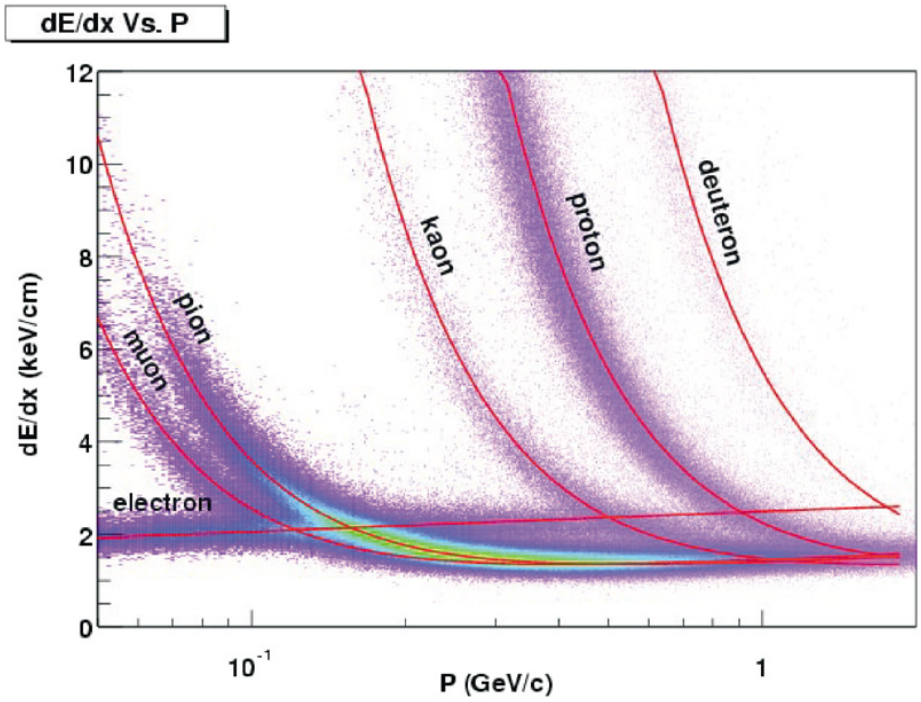

Figure 2.7: The ionization energy loss dE/dx of charged particles as a function of momentum [102].

time is recorded at the end caps. Based on the the start time of a collision and the electron drift velocity, the original z component of the drifting electrons can be calculated. Therefore, the tracks produced in a collision can be reconstructed with the 3-dimensional coordinates of the drifting electrons. The ionization energy loss dE/dx of a track is determined with the avalanche electrons and is used to identify different

particles based on the Bethe-Bloch formula [32]. Figure 2.7 shows the dE/dx of charged particles as a function of particle momentum.

2.2.2 The Barrel Electromagnetic Calorimeter

The Barrel Electromagnetic Calorimeter (BEMC) [107] is positioned between the magnet and the TPC, covering $-1 < \eta < 1$ and 2π in the azimuthal direction, as illustrated in Fig 2.8. Its primary purpose is to investigate and trigger rare or high p_T events, including high p_T jet events, leading hadrons, heavy quarks, and direct photons.

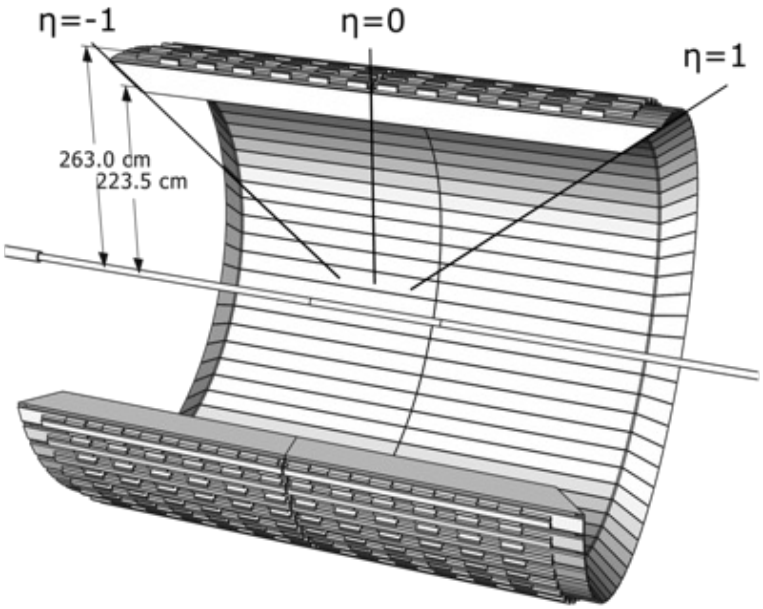

Figure 2.8: The layout of the Barrel Electromagnetic Calorimeter [62].

The BEMC is a segmented lead-scintillator sampling detector. It includes 120 calorimeter modules in total and each module are segmented into 40 towers spanning approximately 0.05 rad in the azimuthal direction and 0.05 in η. In Fig. 2.9, these towers projectively point back to the center of the TPC with a total depth of about 20 radiation lengths at $\eta = 0$. Each towers consist of 19 layers of 5 mm thick scintillator, 2 layers of 6 mm thick scintillator, and 20 layers of 5mm thick lead. Additionally, a shower maximum detector (SMD) is located at a depth of about 5 radiation length of the tower, enabling precise energy measurements for the isolated electromagnetic showers [107]. The SMD plays a crucial role in the identification of direct photons, π^0 reconstruction, and electron identification. Figure 2.10 shows a side view of a module illustrating the detail construction of the module.

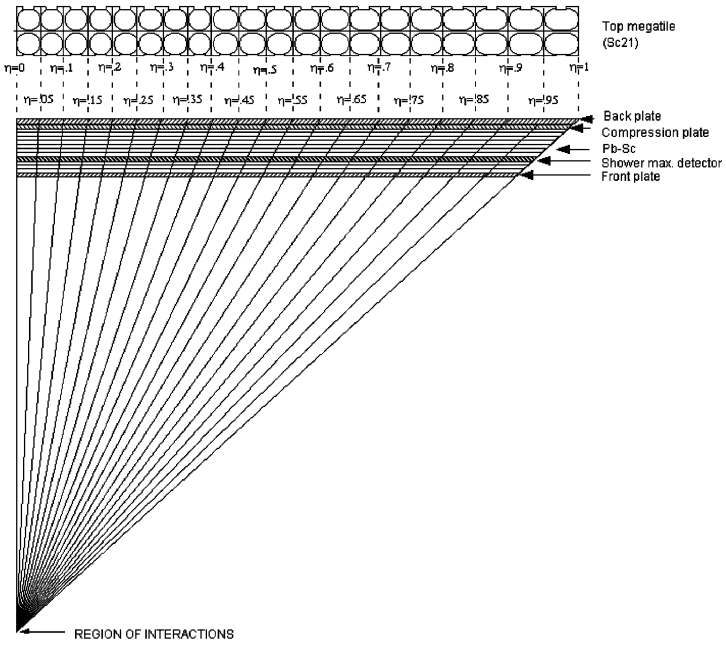

Figure 2.9: The side view of a BEMC module illustrating the projective nature of the towers [107].

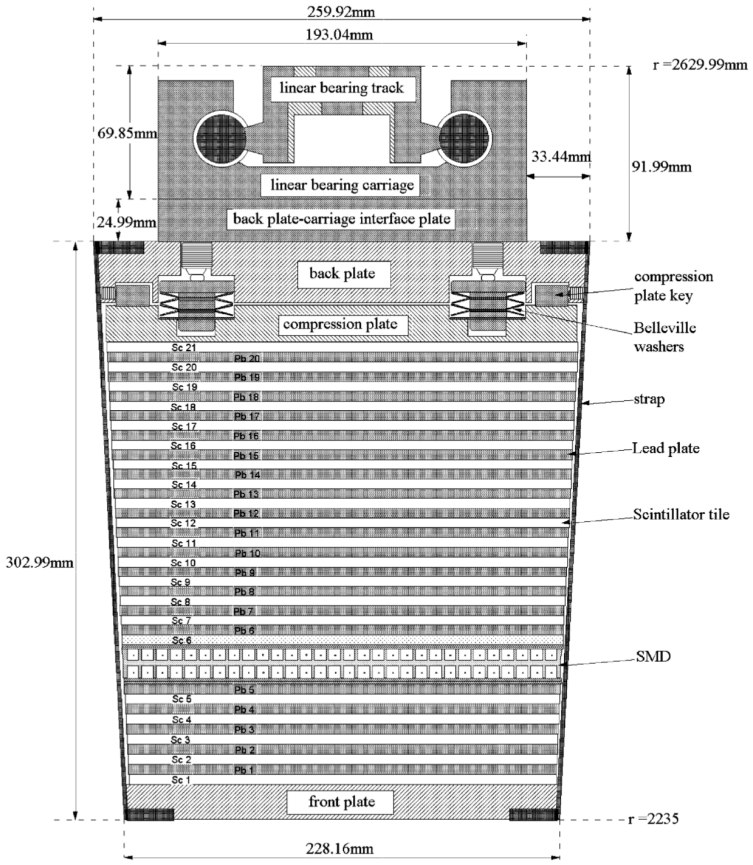

Figure 2.10: The side view of a BEMC module showing the detailed construction of the module [107].

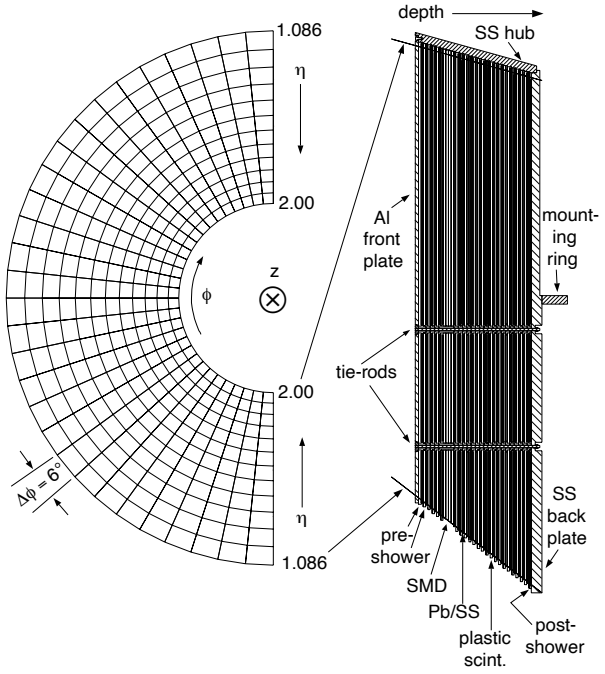

Figure 2.11: Left: the schematic tower structure of the End-cap Electromagnetic Calorimeter. Right: the cut view of the EEMC at constant ϕ [108].

2.2.3 The End-cap Electromagnetic Calorimeter

The End-cap Electromagnetic Calorimeter (EEMC) significantly extends the STAR detector's coverage, encompassing $1.086 < \eta < 2$ and spanning 2π in azimuth [108]. In Fig. 2.11, the left side schematically illustrates the EEMC tower structure, while the right side presents a cross-sectional view of the calorimeter at a constant azimuthal angle ϕ. The EEMC is segmented into 12 modules in azimuth, with each module housing 60 towers. Consequently, there are a total of 720 towers, and each covers 0.1 in the azimuthal direction and varies its size in the η direction, ranging from 0.057 to 0.099. It consists of 24 layers of 4mm thick scintillator, 23 layers of 5 mm thick lead and stainless steel laminate layers.

Similar to the BEMC, the EEMC incorporates a Shower Maximum Detector (SMD), illustrated in Fig. 2.12. Positioned at a depth of about 5 radiation lengths in each tower, the SMD plays a pivotal role in distinguishing between single photons, π^0 and η decays. Additionally, it aids in discriminating between electrons and hadrons and facilitates the matching of electron hits to TPC tracks.

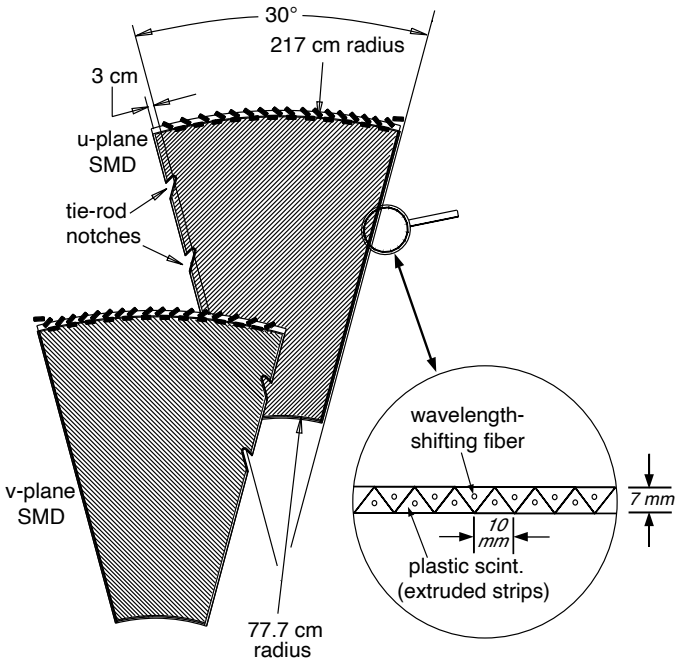

Figure 2.12: Layout of one 30° sector of the EEMC-SMD [108].

2.2.4 The Vertex Position Detector

The Vertex Position Detectors (VPD) [109] are used for triggering on the minimum bias events and monitoring the relative luminosity. They covers $4.24 < |\eta| < 5.1$ and 2π in azimuth and are 5.7 m away from the center of the TPC.

There are two identical detector assemblies located on each side of STAR. Figure 2.13 shows the front view of one assembly. Each assembly consists of 19 detectors, which are composed of a Pb converter and a plastic scintillator. It measures up to 19 times on each side in a collision, and the z component of the collision vertex $Z_{\rm vtx}$ and the start time of a collision $T_{\rm start}$ can be calculated via the following formula:

$$Z_{\rm vtx} = c(T_{\rm east} - T_{\rm west})/2, \tag{2.5}$$

$$T_{\rm start} = (T_{\rm east} + T_{\rm west})/2 - L/c, \tag{2.6}$$

where $T_{\rm east}$ and $T_{\rm west}$ are the times recorded by two VPD assemblies and c is the speed of light. L is the distance of the VPD assembles to the center of the TPC. The typical resolution of the $T_{\rm start}$ is about 80 ps in $p+p$ collisions and about 20-30 ps in 200 GeV Au + Au collisions.

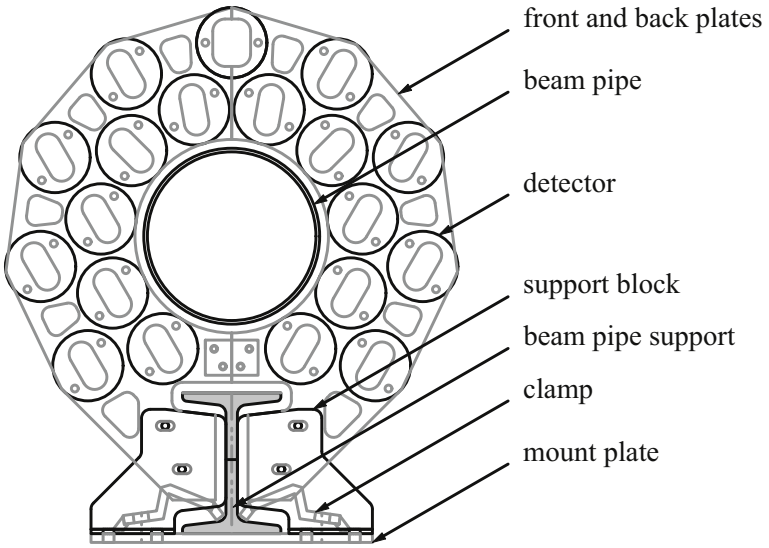

Figure 2.13: The schematic front view of one VPD assembly [109].

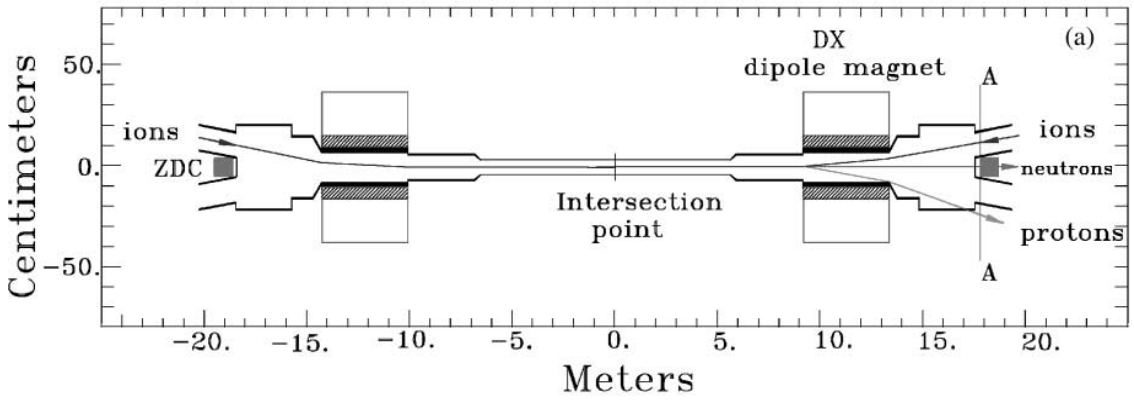

Figure 2.14: The plan view of the interaction region [110].

2.2.5 The Zero Degree Calorimeter

In high energy collisions, the nuclei beams can usually emit evaporation neutrons. In $\sqrt{s_{NN}}$ = 200 GeV heavy ion collisions, the emission angle is less than 2 mrad from the beam axis. The Zero Degree Calorimeter (ZDC) [110] is designed to detect and measure the energy of such emitted neutrons in the downstream of the heavy ion collisions. In every experiment at RHIC, there are two identical ZDCs placed on either sides of the interaction point. Figure 2.14 shows the plan view of the interaction region. As we can see, the DX magnets remove all charged particles out of the acceptance of the ZDC.

There are three modules of each ZDC. Each of them consists of multiple quartz

and tungsten layers, and corresponds to 2 nuclear interaction length and 50 radiation length. Similar to VPD, ZDC can be also used for triggering on minimum bias events and measuring relative luminosity between different spin patterns of bunching crossings.

2.2.6 The Time of Flight Detector

The Time of Flight (TOF) [111] detector is designed to enhance the particle identification (PID) probability of STAR. It covers the $|\eta| < 0.9$ and 2π in azimuth. It is based on the Multi-gap Resistive Plate Chamber (MRPC) [112]. The TOF consists of 120 trays and each tray covers 6° in the azimuthal direction and consists of 32 MRPC modules. As its name implies, the TOF measures the flight time of a particle $\Delta T = T_{\text{end}} - T_{\text{start}}$, where the T_{start} is the start time of a collision provided by VPD or ZDC and the T_{end} is arriving time of the particle at TOF. The typical resolution of the flight time is 80 ps, making TOF a fast detector. With the path length L of a particle measured with the TPC, the velocity β and the mass of a particle m can be calculated by the following formulas:

$$\beta = \frac{L}{c\Delta T}, \tag{2.7}$$

$$m = p\sqrt{\frac{1}{\beta^2} - 1}, \tag{2.8}$$

where c is the speed of light and p is the momentum of a particle measured by the TPC.

2.3 Data Set

STAR concludes its longitudinally polarized proton-proton collision data collection at $\sqrt{s} = 200$ GeV in 2015. The data set used in the analysis was labeled as 'production_pp200long2_2015'. I will called it 'long2' for convenience. The 'long2' data collection lasted about 5 weeks. The sampled data set corresponds to an integrated luminosity of about 52 pb^{-1} with average beam polarization of about 52% and 56% for blue beam and yellow beam, respectively.

At STAR, the smallest data collection period is called a 'run', which usually lasts about 30 minutes. There are 737 runs collected during the 'long2' data collection period. In the case where there were malfunctions of detectors and other effects during the data taking, a run-by-run basis quality assurance (QA) procedure was applied to

the whole data set. Runs that cannot pass the QA criteria will be marked as 'bad runs' and rejected from the analysis. The run-by-run QA has been done in the inclusive jet A_{LL} measurement [53]. There are 557 runs that passed the whole QA procedures, and these runs have been used in our analyses. Detailed information about the run-by-run QA can be found in Ref. [113].

2.3.1 Event Selections

The bunch crossing rate at RHIC for the full-energy collision is about 10 MHz. For high luminosity proton-proton collision, the interaction rate is comparable to the bunch crossing rate. However, the operational rate of the slow detectors at STAR, like the TPC, are only about 100 Hz. To effectively select valuable collision events, STAR designed a multi-level trigger system [114-115] based on the response on the fast detectors, like BEMC, EEMC, VPD etc. Details about the trigger system can be found in Refs. [114-115].

To select high p_T jet events, triggers based on the energy deposits on the EMCs (BEMC and EEMC) have been designed. As described in Sec. 2.2.2, a BEMC tower spans a region of 0.05×0.05 in η and ϕ. A trigger patch in the BEMC comprises 4×4 BEMC towers, covering a larger area of 0.2×0.2 in η and ϕ, and a jet patch consists of 25 trigger patches spanning coverage of 1.0×1.0 in η and ϕ. There are 30 jet patches defined on the BEMC and EEMC overlapping in η. In the analysis, two jet-patch triggers, JP1 and JP2, are used. The JP1, for example, will be fired if the sum of the ADC over a jet patch exceeds a certain threshold. Table 2.1 summarizes the thresholds for JP1 and JP2 used in 2015.

Trigger	ID	Threshold (ADC)	Equivalent E_T (GeV)
JP1	490404	28	5.4
JP2	490401	36	7.3

Table 2.1: The trigger thresholds for JP1 and JP2 used in 2015. The Equivalent transverse energy E_T on the BEMC and EEMC can be calculated approximately with $E_T = 0.236 \times (\mathrm{ADC} - 5)$.

In addition, the z component of the reconstructed collision vertex (primary vertex) is required to fall within ± 90 cm to the center of the TPC, which is reconstructed with the TPC tracks and the energy deposits on the EMCs with a Pile-up Proof Vertex (PPV) finder [116]. For high luminosity collisions, it is likely to reconstruct several

primary vertices in a single event. The PPV finder assigns a rank to each vertex and the higher the rank, the greater the likelihood of it being a real primary vertex of an event that fires triggers. Therefore, the highest ranked vertex is used in the analysis.

2.3.2 Beam Polarization

As mentioned in Sec. 2.1.3, the beam polarization is measured with the p-C polarimetry [100] and the H-jet polarimeter [101]. In a fill, the beam polarization is measured many times and the measured polarization is fitted by an linear function as following:

$$P(t) = P_0 - P^{'}t, \tag{2.9}$$

where t is the time interval starting from the beginning of a fill. P_0 is the beam polarization at the beginning of a fill and $P^{'}$ is the decreasing rate of the beam polarization. These two values and their corresponding uncertainties are provided by the RHIC Polarimetry Group [117].

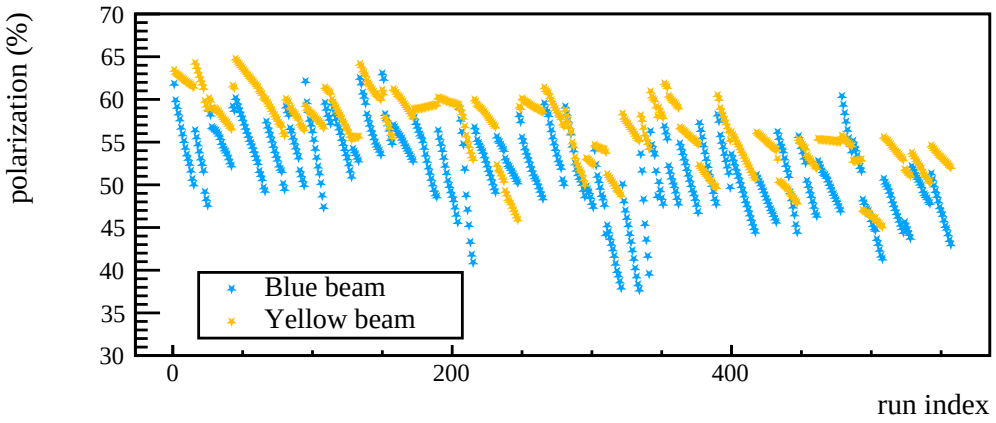

Figure 2.15: Run-by-run beam polarization as a function of run index (early run first) for blue beam and yellow beam.

The run-by-run beam polarization can be obtained based on Eq. (2.9). The middle time of each run is used in the calculation. The calculated run-by-run beam polarization for blue beam and yellow beam is shown in Fig. 2.15. We can see a clear decreasing pattern of the beam polarization for each fill. The average beam polarization P_{set} for

the whole data set can be obtained with the following equation:

$$P_{set} = \frac{\mathcal{L}_{run} P_{run}}{\mathcal{L}_{set}}, \tag{2.10}$$

where the $\mathcal{L}_{run}$ is the luminosity of each run and P_{run} is the beam polarization of each run. The uncertainties of the beam polarization for the whole data set can be determined by following the procedure described in Ref. [118]. These uncertainties will contribute to all the final measurement results as systematic uncertainties in this thesis. The calculated beam polarizations and their uncertainties for blue beam P_B, yellow beam P_Y and their product $P_Y P_B$ are list below:

- $P_B = (51.6 \pm 1.55)\%$, approximately 3.0% relative uncertainty.
- $P_Y = (56.4 \pm 1.69)\%$, approximately 3.0% relative uncertainty.
- $P_Y P_B = (29.7 \pm 1.80)\%$, approximately 6.06% relative uncertainty.

2.3.3 Relative Luminosity

There are 120 bunches in each RHIC ring. For longitudinally polarized proton-proton collision, the helicity state of each bunch can be both '+' and '−' and varies among bunches. Therefore, there are four helicity combinations of two beams ('++', '+−', '−+', '−−'). However, collision data may not be sampled equally among four helicity combinations, leading to a non-physical asymmetry of the sampled data from different helicity combinations. The relative luminosity is used to correct such effect. There are 6 relative luminosities R_1, R_2, R_3, R_4, R_5, and R_6, which are defined as the following:

$$R_1 = \frac{\mathcal{L}^{++} + \mathcal{L}^{-+}}{\mathcal{L}^{--} + \mathcal{L}^{+-}}, \tag{2.11}$$

$$R_2 = \frac{\mathcal{L}^{++} + \mathcal{L}^{+-}}{\mathcal{L}^{--} + \mathcal{L}^{-+}}, \tag{2.12}$$

$$R_3 = \frac{\mathcal{L}^{++} + \mathcal{L}^{--}}{\mathcal{L}^{+-} + \mathcal{L}^{-+}}, \tag{2.13}$$

$$R_4 = \frac{\mathcal{L}^{++}}{\mathcal{L}^{--}}, \tag{2.14}$$

$$R_5 = \frac{\mathcal{L}^{-+}}{\mathcal{L}^{--}}, \tag{2.15}$$

$$R_6 = \frac{\mathcal{L}^{+-}}{\mathcal{L}^{--}}, \tag{2.16}$$

where $\mathcal{L}$ is the luminosity. The first and second superscript of $\mathcal{L}$ denotes the helicity of the blue beam and the yellow beam, respectively. R_1 and R_2 are related to single spin asymmetry measurements of yellow and blue beam, respectively. R_3 is used in the double spin asymmetry calculation, i.e. the longitudinal double spin asymmetry A_{LL} of the $\pi^{\pm}$-tagged jet and Λ, $\overline{\Lambda}$ and K^0_S in this thesis. R_4, R_5, and R_6 are used in the longitudinal spin transfer D_{LL} measurement for Λ and $\overline{\Lambda}$.

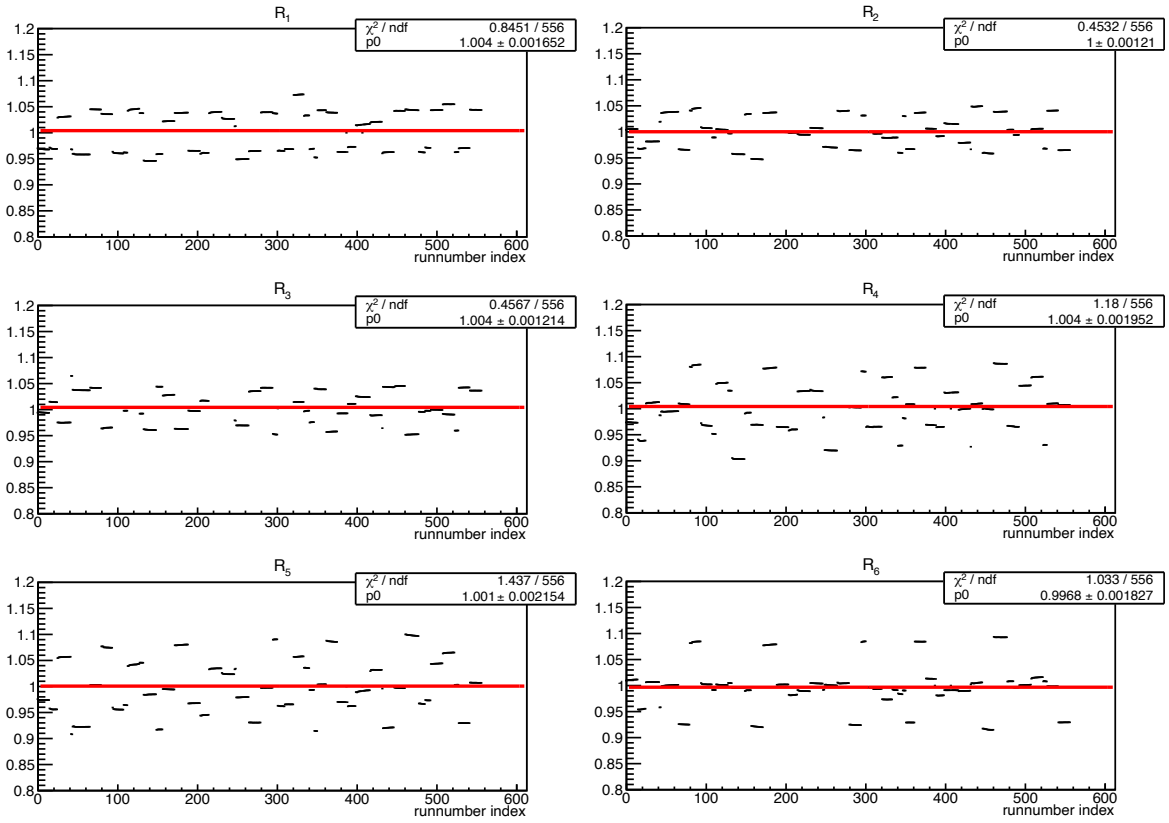

Figure 2.16: Relative luminosities R_1-R_6 as a function of run index. A constant fit (red line) was applied to extract the mean value.

At STAR, relative luminosity is measured with scalar detectors, i.e. the Beam-Beam Counter (BBC) [119], the VPD, and the ZDC. In our analysis, the relative luminosities were calculated in a run-by-run basis with the VPD. Details about the calculation can be found in Refs. [113, 120]. A QA procedure was performed for every runs and fills. Table 2.2 shows the bad bunch crossings founded during the QA. Correspondingly, these data was excluded from the relative luminosity calculation and our analysis. Figure 2.16 shows the calculated R_1-R_6. Their systematic uncertainties were obtained by comparing the results between the VPD and the ZDC, see Ref. [113]. Their differences were fitted with a Gaussian function (see Fig. 2.17) and the fitted width were treated

as the systematic uncertainties of relative luminosities. Table 2.3 summarizes the mean values and the systematic uncertainties of R_1-R_6.

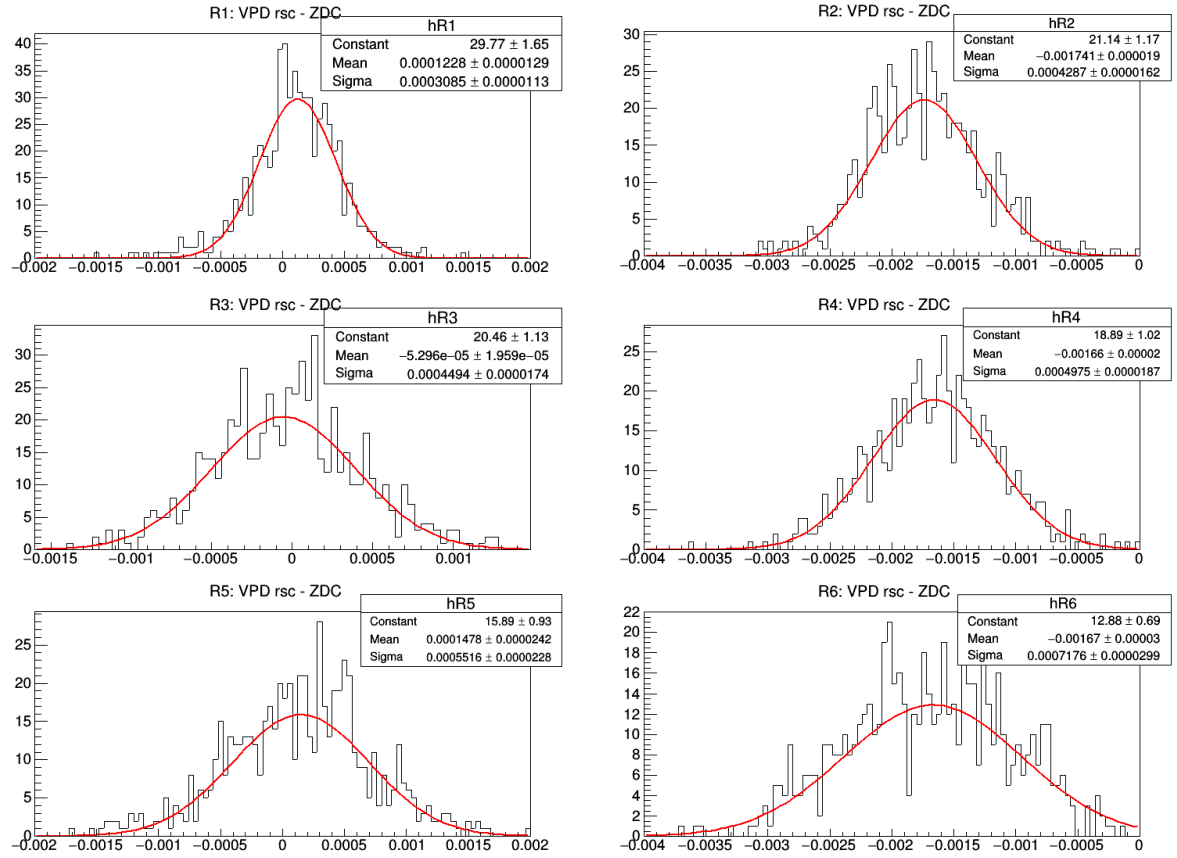

Figure 2.17: The difference of R_1-R_6 calculated with the VPD and the ZDC. A Gaussian fitting was applied (red line).

Fill number	Removed bunch crossing number
18875	0
18876	13
18881	12
18900	30
18907	101
18930	12
18931	20

Table 2.2: The removed bunch crossing number.

Relative luminosity	Results
R_1	1.004 ± 0.00031
R_2	1.000 ± 0.00043
R_3	1.004 ± 0.00045
R_4	1.004 ± 0.00050
R_5	1.001 ± 0.00055
R_6	0.997 ± 0.00072

Table 2.3: The averaged relative luminosities and their systematic uncertainties.

2.4 Summary

In this chapter, a brief introduction on the RHIC facility and some STAR detectors that are relevant to the measurements in this thesis are presented. A brief introduction to the data set used in the measurements of this thesis are presented in the last section.

Chapter 3 Longitudinal Double Spin Asymmetry of $\pi^{\pm}$-tagged Jet

The longitudinal double spin asymmetry A_{LL} of $\pi^{\pm}$-tagged jets is expected to be sensitive to the sign of the gluon helicity distribution. This chapter will present the analysis details of the measurements.

3.1 Jet Reconstruction & $\pi^{\pm}$ Identification

3.1.1 Jet Reconstruction

Similar to STAR previously published results [44, 52-54, 121], jet is reconstructed with the anti-k_T algorithm [122] with the resolution parameter $R = 0.6$ in $\sqrt{s} = 200$ GeV proton-proton collision. The anti-k_T algorithm was found to be insensitive to the soft background from the pile-up events and the underlying events. Event-by-event jet reconstruction was applied using the TPC tracks and the energy deposits inside the towers of the BEMC and EEMC. Primary tracks that directly emitted from the primary vertex were selected. A p_T-dependent Distance of Closest Approach (DCA) cut, which helps to reduce the tracks from pile-ups, was applied to the primary tracks, as shown in the following:

$$DCA < \begin{cases} 2 \text{ cm} & \text{if } p_T < 0.5\text{GeV} \\ -1.0 \text{ cm/GeV} \times p_T + 2.5 \text{ cm} & \text{if } 0.5 < p_T < 1.5\text{GeV} \\ 1 \text{ cm} & \text{if } p_T > 1.5\text{GeV} \end{cases} \tag{3.1}$$

The tracks and the energy deposits inside the EMCs towers are converted into Lorentz 4-vector objects. The tracks are converted with their mass assumed to be the charged pion mass. For the energy deposits in the EMC towers, they are assumed to be massless particles with their momentum pointing from the primary vertex to the center of that tower. For primary tracks pointing to an EMC tower, a 'p_T subtraction' procedure [44, 52] was applied, which subtracts the track p_T from the tower E_T. If the matched tower E_T is less than the track p_T, the tower energy will be excluded from the jet finding inputs. This procedure avoids the double counting of electrons

and positrons that were fully reconstructed by both the TPC and EMCs. For charged hadrons, the average energy deposits in the EMCs count only about 30% of their total energy. However, in some rare cases, this procedure leads to an over-subtraction where a photon hit the same tower as a hadron. Nevertheless, the 'p_T subtraction' procedure reduces the sensitivity to the fluctuation of the energy deposits of charged hadrons and improves the resolution of the jet energy [52]. The selection criteria for the TPC tracks and EMC towers used in the jet reconstruction are summarized in Tab. 3.1.

Selection criteria for tracks
Track flag > 0
Number of TPC hits > 12
Number of TPC hits/Number of geometrically possible TPC hits > 0.51
p_T-dependent DCA, see Eq. (3.1)
$p_T > 0.2$ GeV
$\|\eta\| < 2.5$
Radius of the last point > 125 cm
Selection criteria for towers
Tower status $= 1$
Tower ADC $-$ pedestal > 4
Tower ADC $-$ pedestal > 3RMS
Tower $E_T > 0.2$ GeV

Table 3.1: The selection criteria of the TPC tracks and BEMC and EEMC towers used in the jet reconstruction.

Additional selection criteria were applied to the reconstructed jet candidates, as summarized in Tab. 3.2, to ensure they are covered in the detector acceptance. Cuts on the sum of the in-jet track p_T and the neutral energy fraction R_t were applied to ensure that the reconstructed jet candidates are not fully composed by neutral particles.

An off-axis cone method, adapted from the ALICE experiment [123], was used to estimate the underlying events (UE) contribution, and the jet p_T was corrected by subtracting the estimated UE p_T in a jet-by-jet basis. In our analysis, the UE-corrected jet p_T was divided into 11 bins, and the minimum UE-corrected jet p_T was required to be larger than 6 GeV for JP1 trigger and 8.4 GeV for JP2 trigger. The bin widths were taken as 18% of the lower edge of that bin. Jets are rejected if the UE correction shifts the jet p_T by more than two jet p_T bins. Additionally, as the track reconstruction becomes unreliable at track $p_T > 30$ GeV, jets containing such track were rejected from

our analysis. Each jet is classified into JP1-type jet or JP2-type jet. The classification criteria are:

1. A jet is JP2-type jet if the following criteria fulfilled:
    - JP2 trigger fired and JP2 trigger should fire
    - UE-corrected jet $p_T > 8.4$ GeV
    - Jet axis matches geometrically with at least one triggered jet patch
    - The energy deposits on the matched jet patch are above JP2 threshold
2. A jet is JP1-type jet if the following criteria fulfilled:
    - Jet is not JP2-type jet
    - JP1 trigger fired and JP1 trigger should fire
    - UE-corrected jet $p_T > 6$ GeV
    - Jet axis matches geometrically with at least one triggered jet patch
    - The energy deposits on the matched jet patch are above JP1 threshold

If a jet can neither be classified as JP2-type nor JP1-type, it will be excluded from the analysis. The number of reconstructed jets in each jet p_T bins for two triggers are summarized in Tab. 3.3.

$-0.7 < \eta_{\text{detector}} < 0.9$
$-1.0 < \eta < 1.0$
Jet neutral energy fraction $R_t < 0.95$
Sum of in-jet track $p_T > 0.5$ GeV
$p_T > 0.2$ GeV
$6.0 <$ UE-corrected jet $p_T < 31.6$ GeV for JP1
UE-corrected jet $p_T > 8.4$ GeV for JP2
Jets with individual track $p_T > 30$ GeV are removed

Table 3.2: The selection criteria of the reconstructed jet candidates.

3.1.2 $\pi^{\pm}$ Identification

The charged pions have been identified based on the energy loss dE/dx inside the TPC. At STAR, the measured dE/dx of charged tracks is usually converted into the

Jet p_T range (GeV)	Number of jets for JP1	Number of jets for JP2
6−7.1	10256301	0
7.1−8.4	7522004	0
8.4−9.9	3144570	16766424
9.9−11.7	1474744	13111757
11.7−13.8	566712	8376113
13.8−16.3	189920	4665992
16.3−19.2	54801	2198303
19.2−22.7	14430	940878
22.7−26.8	3369	337816
26.8−31.6	749	107450
31.6−37.3	0	29632

Table 3.3: Number of reconstructed inclusive jets after applying jet selection criteria.

$n\sigma$, which is used to characterize the normalized distance of the measured dE/dx for a charged track to the theoretical dE/dx values of a reference particle. For example, the $n\sigma(\pi)$ can be calculated with the following formula:

$$n\sigma(\pi) = \frac{1}{\sigma_{exp}} \ln \left(\frac{dE/dx_{obs}}{dE/dx_{\pi,cal}} \right), \tag{3.2}$$

where dE/dx_{obs} is the energy loss of a charged track and $dE/dx_{\pi,cal}$ is the theoretical value of the energy loss of the charged pions calculated with the Bichsel formalism [124]. σ_{exp} is the dE/dx resolution of TPC [125-126]. The $n\sigma(K)$, $n\sigma(p)$ and $n\sigma(e)$ for the charged kaons, proton/anti-proton and the electron/positron can be calculated with a similar formula as Eq. (3.2).

Ideally, the $n\sigma(\pi)$ distributions of the charged pions are expected to be a Gaussian distribution with the unit width and the central value being zero. However, according to the previous published results [125-126], a recalibration is required to determine the central value and the width. Such recalibration is also required for the charged kaons, proton/anti-proton and the electron/position. In this analysis, the same recalibration results as Ref. [121] are used. Details about the recalibration procedure can be found in Refs. [121, 127]. Figure 3.1 presents the central values and the width of the charged pions, charged kaons and proton/anti-proton from Ref. [127]. The fitted curves shown in solid and dashed lines in the Fig. 3.1 are used for further analysis. To determine the

in-jet particle fraction, the $n\sigma(\pi)$ distributions for the in-jet tracks are fitted with the Multi-Gaussian function with the fixed mean and width obtained in the recalibration based on the fitting curves shown in the Fig. 3.1. Figure 3.2, as an example, presents the $n\sigma(\pi)$ distribution and the corresponding fitting functions of positive charged tracks. The particle fractions as a function of particle momentum are shown in Fig. 3.3. The fitting curves are used for further analysis. Different fits are also applied to the Fig. 3.3 to estimate systematic uncertainties to the final A_{LL} measurements introduced in the particle identification (PID).

In this analysis, A_{LL} is measured as a function of jet p_T. The particle purity in each jet p_T bin can be calculated with the 'Likelihood method' used in Ref. [121]. For example, the pion likelihood L_π and its purity f_π can be calculated with the following formula:

$$L_\pi = \frac{A_\pi}{(\sigma_\pi)\sqrt{2\pi)}} e^{\frac{-(n\sigma(\pi)-\mu_\pi)^2}{2(\sigma_\pi)^2}}, \tag{3.3}$$

$$f_\pi = \frac{L_\pi}{L_\pi + L_K + L_p + L_e}, \tag{3.4}$$

where the A_π is the pion fraction. μ_π and σ_π is the calibrated central value and width of the $n\sigma(\pi)$. A_π, μ_π and σ_π are obtained with fitting curves mentioned above. The likelihood for other particles can be calculated similarly. The average value is used at each jet p_T bin. In practice, we determined three particle-enriched regions, i.e. pion-enriched region, kaon+proton-enriched region and electron-enriched region, in terms of the $n\sigma(\pi)$, which is summarized in Tab. 3.4. The reason of combining kaon and proton will be explained in the next section. Moreover, only tracks with jet momentum fraction $z \equiv \frac{\vec{p}_\pi \cdot \vec{p}_{jet}}{|\vec{p}_{jet}|^2}$ greater than 0.2 were used for further analysis. Figure 3.4 shows the estimated particle purity as a function of jet p_T at different particle enriched regions for $z > 0.2$. Similar results for particles with $z > 0.3$ are shown in Fig. 3.5. The purity is used to extract the A_{LL}, which will be discussed in the next section.

z	jet p_T (GeV)	$\pi^\pm$-enriched reigon	$K^\pm$+proton-enriched region	$e^\pm$-enriched region
$0.2-0.3$	$6-8.4$	$(-1,2)$	$(-4,-1)$	$(2,7)$
$0.2-0.3$	>8.4	$(-1,2)$	$(-5,-1)$	$(2,7)$
>0.3	>6	$(-1,2)$	$(-5,-1)$	$(2,7)$

Table 3.4: The particle-enriched regions in terms of $n\sigma(\pi)$ of tracks.

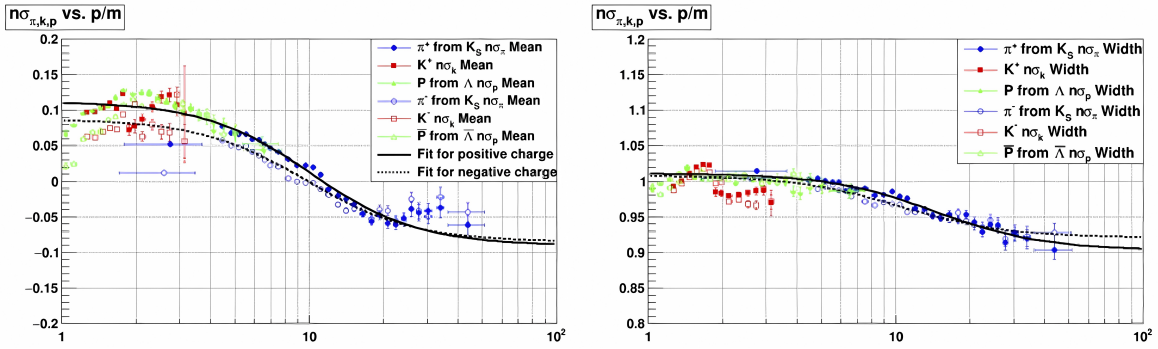

Figure 3.1: The central values (left panel) and the widths (right panel) as a function of the particle p/m for the $n\sigma(\pi)$, $n\sigma(K)$ and $n\sigma(p)$ distributions obtained from pure particle samples. The solid and dashed curves are from the fitting. Plots were taken from Ref. [127]

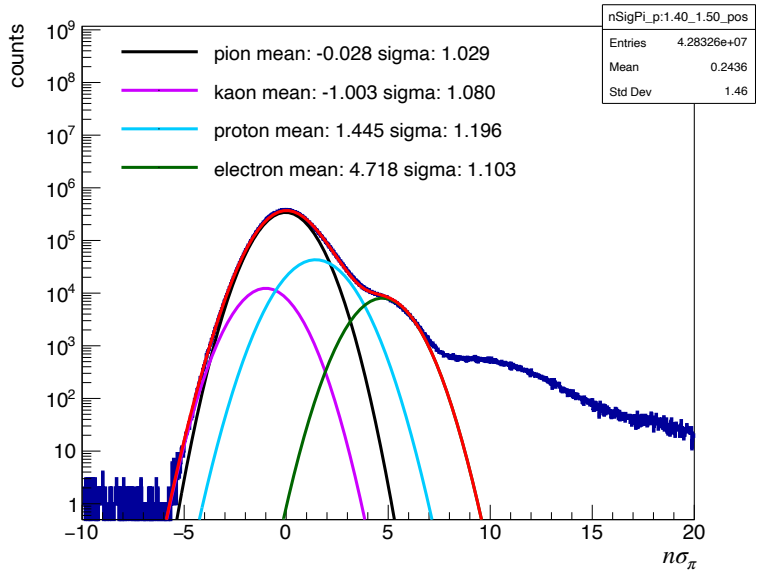

Figure 3.2: The multi-Gaussian fitting of the $n\sigma(\pi)$ distribution of the positive charged tracks with particle momentum $1.4 < p < 1.5$ GeV.

3.2 A_{LL} Extraction

3.2.1 A_{LL} Extraction

In this analysis, a jet is classified as, for example, π^+-tagged jet if it contains a π^+ carrying jet momentum fraction $z > 0.2$ or $z > 0.3$. For very rare cases that both π^+ and π^- satisfy the condition, jets are classified based on pions that carry larger z. At STAR, the longitudinal double spin asymmetry A_{LL} of the $\pi^{\pm}$-tagged jet can be

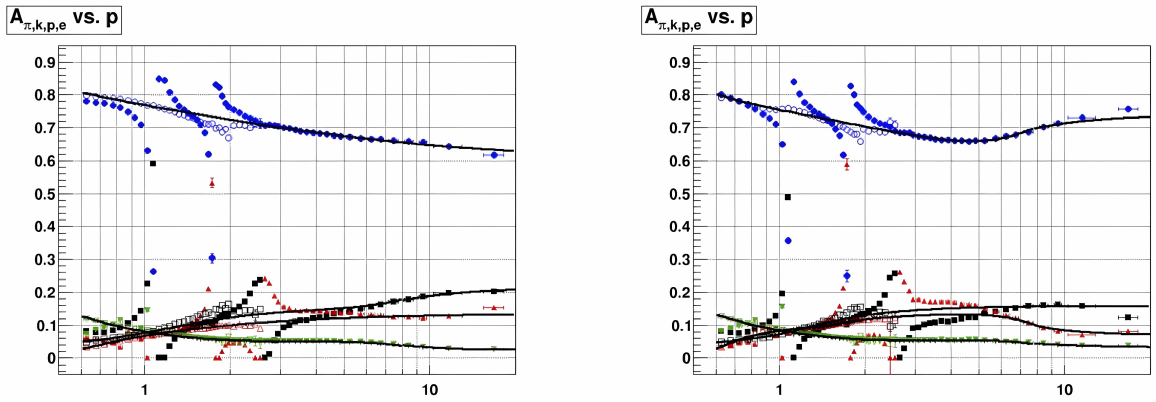

Figure 3.3: The in-jet particle fraction as a function of the particle momentum p for charged pions (blue points), charged kaons (black points), proton/anti-proton (red points), and electron/positron (green points). The left panel is for positive charged tracks and the right panel is for negative charged tracks. Plots were taken from Ref. [127]

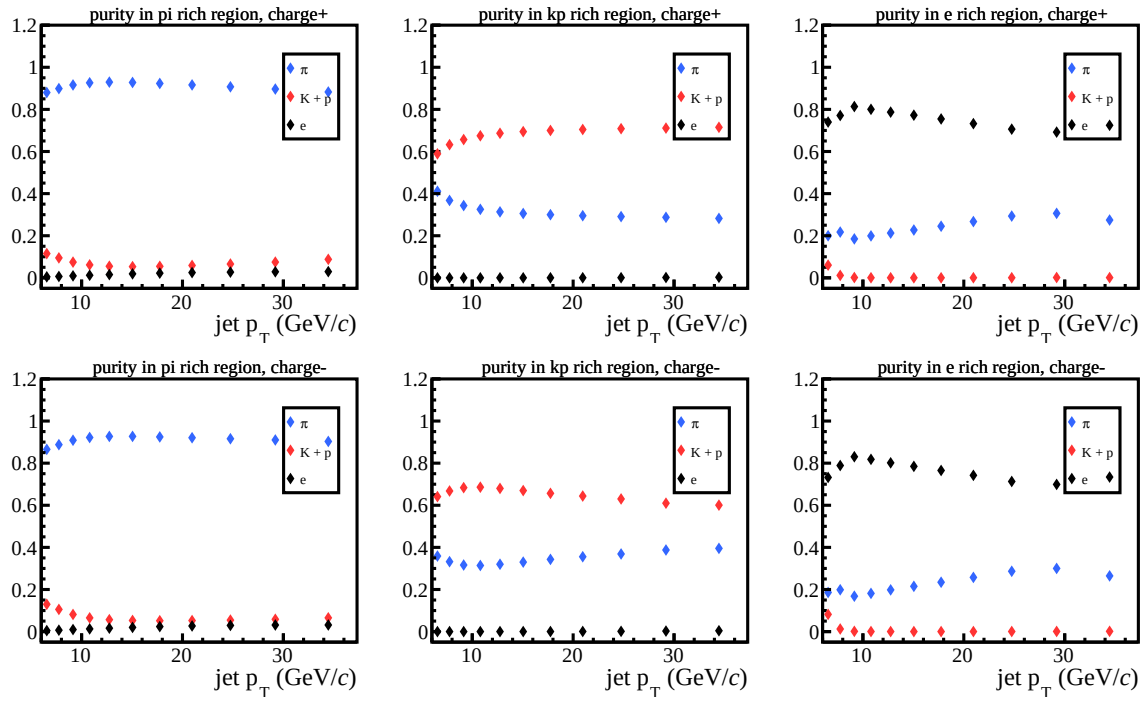

Figure 3.4: The estimated particle purity as a function of jet p_T with jet momentum fraction $z > 0.2$. The first row represents the results of positive-charged tracks, and the second row is for negative-charged tracks. The results at pion-enriched, kaon+proton-enriched and electron-enriched regions are shown from left to right.

measured via the following formula:

$$A_{LL} = \frac{\sum_{runs} P_Y P_B \left[(N^{++} + N^{--}) - R_3(N^{+-} + N^{-+})\right]}{\sum_{runs} (P_Y P_B)^2 \left[(N^{++} + N^{--}) + R_3(N^{+-} + N^{-+})\right]}, \tag{3.5}$$

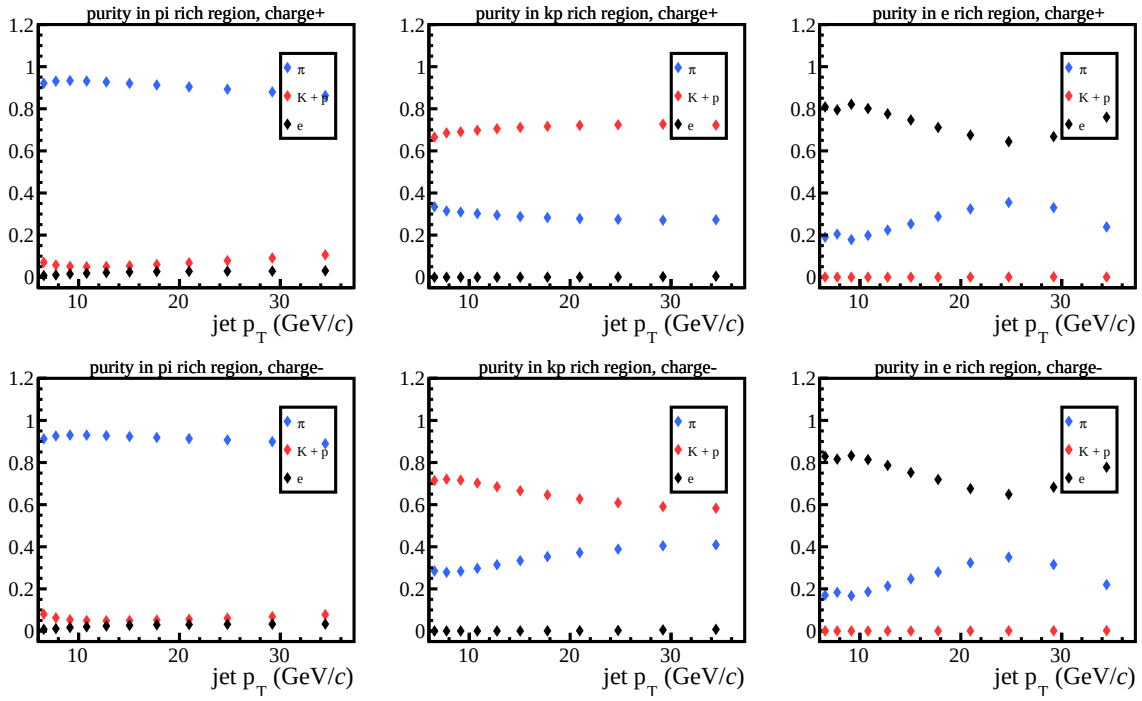

Figure 3.5: The estimated particle purity as a function of jet p_T with jet momentum fraction $z > 0.3$. The first row represents the results of positive-charged tracks, and the second row is for negative-charged tracks. The results at pion-enriched, kaon+proton-enriched and electron-enriched regions are shown from left to right.

where N^{++}, N^{+-}, N^{-+}, and N^{--} are the yields of jet from different helicity configurations of two beams with the first superscript denoting the helicity state of the blue beam and the second for yellow beam. The statistical uncertainty of A_{LL} can be obtained with the Eq. (3.6). It only counts for the statistical uncertainties of the sampled jet yields, which are assumed to follow the Poisson distribution.

$$\delta A_{LL} = \frac{\sqrt{\sum_{run} P_Y^2 P_B^2 [(N^{++} + N^{--}) + R_3^2 (N^{+-} + N^{-+})]}}{\sum_{run} P_Y^2 P_B^2 [(N^{++} + N^{--}) + R_3 (N^{+-} + N^{-+})]} \tag{3.6}$$

The raw A_{LL}^{raw} at each particle-enriched region are extracted with the Eq. (3.5) for both positive-charged and negative-charged particles separately. Figure 3.6 shows the extracted raw A_{LL} results as a function of jet p_T with the jet momentum fraction $z > 0.2$. Similar results for $z > 0.3$ are shown in Fig. 3.7.

At each particle-enriched region, the extracted raw asymmetries A_{LL}^{raw} are linear mixtures of the pure asymmetries A_{LL}^{pure} of each particles. Three particle-enriched regions corresponds to three linear equations and the A_{LL}^{pure} can be obtained by solving

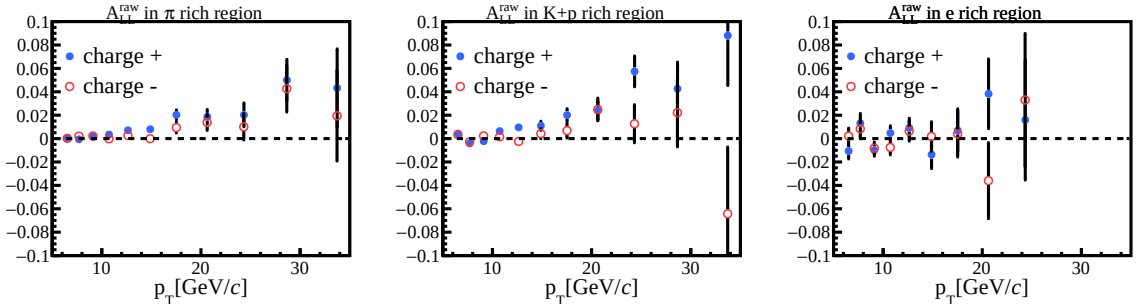

Figure 3.6: The raw asymmetries as a function of jet p_T, which are extracted at each particle-enriched region for both positive-charged and negative-charged particles with the momentum fraction of jets $z > 0.2$ carried by particles. Panels from left to right present the results for pion-enriched, kaon+proton-enriched, and electron-enriched regions, respectively.

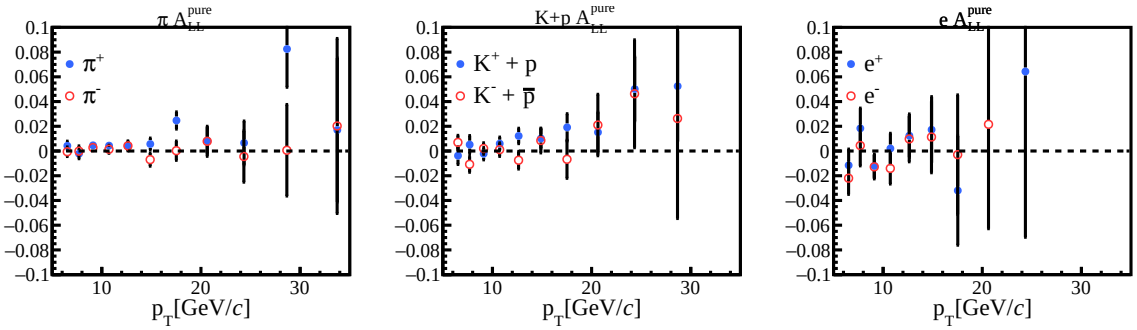

Figure 3.7: The raw asymmetries as a function of jet p_T, which are extracted at each particle-enriched region for both positive-charged and negative-charged particles with the momentum fraction of jets $z > 0.3$ carried by particles. Panels from left to right present the results for pion-enriched, kaon+proton-enriched, and electron-enriched regions, respectively.

the following linear equations:

$$\begin{bmatrix} f^{\pi}_{\pi_{rich}} & f^{K+p}_{\pi_{rich}} & f^{e}_{\pi_{rich}} \\ f^{\pi}_{K+p_{rich}} & f^{K+p}_{K+p_{rich}} & f^{e}_{K+p_{rich}} \\ f^{\pi}_{e_{rich}} & f^{K+p}_{e_{rich}} & f^{e}_{e_{rich}} \end{bmatrix} \begin{bmatrix} A^{\pi}_{LL} \\ A^{K+p}_{LL} \\ A^{e}_{LL} \end{bmatrix} = \begin{bmatrix} A^{raw,\pi_{rich}}_{LL} \\ A^{raw,K+p_{rich}}_{LL} \\ A^{raw,e_{rich}}_{LL} \end{bmatrix}, \tag{3.7}$$

where, for example, $f^{\pi}_{\pi_{rich}}$ is the purity of the charged pion at the pion-enriched region, which is estimated in Sec. 3.1.2. A^{π}_{LL}, A^{K+p}_{LL}, and A^{e}_{LL} are the pure asymmetries of the charged pion, kaon+proton and the electron/positron, respectively. The reason of combining kaon and proton is that the pion and kaon are dominated at kaon-enriched region with close purity and similar case for kaon and proton at proton-enriched region. The relative large and close purity will lead to unstable A_{LL} solutions. Therefore, in

practice, kaon and proton are combined. The extracted pure asymmetries of charged pion as a function of jet p_T are shown in Fig. 3.8. There are no much differences between the raw and pure asymmetries of charged pions as they dominates absolutely at pion-enriched region.

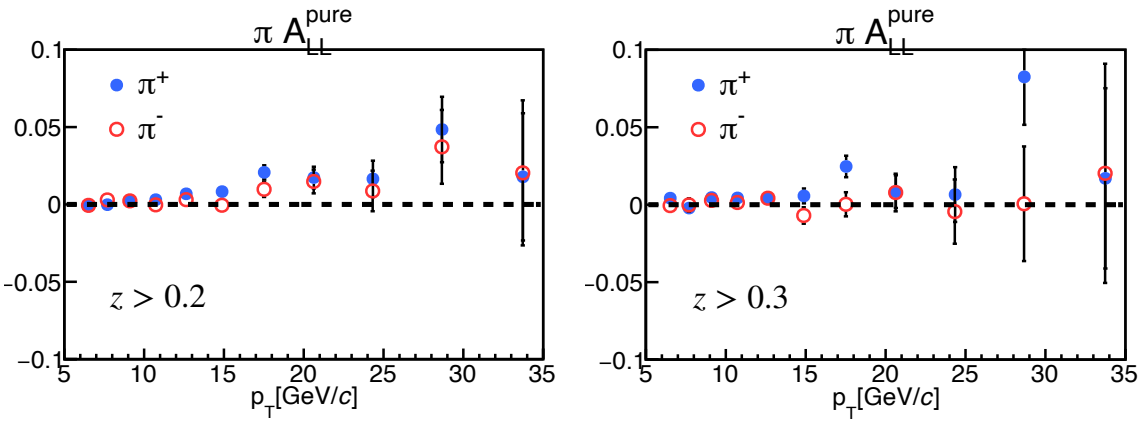

Figure 3.8: The pure asymmetries of the charged pions as a function of jet p_T. Panels from left to right present the results for jet momentum fraction $z > 0.2$ and $z > 0.3$, respectively.

3.2.2 False Asymmetries

Four false asymmetries are extracted, which are good observables to check the validity of the relative luminosities and are expected to be consistent with zero. Experimentally, they are calculated with the following formulas:

$$A_L^B = \frac{\sum_{run} P_B \left[(N^{++} + N^{+-}) - R_2 \left(N^{-+} + N^{--}\right)\right]}{\sum_{run} P_B^2 \left[(N^{++} + N^{+-}) + R_2 \left(N^{-+} + N^{--}\right)\right]} \tag{3.8}$$

$$A_L^Y = \frac{\sum_{run} P_Y \left[(N^{++} + N^{-+}) - R_1 \left(N^{+-} + N^{--}\right)\right]}{\sum_{run} P_Y^2 \left[(N^{++} + N^{-+}) + R_1 \left(N^{+-} + N^{--}\right)\right]} \tag{3.9}$$

$$A_{LL}^{LS} = \frac{\sum_{run} P_Y P_B \left(N^{++} - R_4 N^{--}\right)}{\sum_{run} P_Y^2 P_B^2 \left(N^{++} + R_4 N^{--}\right)} \tag{3.10}$$

$$A_{LL}^{US} = \frac{\sum_{run} P_Y P_B \left(R_5 N^{+-} - R_6 N^{-+}\right)}{\sum_{run} P_Y^2 P_B^2 \left(R_5 N^{+-} + R_6 N^{-+}\right)} \tag{3.11}$$

As the strong interaction dominates the jet productions with small contribution from the parity-violating processes, the single-spin asymmetry for blue beam A_L^B, the single-spin asymmetry for yellow beam A_L^Y, and the like-sign double spin asymmetry A_{LL}^{LS} should be consistent with zero within uncertainties. Due to the geometrical symmetry, the unlike-sign double spin asymmetry A_{LL}^{US}, in principle, should be exactly zero

as the blue beam helicity being positive and the yellow beam helicity being negative are exactly same to the reverse case. Results that significantly deviate from zero could suggest potential issues in the determination of the relative luminosities or the A_{LL} extraction method. Similar to the extraction of A_{LL}, raw asymmetries of these false asymmetries are extracted for each particle-enriched regions. Figure 3.9, as an example, illustrates these false asymmetries as a function of jet p_T in the pion-enriched regions with jet momentum fraction $z > 0.2$. The extracted pure asymmetries of pions are shown in Fig. 3.10, correspondingly. The average values with their statistical uncertainties are shown on these plots and they are consistent with zero within uncertainties.

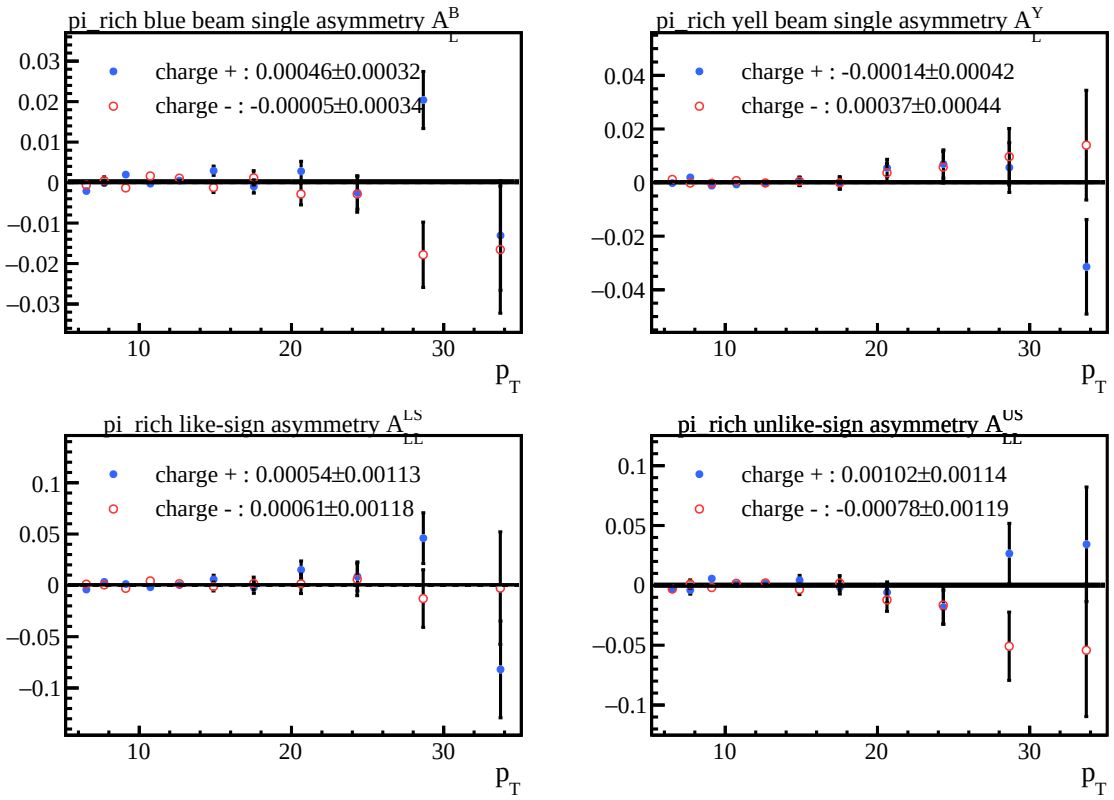

Figure 3.9: The raw false asymmetries as a function of jet p_T at pion-enriched regions with jet momentum fraction $z > 0.2$ carried by in-jet charged tracks.

3.3 Monte Carlo Simulation

Monte Carlo (MC) samples were generated to study possible systematic effects of detector response and to quantify potential distortions. The proton-proton collision events were generated with the PYTHIA generator [128]. The simulated collision events

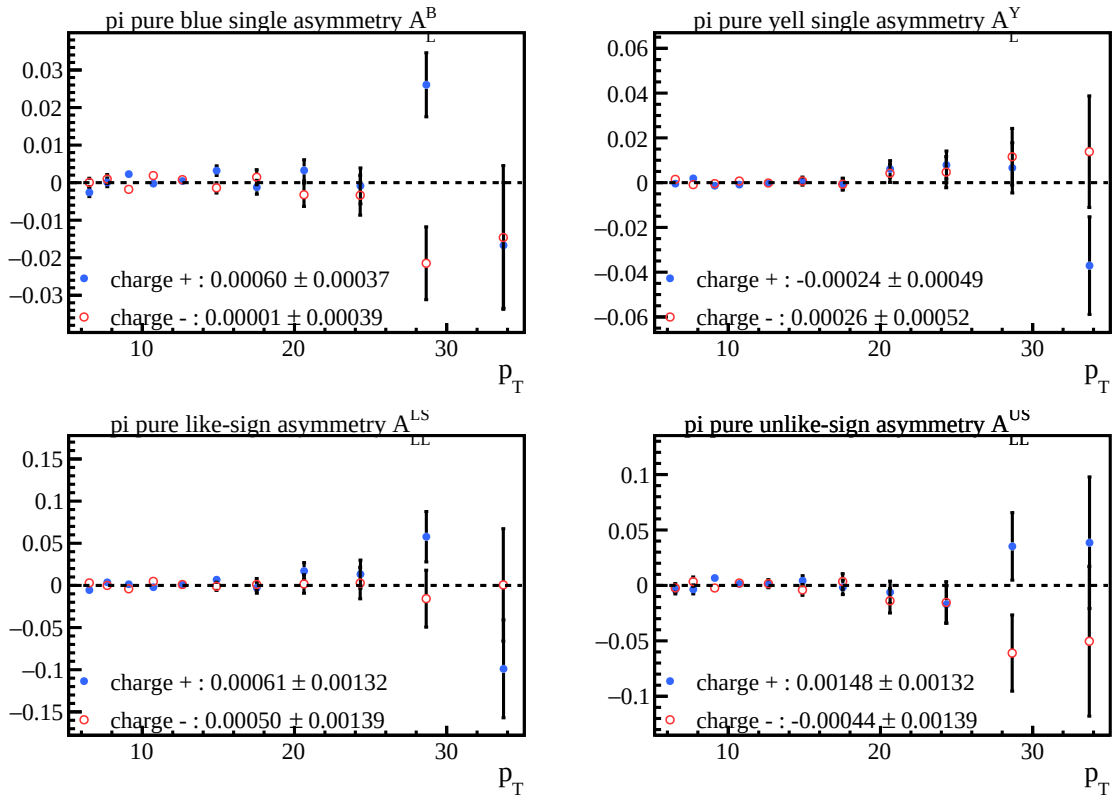

Figure 3.10: The pure false asymmetries of $\pi^{\pm}$-tagged jet with pions carrying jet momentum fraction $z > 0.2$.

were then put into the STAR detector response packages based on GEANT [129] to simulate the detector responses. Subsequently, the detector responses were mixed with the zero-bias events that were collected during the data-taken runs. This procedure is called 'Embedding' at STAR. The zero-bias events are taken randomly without any trigger, making them a suitable approximation for the collision backgrounds and pile-up effects presented in data.

3.3.1 Simulation Setup

In the PYTHIA generator, the $2 \rightarrow 2$ hard QCD sub-processes were turned on, and the perugia 2012 tune [130] was used with PARP(90)=0.213 to better match the published $\pi^{\pm}$ spectrum measurements [131-132]. Details about the adjustments of the PARP(90) can be found in Ref. [133]. The samples were generated in 11 partonic $\hat{p}_T$ bins, and JP1 trigger filter were implemented. Table 3.5 summarizes the Monte Carlo simulation setup. The statistics of the produced embedding MC samples are summarized in Tab. 3.6.

PYTHIA Version	Pythia6_4_28s
Collision System	proton-proton collision
Collision Energy	$\sqrt{s} = 200$ GeV
PYTHIA Tune	Perugia 2012 #370 (CTEQ6L1), PARP(90)=0.213
QCD subprocesses	11: $qq \to qq$ 12: $q\bar{q} \to q\bar{q}$ 13: $q\bar{q} \to gg$ 28: $qg \to qg$ 53: $gg \to q\bar{q}$ 68: $gg \to gg$
Partonic $\hat{p}_T$ Bins (GeV)	2-3, 3-4, 4-5, 5-7, 7-9, 9-11, 11-15 15-20, 20-25, 25-35, > 35
STAR Detector Geometry	y2015c
STAR Software Library	SL16d and SL16d_embed
Production Chains	DbV20160418 pp2015c btof mtd mtdCalib pp2pp Sti fmsDat fmsPoint fpsDat BEmcChkStat -evout CorrX OSpaceZ2 OGridLeak3D -hitfilt DbV20190702_TRG_Calibrations DbV20190702_EEMC_Calibrations DbV20191105_EMC_Calibrations GeomP16id

Table 3.5: Summary on the Monte Carlo simulation setup.

Partonic $\hat{p}_T$ (GeV)	Generated events
$2-3$	12103343
$3-4$	7862602
$4-5$	6739219
$5-7$	3078767
$7-9$	2564991
$9-11$	1727538
$11-15$	826204
$15-20$	601778
$20-25$	391613
$25-35$	391613
>35	183386

Table 3.6: The statistics of the produced embedding MC samples.

3.3.2 Data & Monte Carlo Comparison

Same jet reconstruction procedure is applied to the embedding MC samples. In the embedding MC samples, jets are reconstructed at parton level, particle level, and detector level, which are explained as the following:

- Parton level jets: jets are reconstructed from the scatted partons along with partons from initial-state and final-state radiations. Partons from underlying events and beam remnant are not included.

- Particle level jets: jets are reconstructed from all the stable particles generated with the PYTHIA.

- Detector level jets: simulated tracks and energy deposits in the BEMC and EEMC after detector response are used to reconstruct jets with same procedure applied in data.

Figure 3.11 shows the comparisons for jet p_T, η, ϕ, and detector η between data and embedding MC samples for JP1-type jets. Similar results for JP2-type jets are shown in Fig. 3.12, and results for all JP1-type jets and JP2-type jets are shown in Fig. 3.13, in which the JP1-type jets from embedding MC samples are weighted with the run-by-run prescaling factor in data. In general, results from data and MC are in good agreement.

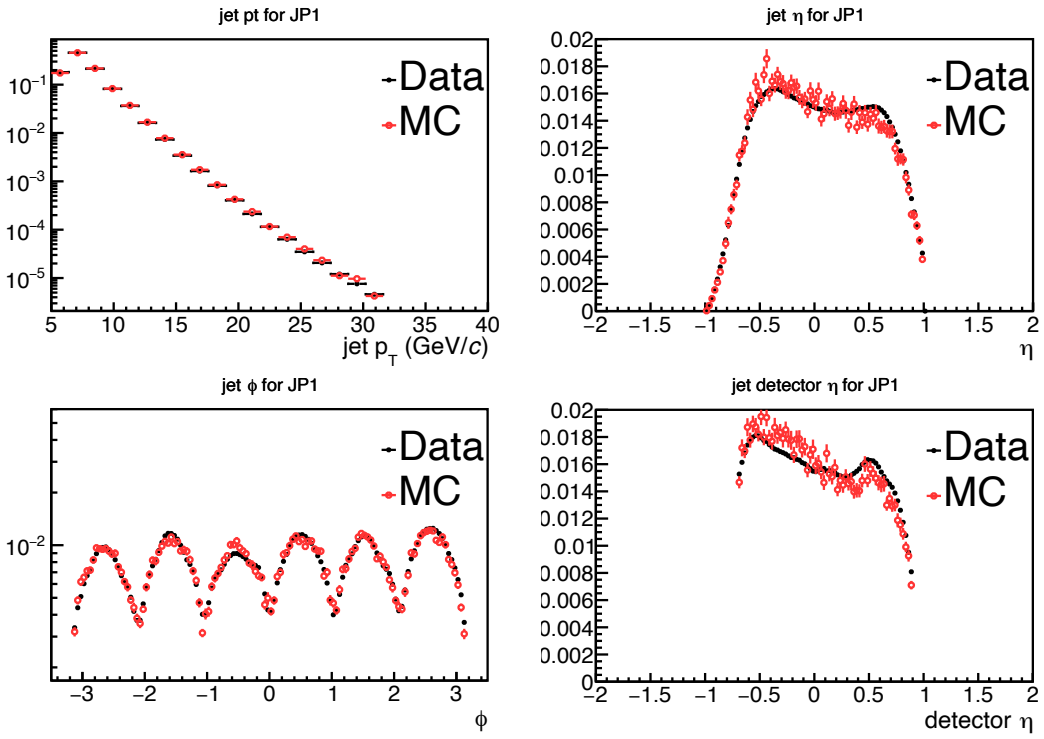

Figure 3.11: The comparison of jet p_T, η, azimuthal angle ϕ, and detector η between data and embedding for JP1 trigger.

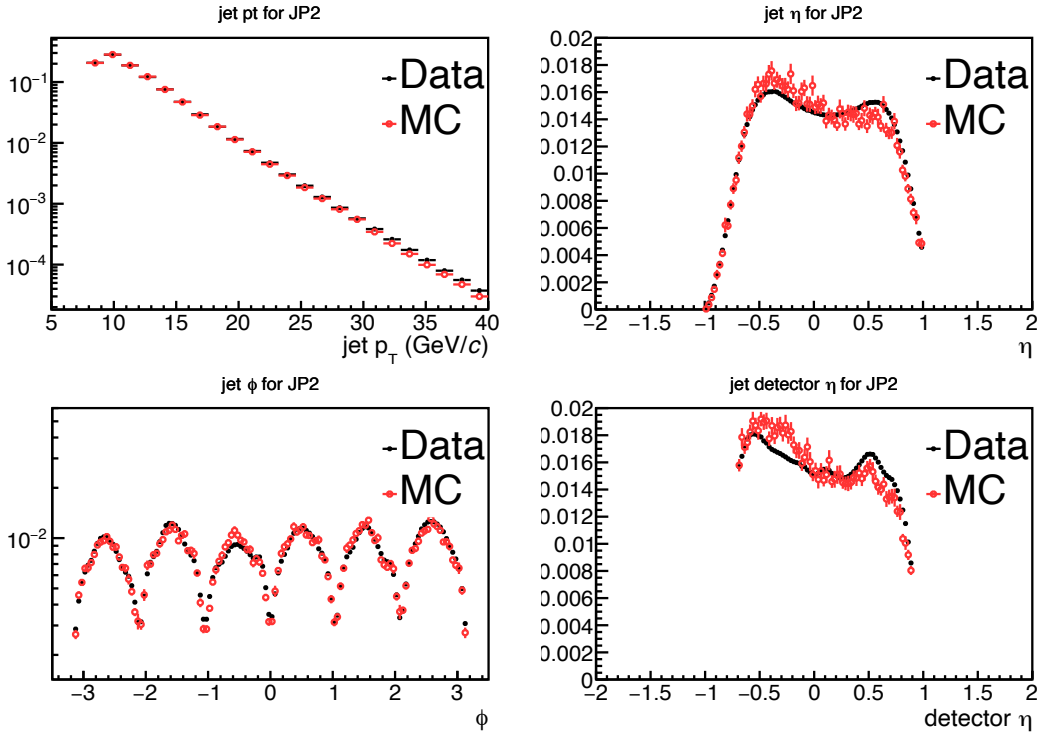

Figure 3.12: The comparison of jet p_T, η, azimuthal angle ϕ, and detector η between data and embedding for JP2 trigger.

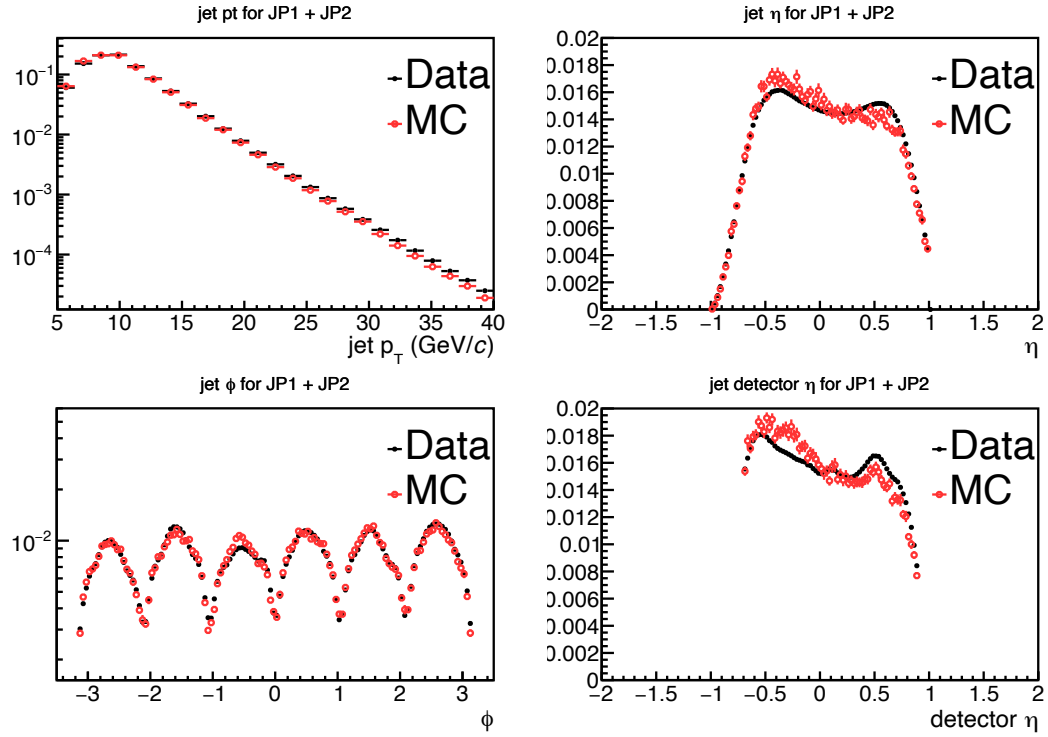

Figure 3.13: The comparison of jet p_T, η, azimuthal angle ϕ, and detector η between data and embedding for JP1 and JP2 combined.

3.4 Systematic Effects

3.4.1 Jet p_T Correction

As jets are reconstructed with the TPC tracks and energy deposits in the BEMC and EEMC, detector responses could introduce potential distortion to the jet p_T. In order to compare the measured results with theoretical calculations, the reconstructed jet p_T in data need to be corrected back to particle level. The corrections are estimated with the embedding MC samples mentioned in Sec. 3.3. In the embedding MC samples, particle level jets were reconstructed using the final state stable particles. In each detector jet p_T bin, the average jet p_T at particle level is obtained. The differences of the average jet p_T between two levels are applied to data as corrections. To match the detector and particle level jets and to make sure the $\pi^{\pm}$ at two levels are the same, the distance ΔR in the η-ϕ space between detector level and particle level jets and $\pi^{\pm}$ are required:

$$\text{For jet: } \Delta R = \sqrt{(\eta_{\text{detector}} - \eta_{\text{particle}})^2 + (\phi_{\text{detector}} - \phi_{\text{particle}})^2} < 0.5, \tag{3.12}$$

$$\text{For } \pi^{\pm}\text{: } \Delta R = \sqrt{(\eta_{\text{detector}} - \eta_{\text{particle}})^2 + (\phi_{\text{detector}} - \phi_{\text{particle}})^2} < 0.05 \tag{3.13}$$

The particle level jets and $\pi^{\pm}$ with smallest ΔR are associated with the detector level jets and $\pi^{\pm}$. The correlation of the jet p_T between detector level and particle level are shown in the left panel of Fig. 3.14 for jet momentum fraction $z > 0.2$. The middle panel of Fig. 3.14 illustrates the differences of jet p_T between detector level and particle level jets. The zoomed-in results of the middle panel are presented on the third column of Fig. 3.14. In Fig. 3.14, the vertical values of the black points indicate average values. Similarly, the results for jet momentum fraction $z > 0.3$ are shown in Fig. 3.15. The numerical values of the average detector level jet p_T shift, $\Delta p_T = p_T^{particle} - p_T^{detector}$, are summarized in the Tab. 3.7.

3.4.2 Trigger Bias

The jet-patch triggers used in this analysis select high p_T jet events based on the energy deposits inside the BEMC and EEMC, which might introduce potential bias on the event selection and eventually impact the A_{LL} measurements. Such trigger bias is estimated with the embedding MC samples by comparing the calculated A_{LL} results

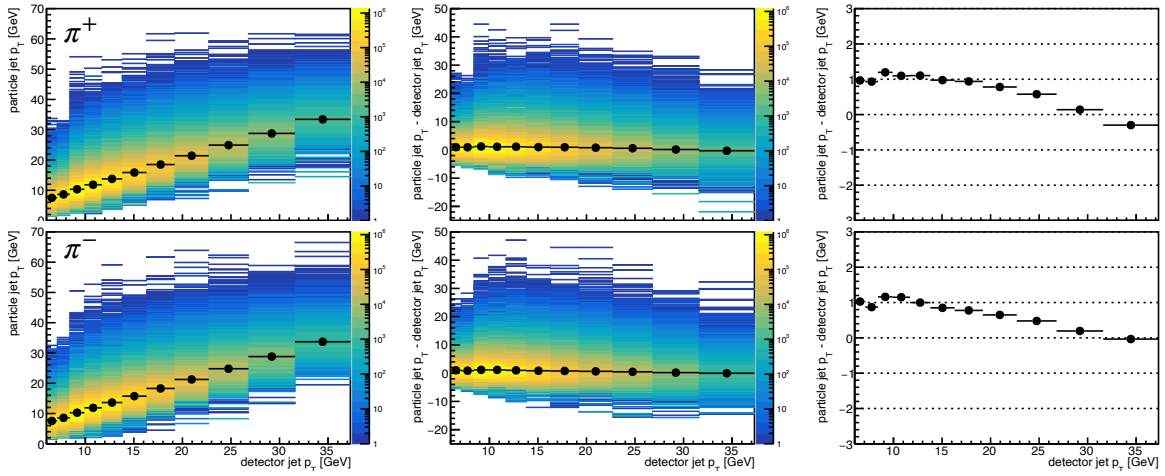

Figure 3.14: The correlation of the jet p_T between detector level and particle level with jet momentum fraction $z > 0.2$. The first row is for π^+-tagged jets and the second row is for π^--tagged jets. The third column is the zoom-in of the second column. The vertical values of the data points in the third column illustrate the average shift of the detector jet p_T.

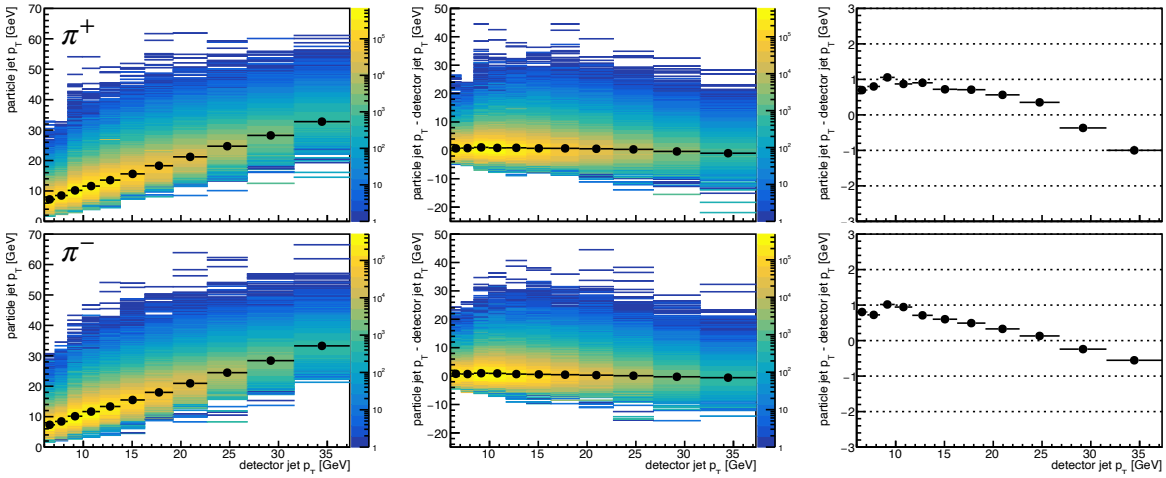

Figure 3.15: The correlation of the jet p_T between detector level and particle level with jet momentum fraction $z > 0.3$. The first row is for π^+-tagged jets and the second row is for π^--tagged jets. The third column is the zoom-in of the second column. The vertical values of the data points in the third column illustrate the average shift of the detector jet p_T.

before and after applying trigger conditions and is applied to the measured A_{LL} as a correction. In the embedding MC samples, the A_{LL} is calculated for both triggered and unbiased samples with the following formula:

$$A_{LL} = \frac{\Delta f_1 \Delta f_2}{f_1 f_2} \hat{a}_{LL}, \tag{3.14}$$

	$\Delta p_T = p_T^{particle} - p_T^{detector}$ (GeV)			
	π^+-tagged jets		π^--tagged jets	
jet p_T (GeV)	$z > 0.2$	$z > 0.3$	$z > 0.2$	$z > 0.3$
$6 - 7.1$	0.97	0.70	1.03	0.81
$7.1 - 8.4$	0.93	0.80	0.87	0.72
$8.4 - 9.9$	1.20	1.06	1.16	1.02
$9.9 - 11.7$	1.10	0.87	1.15	0.94
$11.7 - 13.8$	1.10	0.90	1.00	0.71
$13.8 - 16.3$	0.98	0.72	0.85	0.60
$16.3 - 19.2$	0.94	0.71	0.78	0.49
$19.2 - 22.7$	0.78	0.56	0.65	0.33
$22.7 - 26.8$	0.58	0.35	0.48	0.13
$26.8 - 31.6$	0.14	-0.37	0.19	-0.24
$31.6 - 37.3$	-0.30	-1.00	-0.03	-0.55

Table 3.7: The average detector jet p_T shift.

where $\hat{a}_{LL}$ is the partonic asymmetry of the QCD hard scattering, which can be calculated with the perturbative QCD [45]. Δf is the helicity distribution and the f is the unpolarized parton distribution function taken from NNPDF2.3 [134]. For helicity distribution, the results from the NNPDFpol1.1 [39] global fit with 100 replicas are used. For each replica, the difference $\Delta A_{LL} = A_{LL}^{triggered} - A_{LL}^{unbiased}$ is calculated in each detector jet p_T bin. In the unbiased sample, the calculated A_{LL} as a function of particle level jet p_T for each replica is fitted with a third-order polynomial function. The $A_{LL}^{unbiased}$ is taken as the A_{LL} value at the particle jet p_T obtained in Sec. 3.4.1 using the fitting function for each detector jet p_T bin. The ΔA_{LL} calculated with the best-fit helicity distribution (the default one) is taken as the trigger bias. The standard deviation δA_{LL}^{pdf} of the ΔA_{LL} calculated from 100 replicas is taken as the systematic uncertainty related to the uncertainties of the helicity distribution. Moreover, the statistical uncertainties $\delta A_{LL}^{best-fit}$ from the best-fit distribution of the triggered samples is taken as an additional source of the systematic uncertainty related to the statistics of the embedding MC samples. The total systematic uncertainty δA_{LL}^{trig} from the trigger bias correction is calculated by adding the above two terms in quadrature. Figure 3.16 shows the estimated A_{LL} for both unbiased samples (left column) and triggered samples (middle column) and the trigger bias as a function of detector jet p_T for jet momentum fraction $z > 0.2$. Similarly, the results for $z > 0.3$ are presented in Fig. 3.17. The

numerical values of the calculated trigger bias and the corresponding systematic uncertainties are summarized in Tab. 3.8 and Tab. 3.9 for π^+-tagged jets and π^--tagged jets, respectively. The systematic uncertainties from the estimation of trigger bias are one of the dominant systematic uncertainties on the final A_{LL} results.

	$z > 0.2$			$z > 0.3$		
jet p_T (GeV)	ΔA_{LL}	δA_{LL}^{pdf}	$\delta A_{LL}^{best-fit}$	ΔA_{LL}	δA_{LL}^{pdf}	$\delta A_{LL}^{best-fit}$
$6 - 7.1$	0.0005	0.0002	0.0001	0.0006	0.0001	0.0001
$7.1 - 8.4$	0.0004	0.0001	0.0001	0.0007	0.0002	0.0001
$8.4 - 9.9$	0.0009	0.0002	0.0001	0.0011	0.0002	0.0002
$9.9 - 11.7$	0.0008	0.0002	0.0002	0.0005	0.0002	0.0002
$11.7 - 13.8$	0.0013	0.0003	0.0002	0.0012	0.0002	0.0003
$13.8 - 16.3$	0.0006	0.0002	0.0003	0.0011	0.0002	0.0004
$16.3 - 19.2$	-0.0005	0.0004	0.0004	-0.0011	0.0004	0.0005
$19.2 - 22.7$	0.0006	0.0004	0.0005	0.0001	0.0003	0.0007
$22.7 - 26.8$	0.0005	0.0007	0.0006	0.0002	0.0005	0.0008
$26.8 - 31.6$	-0.0001	0.0007	0.0009	-0.0002	0.0008	0.0011
$31.6 - 37.3$	0.0030	0.0007	0.0013	0.0025	0.0008	0.0017

Table 3.8: The calculated trigger bias ΔA_{LL} and the corresponding systematic uncertainties for π^+-tagged jets.

	$z > 0.2$			$z > 0.3$		
jet p_T (GeV)	ΔA_{LL}	δA_{LL}^{pdf}	$\delta A_{LL}^{best-fit}$	ΔA_{LL}	δA_{LL}^{pdf}	$\delta A_{LL}^{best-fit}$
$6 - 7.1$	0.0002	0.0001	0.0001	0.0003	0.0001	0.0001
$7.1 - 8.4$	0.0000	0.0002	0.0001	0.0001	0.0002	0.0001
$8.4 - 9.9$	0.0002	0.0001	0.0001	-0.0001	0.0001	0.0002
$9.9 - 11.7$	-0.0001	0.0002	0.0002	-0.0001	0.0002	0.0002
$11.7 - 13.8$	-0.0002	0.0003	0.0002	-0.0007	0.0003	0.0003
$13.8 - 16.3$	-0.0008	0.0003	0.0003	-0.0014	0.0003	0.0004
$16.3 - 19.2$	-0.0012	0.0003	0.0004	-0.0009	0.0002	0.0005
$19.2 - 22.7$	-0.0008	0.0004	0.0007	-0.0017	0.0005	0.0011
$22.7 - 26.8$	-0.0025	0.0008	0.0007	-0.0024	0.0007	0.0009
$26.8 - 31.6$	-0.0038	0.0011	0.0009	-0.0052	0.0012	0.0013
$31.6 - 37.3$	-0.0001	0.0005	0.0015	-0.0001	0.0007	0.0020

Table 3.9: The calculated trigger bias ΔA_{LL} and the corresponding systematic uncertainties for π^--tagged jets.

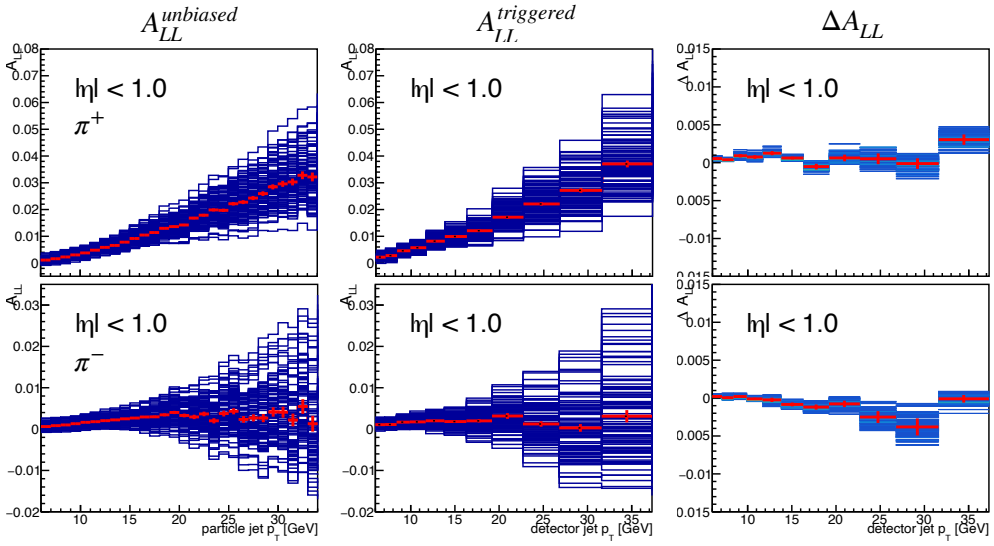

Figure 3.16: Left column: double-spin asymmetry A_{LL} for the unbiased sample as a function of particle jet p_T for all 100 NNPDFpol1.1 replicas. The best-fit result is shown in red. Middle column: A_{LL} for the triggered sample as a function of detector jet p_T for all 100 NNPDF1.1 replicas. Right column: trigger bias for all 100 replicas. The bars show the standard deviation of the ΔA_{LL} from 100 NNPDFpol1.1 replicas. The first and the second rows are for π^+-tagged jets and π^--tagged jets with jet momentum fraction $z > 0.2$, respectively.

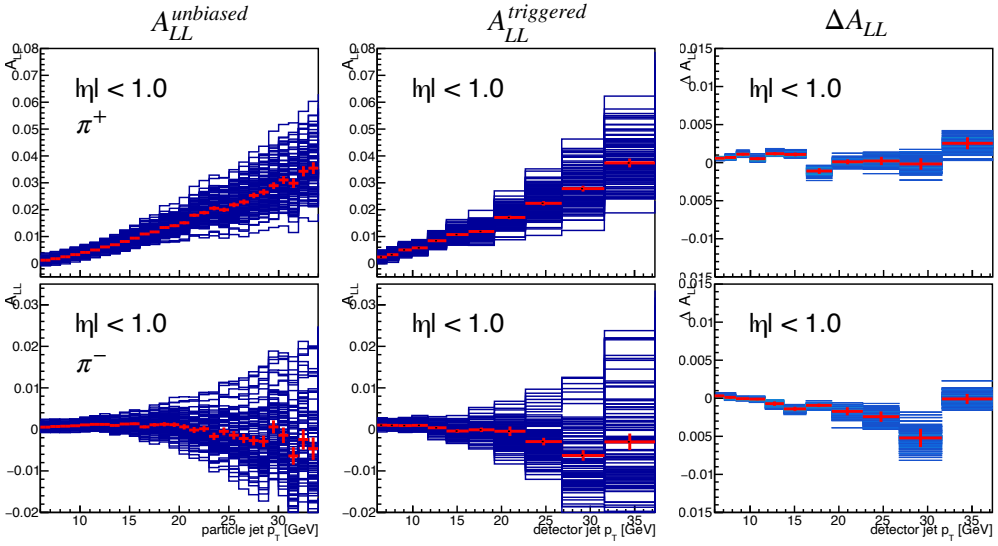

Figure 3.17: Left column: double-spin asymmetry A_{LL} for the unbiased sample as a function of particle jet p_T for all 100 NNPDFpol1.1 replicas. The best-fit result is shown in red. Middle column: A_{LL} for the triggered sample as a function of detector jet p_T for all 100 NNPDF1.1 replicas. Right column: trigger bias for all 100 replicas. The bars show the standard deviation of the ΔA_{LL} from 100 NNPDFpol1.1 replicas. The first and the second rows are for π^+-tagged jets and π^--tagged jets with jet momentum fraction $z > 0.3$, respectively.

3.4.3 Systematic Uncertainties

The systematic uncertainties of the A_{LL} measurements for the $\pi^{\pm}$-tagged jets include the following sources:

- Uncertainty from the beam polarization
- Uncertainty from the particle identification
- Uncertainty for the relative luminosity R_3
- Uncertainty from the trigger bias
- Uncertainty from the underlying event correction

1. Uncertainty from the Beam Polarization As described in Sec. 2.1.3, the relative uncertainty of the beam polarization is about 6.06%. This uncertainty will contribute to all data points as an overall scale uncertainty.

2. Uncertainty from the Particle Identification (PID) As mentioned in Sec. 3.1.2, the particle fraction is fitted with different functions. The A_{LL} results have been calculated with the different fitting results and the differences have been taken as the systematic uncertainties in PID. This part is negligible in this analysis.

3. Uncertainties from Relative Luminosity According to Eq. (3.5), the longitudinal double spin asymmetry of the $\pi^{\pm}$-tagged jet is extracted with the following formula:

$$A_{LL} = \frac{1}{P_Y P_B} \frac{N^+ - R_3 N^-}{N^+ + R_3 N^-}, \tag{3.15}$$

where $N^+ = N^{++} + N^{+-}$ and $N^+ = N^{-+} + N^{--}$. Let $f \equiv N^+/N^-$, and the above equation can be written as:

$$A_{LL} = \frac{1}{P_Y P_B} \frac{f - R_3}{f + R_3} \tag{3.16}$$

and f can be expressed as:

$$f = \frac{1 + P_Y P_B A_{LL}}{1 - P_Y P_B A_{LL}} R_3 \tag{3.17}$$

The uncertainties of A_{LL} contributed from R_3 can be expressed as:

$$\Delta A_{LL} = |\frac{\partial A_{LL}}{\partial R_3}|\Delta R_3 \tag{3.18}$$

$$= \frac{1}{P_Y P_B}\frac{2f}{(f+R_3)^2}\Delta R_3 \tag{3.19}$$

$$= \frac{1}{P_Y P_B}\frac{1-(P_Y P_B A_{LL})^2}{2}\frac{\Delta R_3}{R_3} \tag{3.20}$$

Since P_Y and P_B are less than 1 and $A_{LL} \sim 10^{-2}$, the term $(P_Y P_B A_{LL})^2 \ll 1$ and can be neglected. Therefore, the uncertainty of A_{LL} contributed from the relative luminosity R_3 can be calculated with the following formula:

$$\Delta A_{LL} = \frac{1}{P_Y P_B}\frac{\Delta R_3}{2R_3}, \tag{3.21}$$

where ΔR_3 is the systematic uncertainty of the R_3 described in Sec. 2.3.3. The calculated uncertainty contributed from R_3 is 0.00076. This uncertainty is shared with each measured A_{LL} data points.

4. Uncertainties from Underlying Event Correction Similar to Ref. [53], the contribution from the underlying event correction is estimated with the average spin-independent underlying event correction $\langle dp_T \rangle$ and the double spin asymmetry $A_{LL}^{dp_T}$ of the underlying event correction in data. The $A_{LL}^{dp_T}$ is calculated with the following formula:

$$A_{LL}^{dp_T} = \frac{1}{P_A P_B}\frac{\left(\langle dp_T\rangle^{++} + \langle dp_T\rangle^{--}\right) - \left(\langle dp_T\rangle^{+-} + \langle dp_T\rangle^{-+}\right)}{\left(\langle dp_T\rangle^{++} + \langle dp_T\rangle^{--}\right) + \left(\langle dp_T\rangle^{+-} + \langle dp_T\rangle^{-+}\right)}, \tag{3.22}$$

where, for example, $\langle dp_T\rangle^{++}$ is the average underlying event correction for the '++' beam helicity configuration. The $A_{LL}^{dp_T}$ is calculated at each jet p_T bin in a fill-by-fill basis. Figure 3.18 and 3.19 show the calculated fill-by-fill $A_{LL}^{dp_T}$ results. The $A_{LL}^{dp_T}$ results as a function of jet p_T are presented in the bottom right panels and are fitted with a constant function. The fitting results have been used to calculated systematic uncertainties δA_{LL}^{UE} originating from $A_{LL}^{dp_T}$ with the following formula:

$$\delta A_{LL}^{UE} = \frac{\int_{p_T^{min}-\langle dp_T\rangle A_{LL}^{dp_T}}^{p_T^{max}-\langle dp_T\rangle A_{LL}^{dp_T}} \frac{d\sigma}{dp_T}dp_T - \int_{p_T^{min}+\langle dp_T\rangle A_{LL}^{dp_T}}^{p_T^{max}+\langle dp_T\rangle A_{L}^{dp_T}} \frac{d\sigma}{dp_T}dp_T}{\int_{p_T^{min}-\langle dp_T\rangle A_{LL}^{dp_T}}^{p_T^{max}-\langle dp_T\rangle A_{LL}^{dp_T}} \frac{d\sigma}{dp_T}dp_T + \int_{p_T^{min}+\langle dp_T\rangle A_{LL}^{dp_T}}^{p_T^{max}+\langle dp_T\rangle A_{L}^{dp_T}} \frac{d\sigma}{dp_T}dp_T}, \tag{3.23}$$

where p_T^{max} and p_T^{min} are the upper and lower edge of a jet p_T bin. The $\frac{d\sigma}{dp_T}$ is the unpolarized jet cross section, which is taken from next-to-leading-order pQCD calculation with the CT14 pdf [135]. The numerical values of the estimated δA_{LL}^{UE} are summarized Tab. 3.10.

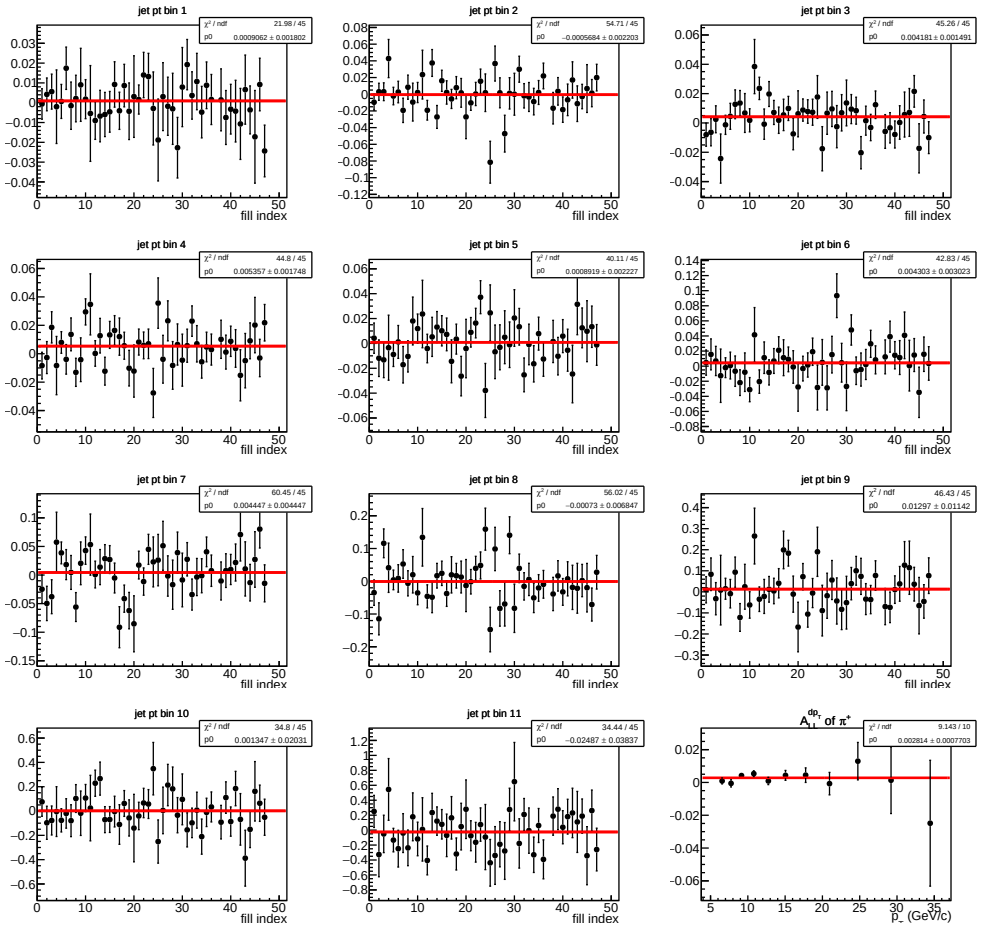

Figure 3.18: The fill-by-fill double spin asymmetry $A_{LL}^{dp_T}$ of the average underlying correction for π^+-tagged jets with $z > 0.2$. The asymmetry is fitted with a constant function marked with red line.

5. Total Systematic Uncertainties The total systematic uncertainties δA_{LL}^{total}, are obtained by adding the uncertainties from different sources in quadrature as they are independent. The numerical values of the systematic uncertainties of each sources and the total uncertainties assigned to the final A_{LL} measurements are summarized in Tab. 3.11 and 3.12 for jet momentum fraction $z > 0.2$ and $z > 0.3$, respectively.

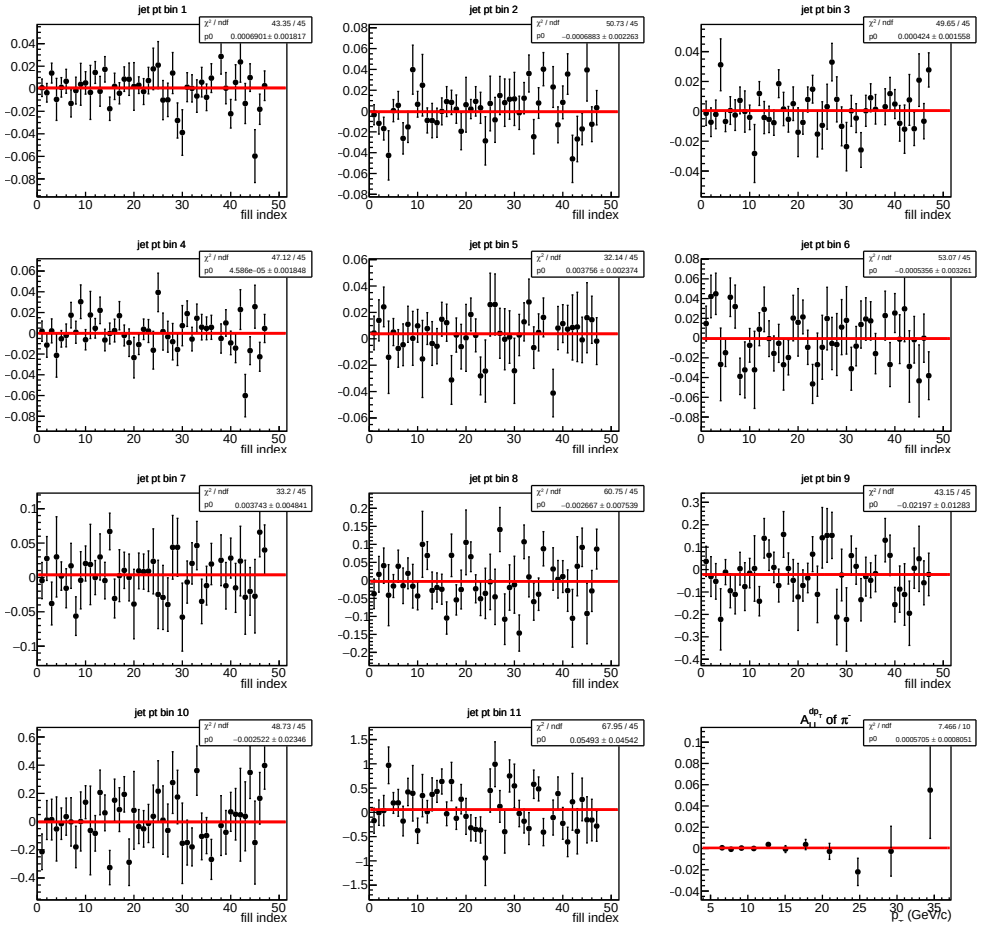

Figure 3.19: The fill-by-fill double spin asymmetry $A_{LL}^{dp_T}$ of the average underlying correction for π^--tagged jets with $z > 0.2$. The asymmetry is fitted with a constant function marked with red line.

	$z > 0.2$		$z > 0.3$	
jet p_T (GeV)	δA_{LL}^{UE} for $A_{LL}^{\pi^+}$	δA_{LL}^{UE} for $A_{LL}^{\pi^-}$	δA_{LL}^{UE} for $A_{LL}^{\pi^+}$	δA_{LL}^{UE} for $A_{LL}^{\pi^-}$
$6 - 7.1$	0.0018	0.0004	0.0016	0.0005
$7.1 - 8.4$	0.0015	0.0003	0.0012	0.0004
$8.4 - 9.9$	0.0013	0.0003	0.0011	0.0003
$9.9 - 11.7$	0.0011	0.0002	0.0009	0.0003
$11.7 - 13.8$	0.0009	0.0002	0.0008	0.0002
$13.8 - 16.3$	0.0008	0.0002	0.0007	0.0002
$16.3 - 19.2$	0.0008	0.0001	0.0007	0.0002
$19.2 - 22.7$	0.0006	0.0001	0.0005	0.0002
$22.7 - 26.8$	0.0004	0.0001	0.0004	0.0001
$26.8 - 31.6$	0.0005	0.0001	0.0005	0.0001
$31.6 - 37.3$	0.0005	0.0001	0.0004	0.0001

Table 3.10: The numerical values of the systematic uncertainty δA_{LL}^{UE} from underlying event correction.

	Systematic uncertainties for the $A_{LL}^{\pi^+}$					
jet p_T (GeV)	P_{beam}	R_3	PID	δA_{LL}^{trig}	δA_{LL}^{UE}	δA_{LL}^{total}
$6-7.1$	6.06%	0.00076	3.1×10^{-5}	0.0002	0.0018	0.0020
$7.1-8.4$	6.06%	0.00076	1.9×10^{-5}	0.0002	0.0015	0.0017
$8.4-9.9$	6.06%	0.00076	9.6×10^{-6}	0.0003	0.0013	0.0015
$9.9-11.7$	6.06%	0.00076	1.3×10^{-6}	0.0003	0.0011	0.0014
$11.7-13.8$	6.06%	0.00076	2.1×10^{-6}	0.0004	0.0009	0.0013
$13.8-16.3$	6.06%	0.00076	4.7×10^{-6}	0.0003	0.0008	0.0012
$16.3-19.2$	6.06%	0.00076	1.4×10^{-6}	0.0005	0.0008	0.0016
$19.2-22.7$	6.06%	0.00076	8.5×10^{-6}	0.0006	0.0006	0.0018
$22.7-26.8$	6.06%	0.00076	5.8×10^{-5}	0.0009	0.0004	0.0013
$26.8-31.6$	6.06%	0.00076	1.4×10^{-5}	0.0011	0.0005	0.0021
$31.6-37.3$	6.06%	0.00076	5.6×10^{-5}	0.0015	0.0005	0.0038
	Systematic uncertainties for the $A_{LL}^{\pi^-}$					
jet p_T (GeV)	P_{beam}	R_3	PID	δA_{LL}^{trig}	δA_{LL}^{UE}	δA_{LL}^{total}
$6-7.1$	6.06%	0.00076	8.1×10^{-6}	0.0001	0.0004	0.0009
$7.1-8.4$	6.06%	0.00076	1.4×10^{-5}	0.0002	0.0003	0.0008
$8.4-9.9$	6.06%	0.00076	4.3×10^{-7}	0.0002	0.0003	0.0008
$9.9-11.7$	6.06%	0.00076	6.7×10^{-6}	0.0002	0.0002	0.0008
$11.7-13.8$	6.06%	0.00076	2.2×10^{-5}	0.0004	0.0002	0.0009
$13.8-16.3$	6.06%	0.00076	2.0×10^{-5}	0.0004	0.0002	0.0009
$16.3-19.2$	6.06%	0.00076	1.1×10^{-5}	0.0005	0.0001	0.0010
$19.2-22.7$	6.06%	0.00076	3.1×10^{-5}	0.0008	0.0001	0.0016
$22.7-26.8$	6.06%	0.00076	3.4×10^{-6}	0.0010	0.0001	0.0013
$26.8-31.6$	6.06%	0.00076	8.1×10^{-6}	0.0015	0.0001	0.0027
$31.6-37.3$	6.06%	0.00076	2.2×10^{-6}	0.0016	0.0001	0.0029

Table 3.11: The numerical values of the systematic uncertainties from different sources and the total uncertainties on the A_{LL} of the $\pi^{\pm}$-tagged jets for $z > 0.2$.

	Systematic uncertainties for the $A_{LL}^{\pi^+}$					
jet p_T (GeV)	P_{beam}	R_3	PID	δA_{LL}^{trig}	δA_{LL}^{UE}	δA_{LL}^{total}
$6-7.1$	6.06%	0.00076	1.0×10^{-5}	0.0002	0.0016	0.0018
$7.1-8.4$	6.06%	0.00076	6.6×10^{-7}	0.0002	0.0012	0.0015
$8.4-9.9$	6.06%	0.00076	5.1×10^{-6}	0.0003	0.0011	0.0014
$9.9-11.7$	6.06%	0.00076	2.0×10^{-6}	0.0003	0.0009	0.0012
$11.7-13.8$	6.06%	0.00076	1.1×10^{-5}	0.0004	0.0008	0.0012
$13.8-16.3$	6.06%	0.00076	5.5×10^{-6}	0.0005	0.0007	0.0012
$16.3-19.2$	6.06%	0.00076	6.5×10^{-6}	0.0007	0.0007	0.0020
$19.2-22.7$	6.06%	0.00076	8.2×10^{-6}	0.0008	0.0005	0.0013
$22.7-26.8$	6.06%	0.00076	3.9×10^{-5}	0.0010	0.0004	0.0014
$26.8-31.6$	6.06%	0.00076	2.3×10^{-5}	0.0013	0.0005	0.0053
$31.6-37.3$	6.06%	0.00076	1.2×10^{-4}	0.0018	0.0004	0.0022
	Systematic uncertainties for the $A_{LL}^{\pi^-}$					
jet p_T (GeV)	P_{beam}	R_3	PID	δA_{LL}^{trig}	δA_{LL}^{UE}	δA_{LL}^{total}
$6-7.1$	6.06%	0.00076	1.7×10^{-5}	0.0002	0.0005	0.0009
$7.1-8.4$	6.06%	0.00076	2.9×10^{-5}	0.0002	0.0004	0.0009
$8.4-9.9$	6.06%	0.00076	2.1×10^{-6}	0.0002	0.0003	0.0009
$9.9-11.7$	6.06%	0.00076	8.9×10^{-7}	0.0003	0.0003	0.0009
$11.7-13.8$	6.06%	0.00076	3.1×10^{-5}	0.0004	0.0002	0.0009
$13.8-16.3$	6.06%	0.00076	2.5×10^{-5}	0.0005	0.0002	0.0010
$16.3-19.2$	6.06%	0.00076	4.1×10^{-6}	0.0006	0.0002	0.0010
$19.2-22.7$	6.06%	0.00076	1.1×10^{-6}	0.0013	0.0002	0.0016
$22.7-26.8$	6.06%	0.00076	8.0×10^{-8}	0.0011	0.0001	0.0014
$26.8-31.6$	6.06%	0.00076	0	0.0017	0.0001	0.0019
$31.6-37.3$	6.06%	0.00076	0	0.0021	0.0001	0.0026

Table 3.12: The numerical values of the systematic uncertainties from different sources and the total uncertainties on the A_{LL} of the $\pi^{\pm}$-tagged jets for $z > 0.3$.

3.5 Results and Discussions

3.5.1 The impact of the $\pi^{\pm}$ tagging

The impact of the jet momentum fraction z cut on the relative fraction of the hard QCD sub-processes is studied with the MC samples generated with PYTHIA [128] by comparing the relative fraction before and after applying the z cut. Figure 3.20 illustrates the ratio of the QCD hard scattering subprocess of jets with $\pi^{\pm}$ tagging to the subprocess for inclusive jets. The contribution from the g-g scattering is suppressed after applying the z cut, which is not sensitive to the sign of the gluon helicity. The π^{+} tagging enhances the u-g scattering with jet p_T approximately smaller than 25 GeV. The d-g scattering is also enhanced with π^{-} tagging with the enhancement up to 40% at high jet p_T. Moreover, the quark-quark scatterings involved with the u quark and d quark are also enhanced at high jet p_T. The enhancements of quark-quark scattering can increase the sensitivity to the quark helicity distributions. When raising the minimum z from 0.2 to 0.3, the enhancements and suppression is further strengthen. Therefore, the measurements of the A_{LL} for the $\pi^{\pm}$-tagged jets provide sensitivity to the sign of the gluon helicity distribution.

3.5.2 The A_{LL} results of $\pi^{\pm}$-tagged jets

The measured results of the longitudinal double spin asymmetry for the $\pi^{\pm}$-tagged jets with the jet momentum fraction $z > 0.2$ are presented in Fig. 3.21 (left). The bars represent the statistical uncertainties while the systematic uncertainties are shown in boxes. Similar results with $z > 0.3$ are shown in Fig. 3.21 (right). In general, the measured A_{LL} results for π^{+}-tagged jets are positive and increase with increasing jet p_T while there is no clear jet p_T dependence for the A_{LL} results of π^{-}-tagged jets. The A_{LL} results of π^{+}-tagged jets are slightly larger than the A_{LL} results for π^{-}-tagged jets. Their numerical values are summarized in Tab. 3.13 and 3.14 for $z > 0.2$ and $z > 0.3$, respectively. The curves shown on these figures are calculated with the unbiased MC sample used in the trigger bias estimation (see Sec. 3.4.2). The helicity distribution and the unpolarized PDFs are taken from the NNPDFpol1.1 [39] and NNPDF2.3 [134]. The predictions show increasing A_{LL} results for π^{+}-tagged jets and weak jet p_T dependence for π^{-}-tagged jets, which are consistent with the measurements. The χ^2 of the measured A_{LL} results of π^{+}-tagged jets to the predictions are $\chi^2_{\pi^+}/ndf = 12.6/11$

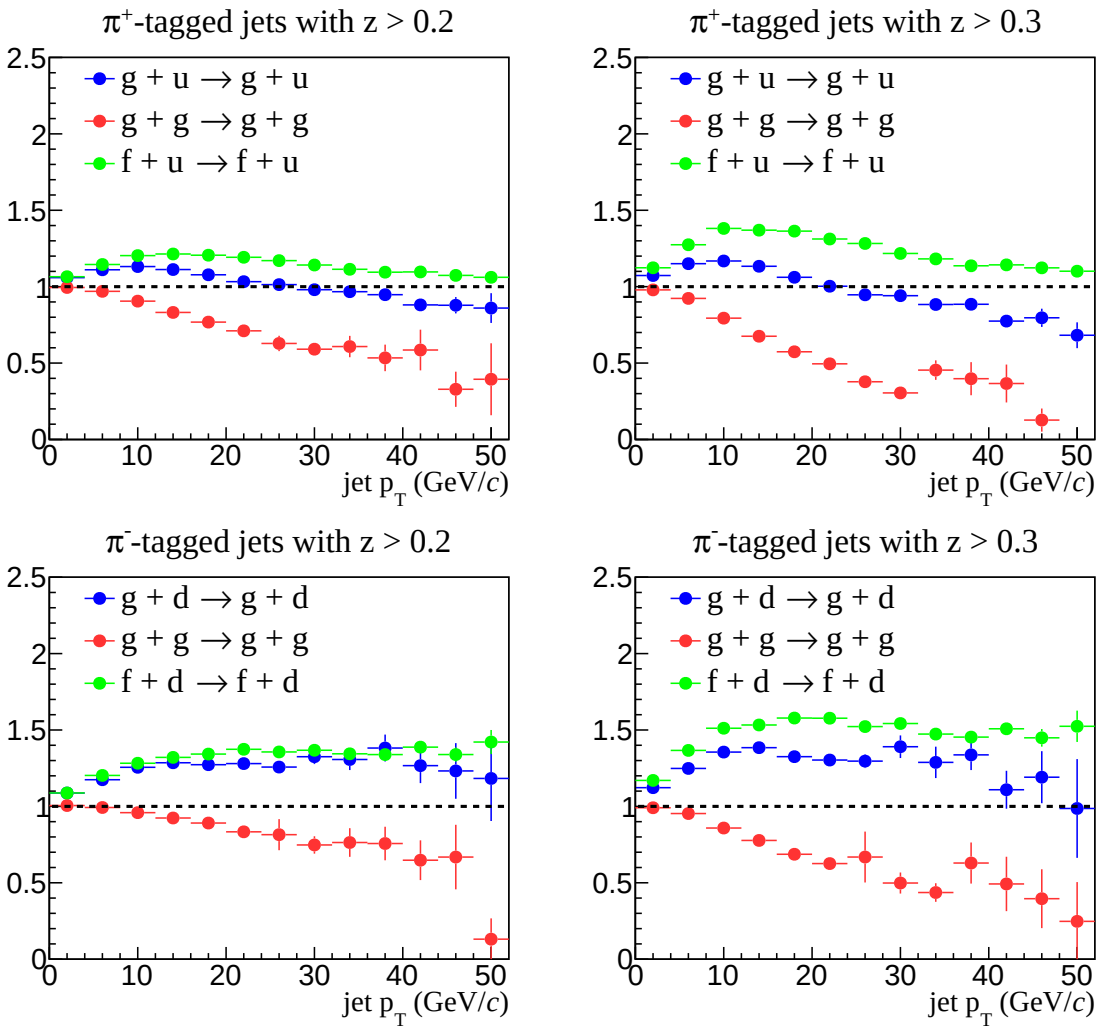

Figure 3.20: The QCD subprocess ratio of the $\pi^{\pm}$-tagged jets to the inclusive jets as a function of jet p_T. The first row is for π^+-tagged jets and the second row is for π^--tagged jets.

and $\chi^2_{\pi^+}/ndf = 13.2/11$ for $z > 0.2$ and $z > 0.3$, respectively. For the A_{LL} results of π^--tagged jets, the χ^2 are $\chi^2_{\pi^-}/ndf = 9.2/11$ and $\chi^2_{\pi^-}/ndf = 3.9/11$ for $z > 0.2$ and $z > 0.3$, respectively. The helicity distribution of gluon in Ref. [39] is positive and our measurements are consistent with the predictions.

The measured A_{LL} results are also compared with the predictions using helicity distribution from JAM22 [57], in which the gluon helicity is negative, with the same unbiased MC sample used in the trigger bias estimation. The comparisons are presented in Fig. 3.22. The left column of Fig. 3.22 shows the comparison for jet momentum fraction $z > 0.2$ while the right panel illustrates the comparison for $z > 0.3$. It is clear that the measured A_{LL} results strongly disfavor the predictions using negative gluon

helicity.

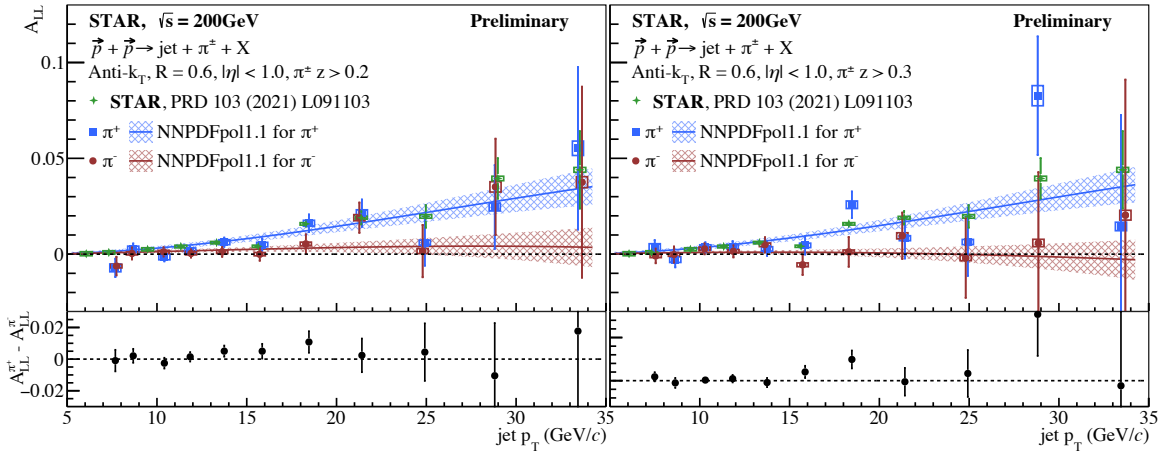

Figure 3.21: The longitudinal double spin asymmetry A_{LL} of the $\pi^{\pm}$-tagged jets as a function of jet p_T in $\sqrt{s}$ = 200 GeV proton-proton collisions with jet momentum fraction $z > 0.2$ (left) and $z > 0.3$ (right). The curves are the predictions with PYTHIA [128] using the helicity distribution and the unpolarized PDFs from the NNPDFpol1.1 [39] and NNPDF2.3 [134], respectively. The bottom panel represents the difference between $A_{LL}^{\pi^+}$ and $A_{LL}^{\pi^-}$. The bars only count for statistical uncertainties.

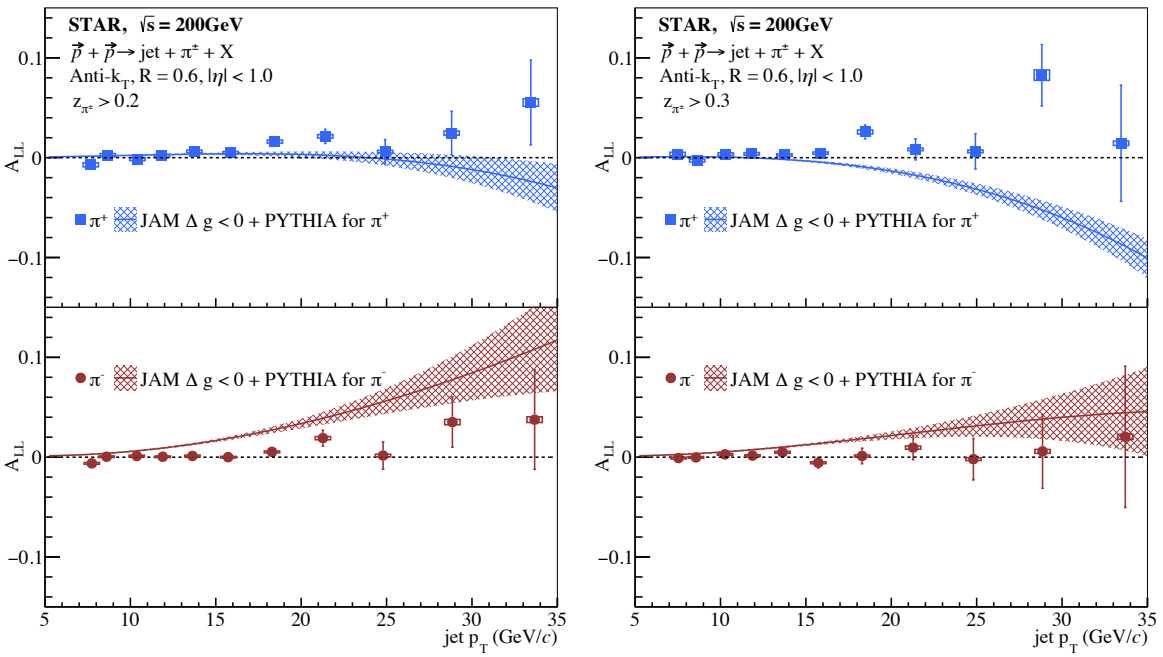

Figure 3.22: The comparison of the measured longitudinal double spin asymmetry A_{LL} of $\pi^{\pm}$-tagged jets with the predictions based on PYTHIA [128] using helicity distribution from JAM22 [57]. The left panel presents the results for jet momentum fraction $z > 0.2$ while the right panel shows the results for $z > 0.3$.

jet p_T (GeV)	$A_{LL}^{\pi^+}$	$A_{LL}^{\pi^+}$ stat.	$A_{LL}^{\pi^+}$ syst.	jet p_T (GeV)	$A_{LL}^{\pi^-}$	$A_{LL}^{\pi^-}$ stat.	$A_{LL}^{\pi^-}$ syst.
7.7	-0.0072	0.0048	0.0020	7.7	-0.0062	0.0049	0.0009
8.7	0.0025	0.0031	0.0017	8.6	0.0004	0.0032	0.0008
10.4	-0.0014	0.0024	0.0015	10.4	0.0012	0.0025	0.0008
11.8	0.0019	0.0021	0.0014	11.9	0.0004	0.0022	0.0008
13.7	0.0062	0.0024	0.0013	13.6	0.0012	0.0026	0.0009
15.9	0.0050	0.0032	0.0012	15.7	-0.0000	0.0034	0.0009
18.5	0.0161	0.0046	0.0016	18.3	0.0053	0.0051	0.0010
21.4	0.0214	0.0071	0.0018	21.3	0.0190	0.0079	0.0016
24.9	0.0060	0.0121	0.0013	24.8	0.0016	0.0137	0.0013
28.8	0.0246	0.0219	0.0021	28.9	0.0351	0.0252	0.0027
33.4	0.0553	0.0424	0.0038	33.7	0.0376	0.0498	0.0029

Table 3.13: The numerical values of the measured A_{LL} results of the $\pi^{\pm}$-tagged jets for $z > 0.2$.

jet p_T (GeV)	$A_{LL}^{\pi^+}$	$A_{LL}^{\pi^+}$ stat.	$A_{LL}^{\pi^+}$ syst.	jet p_T (GeV)	$A_{LL}^{\pi^-}$	$A_{LL}^{\pi^-}$ stat.	$A_{LL}^{\pi^-}$ syst.
7.5	0.0036	0.0037	0.0018	7.5	-0.0009	0.0039	0.0009
8.6	-0.0029	0.0040	0.0015	8.6	-0.0002	0.0042	0.0009
10.3	0.0035	0.0027	0.0014	10.3	0.0028	0.0029	0.0009
11.8	0.0038	0.0030	0.0012	11.9	0.0015	0.0032	0.0009
13.7	0.0027	0.0036	0.0012	13.6	0.0049	0.0040	0.0009
15.9	0.0046	0.0048	0.0012	15.7	-0.0056	0.0053	0.0010
18.5	0.0258	0.0069	0.0020	18.3	0.0012	0.0078	0.0010
21.4	0.0083	0.0106	0.0013	21.3	0.0096	0.0121	0.0016
24.9	0.0063	0.0177	0.0014	24.8	-0.0020	0.0207	0.0014
28.8	0.0827	0.0309	0.0053	28.9	0.0058	0.0370	0.0019
33.5	0.0145	0.0582	0.0022	33.7	0.0203	0.0708	0.0026

Table 3.14: The numerical values of the measured A_{LL} results of the $\pi^{\pm}$-tagged jets for $z > 0.3$.

3.6 Summary

This chapter provides details on the first measurements of longitudinal double spin asymmetry A_{LL} for the $\pi^{\pm}$-tagged jets in $\sqrt{s}$ = 200 GeV proton-proton collisions, including jet reconstruction, particle identification, A_{LL} extraction, estimation of systematic uncertainties, and the final measurement results. The measured $A_{LL}^{\pi^+}$ results increase with increasing jet p_T while $A_{LL}^{\pi^-}$ results is almost independent with the jet p_T. The measured results show that $A_{LL}^{\pi^+} > A_{LL}^{\pi^-}$, which are consistent with the predictions with PYTHIA [128] using the helicity distributions from NNPDFpol1.1 [39] (positive gluon helicity). However, the measurements strongly disfavor the predictions using the

helicity distributions from JAM22 [57] (negative gluon helicity). In conclusion, the first A_{LL} measurements for the $\pi^{\pm}$-tagged jets are sensitive to the sign of the gluon helicity distribution and strongly disfavor the negative gluon helicity.

Chapter 4 Longitudinal Double Spin Asymmetry, A_{LL}, of Λ, $\overline{\Lambda}$, K^0_S

The measurements of longitudinal double spin asymmetry, A_{LL}, of Λ, $\overline{\Lambda}$, K^0_S can shed light on the helicity distributions of strange quark and anti-quark, which are poorly constrained experimentally. In this chapter, the analysis details of the measurements will be presented.

4.1 Reconstruction of Λ, $\overline{\Lambda}$, K^0_S and V_0 Jet

4.1.1 Reconstruction of Λ, $\overline{\Lambda}$ and K^0_S

Similar to previous STAR publications [89-90, 136], Λ, $\overline{\Lambda}$ and K^0_S are reconstructed with their following decay channels at STAR:

$$\Lambda \to p + \pi^-, \quad \overline{\Lambda} \to \overline{p} + \pi^+, \quad K^0_S \to \pi^+ + \pi^- \tag{4.1}$$

Good quality TPC global tracks are selected by requiring the following criteria:

- Track $p_T > 0.15$ GeV
- Number of TPC hits > 14
- Number of TPC hits / number of possible TPC hits > 0.51

The daughter candidates are identified based on their energy loss dE/dx inside the TPC gas and the charge sign measured by the TPC. For example, charged track will be identified as a proton or anti-proton candidate if its $n\sigma(p)$ (converted from dE/dx, see Eq. (3.2)) is between -3 and 3. A set of topological selection criteria based on the decay topology (see Fig. 4.1), which vary with the p_T of the Λ hyperons and K^0_S, were applied to reduce the background. In addition, the selection criteria are divided into two groups in terms of whether their daughter pions can be matched to a TOF hit. Figure 4.2 illustrates the reconstructed Λ candidates under same selection criteria with pion matched to a TOF hit (panel (a)) and with pion not matched to a TOF hit (panel (b)). The reconstructed Λ candidates are much cleaner for the case that pion

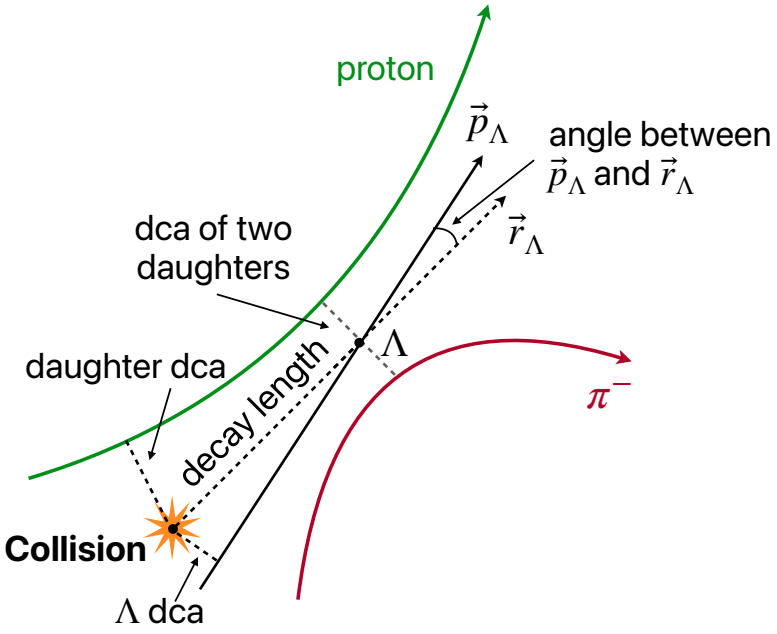

Figure 4.1: The decay topology of $\Lambda \to p + \pi^-$.

matched to a TOF hit as the much shorter response time of the TOF helps to remove pile-up tracks. Therefore, the selection criteria are much looser for this case. Table 4.1 and 4.2 summarize the selection criteria for $\Lambda(\overline{\Lambda})$ and K^0_S, respectively. The residual background fractions are kept at about 10% under the mass peak and are estimated with the side-band method [89-90, 136]. Figure 4.3, as an example, shows the invariant mass of the reconstructed Λ, $\overline{\Lambda}$ and K^0_S candidates with $1 < p_T < 8$ GeV.

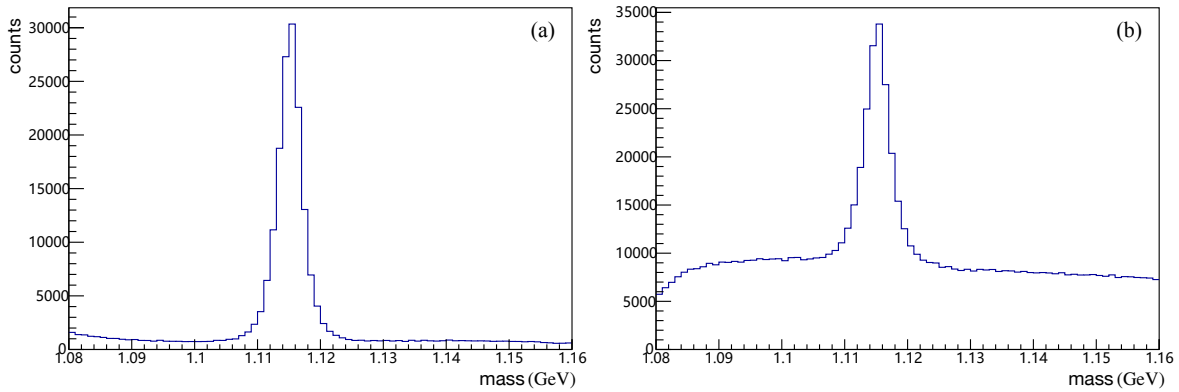

Figure 4.2: The invariant mass distribution of Λ candidates under the same selection criteria. Panel (a) and (b) are the distribution with and without pion matched to a TOF hit, respectively.

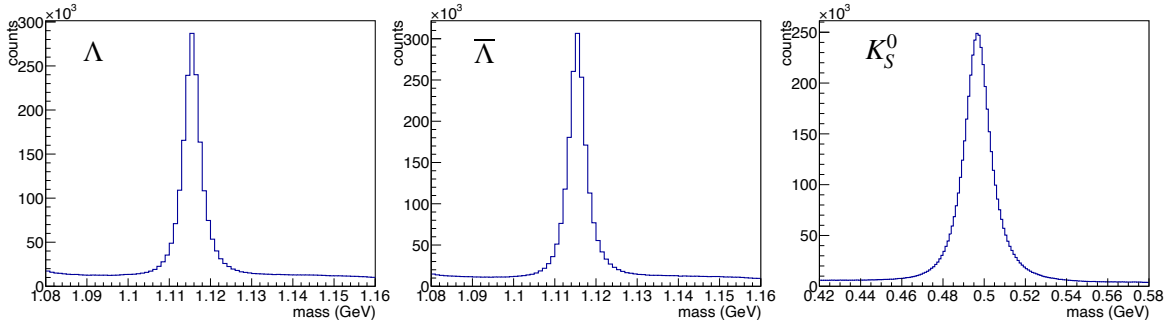

Figure 4.3: The invariant mass distribution of the reconstructed Λ, $\overline{\Lambda}$ and K_S^0 candidates with $1 < p_T < 8$ GeV.

$\pi^{\pm}$ matches a TOF hit						
$p_{T,\Lambda(\overline{\Lambda})}$ (GeV/c)	< 2	$2-3$	$3-4$	$4-5$	$5-6$	> 6
DCA of $p(\overline{p})$ to PV	> 0.2 cm	> 0.15 cm	> 0.05 cm	> 0.005 cm	> 0.005 cm	> 0.005 cm
DCA of $\pi^-(\pi^+)$ to PV	> 0.6 cm	> 0.55 cm	> 0.5 cm	> 0.5 cm	> 0.5 cm	> 0.5 cm
DCA of $p\pi^-$ $(\overline{p}\pi^+)$	< 0.75 cm	< 0.65 cm	< 0.6 cm	< 0.5 cm	< 0.45 cm	< 0.45 cm
DCA of $\Lambda(\overline{\Lambda})$ to PV	< 1 cm	< 1 cm	< 1 cm	< 1 cm	< 1 cm	< 1 cm
Decay Length	> 3 cm	> 3.5 cm	> 3.5 cm	> 4 cm	> 4.5 cm	> 4.5 cm
$\cos(\overrightarrow{r}, \overrightarrow{p})$	> 0.995	> 0.995	> 0.995	> 0.995	> 0.995	> 0.995
$\pi^{\pm}$ does not match a TOF hit						
$p_{T,\Lambda(\overline{\Lambda})}$ (GeV/c)	< 2	$2-3$	$3-4$	$4-5$	$5-6$	> 6
DCA of $p(\overline{p})$ to PV	> 0.45 cm	> 0.3 cm	> 0.25 cm	> 0.2 cm	> 0.15 cm	> 0.15 cm
DCA of $\pi^-(\pi^+)$ to PV	> 0.65 cm	> 0.6 cm	> 0.55 cm	> 0.55 cm	> 0.55 cm	> 0.5 cm
DCA of $p\pi^-$ $(\overline{p}\pi^+)$	< 0.7 cm	< 0.6 cm	< 0.55 cm	< 0.5 cm	< 0.45 cm	< 0.45 cm
DCA of $\Lambda(\overline{\Lambda})$ to PV	< 0.55 cm	< 0.55 cm	< 0.6 cm	< 0.6 cm	< 0.6 cm	< 0.6 cm
Decay Length	> 7 cm	> 7 cm	> 7 cm	> 8.5 cm	> 10 cm	> 10.5 cm
$\cos(\overrightarrow{r}, \overrightarrow{p})$	> 0.995	> 0.995	> 0.995	> 0.995	> 0.995	> 0.995

Table 4.1: The topological selection criteria for $\Lambda(\overline{\Lambda})$ reconstruction: the upper subtable is for candidates with daughter $\pi^-(\pi^+)$ matched to a TOF hit, and the lower subtable is for candidates without $\pi^-(\pi^+)$ matched to a TOF hit. Here, "DCA" denotes "distance of closest approach", "PV" denotes "primary vertex", $\overrightarrow{r}$ is the displacement from the primary vertex to the decay vertex of Λ or $\overline{\Lambda}$ and $\overrightarrow{p}$ denotes the momentum vector of Λ or $\overline{\Lambda}$.

4.1.2 V_0 Jet Reconstruction

In order to make sure that Λ hyperons and K_S^0 are originated from a hard scattering, the reconstructed Λ, $\overline{\Lambda}$ and K_S^0 are required to be a part of jets. Same jet reconstruction procedure as described in Sec. 3.1.1 is used and the reconstructed Λ, $\overline{\Lambda}$ and K_S^0 candidates are included into the input list for the jet reconstruction. Their daughters are removed from the input list to avoid double counting. Moreover, due to the annihilation of the anti-proton with the material of EMCs, extra energy will

π^- matches a TOF hit						
p_{T,K^0_S} (GeV/c)	< 2	$2-3$	$3-4$	$4-5$	$5-6$	> 6
DCA of $\pi^\pm$ to PV	> 0.45 cm	> 0.4 cm	> 0.35 cm	> 0.3 cm	> 0.25 cm	> 0.15 cm
DCA of $\pi^+\pi^-$	< 0.75 cm	< 0.65 cm	< 0.55 cm	< 0.5 cm	< 0.45 cm	< 0.35 cm
DCA of K^0_S to PV	< 0.9 cm	< 0.9 cm	< 0.9 cm	< 0.9 cm	< 0.9 cm	< 0.9 cm
Decay Length	> 3.5 cm	> 3.8 cm	> 4.2 cm	> 4.5 cm	> 4.5 cm	> 5.5 cm
$\cos(\overrightarrow{r}, \overrightarrow{p})$	> 0.995	> 0.995	> 0.995	> 0.995	> 0.995	> 0.995
π^- does not match a TOF hit						
p_{T,K^0_S} (GeV/c)	< 2	$2-3$	$3-4$	$4-5$	$5-6$	> 6
DCA of $\pi^\pm$ to PV	> 0.7 cm	> 0.5 cm	> 0.4 cm	> 0.35 cm	> 0.25 cm	> 0.25 cm
DCA of $\pi^+\pi^-$	< 0.5 cm	< 0.5 cm	< 0.5 cm	< 0.5 cm	< 0.4 cm	< 0.35 cm
DCA of K^0_S to PV	< 0.65 cm	< 0.65 cm	< 0.6 cm	< 0.6 cm	< 0.6 cm	< 0.6 cm
Decay Length	> 6.5 cm	> 6.5 cm	> 6.5 cm	> 7 cm	> 7.5 cm	> 10.5 cm
$\cos(\overrightarrow{r}, \overrightarrow{p})$	> 0.995	> 0.995	> 0.995	> 0.995	> 0.995	> 0.995

Table 4.2: The topological selection criteria for K^0_S reconstruction: the upper sub-table is for candidates with daughter π^- matched to a TOF hit, and the lower sub-table is for candidates without π^- matched to a TOF hit. Here, "DCA" denotes "distance of closest approach", "PV" denotes "primary vertex", $\overrightarrow{r}$ is the displacement from the primary vertex to the decay vertex of K^0_S and $\overrightarrow{p}$ denotes the momentum vector of K^0_S.

deposits inside the EMCs towers. Figure 4.4 illustrates the energy deposits of the anti-proton daughter in the matched tower (left panel) and in the 3×3 towers (right panel) that surround the matched tower. The energy deposits of proton is also shown as a comparison. Clearly, anti-proton daughter deposits more energy within 3×3 towers comparing to energy in single tower, while there is no significant difference for the energy deposits of proton between single tower and 3×3 towers. To correct such effect, if a anti-proton daughter matched to a EMC tower, the energy deposits in 3×3 EMC tower cluster that surround this tower will be removed.

The reconstructed jets p_T after correcting underlying events contributions is required to be larger than 5 GeV for the A_{LL} vs p_T measurements and same cut is used in the longitudinal spin transfer D_{LL} measurements that will be described in the next chapter. The jet p_T cut is smaller than the cut used in the A_{LL} measurements for $\pi^\pm$-tagged jets. The cut used here is only to make sure that Λ hyperons and K^0_S are originated from a hard scattering, and the 5 GeV cut is sufficient. Other selection cuts, listed in Tab. 3.2, are same as the cuts used in the A_{LL} measurements of $\pi^\pm$-tagged jets as described in Sec. 3.1.1. In-jet Λ hyperons and K^0_S are kept for further analysis. Table 4.3 summarizes the ranges of the side-band regions and mass peak regions for

each Λ hyperon and K_S^0 p_T bins. The mass peak width of the Λ hyperons and K_S^0 is nearly independent to the jet p_T. Therefore, an overall mass peak and side-band regions are taken, which are same as the regions for Λ hyperons and K_S^0 at $3 < p_T < 4$ GeV. Figure 4.5, as an example, presents the invariant mass distributions of the reconstructed in-jet Λ hyperons and K_S^0 candidates with $2 < p_T < 3$ GeV. The blue-filled and red-filled areas indicate the regions of the mass peak and side band. The yields of Λ hyperons and K_S^0 under mass peak at each p_T bins are summarized in Tab. 4.4. Similarly, their yields under mass peak at each jet p_T bins are summarized in Tab. 4.5.

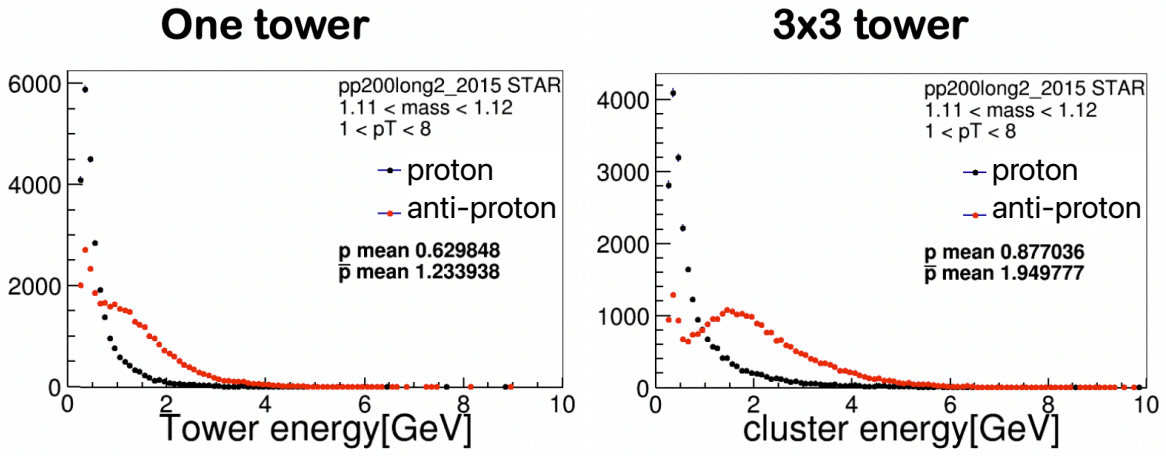

Figure 4.4: The energy deposits for the proton and anti-proton in the matched EMC tower (left panel) and in a 3×3 tower patches (right panel).

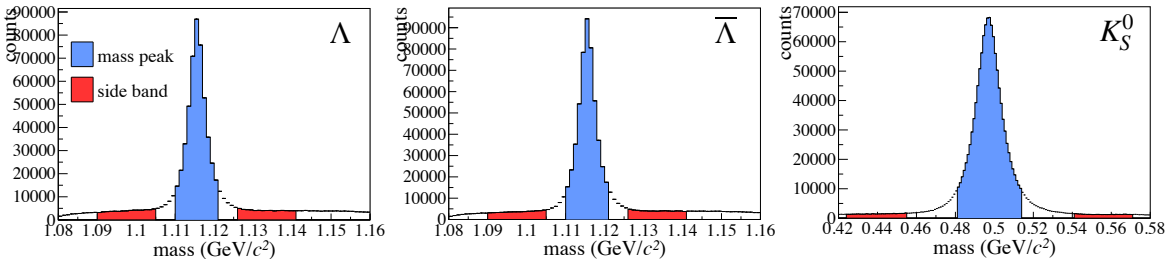

Figure 4.5: The invariant mass distributions of in-jet Λ hyperons and K_S^0 with $2 < p_T < 3$ GeV. The blue-filled and red-filled areas indicate the regions of the mass peak and side band.

	Λ and $\overline{\Lambda}$		
p_T (GeV)	left side-band (GeV)	mass peak (GeV)	right side-band (GeV)
$1-2$	(1.091, 1.106)	(1.111, 1.119)	(1.124, 1.139)
$2-3$	(1.090, 1.105)	(1.110, 1.121)	(1.126, 1.141)
$3-4$	(1.087, 1.102)	(1.109, 1.123)	(1.130, 1.145)
$4-5$	(1.085, 1.100)	(1.108, 1.124)	(1.132, 1.147)
$5-6$	(1.084, 1.099)	(1.107, 1.126)	(1.134, 1.149)
$6-8$	(1.080, 1.095)	(1.105, 1.129)	(1.139, 1.154)
	K_S^0		
$1-2$	(0.423, 0.458)	(0.483, 0.511)	(0.536, 0.571)
$2-3$	(0.424, 0.455)	(0.481, 0.514)	(0.541, 0.571)
$3-4$	(0.424, 0.454)	(0.478, 0.518)	(0.542, 0.572)
$4-5$	(0.423, 0.453)	(0.480, 0.517)	(0.544, 0.574)
$5-6$	(0.422, 0.452)	(0.477, 0.520)	(0.545, 0.575)
$6-8$	(0.422, 0.447)	(0.474, 0.524)	(0.551, 0.576)

Table 4.3: The side-band and mass peak at each p_T bins.

p_T (GeV)	Λ	$\overline{\Lambda}$	K_S^0
$1-2$	602058	619676	1.75×10^6
$2-3$	481821	516345	1.15×10^6
$3-4$	265544	300850	628126
$4-5$	117658	134916	300045
$5-6$	51099	56853	156938
$6-8$	34011	34045	126004

Table 4.4: The yields of in-jet Λ hyperons and K_S^0 under mass peak at each p_T bin.

jet p_T (GeV)	Λ	$\overline{\Lambda}$	K_S^0
$6-7.1$	108028	130171	244954
$7.1-8.4$	90271	89065	221759
$8.4-9.9$	270639	263063	708911
$9.9-11.7$	228075	189563	638895
$11.7-13.8$	155529	115435	471566
$13.8-16.3$	92083	61283	293334
$16.3-19.2$	43922	27356	147971
$19.2-22.7$	18855	11322	65390
$22.7-26.8$	6662	3680	23671

Table 4.5: The yields of in-jet Λ hyperons and K_S^0 under mass peak at each jet p_T bin.

4.2 A_{LL} Extraction for Λ, $\overline{\Lambda}$ and K^0_S

The longitudinal double spin asymmetry A_{LL} can be extracted with the Eq. (3.5). In the analysis, the A^{raw}_{LL} for the Λ hyperons and the K^0_S candidates under the mass peak and A^{bkg}_{LL} for the residual backgrounds are extracted separately. The impact of the residual backgrounds to the final A_{LL} results and the corresponding statistical uncertainties δA_{LL} are corrected with the following formula:

$$A_{LL} = \frac{A^{raw}_{LL} - r A^{bkg}_{LL}}{1 - r}, \tag{4.2}$$

$$\delta A_{LL} = \frac{\sqrt{(\delta A^{raw}_{LL})^2 + (r\delta A^{bkg}_{LL})^2}}{1 - r} \tag{4.3}$$

where r is the residual background fraction under the mass peak, and is estimated with the side-band method. δA^{raw}_{LL} and δA^{bkg}_{LL} are the statistical uncertainties from mass peak and residual background. Figure 4.6, as an example, shows the A^{raw}_{LL} as a function of Λ hyperons and K^0_S p_T (first row) and jet p_T (second row) for Λ, $\overline{\Lambda}$, and K^0_S. Constant fittings (red lines on Fig. 4.6) are applied to the extracted A^{raw}_{LL} and the numerical values of the fitting results are listed on the figure. The extracted numerical values of the A_{LL} and the corresponding statistical uncertainties for each p_T and jet p_T bins after the background correction are summarized in Tab. 4.6 and 4.7, respectively.

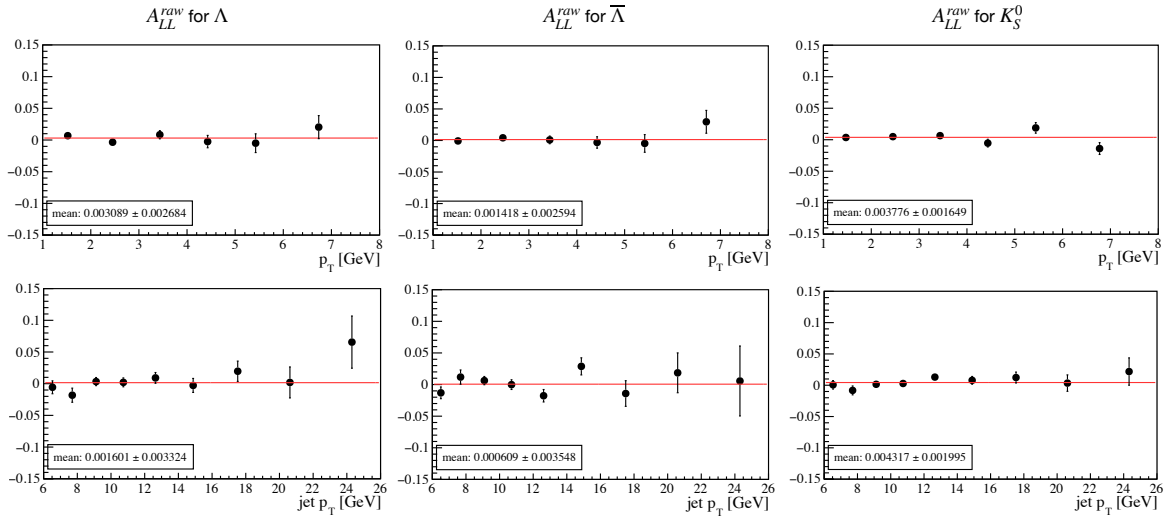

Figure 4.6: The extracted A^{raw}_{LL} under mass peak. The upper row shows the A^{raw}_{LL} as a function of particle p_T and the lower row shows the results as a function of jet p_T. The left, the middle and the right columns show the results for Λ, $\overline{\Lambda}$ and K^0_S, respectively.

p_T (GeV)	Λ	$\overline{\Lambda}$	K^0_S
$1-2$	0.0068 ± 0.0048	-0.0007 ± 0.0046	0.0038 ± 0.0026
$2-3$	-0.0055 ± 0.0054	0.0036 ± 0.0051	0.0045 ± 0.0033
$3-4$	0.0075 ± 0.0071	0.0010 ± 0.0066	0.0072 ± 0.0045
$4-5$	-0.0044 ± 0.0107	-0.0034 ± 0.0099	-0.0061 ± 0.0065
$5-6$	-0.0029 ± 0.0164	-0.0019 ± 0.0156	0.0206 ± 0.0092
$6-8$	0.0176 ± 0.0208	0.0321 ± 0.0208	-0.0163 ± 0.0108

Table 4.6: The numerical values of the extracted A_{LL} at each Λ hyperons and K^0_S p_T bin after correcting residual background.

jet p_T (GeV)	Λ	$\overline{\Lambda}$	K^0_S
$6-7.1$	-0.0098 ± 0.0115	-0.0146 ± 0.0103	0.0009 ± 0.0072
$7.1-8.4$	-0.0207 ± 0.0127	0.0170 ± 0.0127	-0.0078 ± 0.0076
$8.4-9.9$	0.0030 ± 0.0074	0.0059 ± 0.0075	0.0008 ± 0.0042
$9.9-11.7$	0.0035 ± 0.0081	-0.0022 ± 0.0090	0.0028 ± 0.0045
$11.7-13.8$	0.0051 ± 0.0099	-0.0182 ± 0.0117	0.0141 ± 0.0052
$13.8-16.3$	-0.0065 ± 0.0130	0.0396 ± 0.0164	0.0058 ± 0.0067
$16.3-19.2$	0.0203 ± 0.0191	-0.0172 ± 0.0249	0.0126 ± 0.0096
$19.2-22.7$	-0.0003 ± 0.0293	0.0315 ± 0.0393	0.0019 ± 0.0146
$22.7-26.8$	0.0554 ± 0.0500	0.0011 ± 0.0700	0.0249 ± 0.0248

Table 4.7: The numerical values of the extracted A_{LL} at each jet p_T bin after correcting residual background.

Similar to the A_{LL} measurements of the $\pi^{\pm}$-tagged jets, four false asymmetries are extracted with Eq. (3.8) in Sec. 3.2.2. As examples, the extracted asymmetries as a function of jet p_T for the Λ, $\overline{\Lambda}$, and K^0_S are presented in Fig. 4.7. These asymmetries are consistent with zero within uncertainties.

4.3 Systematic Effects

4.3.1 Jet p_T Correction

Similar to the A_{LL} measurements of the $\pi^{\pm}$-tagged jets, the jet p_T is corrected back to particle level. The Λ hyperons, K^0_S, and jets at detector level and the particle level are matched with the same cuts illustrated in Eq. (3.12) and (3.13). Figure 4.8 (left) shows the correlations between detector level jet p_T and particle level jet p_T for Λ jets while the differences of jet p_T between particle level and detector level are shown in the middle panel of Fig. 4.8. In Fig. 4.8, the vertical values of the blacks points illustrate the average values. The right column of Fig. 4.8 is the zoomed-in results of the black

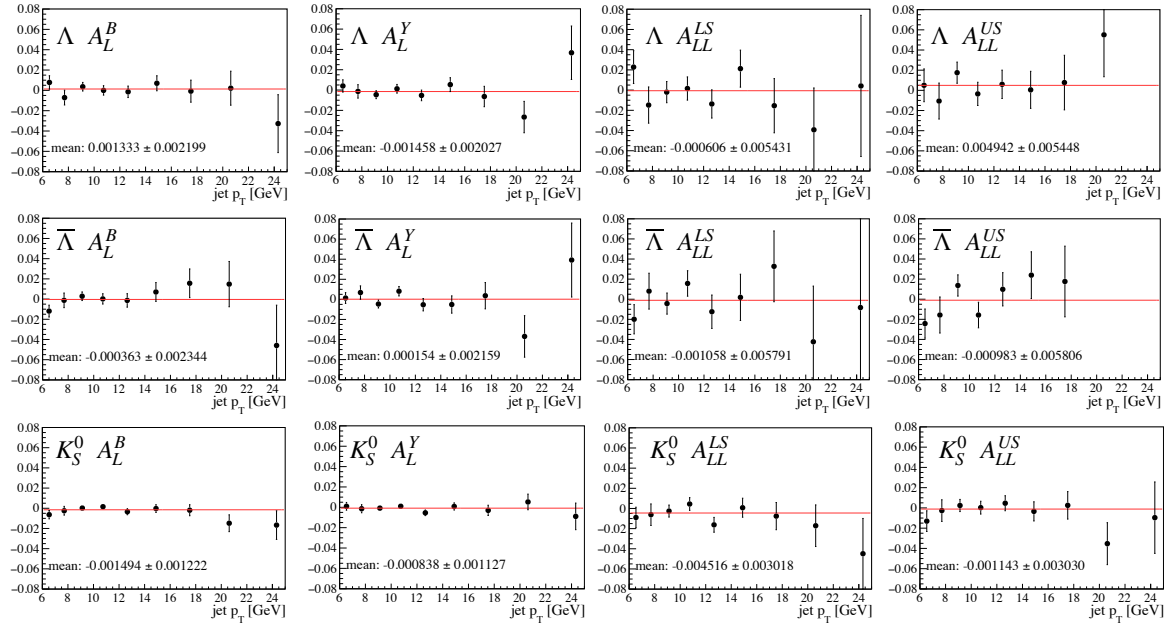

Figure 4.7: False asymmetries for Λ, $\overline{\Lambda}$, and K_S^0 as a function of jet p_T.

points from the middle panel of Fig. 4.8. The corrections are estimated for the JP1 (upper row in Fig. 4.8) and JP2 (lower row in Fig. 4.8) triggers separately and the average corrections weighted with the corresponding yields of the Λ, $\overline{\Lambda}$, and K_S^0 in data are treated as the final corrections to the jet p_T in data. Similar results for the $\overline{\Lambda}$ jets and K_S^0 jets are shown in Fig. 4.9 and 4.10, respectively. The numerical values of the final corrections are summarized in Tab. 4.8.

jet p_T (GeV)	Λ-jets (GeV)	$\overline{\Lambda}$-jets (GeV)	K_S^0-jets (GeV)
6 – 7.1	0.19	0.65	1.00
7.1 – 8.4	-0.12	0.33	0.82
8.4 – 9.9	0.74	1.13	1.23
9.9 – 11.7	0.37	1.28	1.14
11.7 – 13.8	0.46	0.78	0.92
13.8 – 16.3	0.39	1.10	0.73
16.3 – 19.2	0.21	1.43	0.50
19.2 – 22.7	0.17	1.05	0.14
22.7 – 26.8	0.57	0.12	0.06

Table 4.8: The numerical values of the final detector jet p_T correction at each detector jet p_T bin.

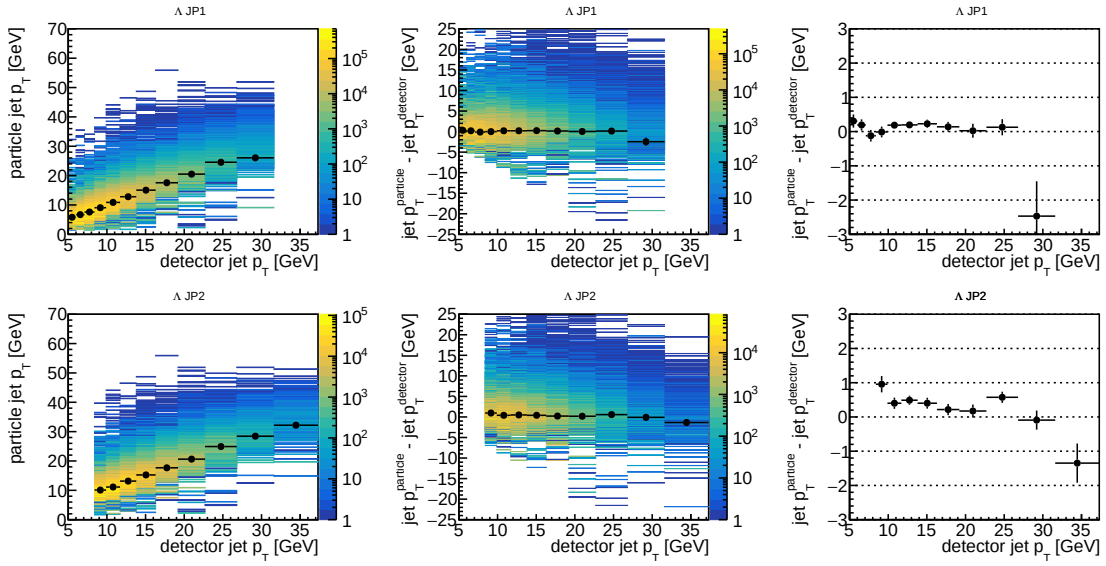

Figure 4.8: Left column: the correlation of the jet p_T between detector level and particle level for Λ jets. Middle column: the difference p_T results between particle level and detector level. The zoomed-in results of the black points in the middle column are shown in the right column. The upper row is for the JP1 trigger and the lower row is for the JP2 trigger. The vertical values of the data points illustrate the average values at each detector level jet p_T bin.

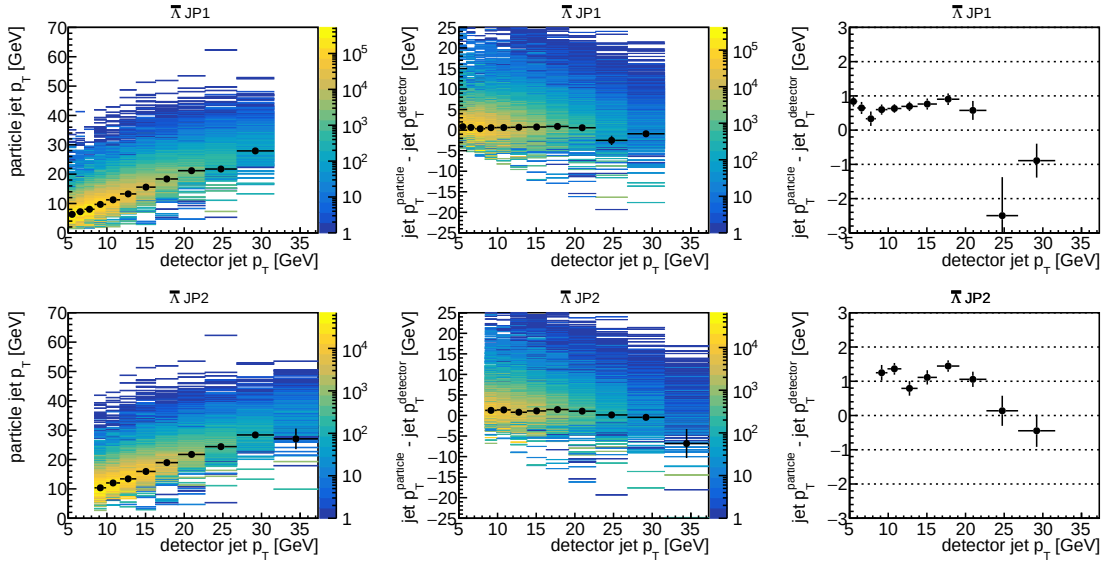

Figure 4.9: Left column: the correlation of the jet p_T between detector level and particle level for $\overline{\Lambda}$ jets. Middle column: the difference p_T results between particle level and detector level. The zoomed-in results of the black points in the middle column are shown in the right column. The upper row is for the JP1 trigger and the lower row is for the JP2 trigger. The vertical values of the data points illustrate the average values at each detector level jet p_T bin.

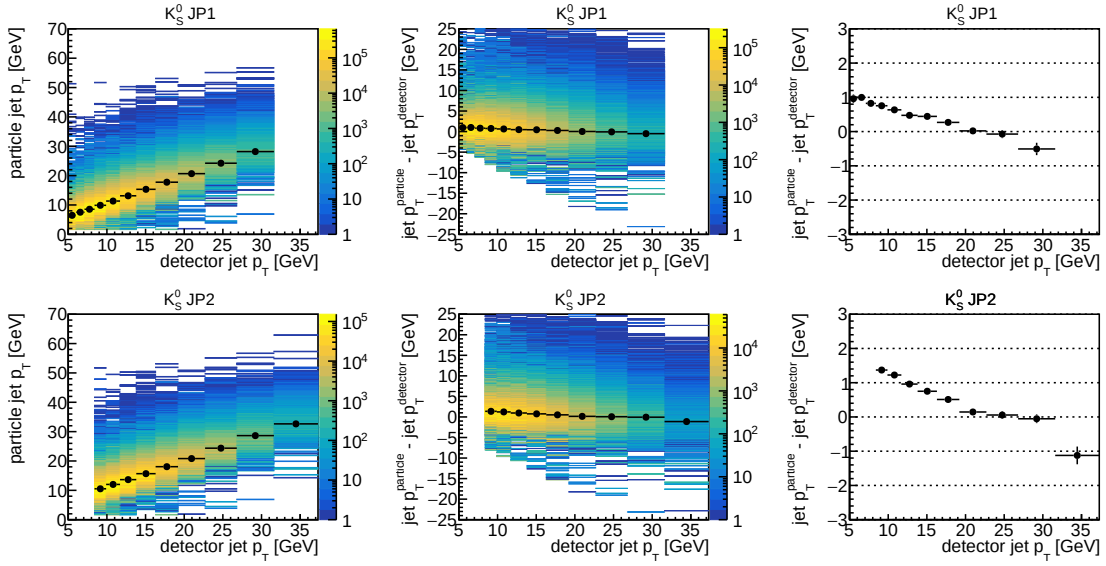

Figure 4.10: Left column: the correlation of the jet p_T between detector level and particle level for K^0_S jets. Middle column: the difference p_T results between particle level and detector level. The zoomed-in results of the black points in the middle column are shown in the right column. The upper row is for the JP1 trigger and the lower row is for the JP2 trigger. The vertical values of the data points illustrate the average values at each detector level jet p_T bin.

4.3.2 Trigger Bias

Similar to the A_{LL} measurements of $\pi^{\pm}$-tagged jets described in Sec. 3.4.2, trigger conditions might introduce potential bias on the measured A_{LL} results. Same embedding MC sample and estimation method used in $\pi^{\pm}$-tagged jets A_{LL} measurements is applied in this analysis. Details about the estimation method can be found in Sec. 3.4.2. In this analysis, the trigger bias is estimated for JP1 and JP2 triggers separately. The final trigger bias is taken as the average values from two triggers weighted with the corresponding particle yields in data. Figure 4.11, as an example, shows the calculated A_{LL} of K^0_S as a function of K^0_S p_T for unbiased asymmetries (left column) and biased asymmetries (middle column). As their name applied, the unbiased asymmetries are calculated with the MC samples without applying trigger conditions while the biased asymmetries are calculated with the MC samples after applying trigger conditions. Their differences are shown on the right column of Fig. 4.11. In general, the JP2 introduces larger bias than JP1 and the estimated trigger bias does not dependent on the K^0_S p_T strongly. Similarly, the results of K^0_S A_{LL} as a function of jet p_T are shown in Fig. 4.12. The numerical values of estimated trigger biases and the related system-

atic uncertainties for each Λ hyperons and K^0_S p_T are summarized in Tab. 4.9. Similar results at each jet p_T bins are summarized in Tab. 4.10.

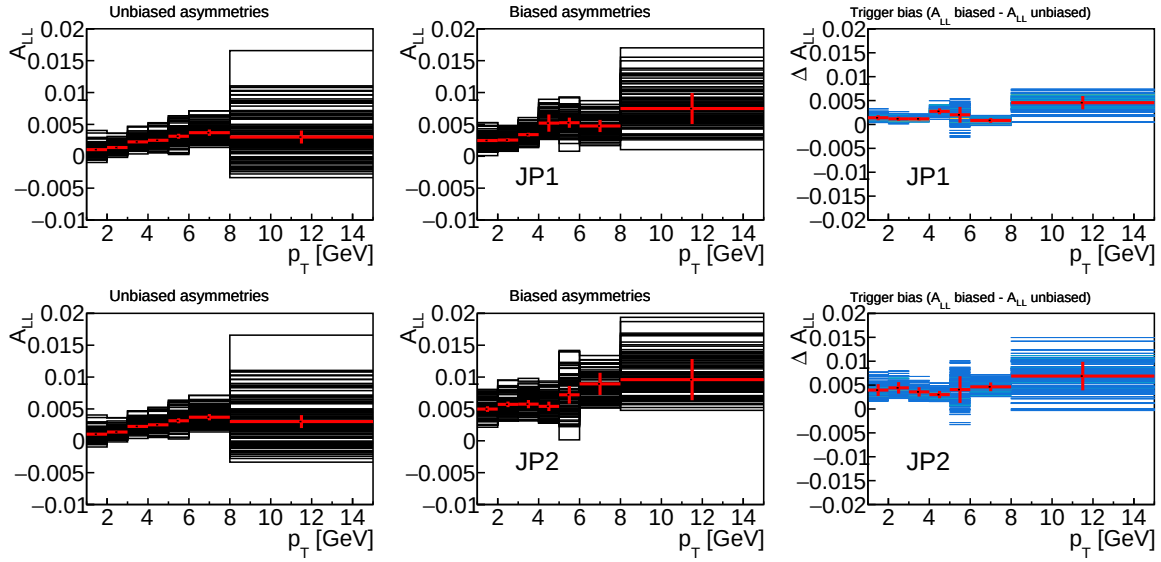

Figure 4.11: Left column: double spin asymmetry A_{LL} of K^0_S for the unbiased MC sample as a function of K^0_S p_T for all 100 NNPDFpol1.1 replicas. The best-fit result is shown in red. Middle column: A_{LL} for the biased sample as a function of K^0_S p_T for all 100 NNPDFpol1.1 replicas. Right column: the trigger bias ΔA_{LL} for all 100 replicas. The bars of the red points show the standard deviation of the ΔA_{LL}.

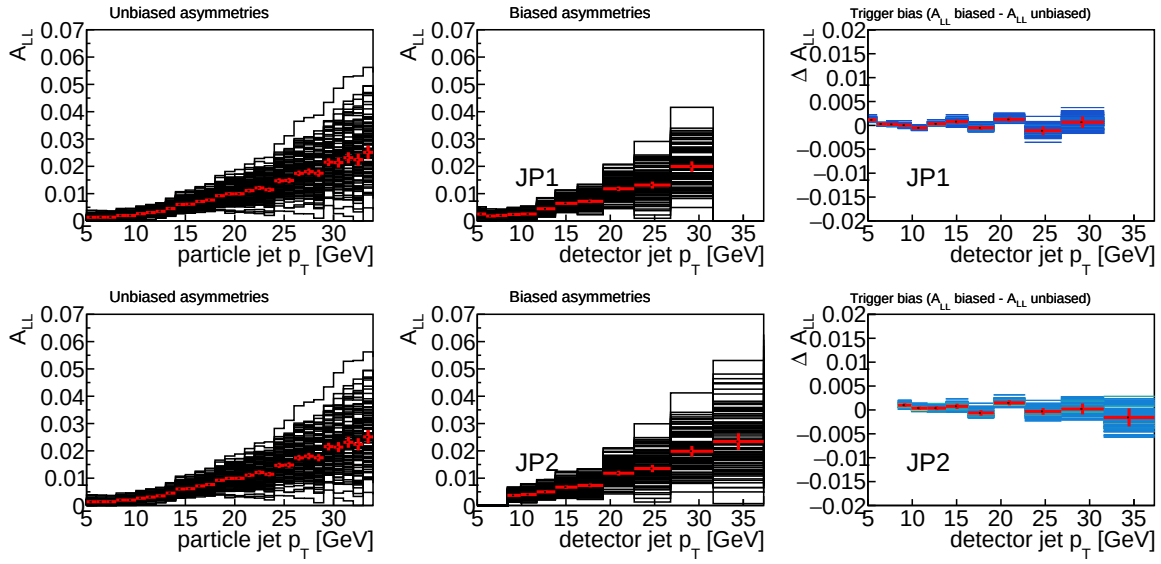

Figure 4.12: Left column: double spin asymmetry A_{LL} of K^0_S for the unbiased MC sample as a function of jet p_T for all 100 NNPDFpol1.1 replicas. The best-fit result is shown in red. Middle column: A_{LL} for the biased sample as a function of jet p_T for all 100 NNPDFpol1.1 replicas. Right column: the trigger bias ΔA_{LL} for all 100 replicas. The bars of the red points show the standard deviation of the ΔA_{LL}.

	Λ			$\overline{\Lambda}$			K_S^0		
p_T (GeV)	ΔA_{LL}	δA_{LL}^{pdf}	$\delta A_{LL}^{best-fit}$	ΔA_{LL}	δA_{LL}^{pdf}	$\delta A_{LL}^{best-fit}$	ΔA_{LL}	δA_{LL}^{pdf}	$\delta A_{LL}^{best-fit}$
$1-2$	0.0026	0.0009	0.0004	0.0032	0.0010	0.0004	0.0034	0.0011	0.0002
$2-3$	0.0032	0.0009	0.0003	0.0035	0.0010	0.0004	0.0030	0.0009	0.0003
$3-4$	0.0024	0.0008	0.0005	0.0030	0.0008	0.0006	0.0025	0.0008	0.0004
$4-5$	0.0021	0.0009	0.0008	0.0030	0.0007	0.0009	0.0022	0.0007	0.0006
$5-6$	0.0042	0.0016	0.0014	0.0037	0.0026	0.0013	0.0021	0.0009	0.0009
$6-8$	0.0024	0.0009	0.0015	0.0042	0.0009	0.0016	0.0005	0.0012	0.0009

Table 4.9: The calculated trigger bias ΔA_{LL} and the corresponding systematic uncertainties for Λ, $\overline{\Lambda}$ and K_S^0 at each p_T bin.

	Λ			$\overline{\Lambda}$			K_S^0		
jet p_T (GeV)	ΔA_{LL}	δA_{LL}^{pdf}	$\delta A_{LL}^{best-fit}$	ΔA_{LL}	δA_{LL}^{pdf}	$\delta A_{LL}^{best-fit}$	ΔA_{LL}	δA_{LL}^{pdf}	$\delta A_{LL}^{best-fit}$
$6-7.1$	0.0002	0.0002	0.0003	0.0007	0.0002	0.0002	0.0003	0.0002	0.0002
$7.1-8.4$	0.0008	0.0002	0.0002	0.0004	0.0002	0.0004	0.0002	0.0002	0.0002
$8.4-9.9$	0.0009	0.0004	0.0005	0.0016	0.0006	0.0005	0.0008	0.0004	0.0004
$9.9-11.7$	0.0011	0.0005	0.0006	0.0016	0.0005	0.0007	0.0002	0.0003	0.0004
$11.7-13.8$	0.0011	0.0004	0.0006	0.0009	0.0005	0.0008	0.0004	0.0004	0.0005
$13.8-16.3$	-0.0001	0.0007	0.0010	0.0021	0.0007	0.0011	0.0008	0.0005	0.0006
$16.3-19.2$	0.0029	0.0010	0.0015	0.0017	0.0007	0.0015	-0.0006	0.0006	0.0007
$19.2-22.7$	-0.0001	0.0007	0.0019	0.0057	0.0016	0.0019	0.0015	0.0005	0.0009
$22.7-26.8$	0.0003	0.0009	0.0023	0.0052	0.0017	0.0028	-0.0003	0.0007	0.0013

Table 4.10: The calculated trigger bias ΔA_{LL} and the corresponding systematic uncertainties for Λ, $\overline{\Lambda}$ and K_S^0 at each jet p_T bins.

4.3.3 Systematic Uncertainties

In this analysis, four sources of systematic uncertainties are considered:

- Uncertainty from the beam polarization
- Uncertainty from relative luminosity R_3
- Uncertainty in the determination of the residual background fraction for Λ, $\overline{\Lambda}$ and K_S^0
- Uncertainties related to the trigger bias estimation

Beam Polarization & Relative Luminosity The same uncertainties from the beam polarization (see Sec. 2.3.2) and the relative luminosity R_3 (see Sec. 2.3.3) are shared with the $\pi^{\pm}$-tagged jets A_{LL} measurements. The beam polarizations contribute to an 6.06% scale uncertainty and the uncertainty of R_3 is 0.00076. These two uncertainties will contribute to all the data points.

Residual Background To estimate the uncertainties in the determination of the residual background fraction, the invariant mass distributions of the reconstructed Λ hyperons and K^0_S are fitted with a Gaussian+linear function. The residual background fractions under the mass peak are calculated with the linear function and the A_{LL} is recalculated with the new residual background fractions. Differences of the A_{LL} results calculated with side-band method and the fitting method are taken as the systematic uncertainties A_{LL} in the determination of the residual background fractions. The invariant mass of the Λ candidates together with fitting function at each jet p_T bin, as an example, is shown in Fig. 4.13. The estimated residual background fractions with side-band method and fitting method are summarized in Tab. 4.11 for each Λ hyperons and K^0_S p_T bins and Tab. 4.12 for each jet p_T bins.

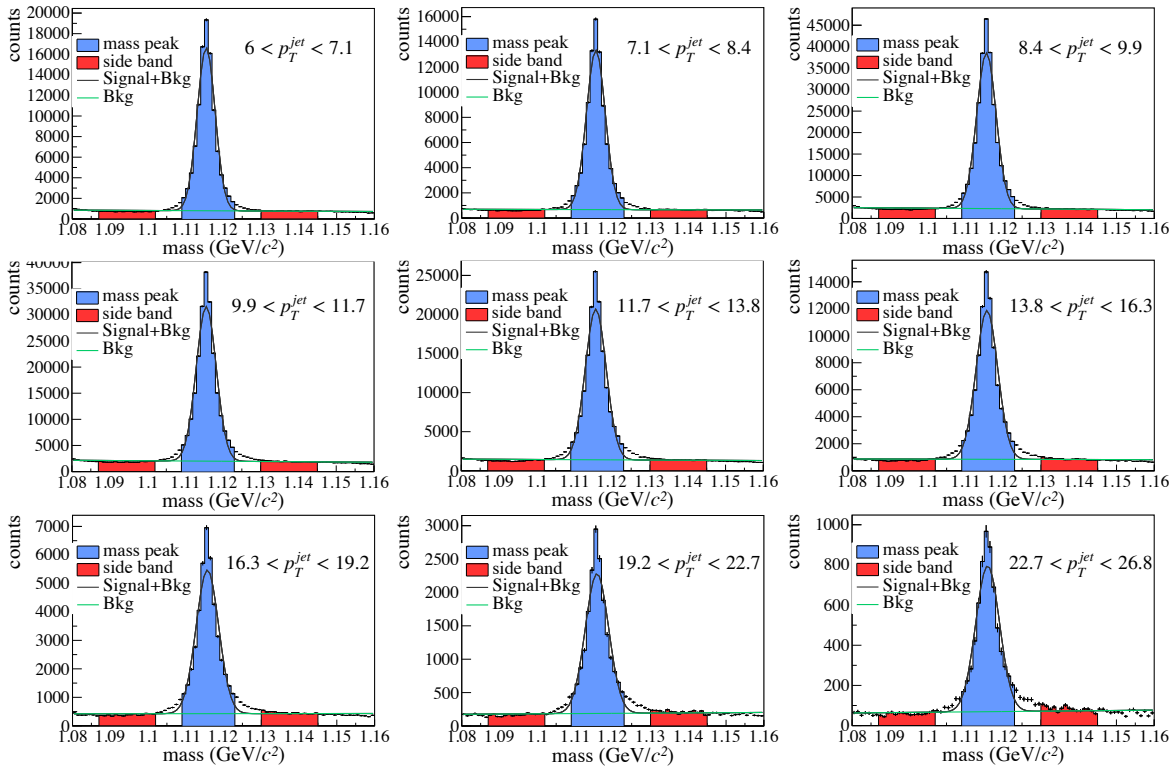

Figure 4.13: The invariant mass of the Λ candidates at each jet p_T bin. The blue-filled and the red-filled areas indicate the mass-peak and the side-band regions, respectively. The linear functions are shown in green line.

	side-band method			fitting method		
p_T (GeV)	Λ	$\overline{\Lambda}$	K^0_S	Λ	$\overline{\Lambda}$	K^0_S
$1-2$	8.9%	7.6%	4.1%	9.2%	7.9%	4.4%
$2-3$	9.3%	8.2%	4.0%	9.6%	8.5%	4.5%
$3-4$	7.6%	6.8%	4.5%	6.8%	6.0%	5.0%
$4-5$	7.0%	6.4%	4.8%	6.2%	5.5%	5.2%
$5-6$	7.8%	7.7%	6.5%	6.6%	6.3%	6.7%
$6-8$	9.4%	9.5%	8.8%	9.1%	9.1%	9.0%

Table 4.11: The residual background fractions under mass peak estimated with both the side-band method and the fitting method at each Λ, $\overline{\Lambda}$, and K^0_S p_T bin.

	side-band method			fitting method		
jet p_T (GeV)	Λ	$\overline{\Lambda}$	K^0_S	Λ	$\overline{\Lambda}$	K^0_S
$6-7.1$	9.6%	8.0%	5.0%	10.3%	8.4%	5.6%
$7.1-8.4$	9.9%	9.4%	4.6%	10.4%	9.8%	5.4%
$8.4-9.9$	11.2%	10.6%	5.0%	11.9%	11.2%	5.8%
$9.9-11.7$	11.6%	12.1%	5.1%	12.2%	12.6%	5.8%
$11.7-13.8$	12.0%	13.4%	5.4%	12.6%	13.8%	6.1%
$13.8-16.3$	12.4%	14.5%	5.9%	12.9%	14.9%	6.6%
$16.3-19.2$	13.4%	15.6%	7.0%	13.6%	16.1%	7.7%
$19.2-22.7$	14.1%	16.7%	8.1%	13.9%	16.7%	8.8%
$22.7-26.8$	14.9%	17.8%	9.7%	14.5%	17.7%	10.2%

Table 4.12: The residual background fractions under mass peak estimated with both the side-band method and the fitting method at each jet p_T bin.

4.4 Results and Discussions

In this section, the measured results of the longitudinal double spin asymmetry A_{LL} for Λ, $\overline{\Lambda}$ and K^0_S in proton-proton collisions at $\sqrt{s} = 200$ GeV are presented, which provide access to the helicity distributions of strange quark and anti-quark.

4.4.1 A_{LL} vs Λ, $\overline{\Lambda}$ and K^0_S p_T

The first measurements of the longitudinal double spin asymmetry A_{LL} for the in-jet Λ, $\overline{\Lambda}$ and K^0_S in the proton-proton collision at $\sqrt{s} = 200$ GeV as a function of Λ, $\overline{\Lambda}$ and K^0_S p_T are presented in Fig. 4.14. The average results over all Λ, $\overline{\Lambda}$ and K^0_S p_T are $-0.0006 \pm 0.0030 \pm 0.0014$, $-0.0020 \pm 0.0029 \pm 0.0014$ and $0.0009 \pm 0.0017 \pm 0.0014$ for Λ, $\overline{\Lambda}$ and K^0_S, respectively. There is no clear p_T dependence and the measured results

are consistent with zero within uncertainty. Predictions from MC samples based on PYTHIA [128] using helicity distributions from the NNPDFpol1.1 [39] are compared and the measurements are consistent with the predictions. The small A_{LL} results might indicate small helicity distributions of the strange quark and anti-quark inside the proton. The numerical values of the measured A_{LL} at each p_T bin are summarized in Tab. 4.13

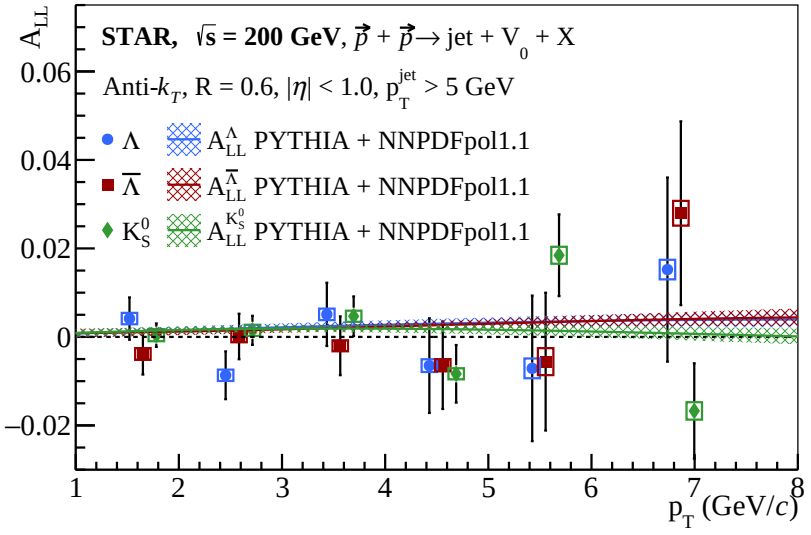

Figure 4.14: The longitudinal double spin asymmetry A_{LL} as a function of Λ, $\overline{\Lambda}$ and K^0_S p_T in proton-proton collisions at $\sqrt{s} = 200$ GeV. Predictions from MC samples based on PYTHIA [128] using helicity distributions from the NNPDFpol1.1 [39] are compared. The results for $\overline{\Lambda}$ and K^0_S are shifted horizontally for clarity.

p_T (GeV)	A_{LL}^{Λ}	$A_{LL}^{\overline{\Lambda}}$	$A_{LL}^{K^0_S}$
$1-2$	$0.0041 \pm 0.0048 \pm 0.0013$	$-0.0039 \pm 0.0046 \pm 0.0013$	$0.0004 \pm 0.0026 \pm 0.0014$
$2-3$	$-0.0087 \pm 0.0054 \pm 0.0013$	$0.0001 \pm 0.0051 \pm 0.0013$	$0.0015 \pm 0.0033 \pm 0.0013$
$3-4$	$0.0051 \pm 0.0071 \pm 0.0013$	$-0.0020 \pm 0.0066 \pm 0.0012$	$0.0047 \pm 0.0045 \pm 0.0013$
$4-5$	$-0.0065 \pm 0.0107 \pm 0.0014$	$-0.0064 \pm 0.0099 \pm 0.0014$	$-0.0083 \pm 0.0065 \pm 0.0013$
$5-6$	$-0.0071 \pm 0.0164 \pm 0.0022$	$-0.0056 \pm 0.0156 \pm 0.0030$	$0.0185 \pm 0.0092 \pm 0.0019$
$6-8$	$0.0152 \pm 0.0208 \pm 0.0022$	$0.0279 \pm 0.0208 \pm 0.0028$	$-0.0167 \pm 0.0108 \pm 0.0020$

Table 4.13: The numerical values of the longitudinal double spin asymmetry A_{LL} and the corresponding statistical and systematic uncertainties for Λ, $\overline{\Lambda}$ and K^0_S at each p_T bin.

4.4.2 A_{LL} vs jet p_T

We also performed the measurement of the A_{LL} as a function of jet p_T. In this measurement, jets are selected with the same cuts as the A_{LL} measurements of the

$\pi^{\pm}$-tagged jets in Sec. 3.1.1. Therefore, the jets used in this measurement is mostly a sub-set of the inclusive jets. By requiring Λ hyperons or K^0_S to be a part of jets, this measurement provides sensitivity to the strange quark and anti-quark helicity distributions. Figure 4.15 shows the measured A_{LL} results as a function of jet p_T. The average results over all jet p_T bins are $0.0011\pm0.0036\pm0.0013$, $-0.0017\pm0.0037\pm0.0013$ and $0.0028 \pm 0.0021 \pm 0.0011$ for jets containing Λ, $\overline{\Lambda}$ and K^0_S, respectively. No clear jet p_T dependence is observed and the measured A_{LL} results are consistent with zero within uncertainties. Predictions from MC samples based on PYTHIA [128] using helicity distributions from the NNPDFpol1.1 [39] are compared with the measurements and are consistent with the measurements. The bottom panel of Fig. 4.15 represents the average jet momentum fraction z carried by the Λ hyperons and K^0_S. Due to the limitation of the statistics, no minimum z cut is applied. Table 4.14 summarizes the numerical values of the measured results. These first measurements at RHIC are expected to provide constraints on the helicity distributions of strange quark and anti-quark.

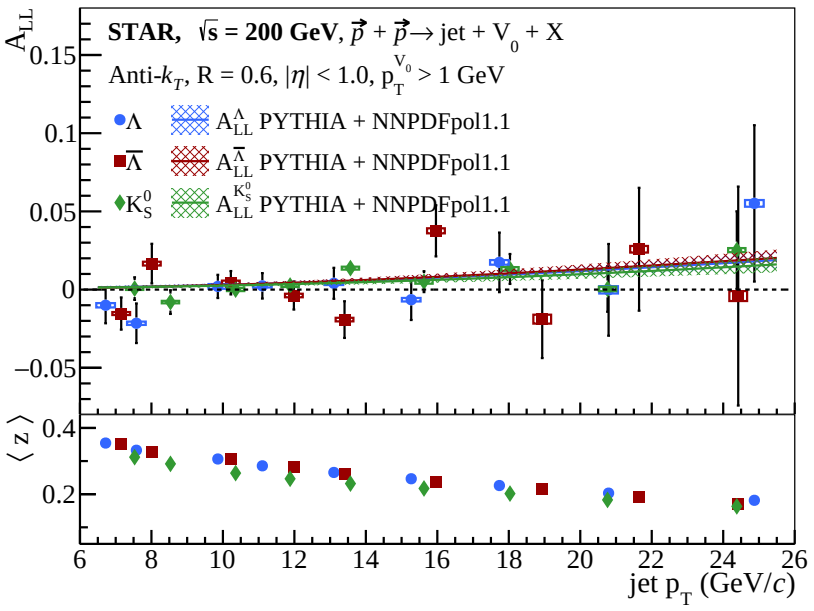

Figure 4.15: The longitudinal double spin asymmetry A_{LL} as a function of jet p_T for jets containing one Λ, $\overline{\Lambda}$ or K^0_S in proton-proton collisions at $\sqrt{s} = 200$ GeV. The jet p_T is corrected back to particle level. Predictions from MC samples based on PYTHIA [128] using helicity distributions from the NNPDFpol1.1 [39] are compared. The bottom panel presents the jet momentum fraction corrected to particle.

jet p_T (GeV)	A_{LL}^{Λ}	$A_{LL}^{\overline{\Lambda}}$	$A_{LL}^{K_S^0}$
$6-7.1$	$-0.0100 \pm 0.0115 \pm 0.0011$	$-0.0153 \pm 0.0103 \pm 0.0012$	$0.0006 \pm 0.0072 \pm 0.0008$
$7.1-8.4$	$-0.0215 \pm 0.0127 \pm 0.0015$	$0.0166 \pm 0.0127 \pm 0.0014$	$-0.0080 \pm 0.0076 \pm 0.0009$
$8.4-9.9$	$0.0020 \pm 0.0074 \pm 0.0010$	$0.0044 \pm 0.0075 \pm 0.0011$	$-0.0000 \pm 0.0042 \pm 0.0009$
$9.9-11.7$	$0.0024 \pm 0.0081 \pm 0.0011$	$-0.0038 \pm 0.0090 \pm 0.0011$	$0.0026 \pm 0.0045 \pm 0.0009$
$11.7-13.8$	$0.0040 \pm 0.0099 \pm 0.0011$	$-0.0192 \pm 0.0117 \pm 0.0016$	$0.0137 \pm 0.0052 \pm 0.0013$
$13.8-16.3$	$-0.0065 \pm 0.0130 \pm 0.0015$	$0.0376 \pm 0.0164 \pm 0.0029$	$0.0051 \pm 0.0067 \pm 0.0012$
$16.3-19.2$	$0.0174 \pm 0.0191 \pm 0.0023$	$-0.0189 \pm 0.0249 \pm 0.0021$	$0.0132 \pm 0.0096 \pm 0.0014$
$19.2-22.7$	$-0.0002 \pm 0.0293 \pm 0.0021$	$0.0258 \pm 0.0393 \pm 0.0032$	$0.0004 \pm 0.0146 \pm 0.0013$
$22.7-26.8$	$0.0551 \pm 0.0500 \pm 0.0043$	$-0.0041 \pm 0.0700 \pm 0.0033$	$0.0252 \pm 0.0248 \pm 0.0023$

Table 4.14: The numerical values of the longitudinal double spin asymmetry A_{LL} and the corresponding statistical and systematic uncertainties for jets containing Λ, $\overline{\Lambda}$ or K_S^0 at each jet p_T bin.

4.5 Summary

The analysis details of the first measurements of longitudinal double spin asymmetry A_{LL} of Λ, $\overline{\Lambda}$ and K_S^0 in proton-proton collisions at $\sqrt{s} = 200$ GeV are presented. The A_{LL} is expected to be sensitive to the helicity distributions of strange quark and anti-quark, which still remain poor experimental constraints. We measured the A_{LL} as a function p_T and jet p_T for in-jet Λ hyperons and K_S^0. Predictions from MC samples generated with PYTHIA [128] using helicity distributions from the NNPDFpol1.1 [39] are compared with the measurements. The measured results are consistent with the predictions within uncertainties. The small A_{LL} results might indicate small helicity distributions of strange quark and anti-quark. The first measurements of longitudinal double spin asymmetry A_{LL} of Λ, $\overline{\Lambda}$ and K_S^0 will provide further constraints on helicity distributions of strange quark and anti-quark.

Chapter 5 Longitudinal Spin Transfer D_{LL} to Λ and $\overline{\Lambda}$

The Longitudinal spin transfer D_{LL} to Λ and $\overline{\Lambda}$ in proton-proton collisions is expected not only to be sensitive to the helicity distributions of strange quark and anti-quark but also can shed light on polarized fragmentation functions. In this chapter, the analysis details will be presented.

5.1 D_{LL} Extraction

5.1.1 Extracting D_{LL} via the hyperon weak decay

The weak decay of $\Lambda(\overline{\Lambda})$ guarantees that its polarization $P_{\Lambda(\overline{\Lambda})}$ can be measured experimentally via its decay channel $\Lambda \to p + \pi^-$ ($\overline{\Lambda} \to \bar{p} + \pi^+$) [70-72]. In the rest frame of $\Lambda(\overline{\Lambda})$, the angular distribution of its decayed daughter proton (anti-proton) can be expressed as the following equation:

$$\frac{dN}{d\cos\theta^*} = \frac{AN_0}{2}\left(1 + \alpha_{\Lambda(\overline{\Lambda})} P_{\Lambda(\overline{\Lambda})} \cos\theta^*\right), \tag{5.1}$$

where θ^* is the angle between the polarization direction of $\Lambda(\overline{\Lambda})$ and the momentum of its daughter proton (anti-proton) in the rest frame of $\Lambda(\overline{\Lambda})$. A is the detector acceptance, which varies with θ^* and other variables. N_0 is the total number of $\Lambda(\overline{\Lambda})$ that decay to proton(anti-proton) and $\pi^-(\pi^+)$. The weak-decay parameter α_Λ is taken to be $\alpha_\Lambda = 0.732$ [32] with $\alpha_\Lambda = -\alpha_{\overline{\Lambda}}$ assuming no CP violation. In the D_{LL} measurement, the polarization direction is taken to be the momentum direction of the $\Lambda(\overline{\Lambda})$ in the center-of-mass frame of the proton-proton collisions.

The details about the reconstruction of Λ hyperons are described in Chapter 4. In-jet hyperons are used for the D_{LL} analysis to study the helicity distribution of strange quark and anti-quark and polarized fragmentation functions. Figure 5.1 shows the 2D distribution of $\cos\theta^*$ and the mass of the reconstructed Λ and $\overline{\Lambda}$ candidates. Experimentally, the spin transfer D_{LL} is extracted from the asymmetry of the Λ hyperon yields with opposite beam helicity in a small $\cos\theta^*$ interval via the following

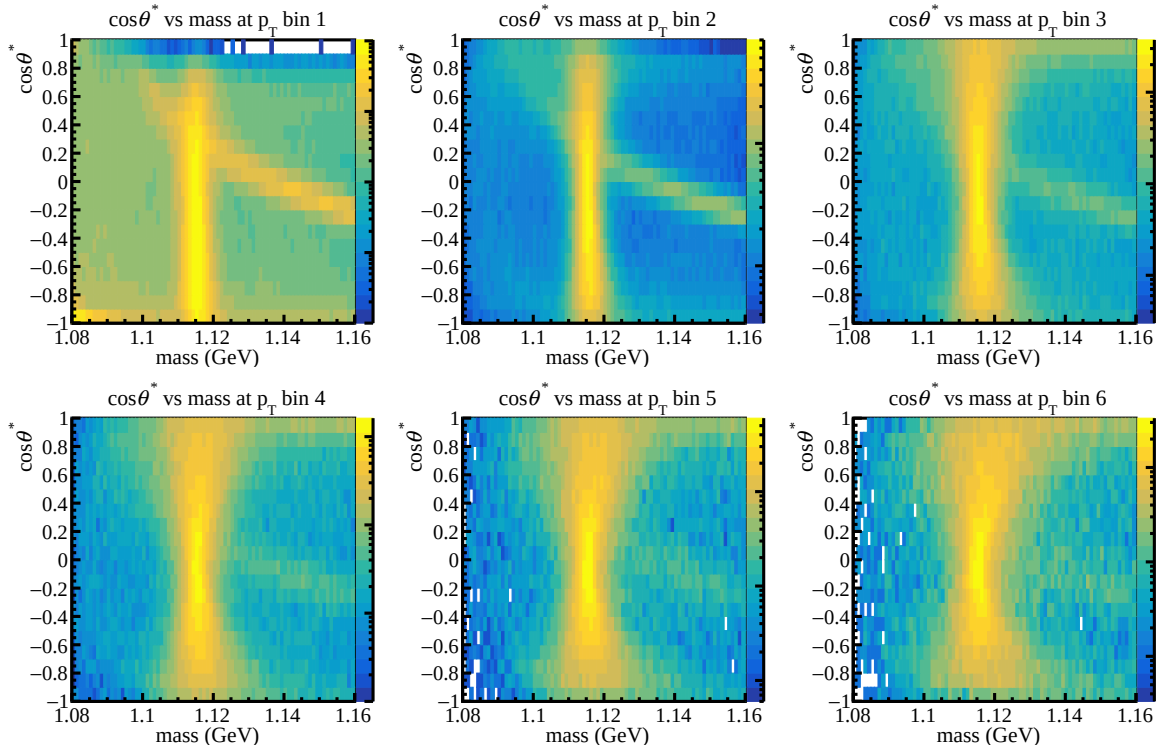

Figure 5.1: The 2D distributions of $\cos\theta^*$ vs hyperon invariant mass for Λ.

equation [89-90]:

$$D_{LL} = \frac{1}{\alpha_{\Lambda(\overline{\Lambda})} P_{\text{beam}} \ \langle \cos\theta^* \rangle} \frac{N^+ - \mathcal{R} N^-}{N^+ + \mathcal{R} N^-}, \tag{5.2}$$

where N^+ and N^- are the yields of Λ hyperons with positive and negative beam helicity, respectively. P_{beam} is the polarization of the proton beam and $\langle \cos\theta^* \rangle$ is the average $\cos\theta^*$ in that bin. In practice, $\cos\theta^*$ is equally divided into 20 bins. $\mathcal{R}$ is the relative luminosity estimated with the VPD [109] and the ZDC [110]. The relative luminosities involved in the D_{LL} measurements are R_4, R_5 and R_6. Details about these relative luminosities are in Sec. 2.3.3.

Equation (5.2) can be derived from Eq. (5.1). As its name implies, D_{LL} measures the spin transfer coefficient from the proton beam to Λ hyperon. In an other word, $P_{\Lambda(\overline{\Lambda})} = D_{LL} P_{\text{beam}}$. In a small $\cos\theta^*$ interval, the detector acceptance A can be replaced with its average value:

$$\langle A(\cos\theta^*) \rangle = \frac{\int A\,(\cos\theta^*)\, N(P, \cos\theta^*) d\cos\theta^*}{\int N(P, \cos\theta^*) d\cos\theta^*}, \tag{5.3}$$

where $N(P, \cos\theta^*) = \frac{N_0}{2}(1 + \alpha P \cos\theta^*)$, and P is the polarization of Λ hyperon. When the hyperon polarization is P and $-P$, the hyperon yields in a small $\cos\theta^*$ bin, $[\cos\theta_1^*, \cos\theta_2^*]$, can be obtained by integrating the Eq. (5.1):

$$N(P) = \langle A(P, \cos\theta^*)\rangle \frac{N_0}{2}\left\{\cos\theta_2^* - \cos\theta_1^* + \frac{\alpha}{2}P\left(\cos^2\theta_2^* - \cos^2\theta_1^*\right)\right\} \tag{5.4}$$

$$N(-P) = \langle A(-P, \cos\theta^*)\rangle \frac{N_0}{2}\left\{\cos\theta_2^* - \cos\theta_1^* - \frac{\alpha}{2}P\left(\cos^2\theta_2^* - \cos^2\theta_1^*\right)\right\} \tag{5.5}$$

The detector acceptance is independent of the Λ polarization when the bin width is small enough. Therefore, P can be obtained by solving the above two equations with the detector acceptance being canceled out:

$$P = \frac{1}{\alpha \langle\cos\theta^*\rangle}\frac{N(P) - N(-P)}{N(P) + N(-P)}. \tag{5.6}$$

Flipping the beam polarization will inverse the polarization of Λ hyperons. Therefore, $N(P)$ and $N(-P)$ correspond to the Λ hyperon yields with positive and negative beam helicity, respectively. The Eq. (5.2) can be obtained by dividing the beam polarization from Eq. (5.6) and the relative luminosity $mathcalR$ in Eq. (5.2) is used to correct the imbalance of the luminosity in the sampling from different beam helicity.

In the D_{LL} measurements, only one beam need to be polarized. The single-spin yields of Λ hyperons can be obtained by combining the double-spin yields weighted with the corresponding relative luminosities. At each $\cos\theta^*$ bin, the D_{LL} can be extracted with Eq. (5.7) and (5.8) assuming the polarized beam is blue beam and yellow beam, respectively.

$$D_{LL} = \frac{1}{\alpha_{\Lambda(\overline{\Lambda})} P_B \langle\cos\theta^*\rangle}\frac{(N^{++}/R_4 + N^{+-}/R_6) - (N^{-+}/R_5 + N^{--})}{(N^{++}/R_4 + N^{+-}/R_6) + (N^{-+}/R_5 + N^{--})} \tag{5.7}$$

$$D_{LL} = \frac{1}{\alpha_{\Lambda(\overline{\Lambda})} P_Y \langle\cos\theta^*\rangle}\frac{(N^{++}/R_4 + N^{-+}/R_5) - (N^{+-}/R_6 + N^{--})}{(N^{++}/R_4 + N^{-+}/R_5) + (N^{+-}/R_6 + N^{--})} \tag{5.8}$$

In this analysis, D_{LL} is measured as a function of Λ hyperons p_T and jet momentum fraction $z \equiv (p_\Lambda \cdot p_{jet})/|p_{jet}|^2$ carried by Λ hyperons as measuring D_{LL} vs z provides direct probe to polarized fragmentation functions according to Ref. [92].

The residual backgrounds under the hyperon mass peak are estimated with the sideband method. At each p_T or z bin, the D_{LL}^{raw} under the mass peak and the D_{LL}^{bkg} from the residual background are obtained by averaging over all $\cos\theta^*$ bins. The influence

of the residual background on the D_{LL} is subtracted with the following equation:

$$D_{LL} = \frac{D_{LL}^{raw} - rD_{LL}^{bkg}}{1-r}, \tag{5.9}$$

where r is the residual background fraction under the mass peak, estimated with the side-band method. Figure 5.2, as examples, presents the D_{LL}^{raw} as a function of $\cos\theta^*$ in each p_T bins with the blue beam polarized for positive pseudo-rapidity region $0 < \eta_\Lambda < 1.2$, where η_Λ is defined as the pseudo-rapidity relative to the polarized beam direction. Similar results of D_{LL}^{raw} for Λ is shown in Fig. 5.3.

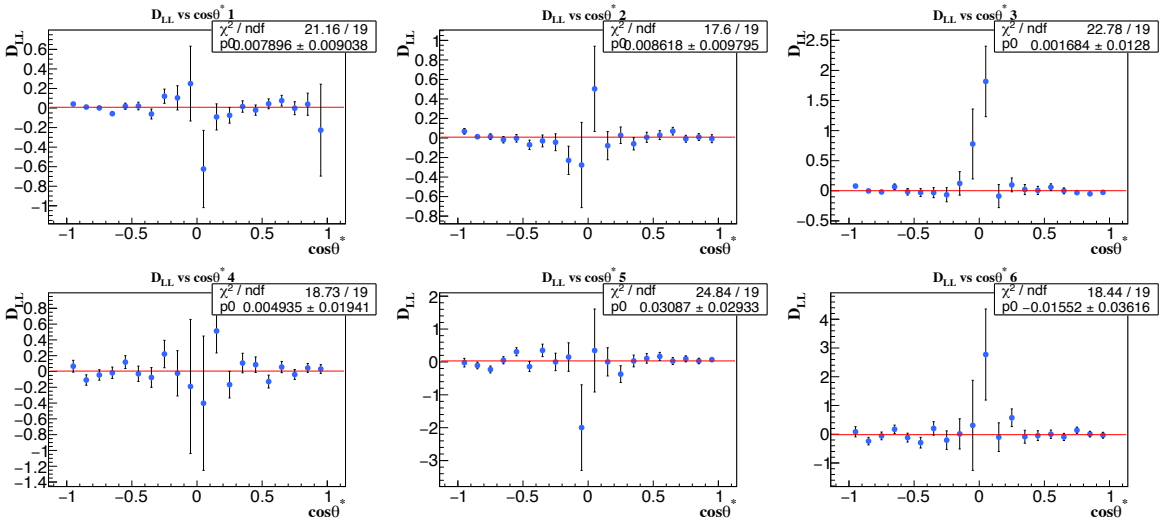

Figure 5.2: The D_{LL}^{raw} of Λ as a function of $\cos\theta^*$ with blue beam polarized in 6 Λ p_T bins at $0 < \eta_\Lambda < 1.2$ with respect to the polarized beam.

In principle, the D_{LL} results extracted with blue beam polarized and yellow beam polarized should be consistent with each other. The final D_{LL} results are the statistical average of the results for blue beam and yellow beam. Figure 5.4, as an example, shows the comparison of the D_{LL} results between blue beam and yellow beam. As we can see in Fig. 5.4, results between blue beam and yellow beam are consistent. The combined results for blue beam and yellow beam Λ and $\overline{\Lambda}$ are presented in Fig. 5.5.

5.1.2 Jet Momentum Fraction Carried by Λ and $\overline{\Lambda}$

Theoretical study from Ref. [92] proposed that measuring D_{LL} as a function of jet momentum fraction z carried by Λ hyperons can directly probe polarized fragmentation functions. Therefore, we performed the first measurement of D_{LL} vs z. However, due to detector responses, z calculated with the reconstructed jets and hyperons needs

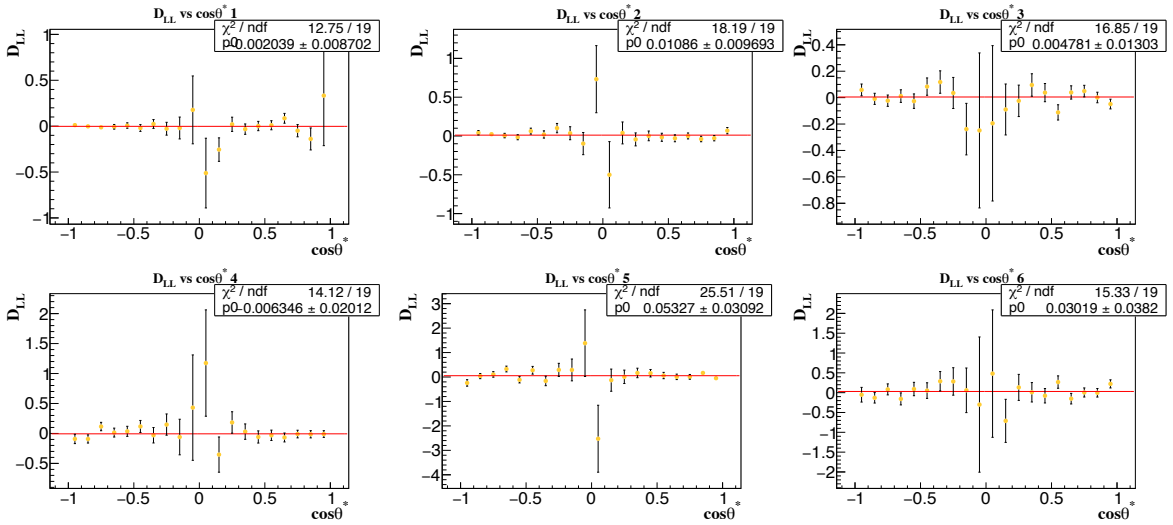

Figure 5.3: The D_{LL}^{raw} of $\overline{\Lambda}$ as a function of $\cos\theta^*$ with yellow beam polarized in 6 $\overline{\Lambda}$ p_T bins at $0 < \eta_\Lambda < 1.2$ with respect to the polarized beam.

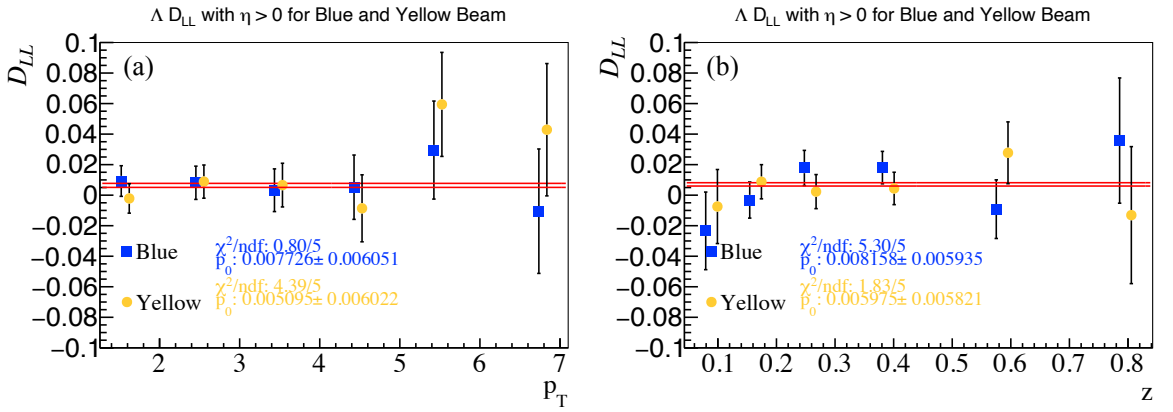

Figure 5.4: Comparison of D_{LL} of Λ for blue beam and yellow beam at $0 < \eta_\Lambda < 1.2$ with respect to the polarized beam. Panel (a) are the results of D_{LL} vs hyperon p_T and panel (b) is for D_{LL} vs z. Results for yellow beam are shifted horizontally for clarity.

correction. In order to compare the measured results with theoretical calculations, which are calculated at the particle level, z at detector level needs to be corrected back to particle level in our measurement. The correction is realized with the same embedding MC samples described in Sec. 3.3. Figure 5.6 illustrates the comparison of detector level z between data and embedding MC samples. In general, they are in good agreement. Similar to the jet p_T correction in the $\pi^{\pm}$-tagged jet A_{LL} measurements, jets and hyperons at the detector level are associated to their corresponding particle

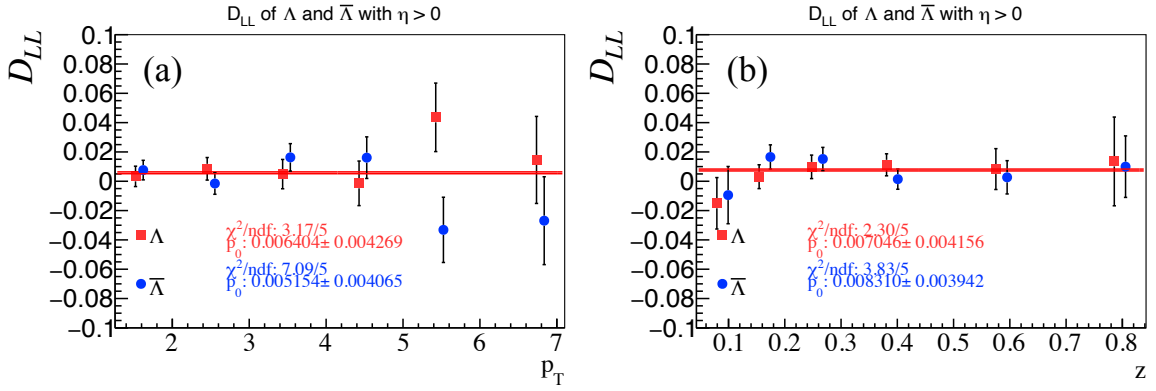

Figure 5.5: The D_{LL} of Λ and $\overline{\Lambda}$ at $0 < \eta_{\Lambda(\overline{\Lambda})} < 1.2$ with respect to the polarized beam. Panel (a) is the results of D_{LL} vs p_T and panel (b) is for D_{LL} vs z. Results for $\overline{\Lambda}$ are slightly offset horizontally for clarity.

level objects by applying the ΔR cut on their separation in η and ϕ space:

$$\text{For jet: } \Delta R = \sqrt{(\eta_{\text{detector}} - \eta_{\text{particle}})^2 + (\phi_{\text{detector}} - \phi_{\text{particle}})^2} < 0.5, \tag{5.10}$$

$$\text{For } \Lambda(\overline{\Lambda})\text{: } \Delta R = \sqrt{(\eta_{\text{detector}} - \eta_{\text{particle}})^2 + (\phi_{\text{detector}} - \phi_{\text{particle}})^2} < 0.05 \tag{5.11}$$

The two-step matching procedure is similar to the procedure used in Sec. 3.4.1. Figure 5.7 shows the matching fraction from detector level to particle level. Figure 5.8 shows the correlation of detector z and particle z for Λ and $\overline{\Lambda}$ in the embedding MC samples. The points indicate the mean values of detector z and particle z, and the standard deviations of the particle z in each detector z bin are shown in bars. In each detector z bin, the average particle z is calculated with the matched hyperon and jet. The differences between the averaged values of detector z and particle z are taken as the corrections. The corrections are estimated independently for two triggers and the final corrections are determined by weighting the corrections of each trigger by their corresponding hyperon yields associated with that trigger in data.

5.1.3 K^0_S as null check

With the same method as D_{LL}, the 'spin transfer' δ_{LL} of K^0_S is extracted with Eq. (5.2). The decay parameter $\alpha_{K^0_S}$ is artificially taken to be one as there is no such parameter for K^0_S. Figure 5.9, as an example, shows the δ_{LL} of K^0_S as a function of $\cos\theta^*$ at $2 < p_T < 3$ GeV for blue beam polarized (left panel) and yellow beam polarized (right panel) with $0 < \eta_{K^0_S} < 1.2$ with respect to the polarized beam. As K^0_S is a spin-0

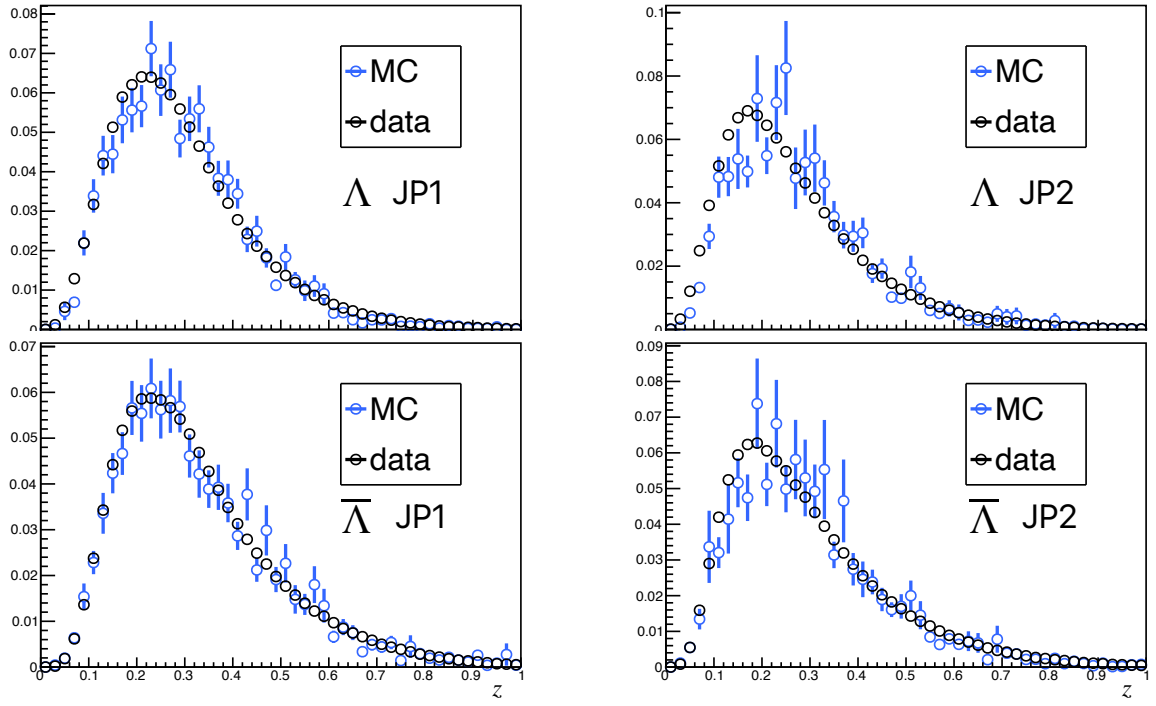

Figure 5.6: The comparison of the detector z between data and the embedding.

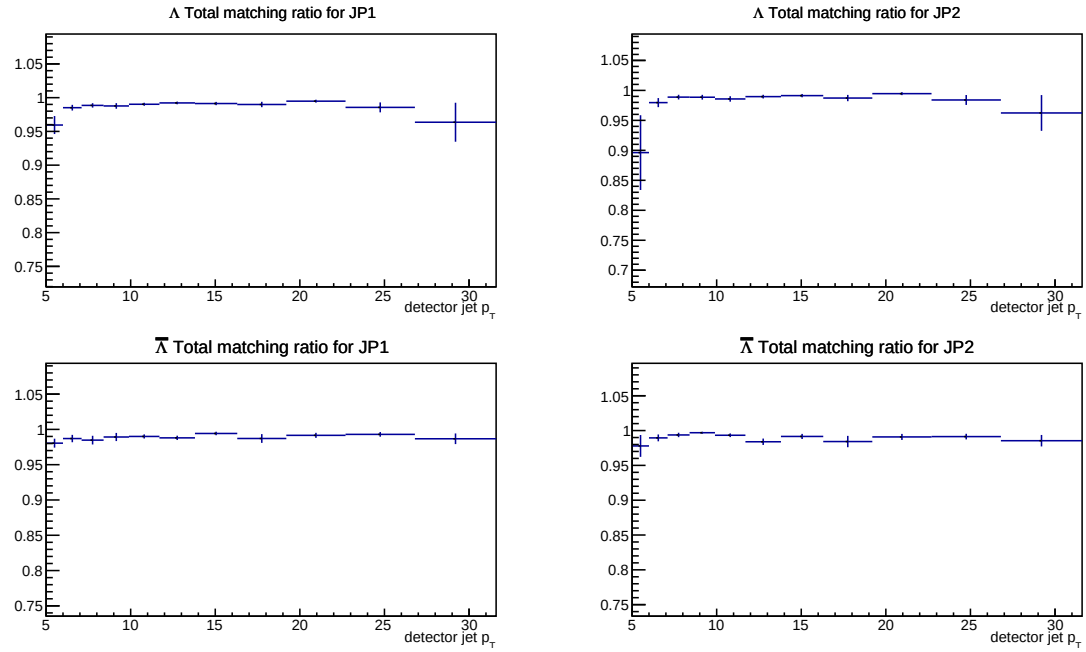

Figure 5.7: The matching fraction as a function of detector jet p_T from detector level to particle level.

particle, such 'spin transfer' δ_{LL}, in principle, should be zero. Non-zero results may indicate some issues of the D_{LL} extracting method and/or other effects. The extracted δ_{LL} results as a function of p_T and z are shown in Fig. 5.9(a) and (b), respectively. The

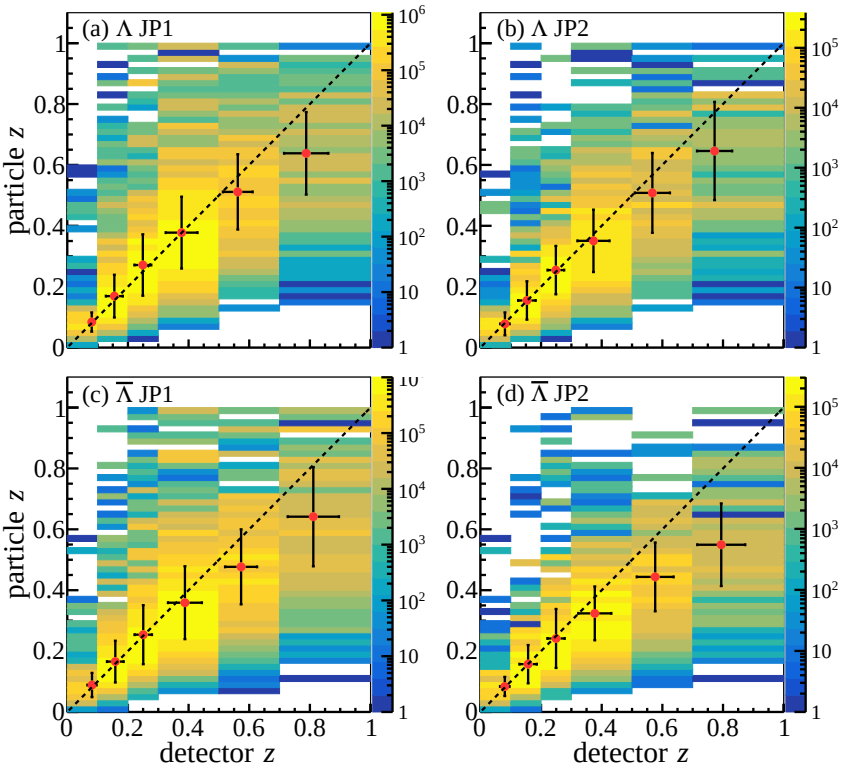

Figure 5.8: The correlation of jet momentum fraction z carried by Λ (upper panels) and $\overline{\Lambda}$ (lower panels) at particle level and detector level for two triggers. The red points show the mean values of detector z and particle z in each bin while the standard derivations of particle z are presented in bars. The dashed lines at $y = x$ are for guidance.

results are consistent with zero within uncertainties.

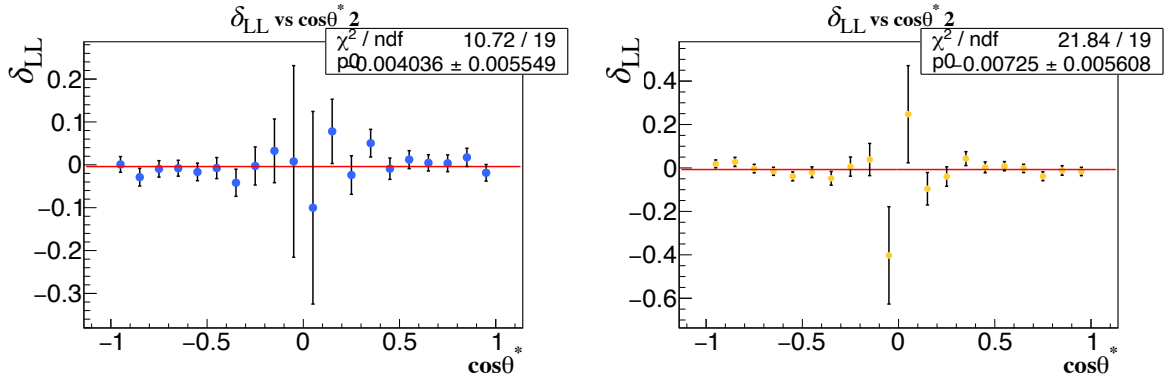

Figure 5.9: δ_{LL} of K^0_S as a function of $\cos\theta^*$ at $2 < p_T < 3$ GeV for blue beam polarized (left panel) and yellow beam polarized (right panel) with $0 < \eta_{K^0_S} < 1.2$ with respect to the polarized beam.

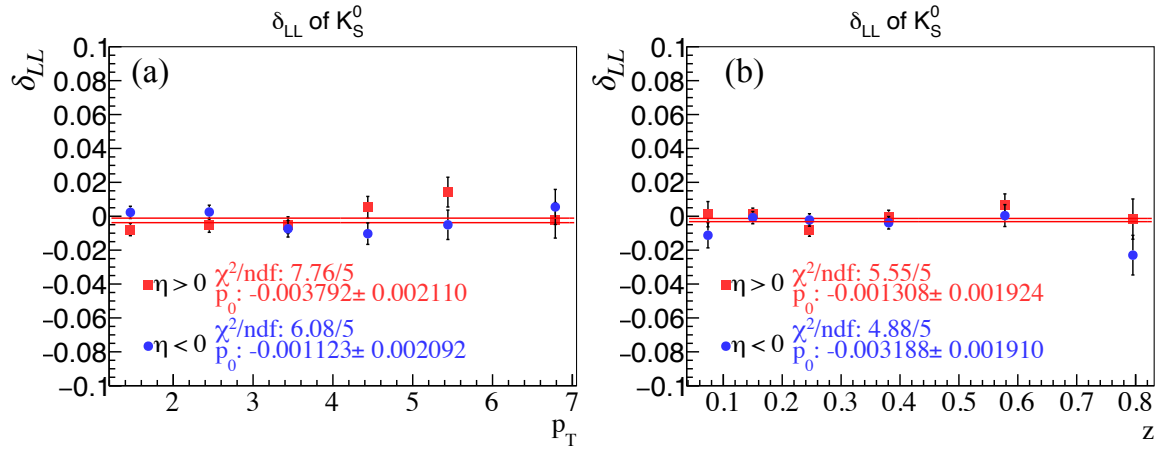

Figure 5.10: The δ_{LL} of K^0_S for both positive and negative η. Panel (a) is the results of δ_{LL} vs p_T and panel (b) is for δ_{LL} vs z.

5.2 Monte Carlo Simulation

In order to estimate systematic uncertainties in the analysis, a Monte Carlo (MC) simulation samples are generated with PYTHIA 6.4.28[128]. The generated events are then passed through the STAR detector simulation software packages based on GEANT3[129] to simulate the detector response. The simulation setup is mostly same as the embedding sample used in Sec. 3.3. Simulation of the detector response in the GEANT3 is the most time-consuming step in the whole simulation procedure. A relatively low production rate of Λ hyperons means that the vast majority of generated events are useless. To address this issue, we applied a 'Λ filter' to the events generated by the PYTHIA, which requires at least one Λ or $\overline{\Lambda}$ produced in a PYTHIA events. Only events that pass the 'Λ filter' are allowed to enter the detector simulation. The simulation samples are generated for each hyperon p_T bin separately, and at each p_T bin, the partonic scattering $\hat{p}_T$ is divided into 6 bins, i.e. 3-4, 4-5, 5-6, 6-8, 8-15, and > 15 (GeV). The simulation samples generated at various $\hat{p}_T$ bins are normalized by the luminosity, determined through events generated in PYTHIA, and the corresponding hard scattering cross section from PYTHIA. Figure 5.11, as an example, presents the weighted $\hat{p}_T$ distribution for unbiased (labeled as 'ZB') and triggered samples (JP1 and JP2). Figure 5.13, as an example, shows the comparison of invariant mass, p_T, azimuthal angle ϕ, and the pseudo-rapidity η of Λ with $2 < p_T < 3$ GeV between data and MC. Similar results for $\overline{\Lambda}$ are shown in Fig. 5.12

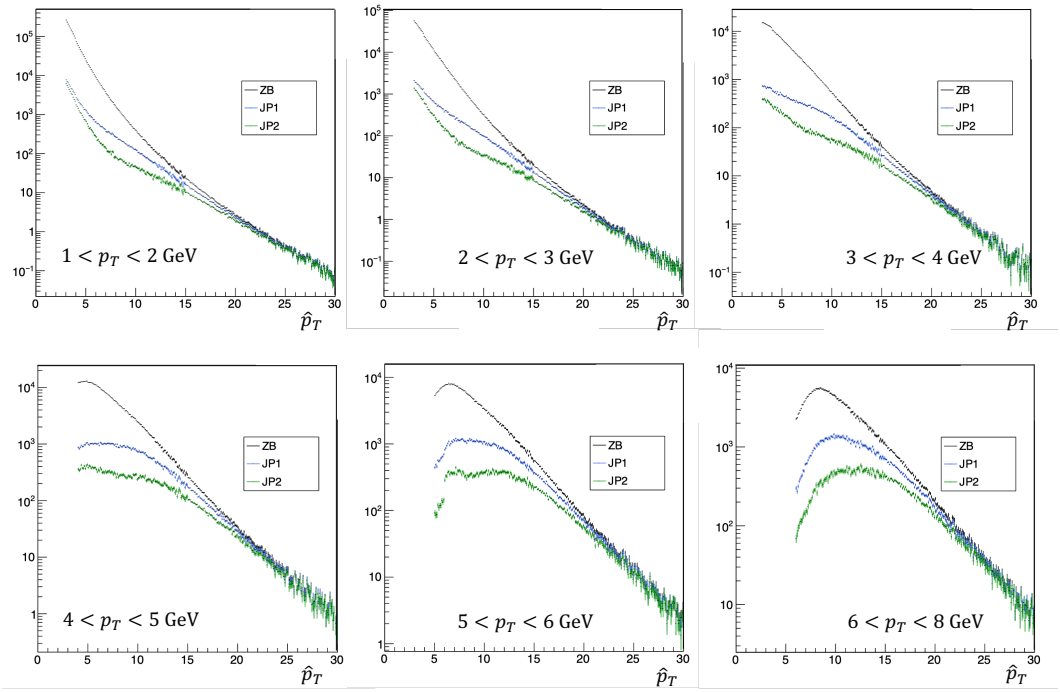

Figure 5.11: The weighted partonic scattering $\hat{p}_T$ at 6 Λ p_T bins for unbiased (labeled as 'ZB') and triggered samples.

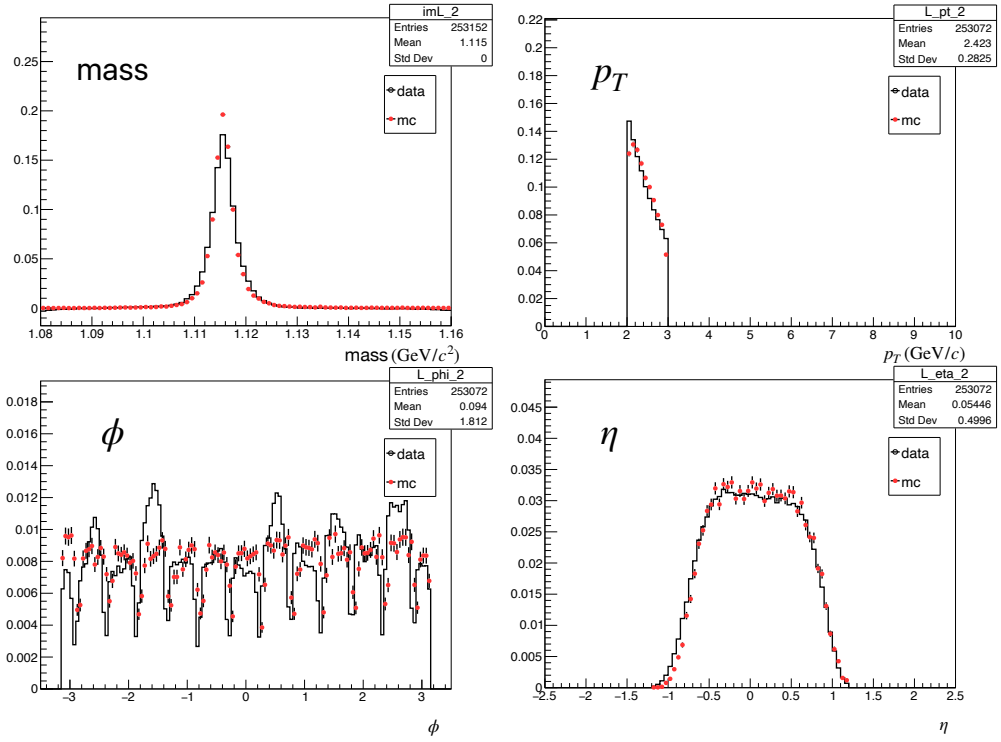

Figure 5.12: The comparison invariant mass, p_T, azimuthal angle ϕ, and the pseudo-rapidity η of Λ with $2 < p_T < 3$ GeV between data and MC. The background from data has been subtracted.

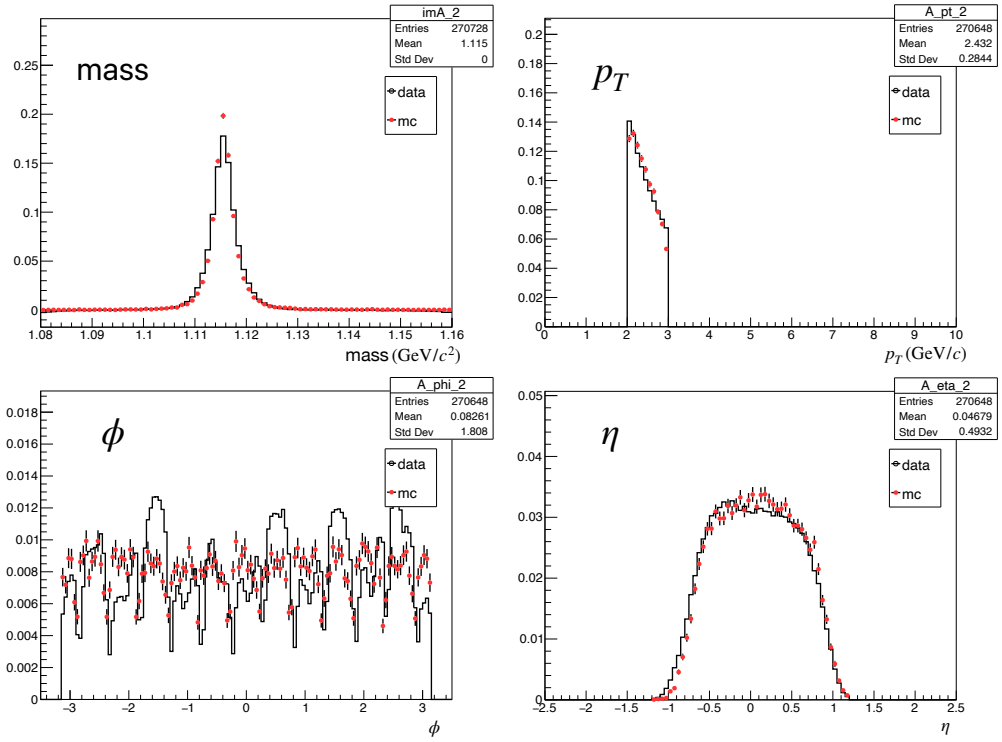

Figure 5.13: The comparison invariant mass, p_T, azimuthal angle ϕ, and the pseudo-rapidity η of $\overline{\Lambda}$ with $2 < p_T < 3$ GeV between data and MC. The background from data has been subtracted.

5.3 Systematic Uncertainties

In the D_{LL} measurement, 5 sources of systematic uncertainties are considered, which are listed below:

- Weak decay parameter
- Beam polarization
- Relative luminosity
- Residual background fraction
- Trigger bias

5.3.1 Weak decay parameter and beam polarization

The weak decay parameter $\alpha_\Lambda = 0.732 \pm 0.014$ [32] with $\alpha_\Lambda = -\alpha_{\overline{\Lambda}}$ (assuming no CP violation) corresponds to a relative uncertainty of about 1.9%. This uncertainty contributes to the measured D_{LL} as an overall scale uncertainty. As mentioned

in Sec. 2.1.3, the relative uncertainties of the beam polarization for both blue beam and yellow beam are 3.0%, and are applied to the measured D_{LL} as an overall scale uncertainty.

5.3.2 Relative luminosity

In the D_{LL} measurement, the related relative luminosities are R_4, R_5 and R_6. The systematic uncertainties of themselves are listed in Tab. 2.3. Their contributions to the D_{LL} can be calculated with the following equation:

$$(\delta D_{LL})^2 = \sum_{i=4,5,6} (\frac{\partial D_{LL}}{\partial R_i})^2 (\delta R_i)^2 + 2 \sum_{i<j} \left| \frac{\partial D_{LL}}{\partial R_i} \frac{\partial D_{LL}}{\partial R_j} \rho(R_i, R_j) \delta R_i \delta R_j \right|, \tag{5.12}$$

where $\rho(R_i, R_j)$ is the correlation factor between two relative luminosities, and are listed below:

$$\rho(R_4, R_5) = 0.70, \quad \rho(R_4, R_6) = 0.47, \quad \rho(R_5, R_6) = 0.44$$

Figure 5.14 shows the correlations between R_4, R_5 and R_6. These relative luminosities are obtained with the STAR VPD [109] and ZDC [110] detectors. The partial derivatives of D_{LL} in terms of R_4, R_5 and R_6 can be calculated with the following formulas:

$$\frac{\partial D_{LL}}{\partial R_4} = \frac{-1}{4\alpha P_{beam} \langle \cos\theta^* \rangle} \frac{1}{R_4} \tag{5.13}$$

$$\frac{\partial D_{LL}}{\partial R_5} = \frac{-1}{4\alpha P_{beam} \langle \cos\theta^* \rangle} \frac{1}{R_5} \tag{5.14}$$

$$\frac{\partial D_{LL}}{\partial R_6} = \frac{-1}{4\alpha P_{beam} \langle \cos\theta^* \rangle} \frac{1}{R_6} \tag{5.15}$$

Details about the derivations of these formulas can be found in Ref. [137]. The calculated systematic uncertainty of D_{LL} from R_4, R_5 and R_6 is 0.0020 for all hyperon p_T and z bins.

5.3.3 Residual background fraction

To estimate the systematic uncertainties due to the determination of the residual background fraction, the invariant mass distributions of Λ hyperons are fitted with Gaussian+linear functions. The residual background fractions under hyperon mass peak are calculated with the linear function, and the D_{LL} is recalculated with

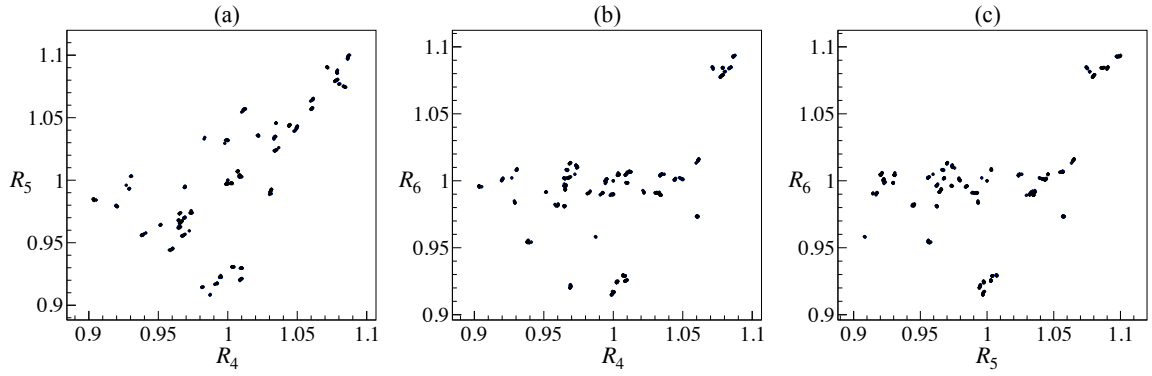

Figure 5.14: Correlation between R_4, R_5 and R_6.

Eq. (5.9) with the new estimated residual background fraction. The differences between D_{LL} with the residual background fraction from the side-band method and the fitting method are the systematic uncertainties contributed from the determination of the residual background fraction. Same method is used in the measurements of A_{LL} for Λ hyperons and K^0_S, described in Sec. 4.3.3. Figure 5.15, as an example, shows the invariant mass distributions of the reconstructed Λ and $\overline{\Lambda}$ together with the fitting functions. The residual background fractions estimated with both the side-band method and the fitting method are summarized in Tab. 5.1 and 5.2 for 6 p_T and 6 z bins , respectively. Table 5.3 and 5.4 summarize the systematic uncertainties from residual background fractions in the D_{LL} vs p_T and D_{LL} vs z measurements, respectively. These uncertainties are very small and are negligible.

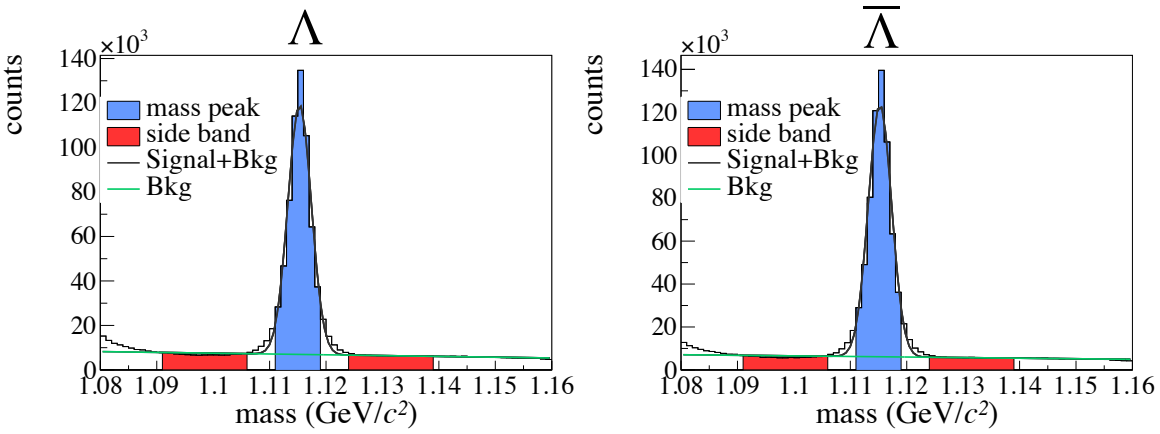

Figure 5.15: Invariant mass distributions of Λ and $\overline{\Lambda}$ with $1 < p_T < 2$ GeV.

	Λ		$\overline{\Lambda}$	
p_T (GeV)	Side-band method	Fitting method	Side-band method	Fitting method
1−2	8.9%	9.2%	7.6%	7.9%
2−3	9.3%	9.6%	8.2%	8.5%
3−4	7.6%	6.8%	6.8%	6.0%
4−5	7.0%	6.2%	6.4%	5.5%
5−6	7.8%	6.6%	7.7%	6.3%
6−8	9.4%	9.1%	9.5%	9.0%

Table 5.1: The residual background fraction in 6 p_T bins.

	Λ		$\overline{\Lambda}$	
z	Side-band method	Fitting method	Side-band method	Fitting method
0−0.1	12.8%	13.1%	8.5%	8.9%
0.1−0.2	11.5%	12.1%	10.3%	10.8%
0.2−0.3	11.8%	12.0%	10.8%	11.1%
0.3−0.5	9.4%	9.2%	8.3%	8.2%
0.5−0.7	7.5%	7.0%	6.1%	5.8%
0.7−1.0	8.2%	8.7%	6.6%	6.9%

Table 5.2: The residual background fraction in 6 z bins.

	$0 < \eta_{\Lambda(\overline{\Lambda})} < 1.2$		$-1.2 < \eta_{\Lambda(\overline{\Lambda})} < 0$	
p_T (GeV)	Λ	$\overline{\Lambda}$	Λ	$\overline{\Lambda}$
1−2	2.5×10^{-5}	2.6×10^{-5}	3.6×10^{-5}	9.8×10^{-7}
2−3	4.7×10^{-5}	1.2×10^{-5}	3.7×10^{-6}	3.6×10^{-5}
3−4	1.9×10^{-4}	6.9×10^{-5}	5.8×10^{-5}	1.6×10^{-4}
4−5	1.1×10^{-4}	5.0×10^{-4}	4.7×10^{-4}	8.8×10^{-4}
5−6	3.4×10^{-4}	1.1×10^{-4}	9.5×10^{-4}	6.7×10^{-4}
6−8	3.1×10^{-4}	1.1×10^{-6}	2.0×10^{-4}	3.3×10^{-4}

Table 5.3: The systematic uncertainties of D_{LL} vs p_T from residual background.

	$\eta_{jet} > 0$		$\eta_{jet} < 0$	
z	Λ	$\overline{\Lambda}$	Λ	$\overline{\Lambda}$
0−0.1	1.1×10^{-4}	2.7×10^{-5}	2.5×10^{-5}	9.2×10^{-5}
0.1−0.2	1.6×10^{-5}	9.1×10^{-5}	1.0×10^{-5}	2.2×10^{-6}
0.2−0.3	5.4×10^{-6}	1.1×10^{-4}	1.9×10^{-6}	1.0×10^{-5}
0.3−0.5	1.8×10^{-5}	1.4×10^{-5}	4.6×10^{-5}	1.3×10^{-5}
0.5−0.7	1.2×10^{-4}	1.4×10^{-4}	2.6×10^{-4}	3.7×10^{-5}
0.7−1.0	3.8×10^{-4}	1.2×10^{-4}	5.4×10^{-4}	6.9×10^{-5}

Table 5.4: The systematic uncertainties of D_{LL} vs z from residual background.

5.3.4 Trigger bias

As mentioned in Sec. 2.3.1, the jet-patch triggers (JP1 and JP2) used in the analysis are designed to select high-p_T jets. Since they do not directly trigger on Λ hyperons, the trigger conditions might introduce a potential bias to the D_{LL} measurements in several ways. For example, a distortion can be introduced by the trigger condition on sampling for different jet momentum fraction z carried by hyperons in the fragmentation process. It can also change the relative fraction of the partonic hard scattering processes. Moreover, the fraction of the contributions from decay of heavier hyperons may also be distorted by the trigger conditions. In this analysis, 3 effects of the trigger conditions are estimated with a model from Refs. [81, 83, 138], and they are listed below:

- The changes of the jet momentum fraction carried by Λ hyperons.
- The distortion of the fraction of QCD subprocesses and parton flavors in the fragmentation processes.
- The changes of the fractions between directly produced hyperons and Λ hyperons from the decay of heavier particles.

These effects are studied with the MC simulation samples described in Sec. 5.2. The D_{LL} results from the MC simulation are calculated with a model [81, 83, 138]. The uncertainties introduced by the trigger conditions are evaluated by calculating the difference of D_{LL} results before and after applying the trigger conditions in the MC simulation samples.

D_{LL} model calculation In the factorization framework, the longitudinal spin transfer D_{LL} in the proton-proton collision can be written as the convolution of parton distribution functions, partonic scattering cross section and the fragmentation functions. According to Ref. [81], the polarization P_{H_i} of the hyperon H_i can be written as the following:

$$P_{H_i} = \sum_f t^F_{H_i,f} P^{(q)}_f R_{H_i,f} + \sum_j t^D_{H_i,H_j} P_{H_j} R_{H_i,H_j} \tag{5.16}$$

The first term corresponds to the hyperons directly produced from the fragmentation of the outgoing parton and the second term corresponds to the contributions from the

decay of heavier hyperons. In Eq. (5.16), the $P_f^{(q)}$ is the polarization of the outgoing parton with flavor f. The $t_{H_i,f}$ is the spin transfer from the outgoing parton to the hyperon in the fragmentation processes. $R_{H_i,f}$ is the fraction of the directly produced hyperon yields with the parton f being the constituent of the hyperon H_i. For the second term of Eq. (5.16), $t^D_{H_i,H_j}$ is the spin transfer from the decay of $H_j \to H_i + X$, where P_{H_j} and R_{H_i,H_j} are the polarization of the hyperon H_j and the fraction of the yields for hyperon H_i from the decay of H_j, respectively. The fractions of different contributions including contributions from heavier hyperon decay can be obtained from PYTHIA generator.

The polarization P_f^q of the outgoing parton f can be calculated with the following formula:

$$P_f^q = \frac{\Delta q(x,Q^2)}{q(x,Q^2)} D_L^{q\to f}, \tag{5.17}$$

where $\Delta q(x,Q^2)$ is the helicity distribution of parton q and $q(x,Q^2)$ is the unpolarized parton distribution function. $D_L^{q\to f}$ is the spin transfer in the partonic scattering, and can be calculated with the perturbative QCD. The spin transfer $t_{H_i,f}$ from the outgoing parton to the final state hyperon is calculated with the SU(6) picture, in which the spin content of a hyperon from its constituent quarks can be determined by its SU(6) wave function. Details can be found in Ref. [81].

Systematic uncertainties from the distortion of the z distribution The systematic uncertainties of this part only contribute to the D_{LL} vs p_T results. In each p_T bin, the D_{LL} from the unbiased and the triggered samples is calculated with the following formula:

$$D_{LL} = \frac{\sum_i D^i_{\mathrm{LL}} N^i}{\sum_i N^i}, \tag{5.18}$$

where D^i_{LL} is the theoretical calculation [81] for the i-th z bin. N^i is the Λ hyperon yields that fall in this z bin from the MC samples. The differences of D_{LL} between triggered samples and unbiased sample are treated as the systematic uncertainties. Figure 5.16 shows the z distributions of triggered samples and unbiased samples for Λ and similar results for $\overline{\Lambda}$ are shown in Fig. 5.17. In general, the z from triggered samples is smaller than the unbiased results. This is because that the JP1 and JP2

triggers favor high p_T jets, which lead to smaller z for triggered sample. The calculated systematic uncertainties are summarized in Tab. 5.5.

	$0 < \eta_{\Lambda(\overline{\Lambda})} < 1.2$				$-1.2 < \eta_{\Lambda(\overline{\Lambda})} < 0$			
	Λ		$\overline{\Lambda}$		Λ		$\overline{\Lambda}$	
p_T GeV	JP1	JP2	JP1	JP2	JP1	JP2	JP1	JP2
1−2	0.0005	0.0006	0.0002	0.0003	0.0000	0.0000	0.0000	0.0000
2−3	0.0006	0.0008	0.0003	0.0005	0.0001	0.0001	0.0001	0.0001
3−4	0.0017	0.0020	0.0010	0.0016	0.0002	0.0001	0.0001	0.0001
4−5	0.0041	0.0051	0.0028	0.0042	0.0001	0.0002	0.0001	0.0002
5−6	0.0054	0.0076	0.0040	0.0068	0.0005	0.0008	0.0004	0.0007
6−8	0.0052	0.0086	0.0042	0.0068	0.0007	0.0012	0.0006	0.0011

Table 5.5: The systematic uncertainties from the distortions of the z distribution for JP1 and JP2 triggers

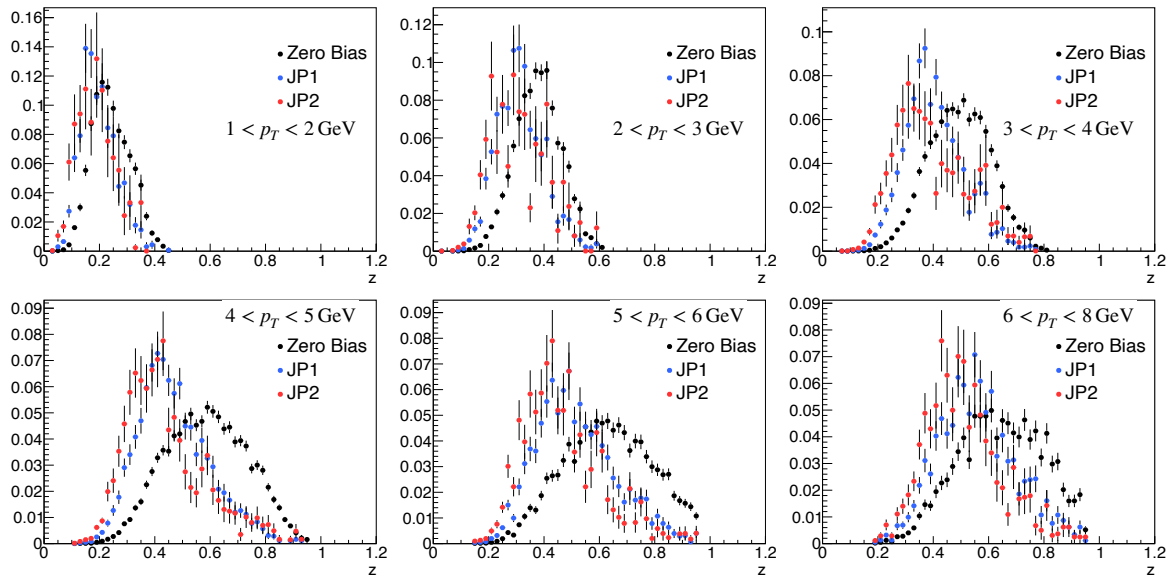

Figure 5.16: The z distributions of Λ in each p_T bins in $\sqrt{s} = 200$ GeV proton-proton collisions.

Systematic uncertainties from the distortion parton flavors in the fragmentation The jet patch triggers favor the energy deposits inside the EMCs, which could distort the relative fractions of different parton flavors in the fragmentation processes. Correspondingly, the fractions of QCD subprocesses are changed. The subprocesses fractions and the parton flavor fractions in the fragmentation processes with/without trigger conditions are extracted with the MC samples. With these fractions, we

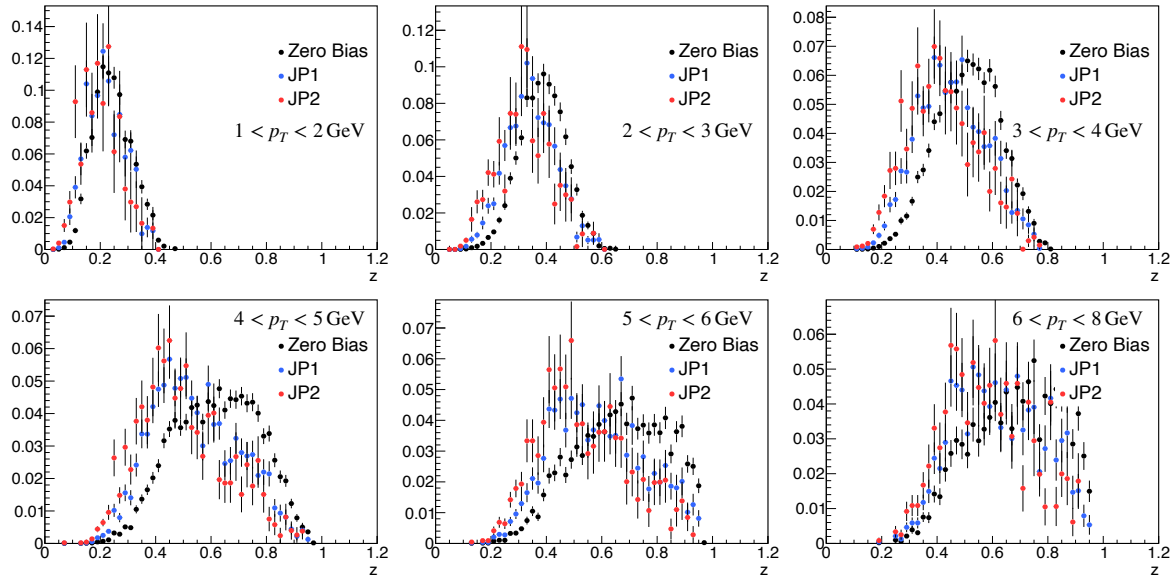

Figure 5.17: The z distributions of $\overline{\Lambda}$ in each p_T bins in $\sqrt{s} = 200$ GeV proton-proton collisions.

calculated the D_{LL} results with the model mentioned in Sec. 5.3.4. The systematic uncertainties are obtained by comparing the D_{LL} results before and applying trigger conditions. Figure 5.18 and 5.19 show the QCD subprocess fractions in different hyperon p_T bins for Λ and $\overline{\Lambda}$, respectively. The relative fractions of Λ and $\overline{\Lambda}$ originating from different parton flavors are presented in Fig. 5.20 and 5.21, respectively. These fractions are obtained with the MC samples based on PYTHIA. In general, 3 QCD subprocesses dominate, i.e. $gg \to gg$, $qg \to qg$ and $qq \to qq$. The $qq \to qq$ and $qg \to qg$ scatterings increase with increasing hyperon p_T as quarks carry relatively larger Bjorken-x of the proton, making it easier to produce higher p_T hadrons. As to the relative fraction in the fragmentation, contributions from gluons dominate at low p_T, and contributions of quarks increase with increasing hyperon p_T, especially for strange quark and anti-quark. The systematic uncertainties for D_{LL} vs p_T and D_{LL} vs z measurements are summarized in Tab. 5.6 and 5.7, respectively.

Systematic uncertainties from the changes of the Λ hyperons fractions from decay of heavier hyperons. As jet patch triggers prefer energy deposits in the EMCs, they could change the relative fractions of Λ hyperons from the decay of heavier hyperons. For example, photons produced via the channel $\Sigma^0 \to \Lambda + \gamma$ and the π^0 produced via $\Xi^0 \to \Lambda + \pi^0$ deposit more energy in the EMCs, making the triggers easier to fire. Such effect can distort the relative fraction of Λ hyperons. Figure 5.22

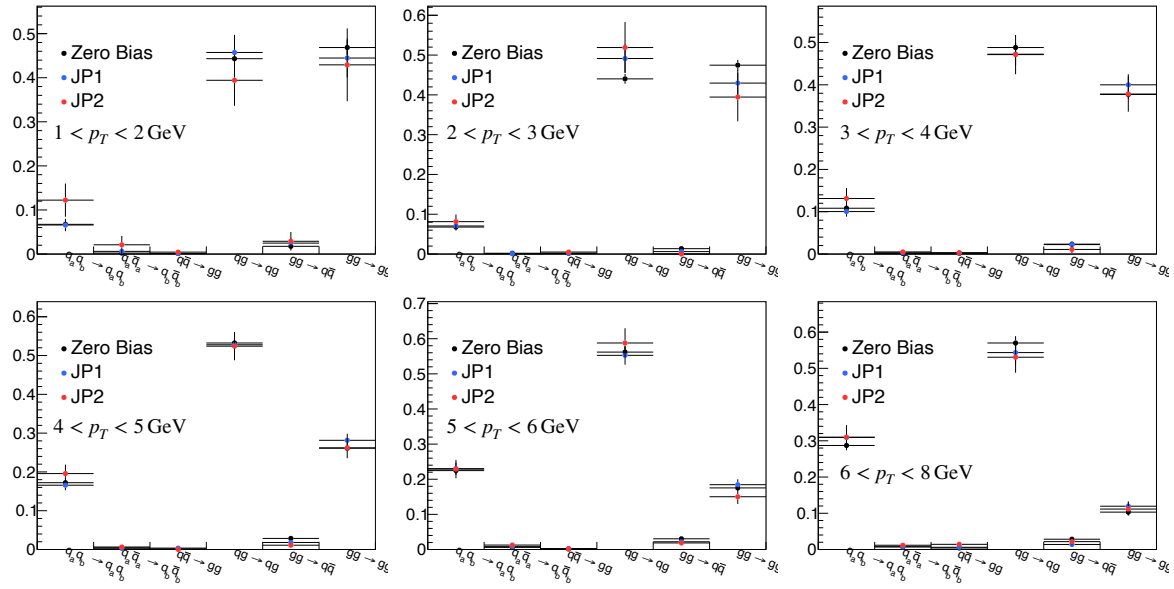

Figure 5.18: The fractions of Λ from different subprocesses in each p_T bins in $\sqrt{s} = 200$ GeV proton-proton collisions obtained from MC sample.

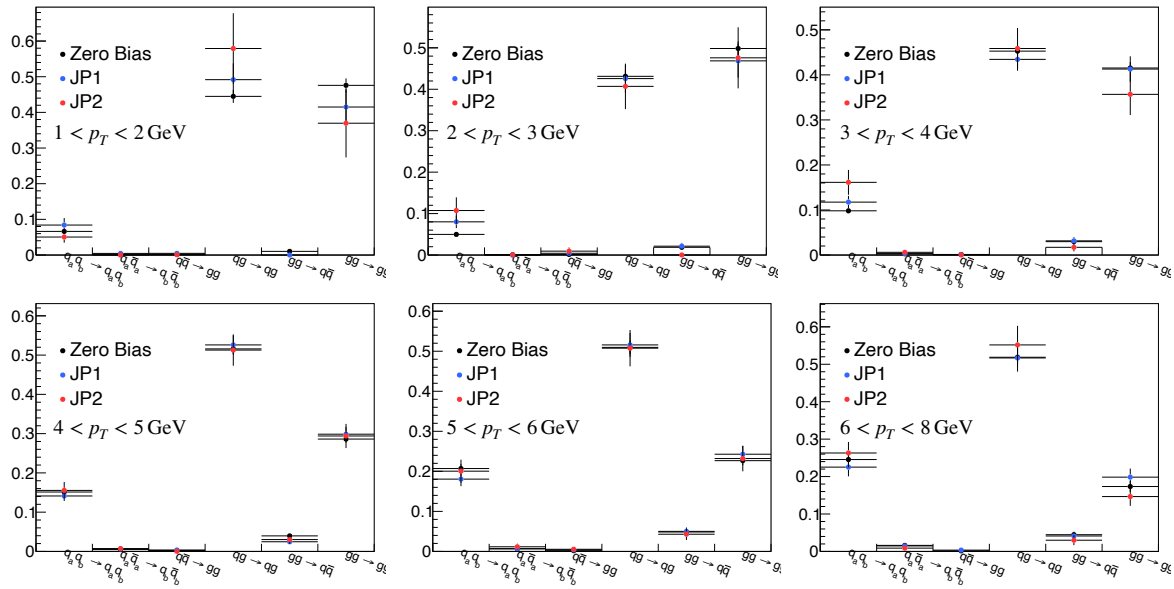

Figure 5.19: The fractions of $\overline{\Lambda}$ from different subprocesses in each p_T bins in $\sqrt{s} = 200$ GeV proton-proton collisions obtained from MC sample.

and 5.23 show the fractions of Λ and $\overline{\Lambda}$ from the direct production and the decay of different particles, respectively. The calculated systematic uncertainties in each p_T bins and z bins are summarized in Tab. 5.8 and 5.9, respectively.

Total Trigger bias The trigger bias for each trigger is obtained by adding the contributions from each sources. The total trigger bias for the whole dataset is obtained by weighting the trigger bias of two triggers with their corresponding yields in data.

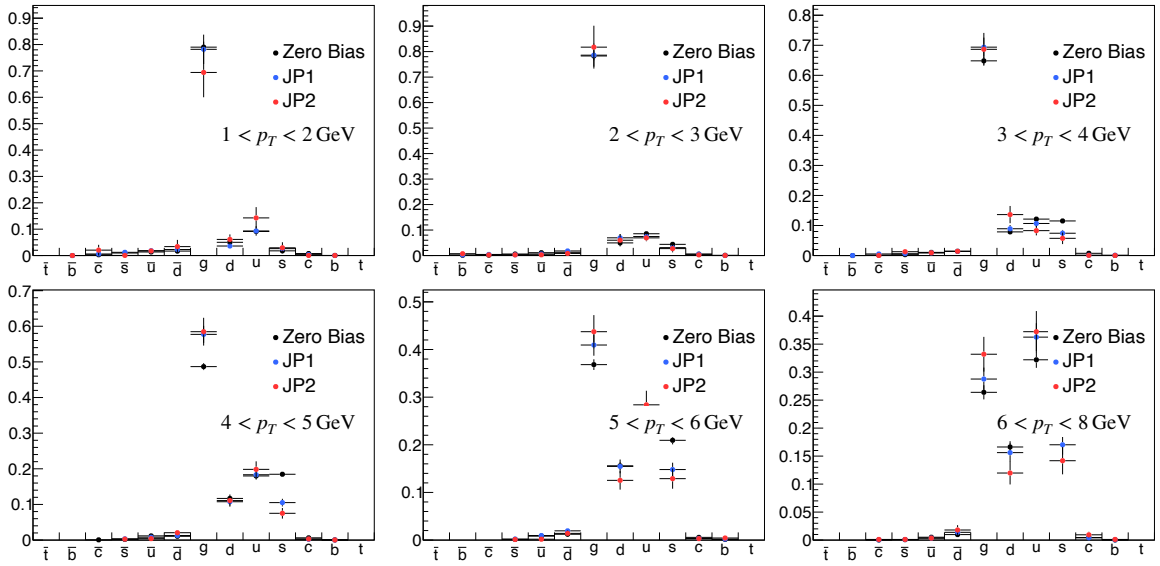

Figure 5.20: The fractions of Λ from different parton flavors in each p_T bins in $\sqrt{s} = 200$ GeV proton-proton collisions obtained from MC sample.

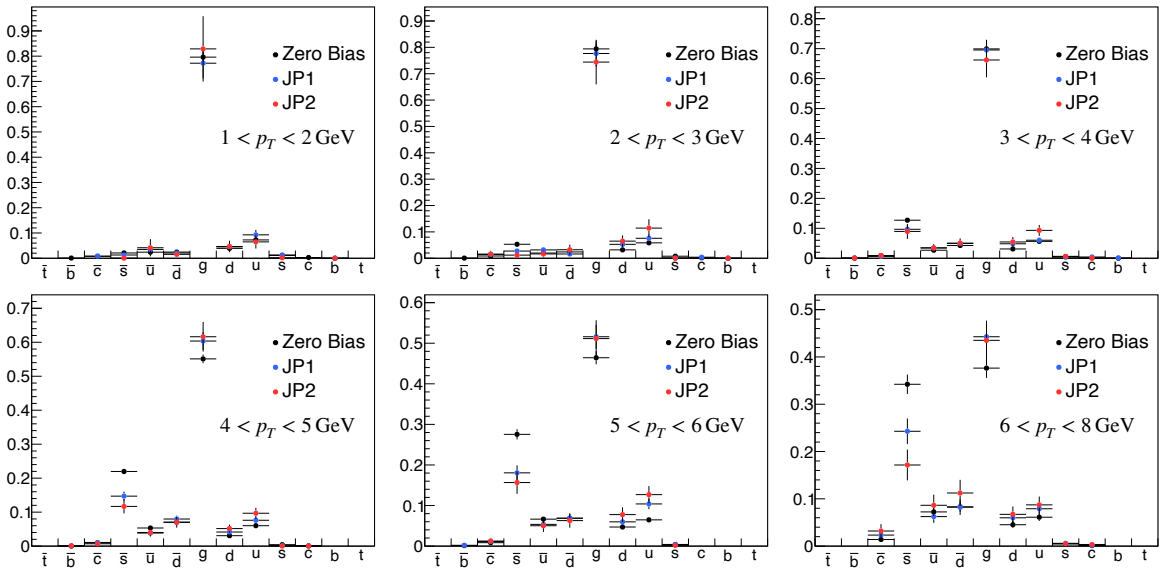

Figure 5.21: The fractions of $\overline{\Lambda}$ from different parton flavors in each p_T bins in $\sqrt{s} = 200$ GeV proton-proton collisions obtained from MC sample.

Table 5.10 summarizes the total trigger bias in D_{LL} vs p_T and D_{LL} vs z measurements.

5.3.5 Total Systematic Uncertainties

As the weak decay parameter, the beam polarization and the relative luminosity are shared with all kinematic bins for Λ hyperons, they contribute to an overall systematic uncertainties. The uncertainties from the residual background fraction and the trigger bias vary point by point. Different sources of the systematic uncertainties are

	$0 < \eta_{\Lambda(\overline{\Lambda})} < 1.2$				$-1.2 < \eta_{\Lambda(\overline{\Lambda})} < 0$			
	Λ		$\overline{\Lambda}$		Λ		$\overline{\Lambda}$	
p_T GeV	JP1	JP2	JP1	JP2	JP1	JP2	JP1	JP2
1−2	0.0000	0.0001	0.0000	0.0001	0.0000	0.0000	0.0000	0.0000
2−3	0.0002	0.0002	0.0004	0.0011	0.0000	0.0000	0.0000	0.0000
3−4	0.0015	0.0023	0.0015	0.0020	0.0002	0.0003	0.0002	0.0003
4−5	0.0038	0.0054	0.0050	0.0078	0.0007	0.0010	0.0010	0.0016
5−6	0.0050	0.0051	0.0083	0.0126	0.0013	0.0013	0.0022	0.0032
6−8	0.0048	0.0084	0.0044	0.0112	0.0014	0.0025	0.0016	0.0040

Table 5.6: The systematic uncertainties of D_{LL} vs p_T from the changes in the fraction of QCD subprocesses and parton flavors in the fragmentation.

	$\eta_{jet} > 0$				$\eta_{jet} < 0$			
	Λ		$\overline{\Lambda}$		Λ		$\overline{\Lambda}$	
z	JP1	JP2	JP1	JP2	JP1	JP2	JP1	JP2
0−0.1	0.0000	0.0000	0.0001	0.0000	0.0000	0.0000	0.0000	0.0000
0.1−0.2	0.0000	0.0001	0.0000	0.0000	0.0001	0.0001	0.0000	0.0000
0.2−0.3	0.0001	0.0002	0.0000	0.0000	0.0001	0.0002	0.0000	0.0000
0.3−0.5	0.0004	0.0003	0.0002	0.0003	0.0004	0.0005	0.0000	0.0000
0.5−0.7	0.0007	0.0011	0.0010	0.0012	0.0005	0.0008	0.0002	0.0001
0.7−1.0	0.0022	0.0027	0.0025	0.0036	0.0025	0.0012	0.0015	0.0012

Table 5.7: The systematic uncertainties of D_{LL} vs z from the changes in the fraction of QCD subprocesses and parton flavors in the fragmentation.

	$0 < \eta_{\Lambda(\overline{\Lambda})} < 1.2$				$-1.2 < \eta_{\Lambda(\overline{\Lambda})} < 0$			
	Λ		$\overline{\Lambda}$		Λ		$\overline{\Lambda}$	
p_T GeV	JP1	JP2	JP1	JP2	JP1	JP2	JP1	JP2
1−2	0.0000	0.0000	0.0000	0.0000	0.0000	0.0000	0.0000	0.0000
2−3	0.0000	0.0000	0.0000	0.0001	0.0000	0.0000	0.0000	0.0000
3−4	0.0000	0.0000	0.0003	0.0002	0.0000	0.0000	0.0000	0.0000
4−5	0.0002	0.0004	0.0007	0.0012	0.0001	0.0001	0.0001	0.0001
5−6	0.0006	0.0012	0.0009	0.0017	0.0001	0.0002	0.0002	0.0003
6−8	0.0010	0.0020	0.0009	0.0020	0.0002	0.0004	0.0002	0.0004

Table 5.8: Systematic uncertainty of D_{LL} vs p_T from the changes of feed-down fractions.

independent, and the total systematic uncertainties are calculated by adding them in a quadratic way. The uncertainties from the relative luminosity dominate at low hyperon

	$\eta_{jet} > 0$				$\eta_{jet} < 0$			
	Λ		$\overline{\Lambda}$		Λ		$\overline{\Lambda}$	
z	JP1	JP2	JP1	JP2	JP1	JP2	JP1	JP2
0−0.1	0.0000	0.0000	0.0000	0.0000	0.0000	0.0000	0.0000	0.0000
0.1−0.2	0.0000	0.0000	0.0000	0.0000	0.0000	0.0000	0.0000	0.0000
0.2−0.3	0.0001	0.0002	0.0000	0.0001	0.0000	0.0001	0.0000	0.0000
0.3−0.5	0.0000	0.0001	0.0000	0.0003	0.0000	0.0000	0.0000	0.0000
0.5−0.7	0.0005	0.0008	0.0002	0.0004	0.0001	0.0001	0.0000	0.0000
0.7−1.0	0.0016	0.0030	0.0000	0.0015	0.0007	0.0007	0.0000	0.0002

Table 5.9: Systematic uncertainty of D_{LL} vs z from the changes of feed-down fractions.

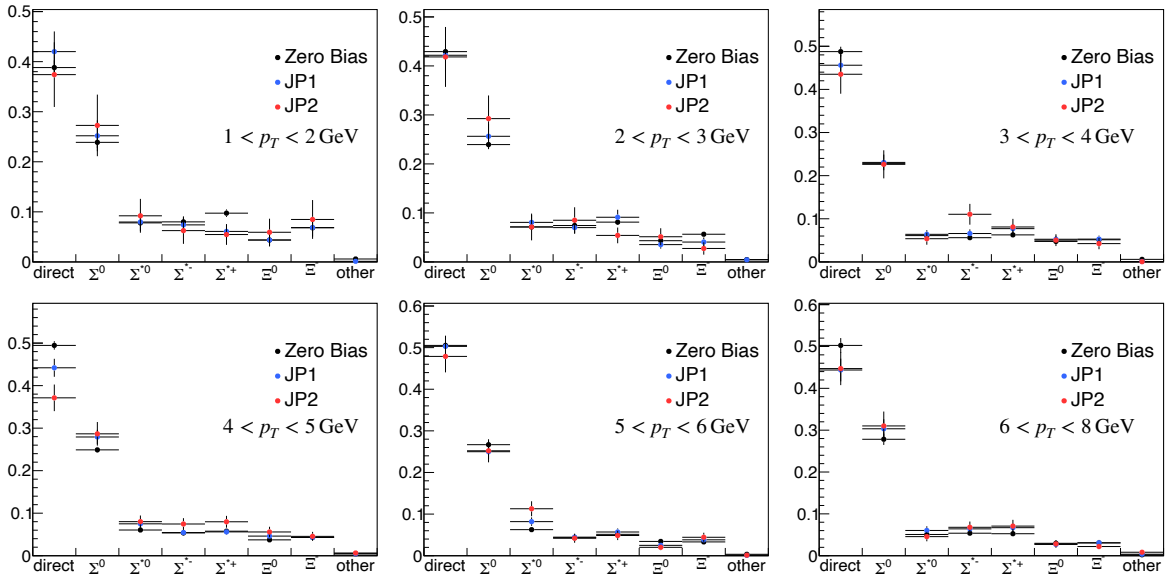

Figure 5.22: The fraction of Λ from different sources at each p_T bins.

	$0 < \eta_{\Lambda(\overline{\Lambda})} < 1.2$		$-1.2 < \eta_{\Lambda(\overline{\Lambda})} < 0$			$\eta_{jet} > 0$		$\eta_{jet} < 0$	
p_T GeV	Λ	$\overline{\Lambda}$	Λ	$\overline{\Lambda}$	z	Λ	$\overline{\Lambda}$	Λ	$\overline{\Lambda}$
1−2	0.0006	0.0003	0.0000	0.0000	0−0.1	0.0000	0.0000	0.0000	0.0000
2−3	0.0008	0.0009	0.0001	0.0001	0.1−0.2	0.0001	0.0000	0.0001	0.0000
3−4	0.0028	0.0023	0.0003	0.0002	0.2−0.3	0.0002	0.0001	0.0003	0.0000
4−5	0.0069	0.0081	0.0010	0.0014	0.3−0.5	0.0004	0.0003	0.0010	0.0000
5−6	0.0088	0.0131	0.0015	0.0031	0.5−0.7	0.0012	0.0012	0.0015	0.0002
6−8	0.0110	0.0119	0.0025	0.0037	0.7−1.0	0.0036	0.0034	0.0025	0.0013

Table 5.10: Total trigger bias for D_{LL} vs p_T and D_{LL} vs z measurements.

p_T and z while the trigger bias dominates at high p_T and z. Table 5.11 summarizes the total systematic uncertainties for D_{LL} vs p_T and D_{LL} vs z measurements.

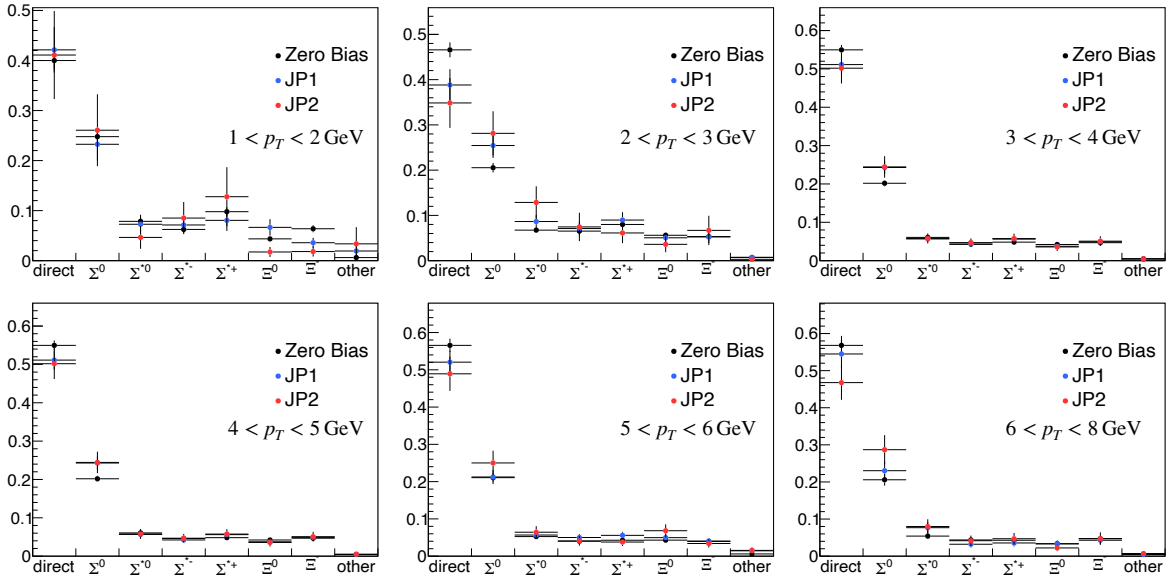

Figure 5.23: The fraction of $\overline{\Lambda}$ from different sources at each p_T bins.

	$0 < \eta_{\Lambda(\overline{\Lambda})} < 1.2$		$-1.2 < \eta_{\Lambda(\overline{\Lambda})} < 0$			$\eta_{jet} > 0$		$\eta_{jet} < 0$	
p_T GeV	Λ	$\overline{\Lambda}$	Λ	$\overline{\Lambda}$	z	Λ	$\overline{\Lambda}$	Λ	$\overline{\Lambda}$
1−2	0.0021	0.0020	0.0020	0.0020	0−0.1	0.0020	0.0020	0.0021	0.0021
2−3	0.0022	0.0022	0.0020	0.0020	0.1−0.2	0.0020	0.0021	0.0020	0.0020
3−4	0.0034	0.0031	0.0020	0.0021	0.2−0.3	0.0020	0.0021	0.0020	0.0020
4−5	0.0072	0.0084	0.0023	0.0026	0.3−0.5	0.0020	0.0020	0.0020	0.0020
5−6	0.0092	0.0133	0.0031	0.0037	0.5−0.7	0.0023	0.0023	0.0021	0.0021
6−8	0.0112	0.0121	0.0035	0.0043	0.7−1.0	0.0041	0.0039	0.0030	0.0025

Table 5.11: Total systematic uncertainties for D_{LL} vs p_T and D_{LL} vs z measurements.

5.4 Results and Discussions

With the longitudinally polarized proton-proton data taken at STAR in 2015, we performed the improved measurement of the longitudinal spin transfer D_{LL} to Λ and $\overline{\Lambda}$ as a function of hyperon p_T and the first measurement of D_{LL} as a function of the jet momentum fraction z carried by hyperons. The statistics are about 2−3 times larger than previously published measurements [90]. The first measurements of D_{LL} vs z can provide direct probe to the polarized fragmentation functions [92].

5.4.1 D_{LL} vs p_T

The D_{LL} vs hyperon p_T measurements cover the pseudo-rapidity $-1.2 < \eta < 1.2$ and hyperon transverse momentum $1.0 < p_T < 8.0$ GeV. The pseudo-rapidity η is

divided into two bins, namely positive η and negative η with respect to the polarized beam. The spin transfer D_{LL} is expected to be larger at positive η region. The measured D_{LL} results as a function of p_T are shown in Fig. 5.24. The bars represent the statistical uncertainties while the systematic uncertainties are shown in boxes. Table 5.12 summarizes the numerical values of the measured D_{LL}. Comparison of the D_{LL} results between this measurement and previous published results [90] with the data taken in 2009 is illustrated in Fig. 5.25 (a). Results are consistent with each other. The statistical average of the new measurements and the previous ones are calculated, with systematic uncertainties taken as their weighted average by the hyperon yields from different years. The theoretical predictions denoted as 'LM' in Ref.[91], which accounts for D_{LL} with Λ and $\overline{\Lambda}$ separately and incorporates STAR 2009 results as input, are generally consistent with the combined D_{LL} results shown in the upper sub-panel of Fig. 5.25 (b). The predictions labeled as 'DSV' from Ref. [84, 93] with Λ and $\overline{\Lambda}$ combined, are compared with the $\Lambda + \overline{\Lambda}$ results in the lower sub-panel of Fig. 5.25 (b). In the 'DSV' calculations, 3 scenarios of polarized fragmentation functions [84] are considered, which remain poorly constrained by experimental data. These scenarios consider different polarization contributions from quarks to Λ hyperons [87]:

- scenario 1: only s quark contributes to polarized Λ
- scenario 2: u and d quarks have same contribution to polarized Λ but with opposite sign to s quark
- scenario 3: u, d and s have same contribution to polarized Λ

Results are consistent with predictions from 'DSV $\Lambda + \overline{\Lambda}$ scen.1' and 'DSV $\Lambda + \overline{\Lambda}$ scen.2'. However, the data points lie below the 'DSV $\Lambda + \overline{\Lambda}$ scen.3' predictions, and the calculated χ^2 of the combined $\Lambda + \overline{\Lambda}$ results to this scenario is $\chi^2/ndf = 24.2/5$, which indicates strong disfavor to this scenario.

5.4.2 D_{LL} vs z

The first measurement of longitudinal spin transfer of Λ and $\overline{\Lambda}$ as a function of jet momentum fraction z in proton-proton collisions at $\sqrt{s} = 200$ GeV is shown in Fig. 5.26. The panel (a) and (b) of Fig. 5.26 are for positive and negative jet pseudo-rapidity η_{jet} with respect to the polarized beam, respectively. The average jet p_T, as

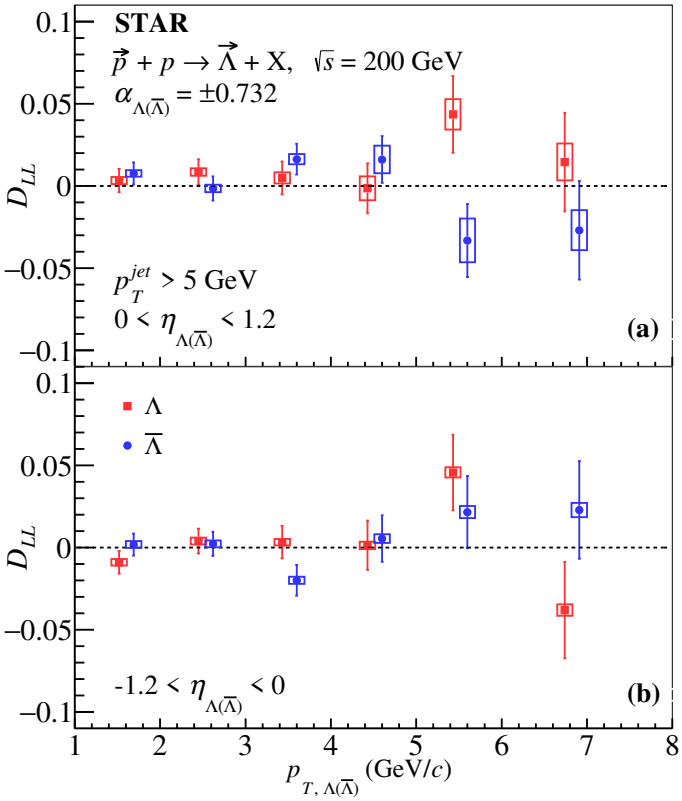

Figure 5.24: Longitudinal spin transfer D_{LL} of Λ and $\overline{\Lambda}$ as a function of hyperon p_T in proton-proton collisions at $\sqrt{s} = 200$ GeV. Panels (a) and (b) show the results for positive and negative η region relative to polarized beam, respectively. The vertical bars indicate the statistical while the systematic uncertainties are shown in boxes. The results for $\overline{\Lambda}$ are slightly offset horizontally for clarity.

	Λ		$\overline{\Lambda}$	
p_T	$0 < \eta_{\Lambda(\bar{\Lambda})} < 1.2$	$-1.2 < \eta_{\Lambda(\bar{\Lambda})} < 0$	$0 < \eta_{\Lambda(\bar{\Lambda})} < 1.2$	$-1.2 < \eta_{\Lambda(\bar{\Lambda})} < 0$
$1-2$	0.0033 ± 0.0070 ± 0.0021	-0.0090 ± 0.0069 ± 0.0020	0.0076 ± 0.0067 ± 0.0020	0.0019 ± 0.0067 ± 0.0020
$2-3$	0.0085 ± 0.0077 ± 0.0022	0.0040 ± 0.0076 ± 0.0020	-0.0015 ± 0.0073 ± 0.0022	0.0023 ± 0.0073 ± 0.0020
$3-4$	0.0049 ± 0.0100 ± 0.0034	0.0033 ± 0.0099 ± 0.0020	0.0163 ± 0.0094 ± 0.0031	-0.0199 ± 0.0093 ± 0.0021
$4-5$	-0.0014 ± 0.0152 ± 0.0072	0.0014 ± 0.0150 ± 0.0023	0.0161 ± 0.0142 ± 0.0084	0.0055 ± 0.0141 ± 0.0026
$5-6$	0.0436 ± 0.0234 ± 0.0092	0.0457 ± 0.0230 ± 0.0031	-0.0332 ± 0.0223 ± 0.0133	0.0216 ± 0.0220 ± 0.0037
$6-8$	0.0146 ± 0.0300 ± 0.0112	-0.0380 ± 0.0293 ± 0.0035	-0.0269 ± 0.0300 ± 0.0121	0.0229 ± 0.0297 ± 0.0043

Table 5.12: Numerical values of D_{LL} vs p_T results for Λ and $\overline{\Lambda}$ in proton-proton collisions at $\sqrt{s} = 200$ GeV. The first terms of these values indicate the central value of D_{LL}. The statistical and systematic uncertainties are shown in the second and third terms, respectively.

shown in the Fig. 5.26 (c) for each z bin is corrected back to particle level using the embedding MC sample mentioned in Sec. 3.3. The numerical values of the measured D_{LL} results are summarized in Tab. 5.13. Theoretical predictions 'KLZ' from Ref. [92] are compared with the measurements. Similar to the predictions from Refs. [84, 93], 3 same

	Λ		$\overline{\Lambda}$	
z	$0 < \eta_{jet}$	$\eta_{jet} < 0$	$0 < \eta_{jet}$	$\eta_{jet} < 0$
$0 - 0.1$	-0.0150 ± 0.0176 ± 0.0020	-0.0238 ± 0.0175 ± 0.0021	-0.0094 ± 0.0195 ± 0.0020	0.0202 ± 0.0195 ± 0.0021
$0.1 - 0.2$	0.0031 ± 0.0081 ± 0.0020	0.0029 ± 0.0081 ± 0.0020	0.0166 ± 0.0083 ± 0.0021	-0.0062 ± 0.0083 ± 0.0020
$0.2 - 0.3$	0.0098 ± 0.0080 ± 0.0020	-0.0016 ± 0.0080 ± 0.0020	0.0152 ± 0.0079 ± 0.0021	-0.0022 ± 0.0079 ± 0.0020
$0.3 - 0.5$	0.0112 ± 0.0075 ± 0.0020	-0.0008 ± 0.0074 ± 0.0020	0.0014 ± 0.0069 ± 0.0020	-0.0021 ± 0.0069 ± 0.0020
$0.5 - 0.7$	0.0083 ± 0.0139 ± 0.0023	-0.0046 ± 0.0138 ± 0.0021	0.0027 ± 0.0113 ± 0.0023	-0.0156 ± 0.0113 ± 0.0021
$0.7 - 1.0$	0.0135 ± 0.0303 ± 0.0041	-0.0321 ± 0.0298 ± 0.0030	0.0100 ± 0.0210 ± 0.0039	0.0232 ± 0.0208 ± 0.0025

Table 5.13: Numerical values of D_{LL} vs z results for Λ and $\overline{\Lambda}$ in proton-proton collisions at $\sqrt{s} = 200$ GeV. The first terms of these values indicate the central value of D_{LL}. The statistical and systematic uncertainties are shown in the second and third terms, respectively.

scenarios of the polarized fragmentation functions [87] are also used. The measured results are consistent with these predictions within uncertainties. The measurements can provide further constraints on polarized fragmentation functions. More data is needed to distinguish between different scenarios.

5.5 Summary

This chapter presented the analysis details on the measurements of longitudinal spin transfer D_{LL} to Λ and $\overline{\Lambda}$ in proton-proton collisions at $\sqrt{s} = 200$ GeV. The statistics used in the measurements are about 2-3 times larger than the STAR previous published results [90] using STAR 2009 data. For the D_{LL} vs hyperon p_T measurements, the new measurements are combined with the previous published results [90] using STAR 2009 data. The combined results are compared with theoretical predictions. The measurements are consistent with the predictions from Ref. [91]. However, the measurements strongly disfavor one prediction from Ref. [84], which is based on an extreme assumption of polarized fragmentation functions that u, d and s quarks have equal contribution to Λ polarization. We also performed first measurements on D_{LL} as a function of jet momentum fraction z carried by Λ hyperons, which can directly probe polarized fragmentation functions [92].

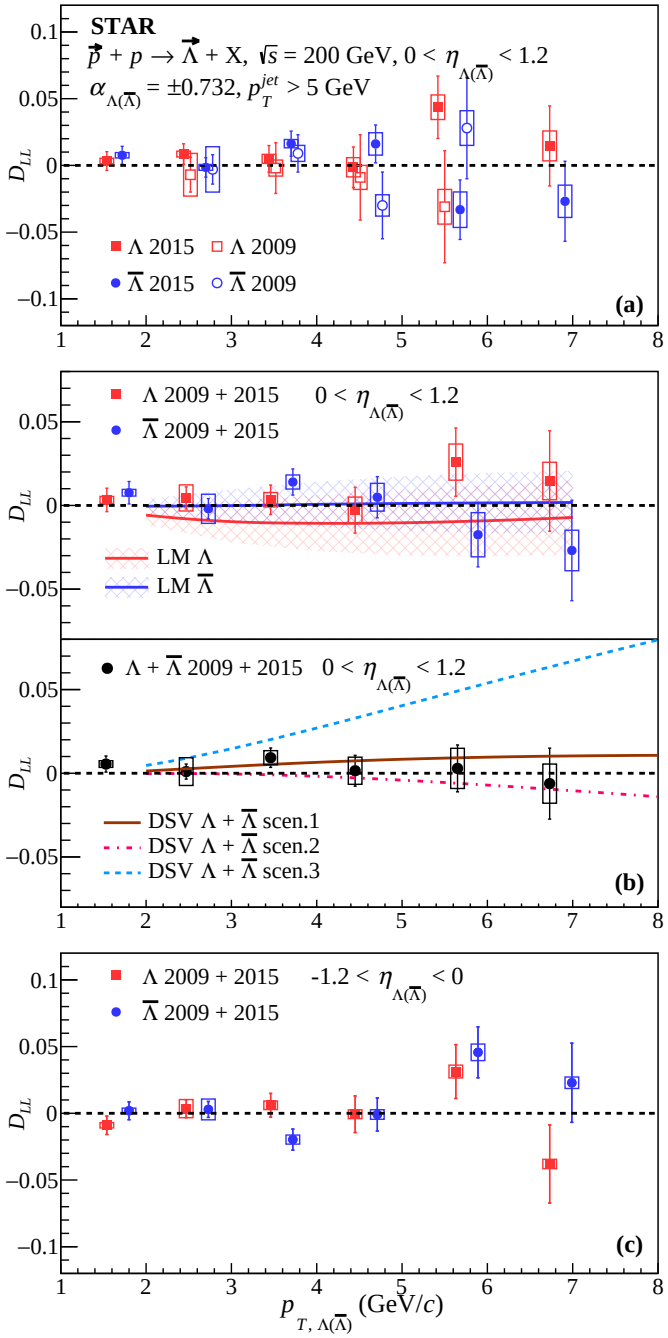

Figure 5.25: (a): Comparison of D_{LL} as a function of the hyperon p_T for positive η with previously published results using STAR 2009 data [90]. Upper sub-panel of (b): combined results of D_{LL} for positive η from this measurements and previous measurements, in comparison with theoretical prediction [91]; Lower sub-panel of (b): comparison of the combined $\Lambda + \overline{\Lambda}$ results with DSV predictions [84]. (c) Combined results of D_{LL} for negative η from this measurements and previous measurements. The previously published results in panel (a) and the results of $\overline{\Lambda}$ in all panels are slightly offset horizontally for clarity.

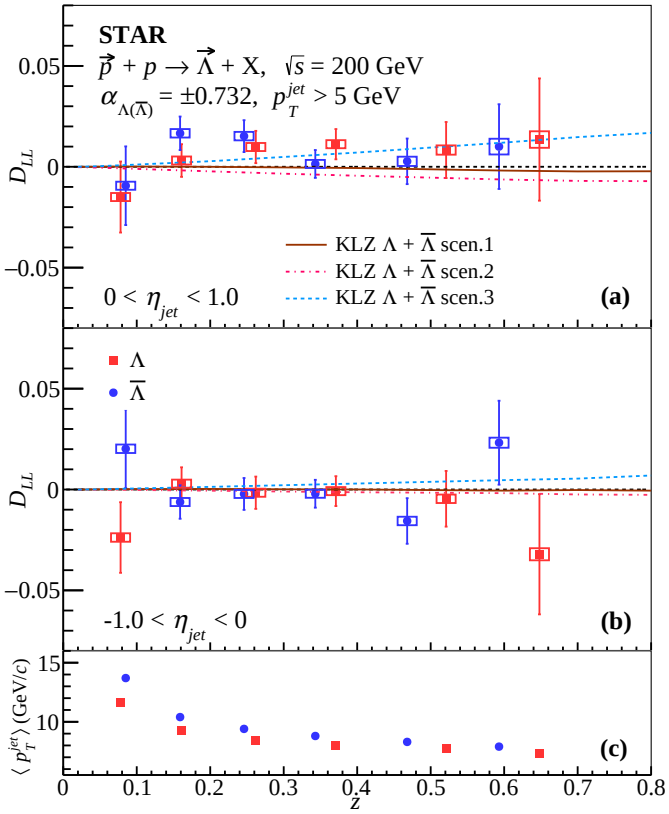

Figure 5.26: Longitudinal spin transfer D_{LL} as a function of the jet momentum fraction z carried by the hyperons in proton-proton collisions at $\sqrt{s} = 200$ GeV. Theoretical calculations [92] are compared with the measurements. Panels (a) and (b) show the results for positive and negative η_{jet} relative to polarized beam, respectively. The average jet p_T at corrected to particle level in each z bins is shown in panel (c). Differences of z values for Λ and $\overline{\Lambda}$ along the horizontal axis denote their average z in that bin, not an artificial offset.

Chapter 6 Summary and Outlook

It has been nearly 100 years since the spin-$\frac{1}{2}$ nature of proton was revealed. The surprising results on the proton g_1 structure function from the EMC Collaboration [9] in 1988 triggered tremendous progress on the understanding of the spin structure of proton, which is still a fundamental and challenging question in Quantum Chromodynamics. The helicity distributions of u quark and d quark have been reasonably constrained well. However, the helicity distributions of strange quark and anti-quark are still poorly constrained experimentally. The Relativistic Heavy Ion Collider (RHIC) is the first and only polarized proton-proton collider around the world, which provides unique opportunities to study proton spin structure. RHIC has confirmed sizable positive gluon polarization inside the proton. However, the JAM Collaboration recently proposed that negative gluon polarization may still be allowed [57]. Largest longitudinally polarized proton-proton collision dataset at $\sqrt{s} = 200$ GeV was taken at STAR in 2015 corresponding to an integrated luminosity of about 52 pb^{-1}. With this dataset, we performed 3 measurements aiming at understanding the helicity distributions of gluon, strange quark and anti-quark.

1. Longitudinal Double Spin Asymmetry A_{LL} of $\pi^{\pm}$-tagged Jets

The first measurements of longitudinal double spin asymmetry A_{LL} for $\pi^{\pm}$-tagged jets in proton-proton collisions at $\sqrt{s} = 200$ GeV are expected to be sensitive to the sign of the gluon helicity distributions. The measured A_{LL} results of π^+-tagged jets increase with increasing jet p_T, and the A_{LL} results of π^--tagged jets do not show clear jet p_T dependence. The measured A_{LL} results of π^+-tagged jets is larger than the results of π^--tagged jets. Predictions with MC samples generated by PYTHIA are compared with the measurements. In the predictions, the helicity distributions from the NNPDFpol1.1 [39] (positive gluon helicity distribution) and JAM22 [57] (negative helicity distribution) are used. Our measurements are consistent with predictions from NNPDFpol1.1 [39]. However, the results strongly disfavor the predictions from JAM22 [57]. Therefore, our measurements prefer positive gluon helicity.

2. Longitudinal Double Spin Asymmetry A_{LL} of Λ, $\overline{\Lambda}$ and K^0_S

In this thesis, we report the first measurements of longitudinal double spin asym-

metry A_{LL} of Λ, $\overline{\Lambda}$ and K^0_S in proton-proton collisions at $\sqrt{s} = 200$ GeV. The A_{LL} is expected to be sensitive to the helicity distributions of strange quark and anti-quark, which are still poorly constrained by experimental data. We measured the A_{LL} as a function of Λ hyperon and K^0_S p_T and jet p_T. Predictions from MC samples generated with PYTHIA [128] using helicity distribution from the NNPDFpol1.1 [39] are compared with the measurements. Our measurements are consistent with the predictions within uncertainties. The small A_{LL} results might indicate small helicity distributions of strange quark and anti-quark. The measurements will provide further constraints on helicity distributions of strange quark and anti-quark when included into global analysis.

3. Longitudinal Spin Transfer D_{LL} of Λ and $\overline{\Lambda}$

In polarized proton-proton collisions, longitudinal spin transfer D_{LL} to Λ and $\overline{\Lambda}$ are not only sensitive to the helicity distributions of strange quark and anti-quark but also can shed light on polarized fragmentation functions. Using the proton-proton collision data taken at STAR in 2015, we performed more precise measurements on D_{LL} as a function of hyperon p_T. The statistics are about 2-3 times larger than the dataset taken in 2009 used in the previous measurements [90]. Two years' measurements are consistent with each other. The two-year combined results are compared with model calculations. The results are consistent with the prediction from Ref. [91]. In the predictions from Ref. [84], 3 scenarios of polarized fragmentation functions [87] are considered. However, our measurements strongly disfavor the prediction based on scenario 3, in which u, d and s quarks have equal contributions to the Λ hyperon polarization. We also performed the first measurements of D_{LL} as a function of jet momentum fraction carried by Λ hyperons, which can directly probe polarized fragmentation functions. The measurements are compared with model predictions [92], and are consistent with the predictions within uncertainties.

Much larger longitudinally polarized proton-proton collision dataset of $\sqrt{s} = 500/510$ GeV taken at STAR ($\sim$382 pb^{-1}) will allow more precise measurements of A_{LL} and D_{LL} with the extension to lower x region. The future frontiers in studying the nucleon spin structure are the Electron Ion Collider (EIC) [139] in US and the Electron Ion Collider in China (EicC) [140]. For the gluon helicity distribution, our current knowledge only covers x of about $0.02 < x < 0.4$. One of the important goals for EIC is to measure the gluon helicity at much smaller x region ($x \sim 10^{-4}$) with much higher

precision. On the other hand, the kinematic coverage of EicC is mainly located at sea-quark region, which will provide precise measurements on the spin structure of the nucleon for sea quarks including the asymmetry between helicity distributions of $\bar{u}$ and $\bar{d}$ quarks and the contribution of the strange quark and anti-quark to the proton spin. The EIC and EicC cover complementary kinematic regions and will greatly advance our knowledge on nucleon spin structure in the future.

Reference

[1] E. Rutherford. Collision of α particles with light atoms. IV. An anomalous effect in nitrogen. *Phil. Mag. Ser. 6*, **37**(sup1):581, 1919.

[2] D. M. Dennison. A note on the specific heat of the hydrogen molecule. *Proc. R. Soc. Lond. A*, **115**:483, 1927.

[3] R. Frisch and O. Stern. Über die magnetische ablenkung von wasserstoffmolekülen und das magnetische moment des protons. I. *Zeitschrift für Physik*, **85**(1):4, 1933.

[4] I. Estermann, R. Frisch, and O. Stern. Magnetic moment of the proton. *Nature*, **132**(3326):169, 1933.

[5] P. Dirac. The quantum theory of the electron. *Proc. R. Soc. London A.*, **117**(778):610, 1928.

[6] M. Gell-Mann. A schematic model of baryons and mesons. *Phys. Lett.*, **8**(3):214, 1964.

[7] G. Zweig. An SU_3 model for strong interaction symmetry and its breaking; version 1. *CERN-TH-401*, 1964.

[8] G. Zweig. An SU_3 model for strong interaction symmetry and its breaking; version 2. *CERN-TH-412*, 1964.

[9] J. Ashman et al. [European Muon Collaboration], A measurement of the spin asymmetry and determination of the structure function g_1 in deep inelastic muon-proton scattering. *Phys. Lett. B*, **206**(2):364, 1988.

[10] J. Ashman et al. [European Muon Collaboration], An investigation of the spin structure of the proton in deep inelastic scattering of polarised muons on polarised protons. *Nucl. Phys. B*, **328**(1):1, December 1989.

[11] F. Halzen and A. D. Martin. *Quarks and Leptons: An Introductory Course In Modern Particle Physics.* John Wiley & Sons, 1984.

[12] R. G. Roberts. *The structure of the proton: deep inelastic scattering.* Cambridge monographs on mathematical physics. Cambridge University Press, 1990.

[13] R. K. Ellis, W. J Stirling, and B. R. Webber. *QCD and collider physics.* Cambridge University Press, 2003.

[14] M. Thomson. *Modern Particle Physics.* Cambridge University Press, 2013.

[15] Y. K. Song, J. Zhou, and Z. T. Liang. What is the structure and spin decomposition of the proton? *Chin. Sci. Bull.*, **63**(24):2546, 2018.

[16] R. P. Feynman. Very high-energy collisions of hadrons. *Phys. Rev. Lett.*, **23**(24):1415, 1969.

[17] J. D. Bjorken and E. A. Paschos. Inelastic electron-proton and γ-proton scattering and the structure of the nucleon. *Phys. Rev.*, **185**(5):1975, 1969.

[18] S. Bailey et al. Parton distributions from LHC, HERA, Tevatron and fixed target data: MSHT20 PDFs. *Eur. Phys. J. C*, **81**(4):341, 2021.

[19] R. L. Workman et al. (Particle Data Group), Review of particle physics. *Prog. Theor. Exp. Phys.*, **2022**(8):83C01, 2022.

[20] S. D. Bass. *The spin structure of the proton*. World Scientific, Singapore ; Hackensack, NJ, 2008.

[21] M. J. Alguard et al. Deep inelastic scattering of polarized electrons by polarized protons. *Phys. Rev. Lett.*, **37**(19):1261, 1976.

[22] M. J. Alguard et al. Deep-inelastic *e-p* asymmetry measurements and comparison with the Bjorken sum rule and models of proton spin structure. *Phys. Rev. Lett.*, **41**(2):70, 1978.

[23] G. Baum et al. Measurement of asymmetry in spin-dependent *e-p* resonance-region scattering. *Phys. Rev. Lett.*, **45**(25):2000, 1980.

[24] G. Baum et al. New measurement of deep-inelastic *e-p* asymmetries. *Phys. Rev. Lett.*, **51**(13):1135, 1983.

[25] K. Abe et al. [E143 Collaboration], Measurements of the proton and deuteron spin structure functions g_1 and g_2. *Phys. Rev. D*, **58**(11):112003, 1998. Publisher: American Physical Society.

[26] B. Adeva et al. [Spin Muon Collaboration], Spin asymmetries a_1 and structure functions g_1 of the proton and the deuteron from polarized high energy muon scattering. *Phys. Rev. D*, **58**(11):112001, 1998.

[27] P. L Anthony et al. [E155 Collaboration], Measurements of the Q^2-dependence of the proton and neutron spin structure functions g_1^p and g_1^n. *Phys. Lett. B*, **493**(1):19, 2000.

[28] K. V. Dharmawardane et al. [CLAS Collaboration], Measurement of the x- and Q^2-dependence of the asymmetry A_1 on the nucleon. *Phys. Lett. B*, **641**(1):11, 2006.

[29] A. Airapetian et al. [HERMES Collaboration], Precise determination of the spin structure function g_1 of the proton, deuteron, and neutron. *Phys. Rev. D*, **75**(1):12007, 2007.

[30] M. G. Alekseev et al. [COMPASS Collaboration], The spin-dependent structure function of the proton g_1^p and a test of the Bjorken sum rule. *Phys. Lett. B*, **690**(5):466, 2010.

[31] C. Adolph et al. [COMPASS Collaboration], The spin structure function g_1^p of the proton and a test of the Bjorken sum rule. *Phys. Lett. B*, **753**:18, 2016.

[32] P. A. Zyla et al. (Particle Data Group), Review of particle physics. *Prog. Theor. Exp. Phys.*, **2020**(8):083C01, 2020.

[33] C. A. Aidala et al. The spin structure of the nucleon. *Rev. Mod. Phys.*, **85**(2):655, 2013.

[34] B. Adeva et al. [Spin Muon Collaboration], Polarised quark distributions in the nucleon from semi-inclusive spin asymmetries. *Phys. Lett. B*, **420**(1):180, 1998.

[35] B. W. Filippone and X. Ji. The spin structure of the nucleon, 2001. arXiv:hep-ph/0101224.

[36] S. D. Bass. The spin structure of the proton. *Rev. Mod. Phys.*, **77**(4):46, 2005.

[37] W. C. Chang and J. C. Peng. Flavor structure of the nucleon sea. *Prog Particle Nucl Phys*, **79**:95, 2014.

[38] A. Deur, S. J. Brodsky, and G. F. De Téramond. The spin structure of the nucleon. *Rep. Prog. Phys.*, **82**(7):076201, 2019.

[39] E. R. Nocera et al. [NNPDF Collaboration], A first unbiased global determination of polarized PDFs and their uncertainties. *Nucl. Phys. B*, **887**:276, 2014.

[40] D. de Florian et al. Global analysis of helicity parton densities and their uncertainties. *Phys. Rev. Lett.*, **101**(7):72001, 2008.

[41] G. Bunce et al. Prospects for spin physics at RHIC. *Annu. Rev. Nucl. Part. Sci.*, **50**(1):525, 2000.

[42] J. Pumplin et al. New generation of parton distributions with uncertainties from global QCD analysis. *J. High Energy Phys.*, **2002**(7):12, 2002.

[43] A. Mukherjee and W. Vogelsang. Jet production in (un)polarized *pp* collisions: Dependence on jet algorithm. *Phys. Rev. D*, **86**(9):094009, 2012.

[44] J. Adam et al. [STAR Collaboration], Longitudinal double-spin asymmetry for inclusive jet and dijet production in *pp* collisions at $\sqrt{s} = 510$ GeV. *Phys. Rev. D*, **100**(5):052005, 2019.

[45] E. Leader. *Spin in Particle Physics*. Cambridge University Press, 1 edition, 2001.

[46] B. I. Abelev et al. [STAR Collaboration], Longitudinal double-spin asymmetry and cross section for inclusive jet production in polarized proton collisions at $\sqrt{s} = 200$ GeV. *Phys. Rev. Lett.*, **97**(25):252001, 2006.

[47] B. I. Abelev et al. [STAR Collaboration], Longitudinal double-spin asymmetry for inclusive jet production in $\overrightarrow{p} + \overrightarrow{p}$ collisions at $\sqrt{s} = 200$ GeV. *Phys. Rev. Lett.*, **100**(23):232003, 2008.

[48] L. Adamczyk et al. [STAR Collaboration], Longitudinal and transverse spin asymmetries for inclusive jet production at mid-rapidity in polarized p+p collisions at $\sqrt{s} = 200$ GeV. *Phys. Rev. D*, **86**:032006, 2012.

[49] L. Adamczyk et al. [STAR Collaboration], Precision measurement of the longitudinal double-spin asymmetry for inclusive jet production in polarized proton collisions at $\sqrt{s} = 200$ GeV. *Phys. Rev. Lett.*, **115**(9):092002, 2015.

[50] D. de Florian et al. Evidence for polarization of gluons in the proton. *Phys. Rev. Lett.*, **113**(1):012001, 2014.

[51] L. Adamczyk et al. [STAR Collaboration], Measurement of the cross section and longitudinal double-spin asymmetry for dijet production in polarized *pp* collisions at $\sqrt{s} = 200$ GeV. *Phys. Rev. D*, **95**(7):71103, 2017.

[52] J. Adam et al. [STAR Collaboration], Longitudinal double-spin asymmetries for dijet production at intermediate pseudorapidity in polarized *pp* collisions at $\sqrt{s} = 200$ GeV. *Phys. Rev. D*, **98**(3):032011, 2018.

[53] M. S. Abdallah et al. [STAR Collaboration], Longitudinal double-spin asymmetry for inclusive jet and dijet production in polarized proton collisions at $\sqrt{s} = 200$ GeV. *Phys. Rev. D*, **103**(9):L091103, 2021.

[54] M. S. Abdallah et al. [STAR Collaboration], Longitudinal double-spin asymmetry for inclusive jet and dijet production in polarized proton collisions at $\sqrt{s} = 510$ GeV. *Phys. Rev. D*, **105**(9):092011, 2022.

[55] Z. Chang and T. Lin. Precision measurement of the longitudinal double-spin asymmetry for dijet production at intermediate pseudorapidity in polarized proton+proton collisions at $\sqrt{s} = 200$ GeV, 2023. arXiv:2306.11306.

[56] E. C. Aschenauer et al. The RHIC cold QCD program, 2023. arXiv:2302.00605.

[57] Y. Zhou, N. Sato, and W. Melnitchouk. [JAM Collaboration], How well do we know the gluon polarization in the proton? *Phys. Rev. D*, **105**(7):074022, 2022.

[58] N. J. Abdulameer et al. [PHENIX Collaboration], Measurement of direct-photon cross section and double-helicity asymmetry at $\sqrt{s} = 510$ GeV in $\overrightarrow{p} + \overrightarrow{p}$ collisions. *Phys. Rev. Lett.*, **130**(25):251901, 2023.

[59] A. Adare et al. [PHENIX Collaboration], Charged-pion cross sections and double-helicity asymmetries in polarized $p + p$ collisions at $\sqrt{s} = 200$ GeV. *Phys. Rev. D*, **91**(3):032001, 2015.

[60] U. Acharya et al. [PHENIX Collaboration], Measurement of charged pion double spin asymmetries at midrapidity in longitudinally polarized $p+p$ collisions at$\sqrt{s} = 510$ GeV. *Phys. Rev. D*, **102**(3):32001, 2020.

[61] R. M. Whitehill et al. [JAM Collaboration], Accessing gluon polarization with high-p_T hadrons in SIDIS. *Phys. Rev. D*, **107**(3):034033, 2023.

[62] J. L. Zhang. *Measurement of Longitudinal Single-Spin Asymmetry of $W^{\pm}$ Bosons Production at RHIC-STAR*. PhD thesis, Shandong University, 2016.

[63] Q. H. Xu and Z. T. Liang. Nucleon spin structure and measurements on sea quark polarization at RHIC. *Sci. Sin.-Phys. Mech. Astron.*, **49**(10):102007, 2019.

[64] M. M. Aggarwal et al. [STAR Collaboration], Measurement of the parity-violating longitudinal single-spin asymmetry for $W^{\pm}$ boson production in polarized proton-proton collisions at $\sqrt{s} = 500$ GeV. *Phys. Rev. Lett.*, **106**(6):62002, 2011.

[65] A. Adare et al. [PHENIX Collaboration], Cross section and parity-violating spin asymmetries of $W^{\pm}$ boson production in polarized $p+p$ collisions at $\sqrt{s} = 500$ GeV. *Phys. Rev. Lett.*, **106**(6):62001, 2011.

[66] L. Adamczyk et al. [STAR Collaboration], Measurement of longitudinal spin asymmetries for weak boson production in polarized proton-proton collisions at RHIC. *Phys. Rev. Lett.*, **113**(7):72301, 2014.

[67] A. Adare et al. [PHENIX Collaboration], Measurement of parity-violating spin asymmetries in $W^{\pm}$ production at midrapidity in longitudinally polarized $p+p$ collisions. *Phys. Rev. D*, **93**(5):51103, 2016.

[68] A. Adare et al. [PHENIX Collaboration], Cross section and longitudinal single-spin asymmetry A_L for forward $W^{\pm} \to \mu^{\pm}\nu$ production in polarized $p+p$ collisions at $\sqrt{s} = 500$ GeV. *Phys. Rev. D*, **98**(3):32007, 2018.

[69] J. Adam et al. [STAR Collaboration], Measurement of the longitudinal spin asymmetries for weak boson production in proton-proton collisions at $\sqrt{s} = 500$ GeV. *Phys. Rev. D*, **99**(5):51102, 2019.

[70] T. D. Lee and C. N. Yang. General partial wave analysis of the decay of a hyperon of spin $\frac{1}{2}$. *Phys. Rev.*, **108**(6):1645, 1957.

[71] F. S. Crawford et al. Detection of parity nonconservation in Λ decay. *Phys. Rev.*, **108**(4):1102, 1957.

[72] J. W. Cronin and O. E. Overseth. Measurement of the decay parameters of the Λ^0 particle. *Phys. Rev.*, **129**(4):1795, 1963.

[73] G. Bunce et al. Λ^0 hyperon polarization in inclusive production by 300-GeV protons on beryllium. *Phys. Rev. Lett.*, **36**:1113, 1976.

[74] X. Artru and M. Mekhfi. What can we learn from unpolarized and polarized electroproduction of fast baryons? *Nucl. Phys. A*, **532**:351, 1991.

[75] W. Lu and B. Q. Ma. The strange quark spin of the proton in semi-inclusive Λ leptoproduction. *Phys. Lett. B*, **357**:419, 1995.

[76] J. Ellis, D. Kharzeev, and A. Kotzinian. The proton spin puzzle and Λ polarization in deep-inelastic scattering. *Z. Phys. C*, **69**(3):467, 1996.

[77] R. L. Jaffe. Polarized Λ's in the current fragmentation region. *Phys. Rev. D*, **54**(11):R6581, 1996.

[78] B. Q. Ma et al. Λ, $\overline{\Lambda}$ polarization and spin transfer in lepton deep inelastic scattering. *Eur. Phys. J. C*, **16**:657, 2000.

[79] J. Ellis, A. Kotzinian, and D. V. Naumov. Intrinsic polarized strangeness and Λ^0 polarization in deep inelastic production. *Eur. Phys. J. C*, **25**:603, 2002.

[80] S. S. Zhou et al. Longitudinal polarization of hyperon and anti-hyperon in semi-inclusive deep-inelastic scattering. *Phys. Rev. D*, **79**:094018, 2009.

[81] Q. H. Xu, C. X. Liu, and Z. T. Liang. Longitudinal polarization of hyperons in high $p_\perp$ jets in singly polarized *pp* collisions at high energies. *Phys. Rev. D*, **65**(11):114008, 2002.

[82] Q. H. Xu and Z. T. Liang. Probing gluon helicity distribution and quark transversity through hyperon polarization in singly polarized pp collisions. *Phys. Rev. D*, **70**(3):034015, 2004.

[83] Q. H. Xu, Z. T. Liang, and E. Sichtermann. Anti-Lambda polarization in high energy pp collisions with polarized beams. *Phys. Rev. D*, **73**(7):077503, 2006.

[84] D. de Florian, M. Stratmann, and W. Vogelsang. Polarized Λ-baryon production in *pp* collisions. *Phys. Rev. Lett.*, **81**(3):530, 1998.

[85] C. Boros, J. T. Londergan, and A. W. Thomas. Spin and flavor dependent structure and production of Lambda baryons. *Nucl. Phys. A*, **680**(1):66, 2001.

[86] B. Q. Ma et al. Spin transfers for baryon production in polarized *pp* collisions at RHIC-BNL. *Nucl. Phys. A*, **703**(1-2):346, 2002.

[87] D. de Florian, M. Stratmann, and W. Vogelsang. QCD analysis of unpolarized and polarized Λ-baryon production in leading and next-to-leading order. *Phys. Rev. D*, **57**(9):5811, 1998.

[88] M. Glück et al. Models for the polarized parton distributions of the nucleon. *Phys. Rev. D*, **63**(9):94005, 2001.

[89] B. I. Abelev et al. [STAR Collaboration], Longitudinal spin transfer to Λ and $\overline{\Lambda}$ hyperons in polarized proton-proton collisions at $\sqrt{s} = 200$ GeV. *Phys. Rev. D*, **80**(11):111102, 2009.

[90] J. Adam et al. [STAR Collaboration], Improved measurement of the longitudinal spin transfer to Λ and $\overline{\Lambda}$ hyperons in polarized proton-proton collisions at $\sqrt{s} = 200$ GeV. *Phys. Rev. D*, **98**(11):112009, 2018.

[91] X. Liu and B. Q. Ma. Nucleon strangeness polarization from $\Lambda/\overline{\Lambda}$ hyperon production in polarized proton–proton collision at RHIC. *Eur, Phys, J. C*, **79**:409, 2019.

[92] Z. B. Kang, K. Lee, and F. Y. Zhao. Polarized jet fragmentation functions. *Phys. Lett. B*, **809**:135756, 2020.

[93] W. Vogelsang. (priviate communication).

[94] L. C. Bland. Transverse single spin asymmetries in hadronic interactions: an experimental overview and outlook. *EPJ Web Conf.*, **85**:1008, 2015.

[95] A. N. Zelenski et al. Optically pumped polarized H^- ion sources for RHIC and HERA colliders. *Hyperfine Interactions*, **127**(1):475, 2000.

[96] L. H. Thomas. The kinematics of an electron with an axis. *Philos. Mag*, **3**(13):1, 1927.

[97] V. Bargmann, L. Michel, and V. L. Telegdi. Precession of the polarization of particles moving in a homogeneous electromagnetic field. *Phys. Rev. Lett.*, **2**(10):435, 1959.

[98] Ya. S. Derbenev et al. Radiative polarization: Obtaining, control, using. *Part. Accel.*, **8**:115, 1978.

[99] T. Roser. Configuration manual polarized proton collider at RHIC. Technical Report BNL-97226-2012-TECH, Brookhaven National Laboratory, 2006.

[100] I. Nakagawa et al. Polarization measurements of RHIC-pp RUN05 using CNI pC-polarimeter. *AIP Conf. Proc.*, **915**(1):912, 2007.

[101] H. Okada et al. Measurement of the analyzing power A_N in pp elastic scattering in the CNI region with a polarized atomic hydrogen gas jet target, 2005. arXiv:hep-ex/0601001.

[102] M. Anderson et al. The STAR time projection chamber: a unique tool for studying high multiplicity events at RHIC. *Nucl. Instrum. Methods Phys. Res., Sect. A*, **499**(2-3):659, 2003.

[103] F. Bergsma et al. The STAR detector magnet subsystem. *Nucl. Instrum. Methods Phys. Res., Sect. A*, **499**(2):633, 2003.

[104] The STAR Collaboration. A proposal for STAR inner TPC sector upgrade (iTPC). (STAR Note SN0619), 2015.

[105] F. Shen et al. MWPC prototyping and performance test for the STAR inner TPC upgrade. *Nucl. Instrum. Methods Phys. Res., Sect. A*, **896**:90, 2018.

[106] L. Kotchenda et al. STAR TPC gas system. *Nucl. Instrum. Methods Phys. Res., Sect. A*, **499**(2):703, 2003.

[107] M. Beddo et al. The STAR barrel electromagnetic calorimeter. *Nucl. Instrum. Methods Phys. Res., Sect. A*, **499**(2-3):725, 2003.

[108] C. E. Allgower et al. The STAR endcap electromagnetic calorimeter. *Nucl. Instrum. Methods Phys. Res., Sect. A*, **499**(2-3):740, 2003.

[109] W. J. Llope. The STAR vertex position detector. *Nucl. Instrum. Methods Phys. Res., Sect. A*, **759**:23, 2014.

[110] C. Adler et al. The RHIC zero degree calorimeters. *Nucl. Instrum. Methods Phys. Res., Sect. A*, **470**:488, 2001.

[111] P. Fachini et al. Proposal for a large area time of flight system for STAR, 2004.

[112] E. Cerron Zeballos et al. A comparison of the wide gap and narrow gap resistive plate chamber. *Nucl. Instrum. Methods Phys. Res., Sect. A*, 373(1):35, 1996.

[113] M. Zurek. Longitudinal double-spin asymmetry of inclusive jet production at $\sqrt{s} = 200$ GeV at STAR. (STAR Note PSN0756), 2020.

[114] F. S. Bieser et al. The STAR trigger. *Nucl. Instrum. Methods Phys. Res., Sect. A*, **499**(2):766, March 2003.

[115] E. G. Judd et al. The evolution of the STAR trigger system. *Nucl. Instrum. Methods Phys. Res., Sect. A*, **902**:228, 2018.

[116] R. Reed et al. Vertex finding in pile-up rich events for p+p and d+Au collisions at STAR. *J. Phys. Conf. Ser.*, **219**(3):32020, 2010.

[117] RHIC Spin Group. Run 15 polarization. `https://wiki.bnl.gov/rhicspin/Run_15_polarization`. 2024.

[118] The Polarimetry Group. RHIC polarization for runs 9-15. 2016.

[119] J. Kiryluk. Local polarimetry for proton beams with the star beam beam counters. In *Spin 2004*, page 718. WORLD SCIENTIFIC, 2005.

[120] J. Hays-Wehle et al. Relative luminosity analysis for run9 pp 200 GeV running. 2012.

[121] M. S. Abdallah et al. [STAR Collaboration], Azimuthal transverse single-spin asymmetries of inclusive jets and identified hadrons within jets from polarized *pp* collisions at $\sqrt{s} = 200$ GeV. *Phys. Rev. D*, **106**(7):072010, 2022.

[122] M. Cacciari, G. P. Salam, and G. Soyez. The anti-k_t jet clustering algorithm. *J. High Energy Phys*, **2008**(04):063, 2008.

[123] B. Abelev et al. [ALICE Collaboration], Charged jet cross sections and properties in proton-proton collisions at $\sqrt{s} = 7$ TeV. *Phys. Rev. D*, **91**(11):112012, 2015.

[124] H. Bichsel. A method to improve tracking and particle identification in TPCs and silicon detectors. *Nucl. Instrum. Methods Phys. Res., Sect. A*, **562**(1):154, 2006.

[125] Y. C. Xu et al. Improving the dE/dx calibration of the STAR TPC for the high-p_T hadron identification. *Nucl. Instrum. Methods Phys. Res., Sect. A*, **614**(1):28, 2010.

[126] M. Shao et al. Extensive particle identification with TPC and TOF at the STAR experiment. *Nucl. Instrum. Methods Phys. Res., Sect. A*, **558**(2):419, 2006.

[127] T. Lin and C. Gagliardi. Azimuthal transverse single-spin asymmetries of inclusive jets and identified hadrons within jets from polarized *pp* collisions. (STAR Note PSN0782), 2022.

[128] T. Sjöstrand, S. Mrenna, and P. Skands. PYTHIA 6.4 physics and manual. *J. High Energy Phys.*, **2006**(05):026, 2006.

[129] R. Brun et al. *GEANT 3: user's guide Geant 3.10, Geant 3.11.* CERN, rev. version edition, 1987.

[130] P. Z. Skands. Tuning monte carlo generators: The perugia tunes. *Phys. Rev. D*, **82**(7):074018, 2010.

[131] J. Adams et al. [STAR Collaboration], Identified hadron spectra at large transverse momentum in $p+p$ and $d+Au$ collisions at $\sqrt{s_{NN}} = 200$ GeV. *Phys. Lett. B*, **637**(3):161, 2006.

[132] G. Agakishiev et al. [STAR Collaboration], Identified hadron compositions in $p+p$ and $Au+Au$ collisions at high transverse momenta at $\sqrt{s_{NN}} = 200$ GeV. *Phys. Rev. Lett.*, **108**(7):72302, 2012.

[133] Z. L. Chang. *Inclusive jet longitudinal double-spin asymmetry A_{LL} measurements in 510 GeV polarized pp collisions at STAR.* PhD thesis, Texas A&M University, 2016.

[134] R. D. Ball et al. [NNPDF Collaboration], Parton distributions with LHC data. *Nucl. Phys. B*, **867**(2):244, 2013.

[135] S. Dulat et al. New parton distribution functions from a global analysis of quantum chromodynamics. *Phys. Rev. D*, **93**(3):33006, 2016.

[136] J. Adam et al. [STAR Collaboration], Transverse spin transfer to Λ and $\overline{\Lambda}$ hyperons in polarized proton-proton collisions at $\sqrt{s} = 200$ GeV. *Phys. Rev. D*, **98**(9):091103, 2018.

[137] J. C. Mei. *Measurement of transverse spin transfer to Λ and $\overline{\Lambda}$ in transversely polarized proton-proton collisions at RHIC-STAR.* PhD thesis, Shandong University, 2018.

[138] Q. H. Xu. *Spin effect in fragmentation processes in high energy reactions.* PhD thesis, Shandong University, 2003.

[139] A. Accardi et al. Electron-ion collider: the next QCD frontier. *Eur. Phys. J. A*, **52**(9):268, 2016.

[140] D. P. Anderle et al. Electron-ion collider in China. *Front. Phys.*, **16**(6):64701, 2021.

论文发表与学术报告

发表的论文 (作为主要作者之一)

1. M. I. Abdulhamid et al.,[STAR Collaboration], Longitudinal and Transverse Spin Transfer to Λ and $\overline{\Lambda}$ Hyperons in Polarized $p+p$ Collisions at $\sqrt{s} = 200$ GeV, Phys. Rev. D **109**, 012004 (2024).

会议论文

1. Y. Yu, Measurement of Longitudinal Spin Transfer of the $\Lambda(\overline{\Lambda})$ Hyperon in Polarized $p+p$ Collisions at $\sqrt{s} = 200$ GeV at RHIC-STAR, JPS Conf. Proc. 37, 020303 (2022)

2. Y. Yu, Longitudinal spin transfer of the Λ ($\overline{\Lambda}$) hyperon in the polarized p+p collisions at $\sqrt{s} = 200$ GeV at RHIC-STAR, Zenodo, (2022) DOI:10.5281/zenodo.7236723

学术报告

1. Probing gluon and strange quark helicity distribution in the proton at STAR, 31th International Workshop on Deep Inelastic Scattering and Related Subjects (DIS2024).

2. Longitudinal double spin asymmetry of Λ, $\bar{\Lambda}$, K^0_S and inclusive jets with high-z $\pi^{\pm}$ tagging in polarized proton-proton collisions at $\sqrt{s} = 200$ GeV at STAR, 25th International Spin Symposium (SPIN 2023).

3. Measurement of longitudinal spin transfer of Λ ($\overline{\Lambda}$) hyperon in polarized p+p collisions at $\sqrt{s} = 200$ GeV at RHIC-STAR, 29th International Workshops on Deep-Inelastic Scattering (DIS) and Related Subjects (DIS2022).

4. Measurement of longitudinal spin transfer of the Λ ($\overline{\Lambda}$) hyperon in longitudinally polarized collisions at $\sqrt{s} = 200$ GeV at RHIC-STAR, 24th International Spin Symposium (SPIN2021).

5. Longitudinal and Transverse Spin Transfer of Λ and $\overline{\Lambda}$ Hyperons in Polarized p+p Collisions at $\sqrt{s} = 200$ GeV at RHIC-STAR, 14th Workshops on QCD Phase Transition and Relativistic Heavy-ion Physics (QPT2021).

致　谢

回顾这六年来求学与科研的历程，点滴之间，凝聚着诸多师长、同学以及亲友的关怀与支持。在此，我谨向所有在我求学道路上给予帮助和支持的师长、同学以及家人致以最诚挚的谢意。

首先，我要衷心感谢我的导师徐庆华教授。感谢徐老师将我引入科研，耐心地教导我，不仅在学术上给予了我巨大的指导和帮助，更在我迷茫与困惑时为我指引方向。徐老师学识渊博、治学态度严谨，不管是在科研上还是在生活上都给予了我巨大的支持和悉心的指导。感谢您为我提供的良好的学习平台、参加学术会议等。同时，在本论文的写作及修改过程中，您都花费了大量的精力。正是您的付出使得我能够顺利完成论文。

感谢徐老师自旋课题组的老师和同学们。感谢和你们的每一次讨论，感谢你们中肯的建议和指导。他们是张金龙老师、林挺老师、熊伟志老师、朱展文博士、苟兴瑞博士、纪赵惠子博士、许一可、高涛亚、张宜新、付瞳、王超、何金浩、刘晓慧。感谢 STAR cold QCD/spin 组的各位成员们，感谢你们在我每次汇报上提出的问题和建议。

同时，我要感谢山大 STAR 组的老师们，包括陈震宇老师、聂茂武老师、杨驰老师、杨钱老师、易立老师以及山大自旋组的各位老师们。感谢你们在科研和生活中的指导和支持，这对我而言是莫大的帮助。感谢聂茂武和杨钱两位老师辛苦组织的每周的学生讨论会，感谢在会上给大家作报告的各位同学和老师们，感谢参加讨论会的各位同学们，感谢讨论会上的各种好吃的。通过这个讨论会，我学到了很多知识。

我还要感谢山大的同学们。在求学过程中，同学们给予了我许多支持和鼓励。大家一起讨论问题、分享经验，共同面对科研中的挑战和困难。你们的帮助和支持，使我在科研的道路上不再感到孤单。他们是李长丰博士、陈佳博士、王桢博士、孔凡刚、闫高国、史迎迎、何杨、孙川、张晴、王晓凤、王永红、沈丹丹、汪杰克、包贤文、李辰艳、王玉林、张迪、张思婕以及山大自旋课题组的各位同学们。感谢我在 BNL 值班期间遇到的人以及同去的山大的同学们。感谢大厨们做的美味食物，把 'How to Survive' 变成 'How to Lose Weight'。这会是一段特别的记忆。

最后，我要特别感谢我的父母。感谢他们一直以来对我的理解和支持。他们的无私奉献和无尽的爱，是我坚持不懈、追求梦想的源泉。父母的关心和鼓励，给了我无穷的力量，使我能够在科研的道路上不断前行。没有他们的陪伴和支持，我无法走到

今天。感谢父母在我成长过程中给予的爱与教诲，感谢他们在我求学路上默默付出的一切。你们的支持和鼓励，将永远铭记在我的心中。

在此，我再次向所有在我求学和科研过程中给予帮助和支持的师长、同学以及家人致以最诚挚的谢意。你们的关心和付出，是我前进道路上最宝贵的财富和力量。希望在未来的日子里，我能以更加优异的成绩和更加坚定的信念，回报你们的关爱与支持。

学位论文评阅及答辩情况表

论文评阅人	姓　名	专业技术职　务	是否博导（硕导）	所 在 单 位	总体评价
	匿名评阅				**良好**
	匿名评阅				**良好**
	匿名评阅				**优秀**

答辩委员会成员		姓　名	专业技术职　务	是否博导（硕导）	所 在 单 位
	主席	李澄	教授	博导	中国科学技术大学
	委员	邢宏喜	研究员	博导	华南师范大学
		赵宇翔	研究员	博导	中国科学院近代物理研究所
		周剑	教授	博导	山东大学
		刘天博	教授	博导	山东大学
		杨驰	教授	博导	山东大学
		张金龙	教授	博导	山东大学

答辩委员会对论文的总体评价	优秀	答辩秘书	苟兴瑞	答辩日期	2024-05-22
备注					